Design of Transition Metal-based Nanomaterials for Electrochemical Energy Conversion and Storage

Lu Chen

A Thesis
in
The Department
of
Chemical and Materials Engineering

Presented in Partial Fulfillment of the Requirements
For the Degree of
Doctor of Philosophy (Chemical Engineering) at
Concordia University
Montréal, Québec, Canada

September 2021

CONCORDIA UNIVERSITY

SCHOOL OF GRADUATE STUDIES

This is to certify that the thesis prepared

By: **Lu Chen**

Entitled: **Design of Transition Metal-based Nanomaterials for**

Electrochemical Energy Conversion and Storage

and submitted in partial fulfillment of the requirements for the degree of

Doctor of Philosophy (Chemical Engineering)

complies with the regulations of the University and meets the accepted standards with respect to originality and quality.

Signed by the final examining committee:

_____ Chair
Dr. Ramin Sedaghati

_____ External Examiner
Dr. Shuhui Sun

_____ External to Program
Dr. Catherine Mulligan

_____ Examiner
Dr. Alex De Visscher

_____ Examiner
Dr. Xia Li

_____ Thesis Supervisor
Dr. Zhi Chen

_____ Thesis Supervisor
Dr. Xiaolei Wang

Approved by _____
Dr. Alex De Visscher, Graduate Program Director

September 2021

_____
Dr. Mourad Debbabi, Dean

Gina Cody School of Engineering and Computer Science

Abstract

Design of Transition Metal-based Nanomaterials for Electrochemical Energy Conversion and Storage

Lu Chen, Ph.D.

Concordia University, 2021

Electrochemical energy conversion technologies including Zn-air batteries, water splitting and energy storage devices such as Li-ion batteries, supercapacitors are booming to meet the increasing energy demands owing to their high energy density, excellent durability, low cost and feasible potability. The performance of energy conversion are largely determined by the efficiency of oxygen reactions (oxygen reduction/evolution reaction (ORR/OER)) and hydrogen evolution reaction (HER) facilitated by the high-performance electrocatalysts. While the utilizations and performance of various energy storage devices are limited by the electrode materials properties. Nowadays, transition metal-based materials exhibit their high electrochemical activities due to their adjustable morphologies, controllable structures, and low cost. However, they still face some challenges such as low conductivity, low surface area, and structure collapsing. Hence, this research studies the rational design of three types of transition metal-based nanomaterials for both energy conversion and storage. By investigating physical properties via different characterizations and electrochemical measurements, obtaining a comprehension understanding of correlation of electrocatalytic performance with material's structure and morphology while achieving the goal of " designing one type of material for multiapplication".

In energy conversion, the first is bimetallic CoNi alloy nanoparticles embedded in pomegranate-like nitrogen-doped carbon spheres (N-CoNi/PCS) for oxygen reactions. By studying the morphology configurations, we find that the porous structure possesses plentiful active sites and high surface area enables excellent electrochemical performance, which delivers a low half-wave potential of 0.80 V towards ORR and overpotential of 540 mV towards OER with excellent durability. By combining the results of physical and electrochemical properties, such porous structure play a key role to contribute to high electrochemical performance. Second, a unique

nanostructure of N and S codoped porous carbon (N,S-Co/Zn-ZIF) derived from bimetallic ZIFs as an electrocatalyst for oxygen reactions. By studying the physical properties, we find that the nanostructure forms a rhombic dodecahedron morphology with rough surface, containing abundant active sites of sulfides nanocrystals. Owing to the special structure, such bifunctional electrocatalyst delivers a superior half wave potential of 0.86 V towards ORR and overpotential of 350 mV towards OER. Third, Ni_9S_8/MoS_2 nanosheets decorated $NiMoO_4$ nanorods heterostructure is developed by hydrothermal and sulfurization as an electrocatalyst for water splitting. Core-shell nanorods with diameter of 180-200 nm consisted of 2D Ni_9S_8/MoS_2 nanoflakes as outer shell part and 1D nickel molybdate nanorods inner core, providing plentiful charge transportation channels. According to these features, such nanomaterials present high performance with low overpotentials of 190 and 360 mV for HER and OER in alkaline solution, respectively. Based on these, it's concluded that rational design of electrocatalyst is correlated with electrochemical performance. Furthermore, to explore the electrochemical performance of transition metal-sulfides for energy storage, N,S-codoped carbon dodecahedron/transition metal sulfides are also studied as anode materials for Li-ion intercalation. Surprisingly, such nanocomposites with rough surface area and active sites still donates high-performance Li-ion intercalation with superior initial reversible capacity of 938.2 mA h g^{-1} with a high-capacity retention of 65.6% after 100 cycles at 150 mA g^{-1}. At the same time, hetero-structural core-shell $NiMoO_4@Ni_9S_8/MoS_2$ nanorods are also studied as electrode materials for supercapacitor, which unveils unsurpassed specific capacity of 373.4 F g^{-1} at 10 A g^{-1}. Such excellent electrochemical properties prove that such core shell structure is still favorable for energy storage.

The above results all prove the successful design of three types of transition metal-based nanomaterials and different structural features contribute to excellent electrochemical performance. Thus, there is a strong relationship about structure design and electrochemical performance. Since all of nanomaterials show excellent electrochemical performance in both energy conversion and storage, we have achieved goal of "multiapplication". This research provides the effective design strategies of high-performance transition metal-based nanomaterials for multiapplication which paves a new way of development and understanding of these materials towards electrochemical energy conversion and storage.

Acknowledgments

First of all, I would like to express my sincere gratitude and appreciation to my supervisors, Prof. Xiaolei Wang and Prof. Zhi Chen for leading me to the field of research, providing the great supports in experimental setup and thesis writing, encouraging me when I meet the research challenges and helping me to solve the problems throughout my entire PhD study life. They always gave me the quickest responses and guidance whenever I sent messages and needed their precious advice.

I am deeply grateful to Professor Zhibin Ye in our department. He gave some advice about my research and publication and his students offered the great assistance and supporting when I was working in the lab. Without their helping, I couldn't finish the experiments and projects smoothly.

I am indebted to Ms Harriet Laryea, Ms Kerri Warbanski and Ms. Hong Guan, the experienced technicians of Department of Chemical and Materials Engineering and Building, Civil & Environmental Engineering, respectively. My job would have undoubtedly been more difficult without their constant technical assistance, advice, and valuable supports.

My gratitude also goes to Professor Alex De Visscher, the chair of Department of Chemical and Materials Engineering who helped me solve many problems of my PhD life study and lab working.

I am also grateful to my group member, Miss Xiaolan Gao and all the laboratory members and friends, families for their help and comforts throughout my life during the past four years.

Finally, I would like to sincerely thank my thesis committee Professor Zhibin Ye, Professor Alex De Visscher and Prof. Catherine Mulligan for their interest in my work and their valuable and constructive questions and insightful comments.

Table of Contents

List of Figures

List of Tables

List of Abbreviations

EECS	electrochemical energy conversion and storage
OER	oxygen evolution reaction
ORR	oxygen reduction reaction
HER	hydrogen evolution reaction
Pt	platinum
RuO_2	ruthenium oxide
IrO_2	iridium oxide
LIBs	lithium-ion batteries
EVs	electric vehicles
SCs	supercapacitors
RHE	reversible hydrogen electrode
ΔG_{H^*}	Gibbs free energy
KIBs	potassium-ion batteries
SSCs	symmetric supercapacitors
ASCs	asymmetric supercapacitors
HSCs	hybrid supercapacitors
EDLC	double layered supercapacitors
EDL	electric double layer
CV	cyclic voltammetry
LSV	linear sweep voltammetry
C_{sp}	specific capacitance
E	energy density
P	power density
η	overpotential
iR compensation	ohmic drop compensation
RDE	rotating disc electrode
ECSA	electrochemical surface area
DLC	double layer capacitance
I	constant discharge current

t	discharge time
ΔQ	electrical charge
ΔV	potential window
m	total mass of the electrode material
Pd	palladium
Ru	ruthenium
Ir	iridium
TMOs	transition metal oxides
TMSs	transition metal sulfides
TMPs	transition metal phosphides
AC	activated carbons
CNTs	carbon nanotubes
SEM	scanning electron microscope
TEM	transmission electron microscopy
XRD	X-ray diffraction analysis
XPS	X-ray photoelectron spectroscopy
EDX	energy dispersive X-rays
HRTEM	high resolution transmission electron microscopy
θ	Bragg angle
λ	wavelength of the electron beam
n	an integer number and the direction difference between waves
BET	Brunauer-Emmett-Teller
BJH	Barrett-Joyner-Halenda
IUPAC	International Union of Pure and Applied Chemistry
SCE	saturated calomel electrode
FESEM	field emission scanning electron microscopy
GC	glassy carbon
VC	Vulcan carbon
HAADF-STEM	high-angle annular dark-field scanning transmission electron microscopy
K-L	Koutechy-Levich
EIS	electrochemical impedance spectroscopy

MOFs	metal organic frameworks
ZIFs	zeolitic imidazolate frameworks
ESEM	Environmental Scanning Electron Microscope

Chapter 1 Introduction

1.1. Background

It's widely acknowledged that the massive requirement of energy becomes a global issue with high-speed economic growth and fast increasement of population all over the world. In consequence, traditional fossil fuels like coal, oils, nature gas are tremendously exploited and overutilized causing a series of problems, such as environmental pollution, global warming, international energy wars and shortage of fossil fuel. To achieve a sustainable society, the exploration of alternative energies that are economic, sustainable, renewable is imperatively demanding and desirable. Nowadays, many clean and new energies have been utilized including wind energy, solar power, biomass energy and hydropower but they are limited by the availability of energy sources, specific locations, low efficiency and unmature technologies.[1]

One promising approach is to electrochemical energy conversion and storage (EECS) devices that convert chemical energy to electrical energy or store electrical energy. Due to its portable, economic, high-energy density and efficiency, they have widely explored and utilized in daily life and industrial scale. Over the past decades, a diversity of energy conversion technologies and devices such as hydrogen production via water splitting, fuel cells, metal-air batteries have been broadly exploited due it save operation conditions, high energy density and excellent conversion efficiency. Specifically, metal-air batteries are made up metal anode, electrolyte and air-breathing cathode which is coated on electrocatalysts to boost electrochemical reactions. During battery charging and discharge, oxygen evolution reaction (OER) and oxygen reduction reaction (ORR) happen, respectively. For water splitting, the system includes two half reactions on the cathode and anode coated with electrocatalysts, the hydrogen evolution reaction (HER) and the oxygen evolution reaction (OER). However, the performance of these two technologies are largely determined by the kinetics of OER/ORR/HER which normally requires extra potential called overpotential to drive reaction happen. Hence, the electrocatalyst facilitating the oxygen reactions and water splitting play a key role during the electrochemical conversion.

At the same time, energy storage devices including rechargeable batteries (Li-ion batteries, metal-O_2 batteries, Na-ion batteries) and supercapacitors are the promising technologies to deal with the energy challenges. Although they possess plentiful advantages, there are still some

drawbacks hindering the further development and application in manufacturing. First, practical energy density and rate capacity still fail to meet the requirements at industrial scale. Second, the obtainable or usable capacity is inadequate and diminishment as battery cycling. Third, intensive materials losses during charging/discharging result in low efficiency and reversibility. Fourth, cycling life span is also another obstacle owning to capacitance vanishment. These problems are related with the electrode materials. Above all, the performance of these technologies are highly dependent on the electrocatalyst for energy conversion and electrode materials for energy storage devices. It's important to develop highly active materials to boost the electrochemical reaction and improve the energy storage ability.

1.2. Problem Statement

As we discussed above, the creation of energy conversion technologies and devices is mainly hindered by the reaction kinetics in the air-breathing electrode for metal-air battery and water splitting. Hence, electrocatalysts with high chemical behavior, cheapness and excellent stability are extremely needed to overcome the sluggish kinetic, reduce overpotential. Researchers found that precious metal-based materials including platinum (Pt) is the most active material for ORR and HER, while ruthenium oxide (RuO_2) and iridium oxide (IrO_2) are the superior OER electrocatalyst. Notwithstanding, their expensiveness property, instability, easy dissolution and agglomeration during the electrochemical process and their poor bifunctional behavior fail to meet the demand of large usage for application today.

As for the electrode materials in energy storage devices, we will mainly present the anode material for Li-ion batteries in this thesis. Over recent years, carbon-based materials as the most common materials are widely used for anodes in Li-ion batteries on account of its high surface area and wide pore distribution. Nevertheless, they suffer from the low specific capacity and low-rate capacity. For supercapacitors, electrode materials like carbon-based materials and RuO_2 also excellent behavior with high capacity. However, carbon-based materials are hindered by structure change and low cycling performance while RuO_2 is too expensive and scarce limit their broad applications.

Above all, novel design of new types of electrocatalysts or electrode materials is urgent to overcome these problems and such materials should possess the following features: (1) structural

diversity and easy-controlled morphology; (2) various valence states; (3) high surface area, high electrical conductivity; (4) cheapness and earth-abundance.

1.3. Research Objectives

In this thesis, we will mainly focus on the rational design of transition metal-based materials as an alternative to replace the above-discussed materials. The main research objectives can be summarized as follows:

1. Instead of pursuing materials in practical application, such as Zn-ion battery, supercapacitors, we narrow down the research perspective and focus on the fundamental study of designing and exploring materials, then test their electrochemical performance. So that we have the overall understanding about the properties and predict their values when they are used in practical applications. In addition, such fundamental study work can enlighten the road for further delving novel materials in wide-ranging field of energy conversion and storage.
2. Next step is rational design transition metal-based nanomaterials by different strategies proposed by methodology section. First, all the materials are synthesized by facile procedures to realize economic synthesis process, providing a strategy for designing materials in large-scale application. Next, morphology and structure controlling are proved to be effective strategies by optimizing pore size, surface area and actives. Also, how to improve electrical conductivity of nanomaterials is a question needed to consider. Last, study of functionality and mechanism of different compositions and heteroatoms doping is demanding.
3. After rational construction of transition metal-based nanomaterials, combining different characterizations such as SEM, TEM, XRD, BET, XPS to have a comprehensive study of morphology, structure, pores, and valences states, we have a better understanding that if we have successfully synthesized the nanomaterials and if our design strategies are effective.
4. Next, we will investigate the electrochemical performance of all nanomaterials. For electrocatalysts, activity of ORR/OER/HER, Tafel slope, stability performance are needed. For the electrode materials in Li-ion battery and supercapacitors, specific capacity/capacitance, rate performance, cycling performance are required.

5. Then we combine the result of physical properties and electrochemical results to study the relationship between them. So that we could find the strong relationship of morphology and structure design and electrochemical behaviors in order to design the high-performance nanomaterials and come up the effective design strategies.
6. Finally, we can utilize one type nanomaterials for different applications and study their different functionality. So that we can achieve the goal of "multiapplication" and offer an opportunity for design the high performance and economic materials in multiple application in the future.

1.4. Thesis Outline

The content of this thesis are organized into 6 chapters.

Chapter 1 is a short introduction of background, problem statement and research objective in this thesis.

Chapter 2 includes the brief introduction of background for energy conversion and storage technologies and devices, their working mechanism, and important parameters. The materials widely used in these devices are summarized and find the research limitation.

Chapter 3 introduces the theoretical and experimental design of transition metal-based nanomaterials of this thesis research, including the rational design strategies, the synthesis process and methods, different types of characterization measurements and electrochemical testing.

Chapter 4 describes the design and experimental process and result of transition-based nanomaterials for energy conversion. In section 4.1, we introduce design procedure and result about the CoNi alloy nanoparticles embedded in nitrogen-doped carbon spheres for oxygen reactions. In section 4.2, transition metal sulfides derived from metal-organic framework as high-performance electrocatalyst towards oxygen reactions are proposal. In section 4.3, we introduce the transition metal sulfides/oxides electrocatalyst for water splitting and their experimental procedure. By studying their structure and electrochemical performance to have a better idea about rational design and predict their properties for energy storage.

Chapter 5 presents the performance of transition-based nanomaterials for energy storage devices. In section 5.1, we propose and design the N,S-codoped hollow carbon dodecahedron/sulfides composites for the Li-ion intercalation. We discuss the experimental process and electrochemical result and analyze the mechanism. In section 5.2, a core-shell $NiMoO_4$@Ni_9S_8/MoS_2 nanorods is

suggested and designed for supercapacitors. We also discuss the experimental part and analyze the results.

Chapter 6 includes the highlights and main contribution of thesis, and based on the results we propose some possible research directions for the future exploration.

Chapter 2 Literature Review

In this chapter, we will have a concise overview of energy conversion technologies (e.g., oxygen reactions; water splitting) and energy storage devices such as lithium-ion batteries (LIBs) and supercapacitors and their working mechanisms. Next, we will introduce some important parameters which are widely used to measure the performance of these technologies and devices. The current limitations of research are discussed in the subsequent section.

2.1. Working Mechanism of Energy Conversion Technologies and Storage Devices

The overuses of non-renewable oil and other fossil fuels lead to rapid energy consumption, global warming, and environmental pollution. To realize the sustainable development of economics, it's necessary to explore clean, renewable, and environmental-friendly energy system. Although sustainable energy sources such as sunlight and wind hold the promising future, but their wide-ranging use is limited by distance and affordability. Consequently, demand is on the rise of electrochemical energy conversion and storage (EECS) devices by converting chemical energy or electrical energy, and store/release them based on the redox electrochemical reactions with high energy power density, affordability, long durability, and large-scale portable feasibility.[2] Metal-air batteries, water splitting, and fuel cells through electrocatalysis are the most basic, effective, and dependable energy conversion technologies. In the last few decades, energy storage systems have achieved considerable popularity as lightweight compact electronic equipment and are widely used in electric vehicles (EVs) On account of high energy capacity and cheap cost, various types of rechargeable batteries, such as Li-ion batteries, and supercapacitors (SCs), are extensively researched. Here we will introduce the definition and working mechanism of each type of devices and technology as follows.

2.1.1. Energy Conversion Technology

2.1.1.1. Oxygen reactions

Metal-air batteries as typical energy conversion technology have become a promising power source, due to the nature of superior theoretical energy density and plentiful-oxygen fuel from the atmosphere, facile assembling process, and environmental-benignity. Among the all types, Zn-air batteries have received a lot of interest on account of their high specific energy density (1086 W h kg^{-1}), high performance, and low cost.[3] They consisted the metal anode, air-cathode including electrocatalyst layer, electrolyte, and separator (**Figure 2.1**).[4]

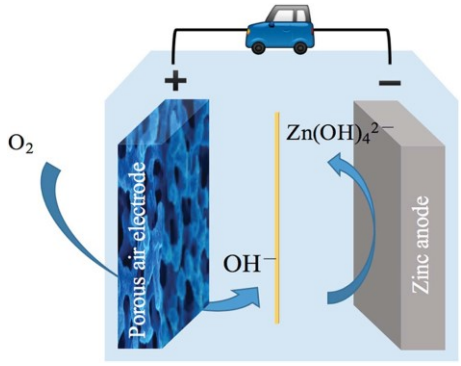

Figure 2.1 Scheme of a typical Zn-air battery.

In alkaline electrolyte, during the discharge, the disparity in oxygen pressure between the exterior and interior of the battery allows atmospheric oxygen to permeate the porous cathode, and the electrocatalysts prompt oxygen reduction reaction; at the same time, the metal zinc is oxidized to form soluble zincate ($Zn(OH)_4^{2-}$) ions by loose electrons.[6] When the battery is charged, the reverse reaction (oxygen evolution reaction) occur and metallic Zn is plated at the anode. The reactions of discharging are illustrated as below:

$$\text{Anode : } Zn \rightarrow Zn^{2+} + 2e^- \quad (1)$$

$$\text{Cathode: } O_2 + 2H_2O + 4\,e^- \rightarrow 4OH^- \quad (2)$$

As mentioned above, based on discharging, and charging processes, electrochemical oxygen reactions including oxygen reduction reaction (ORR) and oxygen evolution reaction (OER) occur

in the cathode part. Generally, oxygen reactions determine the performance of capacity retention, efficiency, and durability of battery. Specially, ORR process typically comprises following steps as the equations below: (1) diffusion and adsorption of oxygen on the surface of electrocatalyst; (2) electron conversion from metal anode to oxygen; (3) deterioration and rupture of the O-O bond; and (4) hydroxide transports to the Zn-anode via solution.[7]

$$\text{Four electron reaction: } O_2 + 2H_2O + 4e^- \rightarrow 4OH^- \quad (3)$$

$$\text{Two electron reaction: } O_2 + H_2O + 2e^- \rightarrow HO_2^- + OH^- \quad (4)$$

As we can see, the oxygen reduction occurs though four-electron pathway or electron pathway which peroxide species are generated. These two pathways are mainly depended on adsorption method.[8] In a four-electron pathway, OH^- is reduced by O_2 sorption while two O atoms accommodate with catalyst. In two-electron pathway, O_2 is directly reduced to OH^- due to end-on oxygen adsorption while one oxygen atom is opposite to the catalyst. The peroxide species generated from two-electron pathway are caustic and have a negative impact on the electrolyte's stability. Hence, four-electron is more desirable. In OER, O_2 is generated through several proton/electron coupled procedures. Different from ORR, because of its more complicated electrochemical reactions, the OER mechanism is arduous to explain, and pH of the reaction is extremely important.[9] Two water molecules are corroded in acidic media, yielding four protons (H^+) and one oxygen molecule, thus losing four electrons. In basic media, oxidation of hydroxyl groups (OH^-) occurs generating H_2O and O_2 with the same number of electrons involved. The two equations are described as below:

$$\text{Acidic electrolyte: } 2H_2O \rightarrow 4e^- + O_2 + 4H^+ \quad (5)$$

$$\text{Alkaline electrolyte: } 4OH^- \rightarrow 2H_2O + 4e^- + O_2 \quad (6)$$

According to the Nernst equation, an external voltage of 1.23 V (*vs.* reversible hydrogen electrode (RHE)) is needed to drive reaction happen.[10] Since both ORR and OER involve the multi- step reactions, the kinetics are extremely torpid and lead to lavish overpotential (η), demanding additional energy to surmount. Therefore, bifunctional electrocatalysts are highly

demanded to decrease the activation energy and facilitate reaction rate and overcome energy barriers.

2.1.1.2. Water Splitting

Hydrogen has been broadly regarded as economic and desirable energy for replacing traditional energy sources due to its superior energy transfer efficiency, excellent energy density, zero CO_2 emissions, and environmental compatibility. However, there is no actual hydrogen on the planet, so it had to be made from other materials. At present, the steam reforming process is the mature strategy to produce hydrogen for large-scale. However, combustion of fossil fuels and large production of CO_2 hinder the development of this method. Therefore, it is desperately necessary to exploit a safe, renewable, and effective hydrogen generation strategy.[11] Water splitting technologies are widely used to produce hydrogen for the energy conversion due to stable form of water. This method utilizes a huge amount of water to produce high quality hydrogen at a low cost while emitting no CO_2 or other contaminated gases and without requiring a high temperature.[12]

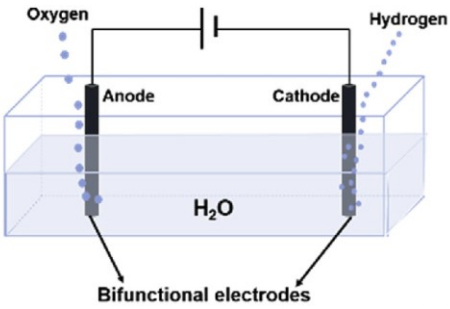

Figure 2.2 Schematic illustration of an electrolytic cell.

As illustrated in **Figure 2.2**, electrolysis cell for water splitting is made of anode, cathode, and electrolyte. Bifunctional electrocatalyst are utilized in both anodes and cathodes to boost the electrochemical reactions. It includes two half reactions on the cathode and anode, the hydrogen evolution reaction (HER) and the oxygen evolution reaction (OER), respectively.[13]

$$\text{Total reaction } H_2O \rightarrow H_2 + 1/2O_2 \quad (7)$$

In acidic solution

$$\text{Cathode: } 2H^+ + 2e^- \rightarrow H_2 \quad (8)$$

$$\text{Anode: } 2H_2O \rightarrow O_2 + 4H^+ + 4e^- \quad (9)$$

In neutral or alkaline solution

$$\text{Cathode: } 2H_2O + 2e^- \rightarrow H_2 + OH^- \quad (10)$$

$$\text{Anode: } 2OH^- \rightarrow H_2O + 1/2O_2 + 2e^- \quad (11)$$

HER is a multi-step procedure that involves two-electron transferring on the electrode surface through two distinct mechanisms, with three potential pathways. It happens depending on either the Volmer-Heyrovsky or Volmer-Tafel mechanisms. Here we mainly discuss the alkaline electrolyte the reaction happens based the ensuing steps[14]:

(1) A proton from water molecule is combined with an electron forming the adsorbed hydrogen intermediate (H*).

$$H_2O + e^- + * \rightarrow H^* + OH^-, \text{ Volmer reaction} \quad (12)$$

(2) The adsorbed hydrogen specie absorbs a water molecule and one electron at the same time, resulting in the formation of a hydrogen molecule.

$$H^* + H_2O + e^- \rightarrow H_2 + OH^-, \text{ Heyrosky reaction} \quad (13)$$

(3) Two absorbed hydrogen species are joined concurrently, generating H_2.

$$H^* + H^* \rightarrow H_2, \text{ Tafel reaction} \quad (14)$$

From above reactions, * represents the catalyst surface and H* is the intermediate hydrogen taken in. Multi-phase HER begins as proton release step, which is also called the Volmer reaction. After via two alternative reaction paths the formation of molecular hydrogen can be followed by either the Heyrosky response or the Tafel Reaction.[15] Due to the water molecule dissociation, the reaction rate of HER in basic electrolyte is very creeping. Looking insight of all pathways, H* is always participates in the HER. Therefore, Gibbs free energy (ΔG_{H^*}) is considered as a standard to measure the rate of HER. The electrocatalyst which ΔG_{H^*} is close to zero shows the high efficiency for HER process since slow adsorption leads to low proton-electrode surface interactions; while electrocatalysts with high ΔG_{H^*} easily impede H_2 by breaking the bonds between hydrogen and catalyst surface.[13]

The pH of electrolyte largely determines the HER rate. According to the Nernst equation, the thermodynamic voltage of water splitting is 1.23 V (*vs.* RHE) in standard condition notwithstanding the reaction media. However, in practical water splitting process, in order to drive reactions, greater potential is required than theoretical potential. The excess potential is also defined as overpotential for electrocatalysis, which is primarily intended to overcome both cathode and anode intrinsic activation obstacles. Also, some factors such as electrode resistance, electrolyte diffusion blockage, bubble production should also be considered. The principal research challenge in this respect is the development of effective bifunctional electrocatalysts, which reduces energy barriers and increase the efficiency of water splitting.

2.1.2. Energy Storage Devices

With the accelerating progression of smart electronic devices, and electronic vehicles, the necessity of energy storage devices and technologies assembled with cost-efficient, environmentally benign, superior specific capacitance, and electrode materials with long life span increase sharply. It stimulates the exploration of various types of rechargeable batteries, such as Li-ion batteries, lithium-sulfur batteries, potassium-ion batteries (KIBs), with high energy density and supercapacitors (SCs).[16] Li-ion batteries have already widely utilized in daily life and industrial-scale due to their remarkable energy and power density. However, their defective safety and poor durability fail to reach the expectation for wide-reaching application in industry. More and more attention has switched to development of Na-ion batteries and K-ion batteries because of decreased metal reactivity and great richness. In addition, on account of their high energy density and fast charge/discharge operation, supercapacitors (SCs) have emerged as a potential energy source. In this thesis, we mainly introduce the mechanism of Li-ion batteries and supercapacitors as below.

2.1.2.1. Lithium-ion Battery

Since the first study of LIBs in 1991, substantial attempts have been made to investigate their properties related to energy density, cycling performance, and safety property.[17] Up-to-now, it have been utilized in extensive variety of portable devices and industrial scale like electric vehicles. The best energy density of LIBs in record in 1991 was 90 Wh kg^{-1}.[18] Currently, the energy density could reach around 120 to 220 Wh kg^{-1} by modifying the electrode material, electrolyte, separator, binder, and current collector. Therefore, in the near future, high performance battery system with excellent

power density could be designed and over the current limit. Thus, without any doubt, Li-ion batteries own several advantages. First, they have high special energy density enabling applications of potable devices or industrial scale. Second, they have durable cycle life, high round-trip efficiency and adequate operational temperature range.[19] Third, it's more environmental-friendly compared to Ni-Fe batteries or lead-acid batteries.

Li-ion battery is made of an anode, cathode and electrolyte as presented in **Figure 2.3.** For commercial Li-ion batteries, anode is usually graphitic carbon. As cathode materials layered oxides $LiMO_2$ or spinel type LiM_2O_4 compounds (M = Co, Ni, other transition metals) have mostly been used.[20] The electrolyte is a solution of a lithium salt typical as $LiPF_6$ in a mixed organic solvent with infiltration of the separator.[21]

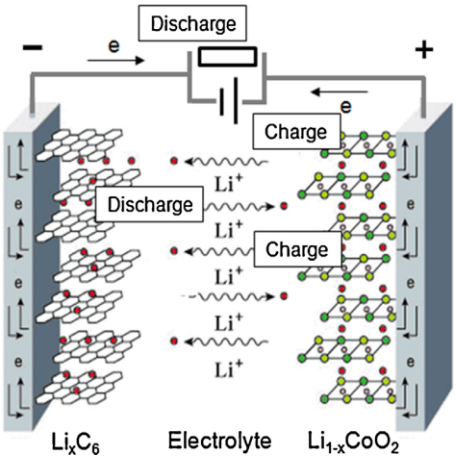

Figure 2.3 Schematic of lithium-ion battery.

During discharging, the electrochemical reactions could be written as below[23]:

$$\text{Cathode: } Li_{1-x}MO_2 + xLi^+ + xe^- \rightarrow LiMO_2 \quad (15)$$

$$\text{Anode: } Li_xC_6 \rightarrow xLi^+ + xe^- + 6C \quad (16)$$

$$\text{Total reaction: } Li_{1-x}MO_2 + Li_xC_6 \rightarrow LiMO_2 + 6C \quad (17)$$

When the battery is charged, the reactions are reversed. For typical Li-ion intercalation batteries, they follow the "rocking-chair" principle, which as shown above.[24] During the charging and discharging, only the Li^+ can transport between the anode and cathode via electrolyte, while the electrons move through the exterior circuit to complete the reaction. Ideally, the reversible battery voltage could be calculated by the redox voltage contrast between the Li^+/Li anode and transition metal oxide cathode during the battery discharge. While during the battery charge, external voltage

is needed to drive the reaction. Lithium ions are realized from the lithium metal oxide in the cathode, transfer through the electrolyte, and are finally inserted into graphite carbon anode. At the same time, metal is reduced from lithium metal oxide. The free electrons are driven across through the external circuit to remain charge neutrality.[25] In practical, the voltage is determined by the properties of anode, cathode material and electrolyte.

However, there are still some challenges remaining for the anode, cathode, and electrolyte. Both anode and cathode electrodes determine the performance of batteries. Here, we mainly discuss on the problem of cathode and anode materials. Cathode materials meet certain obstacles that must be overcome before they can obtain the acceptable performance. First, low conductivity of materials results in poor kinetics, leading to the low-capacity and reversibility of conversion reactions. Second, low energy efficiency results from voltage hysteresis. Third, conversion type materials suffer from large volume changes during the charge/discharge, as well as numerous unfavourable reactions between active materials and electrolytes, both of which may result in low cycling performance and coulombic quality.[26] Besides, anode materials also suffer from degradation caused from SEI formation and Li plating, resulting in the impedance increase, power fade and capacity fade. In addition, low initial coulombic efficiency and poor reversibility are ascribed from structural change and high-volume expansion. Third, dissolution of the active materials leads to unacceptable electronic conductivity or mechanical contact within the anode, which further results in capacity losses and increasing cell resistance.[22] The dissolved species can also precipitate in the reactions, potentially compromising the stability and properties of its SEI, resulting in irreversible Li losses and resistance increase. Hence, rational design of electrode materials is imperative to solve the above problems.

2.1.2.2. Supercapacitors

Besides batteries, supercapacitors (SCs) have been considered as a promising and long cycle life energy storage device in the next generation due to their large capacity and high power density with low cost.[27] Compared to traditional electrolytic capacitors, supercapacitors not only own their features with unlimited cycle life, high electric strength but also can store plentiful energy than traditional capacitors.[28] Since supercapacitors have high power density fast dynamics of charge propagation, they can be utilized in many applications where store or release huge amount of energy in a very short time. Currently, the supercapacitors are used mainly for automotive industry

such as hybrid EVs, and portable electronic devices. With respect to batteries, supercapacitors have plentiful advantages such as higher peak currents, acceptable reversibility, safe operation, unsarcastic electrolyte and low material cost. Albeit supercapacitors provide large power density, most commercial supercapacitor devices possess a specific energy density less than 10 Wh kg^{-1}, which is much lower than Li- ion batteries (150 Wh kg^{-1}).[29] Therefore, there has been intensive research effort in enhancing the performance of supercapacitors to approach and exceed that of batteries.

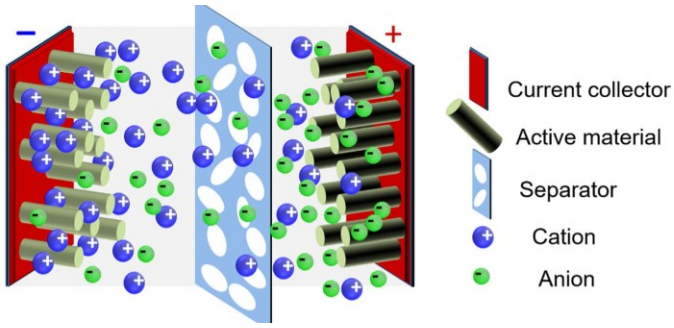

Figure 2.4 Scheme of the configuration of a typical supercapacitor.

As illustrated in **Figure 2.4**, a standard supercapacitor is made up of two operating electrodes with active materials coated on current substrates, electrolyte, and an electrically isolated separator between the two electrodes. Depending on device structure and storage working mechanisms of electrode materials, there are three categories of SCs: symmetric SCs (SSCs), asymmetric SCs (ASCs) and hybrid SCs (HSCs). While in conformity with energy storage rule of electrode materials, SCs can be divided two types: double layered supercapacitors (EDLC), pseudo-supercapacitors.[31]

EDLC supercapacitors utilize liquid electrolyte and have been widely used in commercial market. The mechanism is that a reversible electrolyte ion sorb at the electrode or electrolyte surface, resulting in an electrically double-layered field.[32] During charging, electrons are transmitted from the cathode to the anode via circuit wire. Consequently, cations within the electrolyte gather in cathode and anions in anode to form an electric double layered (EDL) in order to maintain the exterior charge balance. In reverse, when SCs is the discharging, electrons travel from the anode to the cathode via an external route with the ion transport between two electrodes

till the discharging completed.[33] Ions in a bulk electrolyte migrate in a different manner from transporting in electrode. The pore size has a significant impact on the movement of ions into the pores. Large pores are beneficial for ion transport, favoring double layer capacitance. Therefore, the electrode materials possess large surface are and pore volume are recommended to be utilized for this type SCs. For example, carbon-based material like carbon nanotube, graphitic carbon.

The Faradaic charge storage system is used in pseudo-capacitors, which have quick and extremely reversible redox reactions, which enable SCs perform higher charge storage capacity. It also has two electrodes that are bound by an electrolyte. The chemical reactions occur at the electrode and stores the electrical charge storage without contacting between the electrode and the ions. Fundamentally, different charge mechanisms can be classified for pseudo-capacitors: pseudo-capacitance manipulated by surface redox reaction (reduction-oxidation reactions) or commanded by intercalation. Charges can be stored through surface redox reaction procedure by sorption of cations and anions in the electrolyte on the surface of the electrode happening faradaic redox reactions. During the reactions, the oxidization state of species is charge constantly. Once accepting the electron, a reduction reaction happens that material species is reduced. In reverse, losing electrons and enhancing of ion or atom is referred to as oxidation.[28] The reversible intercalation/de-intercalation of electrolyte cations into the crystal structure of electrode materials is conducted by the pseudo-capacitance intercalation mechanism.[30] To retain the electrode's electrical neutrality, a significant number of electrons are involved and transported to the host during inversion. However, it is constrained by the ion's tendency to disperse the electrode material.[28]

Electrode materials for pseudo-supercapacitor with phase transformation during the electrochemical process could be considered as “battery-type” materials.[34] The electrochemical process of these type materials is usually ion diffusion-controlled and experienced “phase-transformation” ion intercalation which obviously reveal from oxidation/reduction peaks of electrochemical reactions curves. Although they have high charge storage capacitors, they endure sluggish kinetics during electrochemical process because of the slow material phase transition.[35] Hence, structure modification and optimization related with particle size and morphologies should be explored of these materials to have high specific surface area, which provides ample active sites and reduce ion diffusion pathway in solution. Transition metal-based materials, carbon and other hybrids are normally used to structure such electrodes due to their morphology and structure feasibility, which we will mainly focus on and further discuss in the next section.

2.1.3. Electrochemical Parameters

For both OER/ORR/HER, the performances of electrocatalysts are normally measured cyclic voltammetry (CV) or linear sweep voltammetry (LSV). Based on these, there are serval parameters like onset/overpotential, Tafel slope, stability, and specific activity to evaluate electrochemical properties and offer key information to explore mechanisms. While for energy storage like Li-ion batteries and supercapacitors, capacity, specific capacitance (C_{sp}), energy density (E), and power density (P) play a key role in investigating for performance of electrodes.

2.1.3.1. Onset/Over Potential

Onset potential is a significant factor to investigate the electrochemical reactions, in which the lowest potential in anodic reaction or highest potential in cathode reaction. As we discussed before, the ideal thermodynamic equilibrium potentials are 0 V and 1.23 V for HER and OER in alkaline electrolyte, respectively. Nevertheless, additional voltage is mandatory to facilitate the reactions because of the sluggish kinetics, which known as overpotential (η). Usually, overpotential is measured at current density of 10 mA cm^{-2} considering it's a common measurement expected in 12.3% efficiency from solar to hydrogen device.[36] Thus, to corresponding to solar water splitting, the overpotential at current density of 10 mA cm^{-2} is also employed to compare the electrocatalysts of HER in electrochemical water splitting. Commonly, three types overpotentials, activation, concentration, and resistance over-potential, are reported to result in the total values.[14] The over-activation potential depends on the electrocatalyst's intrinsic property, so it's significant to design the excellent electrocatalysts to low the value. Overpotential can be divided into concentration overpotential correlated with the concentration difference of the involved ions between the electrolyte and the electrode surface and resistance overpotential which is produced through the electrode interfaces and occurs at measuring device surfaces and interfaces. As the reactions begin, the concentration overpotential of the surface of electrode happens owing to the rapid concentration decrease near the interfaces. Therefore, stirring the electrolyte to facilitate the ion diffusion so that reduce the overpotential.[37] The resistance across the surfaces and interfaces will cause the extra potential decrease, leading to measured potential is not reliable which is larger than the actual value.[11] Hence, ohmic drop compensation (*iR* compensation) conducted by the electrochemical station is utilized to eliminate the resistance overpotential during the measurement. Besides, bubble effect also leads to the overpotential. During the OER/HER, plenty of bubbles are created on the

surface of electrode and if they can not get away, it's detrimental for materials' active parts and increase the reaction overpotential. Hence, to deal with the problem, rotating disc electrode (RDE) with different speed is utilized to measurement the performance.

2.1.3.2. Tafel Slope

Tafel slope is another indicator to investigate the reaction kinetics and charger transfer ability of electrocatalysts. Tafel slope can be achieved via plotting curve of log (current density) and over-potential, according to the equation below[38]:

$$\eta = a + b \log (j) \tag{19}$$

where η, j, and a are the over-potential, current density, and Tafel constant, respectively. b is Tafel slope revealing the kinetic rate of electrocatalyst. Small Tafel slope value demonstrates that rising the same amount of current density requires a lower overpotential, reflecting a boosted charge transport kinetics. When η equals to zero, the calculated j is exchange current density (j_0), revealing that the instinctive electron transport rate between the electrolyte and electrode is in thermal equilibrium situation and is associated with the property of electrocatalysts.[13] Additional, Tafel slope unveils the mechanism of three pathways of HER reaction. Accordingly, the ideal Tafel slopes of the Volmer, Heyrovsky, and Tafel pathways are estimated to be 118.2, 39.4, and 29 mV dec^{-1}, respectively.[39] If the calculated value of s representative electrocatalyst nears 118.2 mV dec^{-1} which means that the Volmer reaction is the rate-controlled procedure and the adsorption of hydrogen atoms onto the catalyst surface has a slow kinetics. If the Tafel slope in the experiment is measured approaching 39.4 mV dec^{-1}, HER process is a determined by Heyrovsky pathway while desorption procedure decided the production of H_2. If the value is close to 29.6 mV dec^{-1}, the reaction is mainly restricted by the adsorption of involved H atoms and the production of H_2.[39] Therefore, Tafel slope is an essential factor to measure reaction kinetics while designing the efficient electrocatalysts with a proper Tafel slope is necessary to boost the OER/HER/ORR.

2.1.3.3. Stability

Undoubtedly, stability is fundamental factor for the electrocatalysts to check if the materials can remain the same activity after long operation period. Generally, it can be measured by the CV or electrolysis method (galvanostatic or potentiostatic electrolysis).[40] The cycling measurement via

CV is conducted by repeating the electrochemical cycles. Commonly, it's better that cycle numbers could more than 1000 times in order to obtain the superior stability of materials. The galvanostatic or potentiostatic electrolytical investigation shows the voltage or current density change with time at fixed current density or potential. Usually, current density at 10 mA cm^{-2} is commonly applied as the conventional value. Also, the period of measurement is up to 12 hours to evaluate the catalytic stability. In Li-ion battery or supercapacitor, stability measurement is also called cycling performance, which shows the capacity variation of material tested in constant current density.

2.1.3.4. Mass and Specific Activities

Mass and specific activities are other quantifiable factors to demonstrate the electrocatalysts catalytic activities. Mass activity is described by amperes per gram (A m^{-1}), which is the current over electrocatalyst loading in the electrode. Specific activity is described as current normalised by electrochemical surface area (ECSA), representing the intrinsic performance of electrocatalyst. Here, we mainly discuss the electrochemical surface area which is frequently utilized to investigate the cumulative quantity of active sites on an electrocatalyst surface and widely explored in the recent research.[41] One method is to decide ECSA by electrochemical measurement is through the double layer capacitance (DLC), which is used for non-precious metal-based electrocatalysts. A rectangular CV scan with a large current plateau around the potential range is suitable for better approximating the ECSA. The slope of the linear fit may be calculated as the electrochemical double-layer capacitance by drawing the measured capacitive current densities at the mean potential in the applied range as a function of the scan rate (C_{dl}).[42] The equation of ECSA could be written as below:[42]

$$\text{ECSA} = \frac{C_{dl}}{C_s} \tag{20}$$

Where C_s is the specific capacitance of the sample and C_s = 0.022-0.130 mF cm^{-2} in KOH or NaOH solution.[43] To estimate ECSA, we use general C_s = 0.05 mF cm^{-2} in 0.1 M KOH, while C_s = 0.04 mF cm^{-2}.[44, 45] By calculating the ECSA, it's better to understand the morphology, shapes, sizes and porous structure of electrocatalysts which offer us a promising strategy to design high performance electrocatalysts.

2.1.3.5. Capacitance

For the energy storage devices, like Li-ion battery or supercapacitors, The total capacitance (C) of is a reflection of electrical charge storage ability under a specific voltage change, the equation can be written as below[28]:

$$C = \frac{\Delta Q}{\Delta V} = \frac{It}{\Delta V} \tag{21}$$

In supercapacitors, I is the constant discharge current (A), t is the discharge time (s), ΔQ is electrical charge, ΔV is the potential window (V). To better measure the property, when we apply the mass of material, we can obtain the specific capacitance (C_{sp}), the equation is also below[46]:

$$C_{sp} = \frac{It}{mV} \tag{22}$$

m is the total mass (g) of the electrode material. For supercapacitors, we usually measure C_{sp} by constant current charge-discharge measurement, which charging and discharge are carried out at a steady current before a predetermined voltage is achieved. Specific capacitance is an important factor to measure the capacity storage of materials. Hence, choosing the materials with high capacitance is significant for both batteries and supercapacitors.

2.1.3.6. Rate Capability

Rate capability has another parameter for designing Li-ion batteries. To measure it, we can calculate the specific capacitance tested in different current density. Usually, the electrode is conducted from low current density to large current density and final back to low current density. From the variation of specific capacitance, we can elevation the performance of electrode. Rate capability is important to value the performance of electric vehicles.

2.2. Electrocatalysts for Energy Conversion

As we discussed above, electrocatalysts play a significant role in enhancing power capacity, energy density and cycling in metal-air batteries and facilitating the chemical kinetics in water splitting. In recent years, massive elbow greases have been devoted in the exploring of oxygen electrocatalysts for metal-air batteries. Furthermore, owing to common ideas, most of the electrocatalysts used in metal-air reactions could also be used in water splitting, so various methods

and techniques are used to facilitate the behavior of reactions. In this thesis, we mainly divide the electrocatalysts into the following two types of categories: (1) precious metal-based electrocatalysts; (2) transition metal-based electrocatalysts, including transition metal oxide, alloy, sulfides, phosphides.

2.2.1. Precious metal-based electrocatalysts

Precious metals, as well as their alloys, oxides, and even compounds have been wide-ranging used in oxygen reactions towards implementations such as fuel cells, water splitting and metal-air batteries, due to their excellent electrocatalytic performances. Precious metals, including platinum (Pt), palladium (Pd), ruthenium (Ru), and iridium (Ir) have been investigated in different compositions as bifunctional electrocatalysts due to their unique characteristics. First, many precious-metal complexes having low-valences are stable enough for oxygen to endure a variety of important catalytic transformations under ambient conditions. Second, precious metal forms metal-metal bond and special structures. As a typical noble metal, due to its superior activity, Pt is one of the earliest precious metals and the most powerful electrocatalyst for ORR and HER reactions. Especially, (110) crystal plane of Pt exhibits the lowest ΔG_{H^*} shows the high efficiency for HER process. However, scarcity and expense of Pt hinder the wide usage so many strategies have been considered to maximum utilize the activity of Pt. First, fabricating Pt with micro/nanostructure, tuning the size and morphology with more dimensional structure so that create ample active sites and expose (110) crystal plane of Pt to improve ORR and HER performances.[47] Pt-based nanomaterials with diversified structures and easily modified electron patten have been rationally developed and manufactured over the last decade. For example, Lou et al. reported 3D Pt nano-assemblies exhibit superior high stability with intensive voltage cycles and excellent electrocatalytic properties.[48] Yang's group synthesized the PtPd nanorods with high-coordination numbers of the growing low-index surfaces showing high-catalytic properties.[49] Moreover, 2D Pt membranes and 3D nanonetworks have been widely explored due to their outstanding porosity and remarkable surface area.[50, 51] Another approach for improving efficiency and lowering costs is to alloy or change Pt with other precisou metals or low-cost transition metals as alternatives to Pt-based electrocatalysts. For instance, Markovic's group deposited 3D-Co/Ni/Fe/Mn hydroxides on Pt and Au substrates with active sites and they exhibited the remarkable ORR and HER properties.[52] Many bimetallic catalysts (PtCo, Pd-Pt, and Pt_3Ni) have

demonstrated significant changes in operation and stability by changing the electronic structure and increasing the active facets.[53, 54]

In comparison to Pt/Pd-based electrocatalysts, Ir and Ru-based electrocatalysts exhibit better active efficiency against OER, yielding lower overpotential and high activity.[41] Up-to-now, much research have investigated intrinsic activity and performance of Ir and Ru-based electrocatalysts. The intrinsic OER behaviours of nanoparticle catalysts are found to decrease in sequence Ru > Ir > Pt.[55] Albeit Ru presents the remarkable OER behavior, unsatisfying durability limit its large employment. Hence, designing more dimensional with various morphologies structure is necessary to achieve excellent activity and remarkable stability. For instance, 3D ultrathin Ir nanosheets Ir had design and obtained excellent catalytic performance in different electrolyte mediums with low Tafel slop.[56]

Regarding to oxides, the most active electrocatalysts for OER are iridium oxide (IrO_2) and ruthenium oxide (RuO_2). They possess flexible redox state, which has wide modulation space in response to the alter in valence state induced by adsorption/desorption for oxygenated species.[57] Most recently, it's found that Ru, Ir with its oxide also displayed high activity both in basic and acidic electrolyte.[58] However, most precious metal-based electrocatalysts still suffer from poor durability, mainly due to 1). the aggregation of catalysts attributes to the decrease of the active sites; 2). the loss of the contact between electrocatalyst and the support resulting in the poor electron transfer; and 3). the change of crystal structures where the electrocatalytic behaviors completely change. Thus, attentions on developing new catalogs bifunctional electrocatalysts have been shifted to non-precious metals.

2.2.2. Transition Metal-Based Electrocatalysts

A wide range of transition metal-based materials have recently been probed as promising substitutes for electrocatalysts in the coming decades. Transition metal with low cost and abundance feature is developed the porous materials with large surface areas and diverse pore size, which is particularly propitious for the EECS systems of batteries, water splitting, fuel cells devices. In this section, we present the various groups transition metal-based materials for oxygen reactions and water splitting, including transition metal alloy/oxides; transition metal sulfides; transition metal phosphides.

2.2.2.1. Transition Metal Alloy/Oxides

Transition metal oxides (TMOs) have attracted enormous interest in the filed of electrocatalysis (OER/ORR/HER) due to its richness, cheapness, and excellent activities behavior. Especially, metal oxides such as NiO,[59] MnO_2[60], Fe_3O_4[61] and Co_3O_4[46] are superb candidates for OER on account of various oxidized valence states ($M^{2+/3+/4+}$) serving as active center for OER.[62, 63] The electrochemical properties of TMOs are mainly depended on their morphologies, structures, crystalline nature, oxidation state, and the surface oxygen binding energy.[64] For instance, Chen's group reported hierarchical three-dimensional ordered mesoporous cobalt oxide through a template-growth method.[65] The hierarchical structure of the this material was strongly ordered and consistent, with typical pores of about 150 nm, making it easier for oxygen diffusion in electrocatalyst during oxygen reaction, resulting in a lower onset potential and increased ORR and OER activity. In another study, Li's group introduced the pomegranate-like Co_3O_4 electrocatalyst presenting the high half-wave potential of 0.842 V for ORR, and a low overpotential of 450 mV for OER.[66]

Similar to cobalt oxide, nickel oxide is also found to be capable as OER electrocatalyst. The anhydrous brucite form of nickel oxide, which has more Ni^{3+} than other structures, is thought as an excellent electrocatalyst due to satisfying conductivity. One of the advantages for nickel oxides is that they are very resistant to corrosion in the electrolyte, but they suffer from the poor stability that they exhibit the slow decreases in activity over time. There has been a lot of research done to create higher oxidation states of Ni of NiO with excellent structure. For example, Fominykh's group designed ultra-small crystalline NiO NPs, where Ni^{3+} state is produced on the surface of small particle NiO.[67] Chen's group reported Ni/NiO micro-particles with subtly distorted lattices derived from metal-organic framework created multiple nickel vacancies and exposed active sites which was favorable for electrocatalytic process.[68] Wang et al. synthesized Ni nanoparticles interpenetrated in porous NiO nanosheets exhibited excellent performance in OER/ORR. Regardless of its capability as an OER catalyst, nickel oxide has disadvantages as bifunctional electrocatalysts. Because of the shift from $Ni^{3+}$to Ni^{2+} and production of NiO impurities under high temperature condition, nickel ions is easy to migrate within crystal structures, resulting in low reversibility and unacceptable stability for their electrochemical properties.[61] Also, the ORR activity of the nickel oxide catalyst fail to meet the requirement. Hence, their robust OER property

but weak ORR behavior demonstrates that it's necessary to combine other materials to achieve the high performance as bifunctional electrocatalysts.

Manganese oxides attract many interests as bifunctional electrocatalysts for electrochemical reactions due to their lavish presence in nature and multiple valence states which is widely applied in water splitting. Manganese oxides have over thirty different crystal configurations and three different oxidation states due to manganese's octahedral composition, which allows for various structural variations, most often layered or tunnelled structures.[69] Such tunable structures also are beneficial for saving H_2O and other species within its pores structure. For example, Meng et al. reported four structures of manganese oxides consisting tunneled structures, a tetragonal structure and layers of spherical structure.[70] More importantly, nano-structing of manganese oxides to maximum utilize its advantage is widely explore in electrochemistry. For instance, α-MnO_2 electrocatalysts of nanoparticle, nanotube and nanowire were explored by Muruganb's group.[71] Among them, α-MnO_2 nanowire had the lowest onset potential which was superior to others at 0.25 mA cm^{-2}. Also, Zhang et al. reported α-MnO_2-SF catalysts with large tunnels and active sites was favorable for ion transport in electrochemical process.[72] However, the conductivity of manganese oxides is even low than nickel oxides, so that more efforts should be devoted to optimizing both the structure and conductivity.

Although have been demonstrated to be promising electrocatalysts and have shown moderate activities as bifunctional catalysts in alkaline electrolytes. However, their ORR activities as single metal materials are unsatisfactory due to sluggish kinetics and require effective catalysts to facilitate the direct four electron pathway mechanism. Recently, the production of electrocatalysts has been a subject of research through the formation of bimetallic oxides such as nickel and cobalt based on the fact that in bimetallic systems, the incorporation of secondary atoms to multivalent transition metal material such as Mn, Co, and Fe can improve ORR activity and stability. As a result, mixed-metal materials have sparked a lot of interest in the ORR and OER because of their additional benefits, such as greater structural stability and the possibility to perform the excellent properties both in ORR and ORR through the mixed composition.[73] For instance, Guo et.al introduced NiO/CoN nanowire arrays with intensive connection within nickel oxide and cobalt nitride, creating plentiful oxygen vacancies which is favorable for electrocatalytic activity.[74] In addition, Ni-/Mn-decorated Co_3O_4 nanoparticles yields an low overpotential of 399 mV for ORR and overpotential of 381 mV for OER.[75]

Alloying is promoted as a clever method of increasing the catalytic behavior and lifespan of transition metal compounds. Transition metal alloys with a synergistic combination of different metal and increase active surface areas, showing the excellent electrocatalytic property. For example, Li's group introduced NiCo alloy nanoparticles encapsulated in N-doped carbon structure displayed low half-wave potential of 0.83 V for ORR and overpotential of 380 mV for OER.[76] Zhou's group introduced CoFe alloy nanoparticles endorsed on N-doped CNT by facile and controllable approach.[77] Li's team fabricated Ni_3Fe alloy-encapsulate CNT developed on N-doped carbon nanofibers, forming one-dimensional configuration with abundant active sites and ion transfer channels. The whole structure could optimize the electronic configuration of exterior carbon fibers, thus elevating the electrocatalytic activity.[78] However, transition metal alloy suffer from the corrosion and oxidation in alkaline or acidic electrolyte during the OER/ORR/HER process, which negatively effect the stability of electrocatalysts. Hence, it's compulsory to construct the morphology and architecture of transition metal alloy to avoid corrosion and oxidation in the future research.

2.2.2.2. Transition Metal Sulfides

Recently, transition metal sulfides (TMSs) materials have received a lot of interest for hydrogen/oxygen electrocatalysis for the sake of excellent electrical conduction, multiple valence states. Many scholars have varied ideas on the significance of S atoms in TMSs related with their electrocatalytic behavior. It's believed that the electron structure of sulfur atom decide the performance of TMSs. Researchers found that sulfur atom has an ability to exact electrons from other elements such as C as long as sulfur maintain the higher electronegativity than others. Hence, we can know that S atom play a key role as active site with the aim of stabilizing the intermediates during the whole reactive procedure. In addition, sulfur atom could produce much defects and vacancies to modulate the electronic arrangement and has a tendency to dissociate water molecule so that it facilitate the catalytic procedure.[79] Currently, MoS_2, Ni_xS_y, Co_xS_y and fabrication and catalysis are the most reported TMSs.

Among them, 2D layered structure of MS_2 (M=Mo, W) have been most extensively developed and considered as a promising alternative HER electrocatalyst. It's shown that bulk MoS_2 fail to perform the excellent electrochemical behavior and it's determined by the amount of reaction sites and edge sites. Moreover, since MS_2 is widely utilized in semiconduction area, it displays more

satisfying electronic conductivity compared with its oxides. Even some layered compositions own the metallic feature as desquamated into multi-layered architecture. Hence, it's desirable to design and modify the structure of MS_2 to optimize the properties. For example, Tour's group reported sponge-like edge-oriented MoS_2 films via facile reaction of sulfur vapor. The obtained material delivered excellent HER performance along with superior durability.[80] In addition to tailor the edge surface, creating the number of active sites is another method. Cui et.al prepared a MoS_2 ultra small film perpendicularly grown on a horizontal plate. The obtained MoS_2 catalyst with rich edges showed superior HER catalytic performance.[81]

Besides of Mo/W, Ni and Fe are cheaper and more abundant and logically the related sulfides have been extensively researched to improve electrochemical property. For example, three-dimensional porous Ni_3S_2 designed on porous Cu films exhibited outstanding HER property in a wide pH range a superior durability.[82] Additionally, the unique architecture accelerated the mass transport and favored more efficient utilization of active sites. For instance, 3D porous MoS_2/Ni_3S_2 foam electrocatalyst with truncated, hexagonal, sheet-like morphology showed excellent HER performance.[83] Fe-based sulfides also unveil excellent behavior as HER, OER and ORR electrocatalysts. For instance, iron-nickel sulfide nanosheets converted from a OH^- precursor presented remarkable overpotential of 105 mV in HER.[84] Another interesting Fe-Ni-S material was designed and reported by Yu's group.[85] They synthesized two-dimensional $FeNiS_2$ nanosheets and used them as bifunctional oxygen catalysts. The nanosheets revealed a low overpotential of 310 mV in OER and a higher onset potential of 0.78 V. Although the transition metal sulfides exhibited excellent performance, they still suffer from low conductivity and phase transformation during the electrocatalytic process. Hence, effective structure modification and various composition is demanded to optimize the properties.

2.2.2.3. Transition Metal Phosphides

Transition metal phosphides (TMPs) also have intensively researched possibilities owing to outstanding electrochemical behaviors and economic expense, and robust stability towards HER in acidic and basic as well as neutral electrolytes. The superior of performance is also mainly due to the feature of P. Similarly, as S atom, P atoms in metal phosphides can draw the electron from the metal because of their remarkable electronegativity. As a result, phosphide atom with negative electrons can attract positive charge. For this reason, metal phosphides with an increased relative

P content usually showed improvement in the catalytic performance.[86] For the same metal phosphides, increasing the P atomic contentment within an appropriate range is effective for the improvement of their HER activity. In addition, chemical compositions and stoichiometric ratios also have a diverse set of structural, electrical, magnetic, and physicochemical properties. In this regard, in contrast to abundant P-P bonds in phosphorus-rich TMPs, enriched metal-metal and metal-phosphorus bonds in metal-rich phosphides can contribute to prompted thermal and electronic conductivity as well as chemical stability.[87] Hence, TMPs' morphology and physicochemical properties may be tweaked and improved by adjusting their corresponding compositions.

Single transition metal phosphides such as Co_xP_y, Ni_xP_y, Fe_xP_y, Mo_xP_y are the most reported and exhibited surprising performance toward HER in alkaline solution.[88-90] Based on the theoretical calculation and experimental practice, (001) surface of Ni_2P have a favourable ΔG_{H^*} for HER, showing the outstanding HER activity.[91] Due to the synergistic effect of multi-compounds, composition modification indeed could change the morphology, structure and electrochemical feature of TMPs. For instance, Sun's group reported a hollow CoP nanostructure with nitrogen-doped carbon framework contributing to high water splitting activity.[92] Liu's team synthesized Ni_xP_y micro-spheres with different ratio of Ni and P, among them, $Ni_{90}P_{10}$ exhibited the most suitable ΔG_{H^*} for excellent HER property.

Bimetallic phosphides outperform single transition metal phosphides in terms of HER activity in alkaline media. The superior performance may ascribes from the synergistic effects of bimetallic active sites with tunable electron arrangement and architectural versatility.[93] For instance, bimetallic $Ni_{2-x}Co_xP$/N-doped carbon nanofibers were reported by Gao's group which shown the excellent HER in base, acidic or neutral electrolytes.[94] In addition, different morphology design such as CoFeP nanosheets,[95] NiFeP/CoP nanosheets/nanowires,[96] MoNiP nanoparticles,[97] Co_3Ni_1P nanocubes,[98] CoFeP hollow microspheres,[99] have been wide-ranging reported these years by modulating the morphologies and structures.

Up-to-now, there are plentiful strategies to construct the architectures. Among them, doping including metal/ non-metal is an productive approach to prompt the property of TMPs. The electronic configuration, morphology, and surface area of TMPs are significantly influenced by metal doping, resulting in improved catalytic efficiency. Hence, atomic level change or more favorable crystal plane modification of the catalyst can optimize catalytic performance of HER

process. For example, Zhang et al. synthesized Fe-doped Co_2P nanorod bundles which could be used for HER in a wide-pH range.[100] The Fe doping supplied the favorable electronic configurations, lattice distortion, and special environment accommodation, resulting in the enhancing of HER. Li's group introduced Cu-doped CoP nanorods achieve remarkable performance towards HER with an overpotential of 44 mV at 10 mA cm^{-2} in acidic and 81 mV in basic and 137 mV in neutral media, which further confirm the importance of metal doping.[101] Besides, nonmetal doping especially heteroatom doping can create the synergistic effect withing the heteroatom and P atom and further effect the electrochemical properties. In this regard, Chai's group synthesized nitrogen-decorated ion phosphide nanorods as excellent electrocatalysts towards overall water splitting.[102] Zhang's group introduced the V/N co-doped into CoP nanoleaf resulted in improved catalytic kinetics and charge transfer due the subtle lattice distortion and extra active sites.[103] Although there are abundant strategies to synthesize the transition metal phosphides, the most convenient two methods are utilization $Na_2HPO_4 \cdot 2H_2O$ in the synthesis process or calcination step. However, it's hard to identify the amount of P in the final product and if the metal phosphides are successfully produced. Another challenge for metal phosphides is its working mechanism. Extensive hypotheses are proposed but it's difficult to illustrate thoroughly the mechanism. Hence, it's necessary to study deeply their structure and mechanism to construct the high effective electrocatalyst rationally.

2.3. Electrodes for Energy Storage

Intensive research has been conducted to develop new, superb performance electrodes for energy storage devices. The ideal design for LIBs and SCs should have the following features: superior energy density, remarkable cycling ability, acceptable rate capacity, portable shape, trustable security, cheap, and recyclability.[104] Hence, extensive research focus on the structure modification and configuration. Here, we will discuss the electrode materials for the Li-ion battery and supercapacitors separately.

2.3.1. Anode Electrode for Li-ion Batteries

As we discussed above, there are two approaches enhancing the performance of LIBs. One is designing high voltage cathode materials; another is exploring excellent anode/cathode materials with high energy density. In this thesis, we mainly discuss the anode materials for Li-ion batteries.

For designing the suitable electrode materials, the follow requirements are: (1) The composite must contain non-atomic-weight elements or compounds, have a low density, and be able to hold significant quantities of lithium. (2) The materials should be stable, electrically conductive, long cycling life and chemical reversibility. (3) Anode materials should have an ability to operate the battery in normal, safe conditions when it's assembled with cathode materials with a high potential. (4) It's requiring that anode materials should be chemically stable in electrolyte and can not react with the solvent. (5) Lastly, the material should be low cost, environmentally friendly, safe. Therefore, there have been numerous developments in nanostructured anode materials. In comparison with bulk compositions, they display diverse characteristics in batteries, including tunable morphology and structure, high surface area and conductivity, featured architectures, and low resistance.

In this thesis, we mainly focus on the state of the art in anode materials for LIBs, along with three classifications based on their reaction mechanism for Li-ion batteries as below:

(a) Intercalation/de-intercalation materials especially carbon-based materials, such as carbon nanotubes, graphene, titanium dioxide.[105, 106] During the charging and discharge, Li ions are inserted into their crystalline structure without changing the crystal structure of the hosts. They have been broadly utilized and explored due to their excellent Li ion intercalation reversibility, richness, cheapness, chemical tolerance.[107] Nanostructured carbon materials are combined with other materials eschewing side reactions both in the electrode and electrolyte and delivering high particular capacities as anode-active materials. Hard carbon possesses a remarkable capacity up to 600 mAh g^{-1} in lower voltage range.[108] For example, Ai et al. reported chemically prelithiated hard-carbon anode displaying high performance Li-ion intercalation.[109] Besides, Eli's group introduced packed and condensed carbon nanotubes framework as anode current collectors which achieved lowest irreversible capacity.[110] However, the major drawbacks for pure carbon-based materials are surface erosion or degradation during the electrochemical process, forming a thick non-reactive shell covering electrode which is called a solid electrolyte interface (SEI).[111] Therefore, they suffer from unfavorable initial coulombic efficiency which hinder wide-ranging utilizations as active anode materials for LIBs. TiO_2 is also widely applied as an intercalation-type material because of superb intrinsic features, like negligible volume change and excellent duribility. On the contrary, they are hindered by the non-acceptable theoretical capacity (175 mAh g^{-1}) and poor electronic

conductivity (~10 -13 S cm^{-1}) in broadly implementation.[112] Thus, intensive work has focused on modified morphology and structure to optimize the electrochemical properties.

(b) Alloy/de-alloy materials such as silicon, tin (IV) oxide, germanium etc.[113, 114] These type of materials have high theoretical specific capacitance such as SnO_2 with 783 mAh g^{-1} and Si with 4211 mAh g^{-1}), which are promising candidates for high capacitor batteries.[115, 116] However, they suffer from large volume change and adverse structure expansion and multiple irreversible reactions in the first charge/discharge cycle, contributing to the poor cycling feature and low coulombic efficiency.[2] So to solve above drawbacks, diverse methods have been proposed, such as downsizing composites to nanoscale, and combining both lithium active and inactive material in one composite in which inactive material working as buffer array in order to avoid the large volume change; modifying the morphology like nanotube, nanowires to obtain favorable energy density and remarkable cycling stability.[117, 118] For example, Cui's team fabricated silicon nanotubes and nanowires, displaying reversible capacity over 2000 mAh g^{-1} with remarkable cycling property.[119] Ren's group introduce $Si@SiO_2@C$ nanocomposites with a coral double-shell in which the carbon layer modified the volume expansion during the cycling performance.[120] In addition, SnO_2 with high specific capacity is already applied in industrial. However, its severe electrode degradation can be found because of increasing volume expansion by 200% upon cycling. Hence, multiple porous architectures like nanotube, nanocomposites, nanoparticles are designed to solve the problems. For instance, Ramesha's team reported porous SnO_2 hollow microspheres displaying discharge capacity of 800 mA h g^{-1} and low resistance. Such excellent performance ascribed from the porous structure accommodating volume expansion and synergistic effect of the binders.[121] Xia's group also reported that multi-walled carbon nanotubes coated with SnO_2 films take the fully advantage of the two types of materials showed high charge capacitance and outstanding resistance in Li-ion battery.[122] On account of the significant finding in the Li-ion battery, further development should also be devoted to deal with the problems of alloying materials.

(c) Conversion-type materials like transition metal oxides[123] (Co_3O_4, NiO, Fe_xO_y, etc.), metal sulfides[124], metal phosphides[125] and metal nitrides[126], which we mainly focus on these type of materials in our thesis. The electrochemical reaction mechanisms of these materials involve the chemical redox reactions of transition metal and composition of lithium materials.[127] When it's applied as anode materials, they can reveal high reversible capacities in the range of 500-1000 mAh

g^{-1} owing to multiple involved electrons in the chemical reactions.[128] The redox reaction of transition metal materials is written as below:

$$M_xN_y+zLi^+ +ze^- \leftrightarrow Li_zN_y+xM \text{ (M=Fe, Co,Ni, etc;N=O,S,P,N)} \quad (18)$$

Besides metal oxides, recently metal sulfides and phosphides are widely explored as anode materials due to their high capacities. In addition, metal sulfides and phosphide have strong ability of electron attraction, preventing the oxidation and forming powerful a covalent relationship with metal-S/P bond. Another advantage is structural variation of metal sulfides and lower reaction voltage of metal phosphide than their oxide counterparts. On the contrary, the major disadvantages of these materials are unacceptable electrical conductivity, unfavorable volume changes, corrosion, and particle agglomeration.[129, 130] Currently, much research focuses on tuning the morphology of material like nanosheet, nanorod and nanotube or modifying the electronic configuration to enhance the conductivity.[131-133] For instance, Wang's group introduced α-Fe_2O_3 hollow spheres obtaining outstanding reversibility and excellent capacity up to 700 mAh g^{-1}.[134] Zhang's group introduced ZnS microspheres modified with nitrogen-decorated carbon as anode materials for both lithium and sodium-ion battery.[135] In addition, Park's team reported CoP/C nano-compounds with different element ratios revealing the remarkable initial capacitance of 531 mAh g^{-1} and high cycling ability and Yan et al. synthesized two-dimensional $NiPS_3$ nanosheets as anode material with a favorable reversible capacity of 796.2 mAh g^{-1}.[136, 137] Along with the above anode nanostructures, more efforts are encouraged to construct high performance anode materials.

2.3.2. Electrode Materials for Supercapacitors

As discussed above, energy capacity and cycling performance of SCs are mainly dependent on the electrode materials. Hence, development novel materials with high capacitance and excellent reversibility is exceedingly required to solve this problem. The high-performance electrode materials should meet the following requirements. First, the electrode surface area and pore size has a significant influence on the property of SCs. Since not all the surface area is available, electrochemically active surface area is very important in contacting the electrolyte. Researcher found that the mesopores and macropores are favorable for the ion transport while micropores are similar to the ion size of electrolyte, contributing to the higher double-layer capacitance. Second, the materials with high conductivity are favorable for charge transfers enhancing faradaic reaction capacitance. Third, temperature accommodation, different electrolyte adjustment, durability and

superior corrosion resistance are also the important factors enabling a long-life span for SCs. Based on the varieties of SCs, the electrode material can also be divided into two classifications as below:

2.3.2.1. Carbon-Based Materials

Carbon-based materials are thought to be auspicious for EDLC supercapacitors because of their abundance, cheapness, large surface area, superior electric conduction, thermal resistance, and low-toxicity. Diverse carbon-based materials, including activated carbons (AC), carbon nanotubes (CNTs), graphene, are widely utilized as anode materials for EDLCs recently years. Herein, we briefly introduce these types of EDLCs.

Because of its economic feature and high specific surface area (2000 m^2 g^{-1}), activated carbon is a promising electrode material, delivering capacities of 200 F g^{-1} and 100 F g^{-1} in inorganic and organic solutions, respectively.[35] Owing to various pore sizes, activated carbon materials present a nonlinear specific capacitance. Especially, electrolyte ions fail to penetrate into the ultra small micropores less than around 0.6 nm, which limits the ion transfer speed in the porous pathways further impeding the energy density of EDLCs, particularly in the organic electrolytes. Hence, researchers have modified the morphology and structure of AC to improve the performance. For instance, Ye's team reported porous active carbon fibers via KOH activation generating of ultra-micropores and abundant mesopores. Such nanofibers display remarkable specific capacitance of 225 F g^{-1} at small current density.[138] Jiang's group synthesized microporous active carbon from biowaste with hydrophilic behavior and the appropriate electrical conductance yielding the ultrahigh energy density.[139]

Carbon nanotubes (CNTs) have been regarded as attractive materials for SCs due to acceptable ingrained electrical conduction and chemically durability. Nevertheless, low surface area restricts the enhancement of capacitance in organic solutions. However, it's possible to obtain high performance materials by formation of various nanostructures controlled by their crystalline order. For instance, Shanov et.al reported N-doped CNTs)on CNT fibers achieved stable specific capacity of 144 $mAhg^{-1}$ at 5C.[140] Except this, other morphology like 2D nanosheets,[141] leaf-like interwoven carbon nanosheet/nanotube[142], 3D carbon nanosheet[143], 3D CNT sponge[144] are also further explored.

Graphene made of a one-atom thick sheet possessing high surface area of 2675 m^2 g^{-1}, low electrical resistance, and favorable thermal conductivity, has been estimated as another auspicious

material for SCs. Supercapacitors assembled with graphene-type materials with inorganic media were claimed to have a specific capacitance of 80 F g^{-1} and an energy density of 32 Wh kg^{-1}. For instance, Zhang's group prepared graphene networks decorated with nickel oxide forming the porous ion transport channel, yield excellent specific capacitance of about 816 F g^{-1} and durability performance.[145] Wei's group introduced graphene nanosheet/carbon black composites by an in situ reduction method exhibiting the specific capacitance of 175.0 F g^{-1} at low scan rate.[146] Fan's group synthesized three-dimensional graphene fabricated on carbon nanofiber with remarkable surface area and low resistance.[147]

2.3.2.2. RuO_2

Ruthenium oxide (RuO_2) was reported as the first material to demonstrate pseudocapacitance. Its plentiful merits such as favorable practical specific capacitance of around 900 Fg^{-1} (theoretically 1358 Fg^{-1}) and high electric conduction of 300Ω^{-1} cm^{-1}, multiple valence states, excellent thermic steadiness, durable cycling behavior enable to high performance energy supercapacitor.[148] RuO_2 displays the high performance both in alkaline and acidic electrolyte due to the following reason: (1) large specific surface area. (Since the performance of RuO_2 is largely decided by surface reactions, larger surface area and ample active site enable the redox reactions occur sufficiently, donating higher specific capacity); (2) water combining ability. It's reported that the RuO_2 involving five water molecules prompts ion diffusion in electrolyte.[149] However, RuO_2 with good crystallinity bears structure expansion, which fends off the proton permeation the inside bulk electrode and results in diffusion restriction. In consequence, high speed reversible faradaic reactions are stopped. In addition, the high price and scarcity hinder the development of RuO_2 in a large scale. Hence, more and more research has focused on designing transition metal-based materials as an alternative for SCs.

2.3.2.3. Transition Metal-Based Materials

Transition metal oxides have recently emerged as a feasible option as an electrode material for performance SCs on account of high specific capacity and electrical conduction, various structures, and low cost.[34] Faradic redox reactions and ions sorption and transportation between electrolyte and electrode make a great contribution to enhancing pseudocapacitance of metal oxides. Consequently, compared with carbon-based materials, transition metal oxides demonstrate

remarkable property for pseudo-capacitors. The most common and reported metal oxides are MnO_2, Ni_xO_y, and Co_xO_y. They are earth-abundant and possess different valence states and high theoretical capacitance. Extensive work has been put into developing high-functioning electrodes. For instance, Ma et al. reported three dimensional MnO_2 nanostructures exhibiting specific capacity of 120 F g^{-1} and lower ion diffusion resistance.[150] Qian's group introduced flower-like mesoporous Co_3O_4 nanostructures revealing outstanding rate competences, and remained 93 % of the initial capacity at 5 mA cm^{-2}.[151] Kang's group synthesized loose-packed NiO nanoflakes by a facile chemical precipitation method displaying excellent specific and rate capability.[152] However, metal oxides suffer from poor conductivity like MnO_2, dissipation in different solution, and structural collapse, all these obstacles restrain ion and electron transfer behavior and cycling feature. Hence, morphology design, composition variation, structure modification are of significance to prompt the properties of these materials.

Besides oxides, transition metal sulfides are gradually widely applied as electrode materials for pseudo supercapacitors because of appropriate electrical conduction, various stoichiometric chemistry in comparison of metal oxides, active electrochemical reactions.[30] Similar to metal oxides, transition metal sulfides work as battery-type materials yielding capacity feature via changeable surface redox reactions, distinctly in alkaline media. Much research have been published up to this point. For instance, Zhang's team synthesized porous well-ranged $NiCo_2S_4$ and CoS_2 nanoarrays presenting a extraordinary energy density of 55.8 W h/kg at 695.2 W/kg.[153] Zardkhoshoui et al. synthesized petal-like FeS_2 on a NF substrate as a supercapacitor electrode. The petal-like FeS_2 had a largest specific capacity of 321.30 F g^{-1} in alkaline solution.[154] or example, Wang et al. reported hollow MoS_2 nanospheres, when it's applied as a supercapacitor, it exhibited 142 F g^{-1} at 0.59 A g^{-1} and it preserved 92.9% of its initial capacity after one thousand cycles.[155] However, one major drawback of metal sulfides is the phase transformation and structure collapsing during the electrochemical process leading to the poor cycling performance. Despite current advances in metal sulfides, more studies into their working mechanisms are requested and optimization and tailoring of materials structure are extensively needed to prompt their behavior in SCs.

Encouraged sulfides' superior behavior, transition metal phosphides have also been scrutinized for SCs utilization. Due to lower electronegativity and larger atomic radius than S and O, transition metal phosphides display diverse physical or chemical characteristics in contrast with sulfide and

oxide equivalents.[30] Most phosphides are also battery-type materials, involving redox reactions for charge storage. Fu's group reported porous NiCoP nanosheets with 216.39 m^2 g^{-1} presenting high capacitance and outstanding rate performance.[156] Ji's group reported that hierarchically mesoporous micro/nanostructured CoP nanowire can reach up to superior energy density of 23.4 W h Kg^{-1} at 274 W Kg^{-1}.[157] Liu et.al reported CoP nanocrystals supported on carbon nanofibers forming crêpe-like morphology presenting marvelous specific capacitance 748 F g^{-1} at 2 A g^{-1} and exceptional cycling behavior.[158] However, metal phosphides also face problems such as low conductivity, unclear reaction mechanism and complicated synthesis method which limit the further application in SCs. Hence, more strategies should also be explored in the future.

2.4. Research Gap and Limitations

As the electrocatalysts for oxygen reactions and water splitting, we reviewed that the precious-metal based materials with high intrinsic activity, favorable electrical conductivity, low valences could overcome the sluggish kinetics of ORR/OER/HER. However, they still suffer from easy dissolution, instability, and expensiveness. Hence, we explore the transitional metal-based materials as an alternative to realize the design of high performance bifunctional electrocatalysts due to their relatively low cost, variable valences states and structure diversity, controllable morphologies, and facile synthesis method. The most widely used transition metal-based materials are metal oxide, sulfides, and phosphides. However, they also suffer from some obstacles, such as unstable structures during electrochemical process, easy to be oxidized or corrosion, poor electrical conductivity and lack of active sites and low surface areas.

For the energy storage devices, we discussed the common anode materials for Li-ion battery, such as carbon-based material, alloy materials and transition metal-based materials based on their working mechanisms. Each type shows excellent performance for Li-ion battery, but they still have disadvantages. For instance, carbon-based materials has low specific capacity and low-rate capacity. Low conductivity and large volume expensive limit the development of alloy/de-alloy materials. Also, transition metal-based materials suffer from aggregation and volume change resulting in the low columbic efficiency and low cycling rate. For the electrode materials in supercapacitors, we introduced three classifications, like carbon-based materials for EDLC, RuO_2 and transition metal-based materials for pseudo-capacitors. Notwithstanding, carbon-based materials are hindered by structure changes and low cycling performance, RuO_2 is too expensive

and scarce limit their broad application, while transition metal-based materials also have poor conductivity, poor structural stability, and unclear reaction mechanisms, requiring the more novel design for supercapacitors.

From the above, it's easy to be found that transitional metal-based materials are utilized in both energy conversion and storage devices because of their cheapness feature, tunable valence states and morphologies, high capacitance. However, there are still some limitations for them into large practical application. For the energy conversion, lacking the novelty and concepts to design of these nanomaterials for each particular utilization. For example, how to design the materials by controlling morphologies, dimensional structure, improving the electrical conductivity. Second, lacks a mechanism study of integrated relationship between structure and electrochemical performance. Third, rational design of structure to protect the materials from collapsing and volume changing is required. For the energy storage, the choice of novel electrode for different functionalities is still limited. In addition, systematic investigations of experimental procedures are still needed to be optimized. Right now, most synthesis methods for designing the anode materials are too complex and require complicated conditions which is hard to realize to large practical application for the future. The mechanism and functionality of different heteroatoms (N,S,P) or other composition is not clear. Furthermore, there is lack of mechanism studies of integrated relationship between structure and electrochemical performance. Last is lacking the novelty and concepts for design of one nanomaterial for different applications. Thus, facile and easy synthesis method is of high demand and opens a venue for the future utilization.

Chapter 3 Theoretical and Experimental Design of Transition Metal-based Nanomaterials for Energy Conversion and Storage

In this chapter, we present the methodologies from design, synthesis, to electrochemical measurement. It's divided into three parts. First, we will propose different materials design strategies so that we have a better understanding about how to design high-performance nanomaterials theoretically. Next, we will introduce our experimental design methods including synthesis, characterization, and electrochemical performance. The first part introduces different synthesis method. The second part displays the characterization method, including SEM, TEM, XRD, XPS and BET. The third part is the equipment and electrochemical measurement. Hence, based on these, we have a comprehensive understanding of the design of the testing procedure of transition metal-based materials for energy conversion and storage.

3.1. Rational Design Strategies for Transition Metal-Based Nanomaterials

Nowadays, researchers have devoted many efforts to design the high-performance transition metal-based nanomaterials for both energy conversion and storage by tailoring the structure and engineering, especially the nano-structuring which has been considered as promising way for realizing high-performance electrochemical energy conversion and storage. Hence, we introduce some strategies about how to design the high-performance nanomaterials for both energy conversion and storage.

First is creating more active sites on the surface of nanomaterials where the electrochemical reactions occurs. Recently, constructing atomic metal-nitrogen moieties in carbon matrix to form a M-N-C structure to create the plentiful defective sites serving as vacancies, demonstrating not only good atomic stability but also high catalytic activities toward electrochemical reactions. For example, Li's group prepared single atomic cobalt active sites on hollow N-doped carbon spheres, donating exhibits excellent ORR activity in acid media. Another approach is NH_3 treatment in

which nitrogen groups form in the NH_3 possessing much stronger basicity, demonstrating the high electrocatalytic performance. For instance, Guo's group reported the effective surface-adsorbed N control in nitrogen-doped $Ti_3C_2T_x$ MXene can improve the electrocatalytic performance extensively.[159]

The second strategy is by designing the nanostructured materials which possess distinct features differing from their bulk material counterparts. A large number of nanostructures have been fabricated by constructing more dimensional like 0D, 1D, 2D, and 3D nanostructures. Electrons in different dimensional structures could move along with the crystal plan which facilitates the electron transfer. Tuning the size of particles could effectively optimize the surface-to-volume ratios of nanostructures so that more atoms could be exposed on the structure surface. Besides, the geometrical shape variation is also capable of exerting significant influence upon the chemical and physical properties of a nanostructure. Finally, controlling the spatial arrangement of the arrayed nanostructures like directions and spacing of arrayed nano units is proved to be favorable to utilize collective interunit coupling to enhance the overall performance of the nanostructure ensemble for energy conversion and storage.

The third strategy is optimizing the electronic configuration of nanomaterials. Since the electrochemical reactions involve the adsorption and desorption on the surface of nanomaterials, introducing the foreign species such as metallic dopants and heteroatoms could be effective methods to realize the modulation of electronic configuration of electrocatalysts followed by tuning the absorption properties. Hence, the first one is a metallic dopant by introducing doping or alloying with metal elements in monophase catalysts to tune the electronic structures and optimize the intermediates absorption energy of materials, and thus substantially improved intrinsic catalytic properties of nanomaterials. For example, Jaramillo et al. reported the introducing of Co in Fe_xP alloying compounds and found that different element ratio could tune the electronic structure and further improve the HER/OER performance.[160] Another way is to introduce the heteroatom doping including oxygen, sulfur, nitrogen and phosphide, which modulate the electron configuration and further enhance the electrocatalytic activities.[12] For example, Qiao's group studied the different doping atoms related with the HER property. It's found that dual doping (N,P) could manipulate doping modes, revealing the best HER performance.[161]

The last strategy is to design the multicomponent hybrids which combines all advantages discussed before. The different components/phases in close contact present unique interfacial

interactions which alter the physicochemical properties of the interface and create the synergistic effect. It's reported that heterogeneous structures is favorable for both energy storage and conversion properties.

Based on these design strategies, we could design the heterogenous structure with various pores or active sites for different applications in both energy conversion and storage.

3.2. Experimental Setup

Here, we introduce the three steps of experimental setup to designing the nanomaterials, including different synthesis methods, different characterizations, and electrochemical measurements. So that we could confirm if the nanomaterials are synthesized successfully and if the design strategies are effective or not. We will discuss them and their mechanisms in different sections.

3.2.1. Synthesis

In this research, there are two major synthesis procedures for design the transition metal-based nanomaterials. One is synthesizing materials by hydrothermal process or precipitating method, which is facile and controllable. Another procedure is calcination or sulfurization which convert the materials into carbon-based/ sulfide materials. We will discuss all of them.

The hydrothermal method is a facile and potent tool for optimizing or modifying nanostructure, controlling grain size, crystalline phase and improving product performance. It requires combining precursors to a solvent that allows the synthesis of a crystalline nanostructure in a sufficient proportion. Then the mixed solvent is poured into the Teflon container with different volumes assembled with stainless steel autoclave and heated at particular temperature and time. The temperature and volume of solution decide the internal pressure inside the autoclave. In this process, crystals are grown in an autoclave that contains both materials dissolved in water. A temperature incline is created within the contrasting sides of autoclave chamber. Materials dissolved at high temperature are deposited on the seed crystals at the colder end, resulting in the growth of desired crystals with high quality.[162] The merit of the hydrothermal process is that majority of materials could be dissolved in a suitable solvent by changing temperature and time; the distilled water is used as a primary solvent instead of an organic solvent which is much facile than the solvothermal method. In addition, this process has potential to contribute industrially due to its simple approach. However, it's impossible to detect crystals growth.[162] This method has a relatively low yield of

products in comparison with the coprecipitation methods. The cost of equipment is also high. The stainless-steel autoclave and inner Teflon reaction chamber in the lab is shown as **Figure 3.1**.

Figure 3.1 Stainless-steel autoclave and inner Teflon reaction chamber.

The precipitation synthesis method is another simple technique to synthesize the materials. It includes the concurrent phenomenon of nucleation, maturation, coarsening, agglomeration steps. It possesses serval characteristics: (1) the process can generate insoluble species of high saturation. (2) Nucleation produces huge amounts of tiny particles. (3) agglomeration determines the shape, morphology, and construction of products. (4) The supersaturation environments are significant for producing precipitation resulting of a chemical reaction.[163] There are several merits of precipitation method. First, it's a simple and rapid preparation. Second, the composition and size can be controlled. Third, it usually just occurs at room temperature and it's economic and energy efficient. However, it still has some disadvantages, such as time-consuming, impurities may also get precipitated with the product and reproducibility problem. It can be utilized to get the metal oxide, metal-organic framework, metal sulfides.

Calcination is the process of heating a material in a controlled atmosphere and at a regulated temperature, the purpose of removing volatile substances. In general calcination is used to thermally decompose sparingly soluble precursors to obtain metal carbides, metal oxides, etc. Different gases such as nitrogen or argon are filled in the furnace tube and materials is calcinated at different temperatures. The major advantage of calcination is that the products from different calcination temperatures will exhibit different crystallinities, BET surface areas, and morphological characteristics. However, sometimes the products are easily contaminated by the porcelain boat reacted with different materials. For the sulfurization, it has the similar process which sulfur powder is placed the up stream which the materials are put in the down stream in the same porcelain boat. The equipment of calcination is displayed as **Figure 3.2**.

Figure 3.2 Furnace with tube for calcination.

3.2.2. Characterization

After synthesis the materials, it's importance to identify the morphology, structure, and valence states by different characterization methods. Here, we will introduce several investigations, including scanning electron microscope (SEM), transmission electron microscopy (TEM), X-ray diffraction analysis (XRD), X-ray photoelectron spectroscopy (XPS), and BET surface area analysis & BJH pore size.

Scanning electron microscope (SEM) intends to evaluate surface morphology like roughness, homogeneity of dispersion and structure of materials. SEM portrays the exterior of sample by scanning with a directed electronic beam. The primary electron beam is examined the surface of a sample in vacuum condition. Continuous signals are created as electrons striking the material, then a picture is formed along with its elemental distribution utilizing energy dispersive X-rays (EDX).[164] Although the sample preparation is simple, the electron beam can cause degradation of some materials thus it is limited to specific materials.

Transmission-electron-microscopy (TEM) is another approach and broadly employed to characterize material by providing the information of morphology, structure, porosity, and element distributions. Similar with SEM, TEM applies electrons instead of photons to produce pictures. But the electron beam of TEM is penetrating and passing through the whole sample rather than just scanning the surface, thus sometimes it damages the material and generate defects. The distinguishing feature of TEM is its ability to form images of atomic arrangements and detect the interface between the structure. TEM is composed by the electron emitting part, condenser system, image-creation setup, and picture-capturing setup. The electron gun uses a high accelerating voltage (100-300 kV) to generate the electrons. The high energy electrons travel through vacuum system and interconnect with the material. The emitted electrons are transferred to light and create

a picture by striking the sample. The sample must normally be very thin (5-10 nm thick) in order for the beam to pass through it.[165] To obtain the better-quality images, high resolution transmission electron microscopy (HRTEM) is utilized to capture the details of material. HRTEM can be manipulated at an atomic level to achieve the atomic configuration, defects, and lattice spacing parameters. Hence, it's an important technique to measure the detailed information of materials.

X-ray diffraction analysis (XRD) is a significant methodology for investigating crystalline materials by yielding information on composition, crystal growth directions, average grain size, and crystal defects. The consistent X-ray beam emitted in a particular angle corresponding to special lattice planes and strike with the material then procedure the images. Atomic placement determines the peak intensities. As a result, the XRD pattern serves as a fingerprint of periodic atomic arrangements in a substance.[166] XRD is suitable for wide-ranging materials such as carbon, transition metal-based materials and polymer. XRD is followed by Bragg's equation that associates the wavelength of the X-rays with interfacial spacing to calculate average grain size and other parameters, which is given by the following equation:

$$n\lambda = 2d\sin\theta \tag{23}$$

where d denotes the perpendicular distance within two neighbouring planes, θ is Bragg angle, λ is the wavelength of the electron beam, and n is an integer number and the direction difference between waves scatterd by surrounding planes of atoms regarding with the wavelength.

X-ray photoelectron spectroscopy (XPS) is a quantifiable approach to examine the elemental dispersion of materials as well as elemental binding energy. In this technique, the sample is irradiated with X-rays under ultra-high vacuum leading to the emission of photoelectrons from the top 1-10 nm of the sample surface. Different binding energies of the photoelectrons are determined by an electron energy analyzer, demonstrating the different valence states of particular elements. The proportion of each element is associated with the quantity of photoelectrons. Depending on binding energy and strength of a photoelectron signal, material composition, quantity, and chemical state are determined.[167] XPS yield substantial information such as the overall elements percentage in one sample by a low-resolution scan and elements existence by a survey scan. By analysing different element spectra, we can conclude the valence states and have a comprehensive understanding of chemical reactions during an electrochemical procedure.

Brunauer-Emmett-Teller (BET) surface area measurement donates specific surface area of materials by nitrogen sorption under specific pressure, while Barrett-Joyner-Halenda (BJH) pore size and volume measurement determines pore area and specific pore volume by sorption and methods. Because of the particle size of each material, this technique determines pore size dispersion regardless of external field. By different adsorption and desorption mechanism, there are four types of hysteresis loops (types H1- H4) given by International Union of Pure and Applied Chemistry (IUPAC) which is correlated the with the texture of adsorbent and is showed as below (**Figure 3.3**):

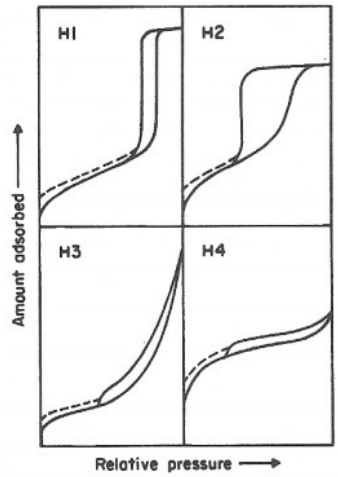

Figure 3.3 IUPAC classification of hysteresis loop.

H1 presents narrow dispersion pores like cylindrical formation; H2 emphasizes complicated pores effecting by blocking or percolation phenomena; H3 displays non-rigid aggregates of plate-like particles; H4 usually exists in material with micro and mesopores.[168] Different pores like micropores, mesopores, and macropores can also be obtained by the measurement.

3.2.3. Electrochemical Measurement

The electrochemical performances of oxygen reactions, water splitting and supercapacitors are measured by a three-electrode system, which can be shown in **Figure 3.4**. It consists of a working electrode, reference electrode and counter electrode employed in the same electrolyte.

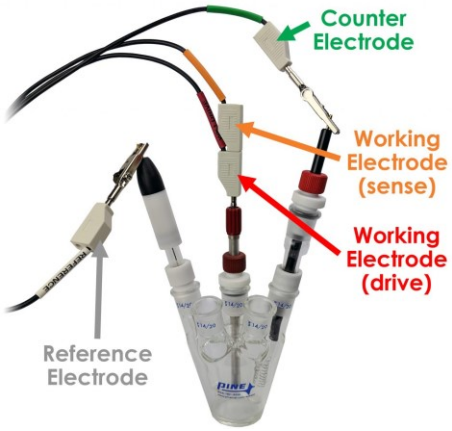

Figure 3.4 Three-electrode system.

The potentiostat station cable can be connected with a three-electrode system to perform the experiments. During the electrochemical experiments, charge, and ion transport between the working electrode and the counter electrode while voltage of testing material is investigated regarding to the reference electrode.

Generally, Pt wire is used as a counter electrode due to its high resistance in all electrolytes, saturated calomel electrode (SCE), Hg/HgO electrode or saturated Ag/AgCl electrode are utilized as reference electrode. Different electrodes have different potential with respect to standard hydrogen electrode. For example, potential of SCE is 0.241 V. Usually, we convert all the voltages to reversible hydrogen electrode (RHE), the converting equation can be described as below:[169]

$$E\ (RHE) = E\ (\text{reference electrode}) + 0.0591 * pH \quad (24)$$

Besides, cyclic voltammetry is one of the most common techniques in electrochemistry. This type of voltammetry is useful for electrochemical behaviour studies (chemical redox process) of the species in which the potential applied to working electrode is swept linearly between the anodic and cathodic peak potentials. By monitoring the current as a function of potential, special current-potential voltammograms can be obtained to the system. Usually, there are two conventions used to report the data, as shown in **Figure 3.5**:[170]

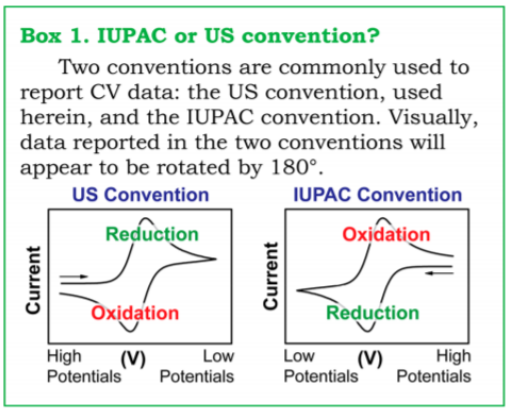

Figure 3.5 Two conversion of CV curves.

The difference of these two types is mainly dependent on the sweep direction and potential range. Both of them are applicable in electrochemical testing. When a pH-dependent redox couple is changed, the concentration of one of the redox couples' changes, resulting in a shift in redox potential and a cyclic voltammogram. CV is commonly used for the electrocatalytic reaction which can reveal the information about catalysts, such as electrochemical behavior of electrocatalysts, the correlation with electrolyte and kinetic performance of materials. It's utilized in wide-ranging testing such as electrocatalysis, batteries performance and supercapacitor behaviors and reflect different information. Linear sweep voltammetry (LSV) is another voltametric technique for studying redox reactions of organic and inorganic species. For ORR, LSV was performed related with electrode rotating rate and limiting current density can be observed. It further reveals the kinetics of catalysts. Besides these, the electrochemical active surface areas, resistance, and other performance should also be measured to investigate the properties of electrocatalysts.

Chapter 4 Design of Transition Metal-based Nanomaterials for Energy Conversion

Based on the above literature review, we know that transition metal-based nanomaterials are widely applied to energy conversion and there are some limitations. This chapter introduces three types of transition metal-based nanomaterials for oxygen reactions and water splitting. They are synthesized either by a hydrothermal process or precipitation method followed by calcination, which is regarded as the economic and facile strategies. We will discuss each type in separate sections. By designing these high-performance materials, we pave the way of exploring the transition metal-based nanomaterials for wide application.

4.1. Bimetallic CoNi Alloy Nanoparticles Embedded in Pomegranate-Like Nitrogen-Doped Carbon Spheres for Electrocatalytic Oxygen Reduction and Evolution

As discussed before, transition metal alloy is widely used as electrocatalyst in metal-air battery due to its high performance. Modifying transition alloy through combing the carbon is considered as another strategy to further improve electrocatalytic performance. Herein, a composite electrocatalyst with bimetallic CoNi alloy nanocrystals embedded within nitrogen-doped highly graphitic carbon spheres (N-CoNi/PCS) for oxygen reactions is design in this report. Owing to the efficient design strategy, such a composite electrocatalyst exhibits a unique pomegranate-like morphology and microstructure, which delivers a low half-wave potential of 0.80 V toward ORR and overpotential of 540 mV toward OER with excellent durability.

The outcome of this research is published in "ACS Applied Nano Materials" (**Chen, L.**; Xu, Z.; Han, W.; Zhang, Q.; Bai, Z.; Chen, Z.; Li, G.; Wang, X., Bimetallic CoNi Alloy Nanoparticles Embedded in Pomegranate-like Nitrogen-Doped Carbon Spheres for Electrocatalytic Oxygen Reduction and Evolution. *ACS Appl. Nano Mater.* **2020,** *3* (2), 1354-1362.)

4.1.1. Introduction

Rechargeable batteries have been extensively studied and developed as power sources for clean energy generation, storage, and utilization, addressing challenges of rapid consumption of fossil fuels triggering serious degradation of environment and climate changing.[171] In many regards, metal-air batteries are held in high esteem owing to the high theoretical specific capacity and energy density (>1000 Wh kg^{-1} vs 150-200 Wh kg^{-1} of lithium-ion batteries), based on the electrocatalytic oxygen redox reactions on the air cathode.[172, 173] However, the large implementation of metal-air batteries toward stationary energy conversion, storage, and automobile applications is still impeded by the sluggish kinetics of the oxygen evolution reaction (OER) and oxygen reduction reaction (ORR),[174-176] leading to not only a high overpotential but also low efficiency and inadequate durability.[177] Therefore, it is necessary to seek and investigate highly efficient and active electrocatalysts to facilitate both OER and ORR in the progression of high-performance metal-air batteries.

Precious metals, especially platinum (Pt), iridium (Ir), and ruthenium (Ru), along with their alloys and oxides are the most commonly known electrocatalysts and have been broadly adopted due to the exceptionally efficient electrocatalytic activities.[57, 178-180] Specifically, Pt alone and Pt-based electrocatalysts are widely used to catalyze ORR due to its unparalleled electrocatalytic capability; while IrO_2 is widely recognized as the best OER electrocatalyst. Researchers have also been devoting much attention to the development of nanostructured precious metal electrocatalysts to further enhance their electrocatalytic activities via improving the exposure of active sites. However, the limited probable reserves of precious metals lead to not only high cost but also unsustainability that slows down the broad implementation of affordable devices. Moreover, nanosized precious metal electrocatalysts are very vulnerable to agglomeration and poisoning, resulting in fast performance decay and poor durability. On the other hand, it is also challenging to integrate ORR and OER catalytic activities when precious metals are used due to the incompatibility.[181]

Nowadays, non-precious metal-based electrocatalysts have been extensively explored and proposed addressing the cost and sustainability concerns.[182] Various morphologies, compositions, as well as microstructures are finely tuned and engineered to enable comparable electrocatalytic capability to that of precious metals.[183] Particularly, carbon materials have been regarded as

superiorly active for ORR owing to the unique electronic configuration which makes dopants surrounding carbon atoms and forming C-dopants bond, serving as host of active sites or working as active sites directly. It is also believed that graphitic carbon component is not only highly conductive providing efficient electron transfer pathways but also robust ensuring a structural stability.[45] Meanwhile, carbon materials can further boost ORR in combination of heteroatoms doping, such as N, P, S, and so on.[184-188] For example, a polyaniline-derived N-doped carbon nanotubes (N-doped CNTs) exhibit a low half-wave potential of 0.84 V (*vs.* RHE).[189] Chen et al. has studied that 3D carbon hybrid N-doped NiCo-CNT shows the high ORR activity with high onset potential (0.89 V) and current density (5.48 mA cm $^{-2}$ at 0.4 V) which outperforms the one without metal alloy or the CoNi-NCNT alone, indicating advantages of the 3D carbon hybrid improving ORR activities.[190]

Recently, transition metal-based materials such as oxides, alloys are much more suitable for OER due to their low-cost and various abilities with different valence states and extra active sites.[191] For example, previous work reports that the lower overpotential of Fe_3C/Fe_2O_3@NGNs heterostructure towards OER performance is ascribed to interior Fe_2O_3 active sites and the protection of N-doped graphene layer.[192] Wu et al. displays Co-N-C species produced by Co_3O_4 nanoparticles cooperated with nitrogen atoms act as a bond bridge to link the Co_3O_4 nanoparticles and N-doped carbon lattice, introducing the extra active sites for OER.[193] Among the many, transition metal alloys, such as CoFe,[194, 195] CoNi,[196] MnCo,[197] have been attracting much attention due to the superior activity to the individual component and corresponding oxide. Particularly, bimetallic CoNi alloy is a potential candidate among various bimetallic alloys because of its earth abundance instinct and are more conductive and stable than Fe as well as its cost effectiveness.[198, 199] Due to the synergistic effect, CoNi alloy not only provides rich valence state changes with a strong electron coupling but also intrigues the surface properties alternation and the intrinsic polarity shift in the process of oxygen reactions.[45, 76, 200] Bifunctional electrocatalysts combined with bimetallic CoNi alloy and doped carbon enable the kinetic promotion of both OER and ORR. For example, Chen et al. demonstrates that a bamboo-like structure carbon hybrid encapsulated with CoNi alloy (N-G@CoNi/BCNT) yields onset potential of 0.06 V (*vs.* Ag/AgCl) and displays high current density (6.7 A m^{-1}) in the application of fuel cells.[34] N-doped CoNi alloy nanoparticles decorated on carbon nanofiber exhibits half-wave potential (0.81 V) towards ORR and overpotential of 530 mV towards OER, showing superior electrocatalytic activities.[45] Nevertheless,

efficiently integrating bimetallic CoNi alloys with doped carbon exhibiting outstanding catalytic performance towards both ORR and OER is still greatly challenging due to the lack of nano-architectural design and synergistic effect. Besides, the uneven distribution of bimetallic alloy elements and phase separation often occur during the integration.

Herein, we demonstrate a novel bifunctional electrocatalyst with bimetallic CoNi alloy nanocrystals embedded within N-doped highly graphitic carbon spheres (N-CoNi/PCS). Such a composite electrocatalyst possesses a unique pomegranate-like nanoarchitecture that exhibits several key features favoring both OER and ORR processes: (i) bimetallic CoNi alloy nanocrystals with small size serving as seeds homogenously distributed in the porous carbon spheres provide not only abundant active sites but also efficient ion transport channels for fast access and electrocatalytic reactions; (ii) highly graphitic carbon within the composite sphere shell enables chemically/electrochemically stable carbon structures protecting the alloy from oxidation and conductive networks facilitating electron transfer; (iii) the effective nitrogen-doping contributes to the higher surface area, while the integration of two types of electrocatalysts provides synergistic effect for superior catalytic activities. Such electrocatalysts show outstanding electrocatalytic performance. The optimized electrocatalyst delivers best OER activity with a low overpotential of 504 mV and half-wave potential (0.80 V) for ORR, which is comparable to the commercial RuO_2 and Pt/C electrocatalysts. The novel composite material design forwards the field of the progression of electrocatalysts; while such bimetallic alloy based electrocatalyst holds great promise towards high-performance metal-air batteries.

4.1.2. Experimental Section

4.1.2.1. Chemicals

Cobalt(II) nitrate hexahydrate ($Co(NO_3)_2 \cdot 6H_2O$, ACS reagent, ⩾ 98%), nickel(II) nitrate hexahydrate ($Ni(NO_3)_2 \cdot 6H_2O$, ACS reagent, ⩾98%) and alcohol (C_2H_6O, 95%) were purchased from Fisher Scientific. Glycerol ($C_3H_8O_3$, 99.5%), isopropyl alcohol (C_3H_8O, ACS reagent, ⩾ 99.5%), glucose ($C_6H_{12}O_6$, ACS reagent) and urea (NH_2CONH_2, ACS reagent, 99.0-100.5%) were purchased from Sigma-Aldrich. DI water was purified with a Millipore Milli-Q system.

4.1.2.2. Preparation of CoNi Precursor

In a typical preparation, $Co(NO_3)_2 \cdot 6H_2O$ (0.165 g), $Ni(NO_3)_2 \cdot 6H_2O$ (0.055 g) and glycerol (16 mL) were dissolved in isopropanol (80 mL) to form a pink solution; the solution was transferred to four 50 mL Teflon-lined stainless-steel autoclaves and kept at 180 ℃ for 6 h; the light pink powder CoNi precursor was separated by centrifugation and washed by ethanol several times then dried under vacuum at 80 ℃.

4.1.2.3. Synthesis of N-CoNi/PCS

In a typical synthesis, CoNi precursor powder (400 mg) was well dispersed in isopropanol (80 mL) with ultrasonication followed by the addition of glucose solution (1.0 M, 8.0 mL), urea (0.960 g) and glycerol (16 mL) in sequence. The homogeneous solution was transferred to four 50 mL Teflon-lined stainless-steel autoclaves and kept at 180 ℃ for 4h. The precipitate was separated by centrifugation and washed by ethanol and water several times. The fine dark brown powder obtained after drying at 80 ℃ was annealed under Ar atmosphere at 700 ℃ for 200 min with a ramp rate of 1 ℃ per min and under NH_3 atmosphere at 700 ℃ for 15 min to get the final product. N-Co/PCS and N-Ni/PCS were synthesised using the same method but without adding cobalt hexahydrate or nickel hexahydrate. Also, CoNi/PCS without nitrogen-doping was annealing under Ar atmosphere in the same condition.

4.1.2.4. Structural Characterization

The morphology of the materials was carried out by Germany Zeiss SUPRA40 field emission scanning electron microscopy (FESEM). Transmission electron microscopy (TEM) was performed with a JEOL 100CX TEM/STEM operated at 150 KV. X-ray photoelectron spectroscopy (XPS) was characterized by a PHI 5000C ESCA system. The pore structure was analyzed with nitrogen adsorption-desorption measurement by a Brunauer, Emmett and Teller surface analyzer (Quantachrome Instruments QuadraSorb SI4) and pore size distribution was measured by a Barrett-Joyner-Halenda (BJH) model. The crystal structure was characterized by a Bruker D8 advanced X-ray diffraction (XRD).

4.1.2.5. Electrochemical Measurements

All electrochemical tests were measured in 0.1 M KOH electrolyte by an electrochemical potentiostat workstation (Biologic VSP300) using a standard three-electrode system. The working electrode is a glassy carbon (GC) electrode with surface area of 0.196 cm^2; a platinum wire was utilized as the counter electrode; and a standard calomel electrode (SCE) was employed as reference electrode. For the preparation of working electrode, 2 mg of as-synthesized electrocatalyst and 2 mg of Vulcan Carbon (VC) were well dispersed in 0.5 mL Nafion solution (0.2 wt%) under ultrasonication for 30 min to obtain a homogeneous slurry.15 μL of slurry were casted on the glassy carbon electrode and dried at room temperature. Linear sweep voltammetry (LSV) was applied at a scan rate of 10 mV s^{-1}. ORR electrocatalytic performance was observed from 0.1 to -1.0 V (*vs.* SCE) at a scan rate of 10 mVs^{-1} with a rotating speed from 400 rpm to 2500 rpm; OER electrocatalytic activity was recorded from -0.1 to 0.8 V (*vs.* SCE) at a scan rate of 10 mV s^{-1} with the same rotating speed. N-Co/PCS, N-Ni/PCS and CoNi/PCS were also measured for comparison.

4.1.3. Results and Discussion

The pomegranate-like N-CoNi/PCS composite spheres were prepared through a two-step synthesis followed by an annealing process. As shown in **Scheme 4.1,** the bimetallic CoNi alloy seeds is synthesized via a facile solvothermal reaction (**Figure S4.1**); the addition of glucose and ammonium treatment facilitate the formation of highly graphitic carbon networks catalyzed by CoNi alloy.[201] The morphological and structural properties of the electrocatalysts were determined by scanning electron microscopy (SEM). **Figure 4.1A** displays a typical SEM image of N-CoNi/PCS composite spheres with an average size of 400 nm. Different from the CoNi precursor with a smooth surface, N-CoNi/PCS possesses a relatively rough surface resulted from the formation of partially graphitic carbon catalyzed by CoNi alloy (**Figure 4.1B**). The pomegranate-like structure was analyzed by transmission electron microscopy (TEM), where seeds encapsulated within carbon framework can be clearly revealed in a representative TEM image of a single N-CoNi/PCS composite sphere (**Figure 4.1C**). It is worth mentioning that a similar pomegranate-like morphology and microstructure can also form when either a Ni or Co precursor is present alone (denoted as N-Ni/PCS and N-Co/PCS, respectively, **Figure S4.2** and **Figure S4.3**). However, their performances are inferior to that of N-CoNi/PCS, which will be discussed later.

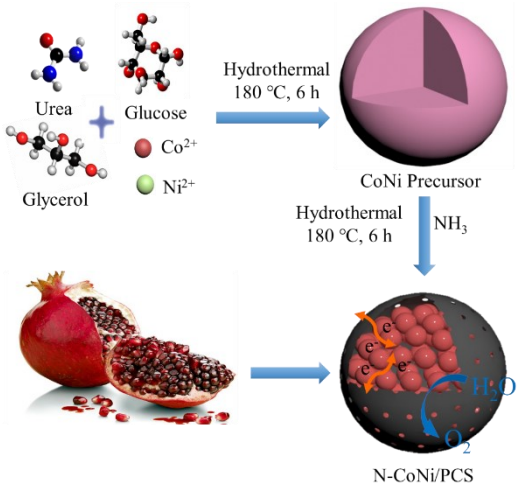

Scheme 4.1 Schematic diagram of the synthesis process of N-CoNi/PCS.

The high-angle annular dark-field scanning transmission electron microscopy (HAADF-STEM) image (**Figure 4.1D**) and corresponding energy-dispersive X-ray spectroscopy (EDS) element mapping (**Figure 4.1E**) confirm the presence of Co, Ni, C and N. Obviously, the Co and Ni are present together, implying the formation of CoNi alloy and its homogeneous dispersion within the carbon sphere. Element N exists and distributes along with element C, indicating the successful nitrogen-doping to a relatively high level of 4.20% (**Figure S4.4**). **Figure 4.1F** shows high-resolution TEM (HRTEM) images of randomly selected two areas of N-CoNi/PCS composites. The clear fringe with lattice spacing of 0.341 nm indicates the carbon is highly graphitized, not only on the carbon shell but also among all the carbon spheres forming a highly conductive network facilitating electrons transfer. Nevertheless, the composite spheres are still porous, making the active sites are fast accessible. The CoNi seeds are highly crystalline, with lattice parameter of 0.197, 0.104, and 0.202 nm, respectively, corresponding to (200), (311), and (111) planes, which can be indexed to Co1Ni1 with a cubic structure (ICSD NO. 187983). The lattice parameters are between pure Co (ICSD No. 622442) and pure Ni (ICSD No. 260172), further confirming the formation of CoNi alloy (**Table S4.1**).

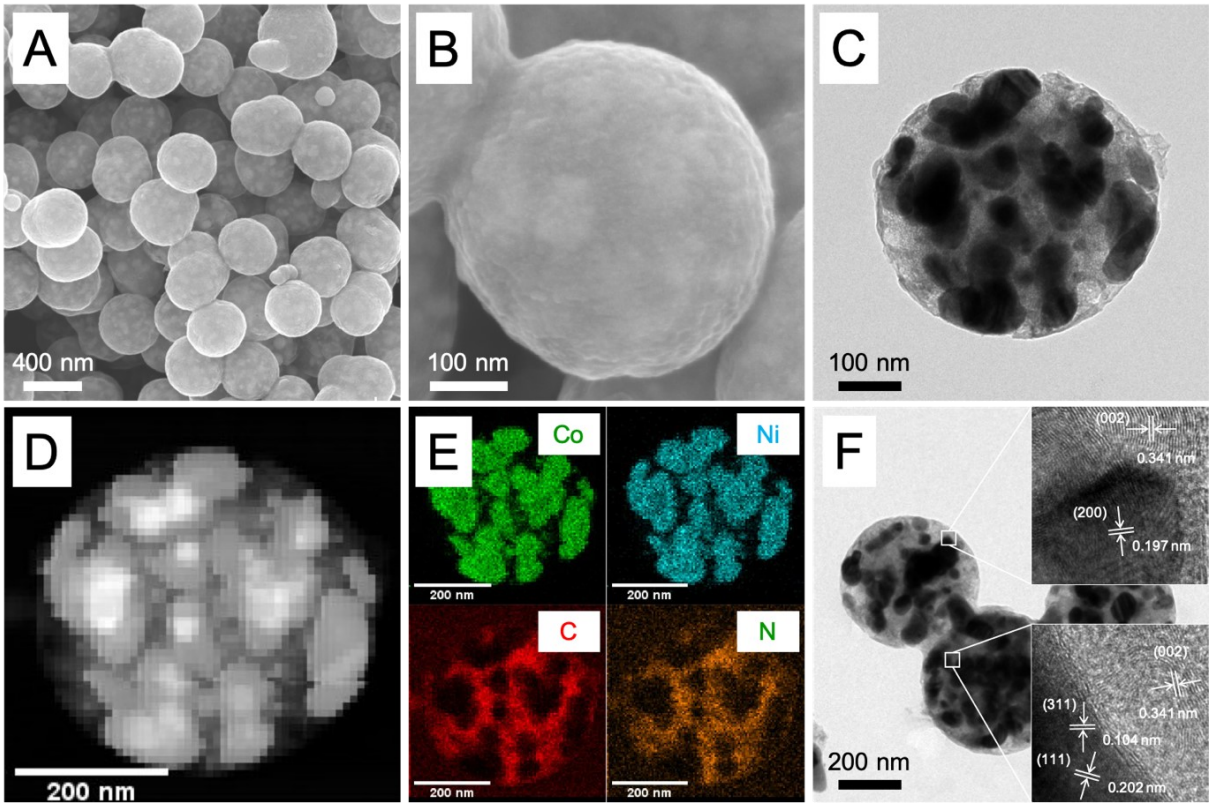

Figure 4.1 (A) SEM image of N-CoNi/PCS; (B) high-magnification SEM image of a single N-CoNi/PCS sphere; (C) TEM image and (D) HAADF-STEM image of a single N-CoNi/PCS sphere; and (E) the corresponding EDS element mapping spectrum of Co, Ni, C and N; (F) HRTEM image images of the selected areas of N-CoNi/PCS composite spheres.

The crystal structure was further revealed by X-ray diffraction (XRD). As exhibited in **Figure 4.2A**, N-CoNi/PCS shares the same XRD pattern with pure Co and Ni with a cubic structure, with the peaks centering between those of pure Co and Ni (**Figure 4.2A, insert**). The domain size was calculated to be ~50 nm depending on Scherrer's equation, consistent with the TEM observations. The pore structure of pomegranate-like N-CoNi/PCS composite spheres was investigated by nitrogen adsorption-desorption technique. **Figure 4.2B** shows the typical nitrogen adsorption-desorption isotherms with a type *IV* hysteresis loop (narrow slit-like pores) at a relative pressure ranging between 0.5 and 1, indicating hollow spheres and a hierarchically porous structure with micropores and mesopores. The Brunauer-Emmett-Teller (BET) surface area and the Barrett-Joyner-Halenda (BJH) pore volume of N-CoNi/PCS with NH_3 treatment are 235.60 m^2 g^{-1} and 0.342 cm^3 g^{-1}, which are much larger than those of the CoNi/PCS composite (186.52 m^2 g^{-1} and

0.133 cm^3 g^{-1}, **Figure S4.5**). This observation can be attributed to the activation of carbon network by NH_3 and the release of volatile compounds.[202, 203] Meanwhile, N-dopants take place of carbon atoms, which not only creates more pores resulting in higher surface area, but also interacts with metal atoms forming metal-N complex structure.[204] The pore size of N-CoNi/PCS centers at 50 nm with macropores contribution (**Figure 4.2B**, inset), which aligns with the TEM observation.

The composition and valence states of elements in N-CoNi/PCS were further characterized by X-ray photoelectron spectroscopy (XPS). The survey-level scan XPS spectra (**Figure S4.6**) confirms the presence of element C, N, Co, and Ni. The N-doping level is around 4.77 %, while the ratio Co/Ni is close to 1.8 (**Table S4.2**), which is consistent with the element mapping result. **Figure 4.2C** exhibits the core-level scan spectrum of element C, where four peaks at 284.8, 285.6 , 286.5 and 289.1 eV can be assigned to C=C, C=N, C-N, and O-C-O, respectively.[205] To further understand how N atoms exist, a core-level scan was also performed on element N, where four N species can be interpreted, including pyridinic-N (398.7 eV), pyrrolic-N (400.3 eV), graphitic-N (401.4 eV), and oxidized-N (406.0 eV) (**Figure 4.2D**). Pyridinic-N and graphitic-N play a vital role during the ORR/OER process, prompting oxygen adsorption while decreasing the overpotential due to their superior electron-accepting capability.[206, 207] **Figure 4.2E** and **4.2F** display the core-level scan spectrum of element Co and Ni, respectively. A low-energy band at 778.6 eV and a high-energy band at 793.3 eV corresponding to Co $2p_{3/2}$ and Co $2p_{1/2}$ along with two satellites can be attributed to metallic Co. A small portion of oxide state of the Co^{2+} can also be found at 780.7 and 796.6 eV, mainly due to the surface oxidation and existence of CoO_x species, which has been widely reported in literatures.[76, 196, 205] The same situation happens to metallic Ni, where Ni $2p_{3/2}$ peak is located at 853.3 eV and Ni $2p_{1/2}$ peak is determined at 870.0 eV.[193, 196, 208] The presence of Ni^{2+} at 855.2 and 872.8 eV results from surface oxidation of the metal.[209] It is reported that surface defect sites with low oxygen coordination attributes to the enhancement of OER process for CoNi alloy nanoparticles and to the configuration and the presence of synergistic effect in CoNi alloy.[198]

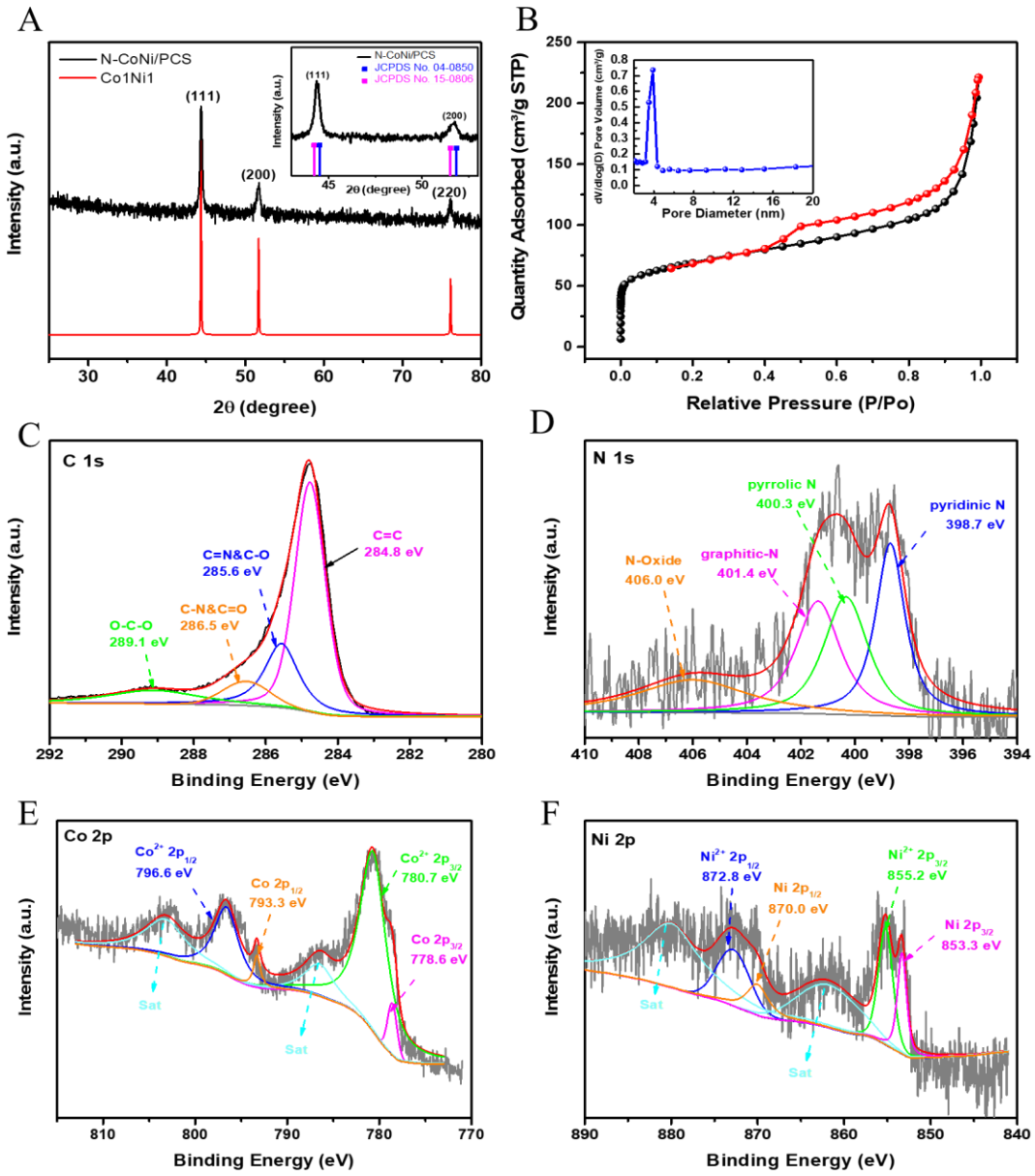

Figure 4.2 (A) Powder XRD patterns of N-CoNi/PCS (inset: Powder XRD patterns of N-CoNi/PCS); (B) N2 sorption isotherms of N-CoNi/PCS (inset: BJH pore size distribution); High-resolution XPS spectrum of (C) C 1s; (D) N 1s; (E) Co 2p; and (F) Ni 2p of the N-CoNi/PCS.

The pomegranate-like N-CoNi/PCS composite possesses a novel morphology and unique architecture that favors electrochemical catalytic oxygen reactions. The electrocatalytic behavior of N-CoNi/PCS composites towards ORR process is investigated by linear sweep voltammetry

(LSV) technique in 0.1M KOH solution. **Figure 4.3A** presents that the N-CoNi/PCS composite shows highly active ORR performance with an onset potential of 0.91 V (*vs.* reversible hydrogen electrode, RHE) and limit current density of -5.2 mA cm^{-2} at a scan rate of 10 mV s^{-1} and a rotation speed of 1600 rpm. By comparison, N-Ni/PCS only exhibits a low onset potential of 0.85 V (*vs.* RHE) and a steep limited current curve, indicating both inferior catalytic activity and ion diffusion. Although N-Co/PCS delivers a similar onset potential of 0.92 V (*vs.* RHE), the low diffusion-limited current density of only -4.8 mA cm^{-2} is not satisfactory. A single metallic Ni composite doesn't display good ORR performance which is consistent with the previous work.[210] It can be explained that O* and OH* species are adhered with Ni species intensively, which leads to the strong activation of proton-transfer steps and therefore inhibits the rate.[211] Thus, current plateau exhibits increasingly inclined with slowly electrocatalytic reaction and ununiformed modification of active sites.[212] It suggests that the presence of CoNi alloy within the graphitic carbon structure attributes to the synergistic catalysis toward ORR activity, which facilitates the electron transportation from the bimetallic alloy to the carbon shell, contributing to a structure modification on the carbon surface.[206] In addition, N-CoNi/PCS composite electrocatalyst with NH_3 treatment also shows superior performance to its counterpart, CoNi/PCS. A half-wave potential difference of 80 mV as well as significantly improved limited current density can be clearly observed from N-CoNi/PCS to CoNi/PCS. It's reported that NH_3 treatment prompts the formation of graphitic N and pyridinic N species.[66] Furthermore, the performance of electrocatalyst was associated with the graphitic N content. Graphitic N atoms attract more electrons from neighbouring C nuclei while N donates electrons, which facilitates electrons transfer from the C to N atoms. Therefore, O_2 is dissociated from the surface of C atoms and it forms the intensive binding between O and C.[213-216] This result shows that the improved electrocatalytic ORR performance is dependent to a complex synergy of higher surface area, graphitic N and pyridinic N. Note that bimetallic CoNi alloy and few NiO_x/CoO_x coordinating active sites can change the electronic configuration on the surface dictate binding site, and further prompts the oxygenation of intermediate molecular species on the surface in the electrocatalytic process. The results prove advantages of the pomegranate-like architecture with N-doped graphitic carbon shell and encapsulated CoNi alloy on improving ORR activities: the improved electrocatalyst activity is attributed to the easy access to the active sites while highly graphitic porous carbon structures speed up fast electron transportation/donation; CoNi alloy creates extra active sties inside the carbon shell and exhibits the excellent electronic

conductivity, which further boosts the electron transportation during electrocatalysis. These mechanisms explain why N-CoNi/PCS electrocatalyst possesses high electrocatalytic activity comparable to commercial Pt/C electrocatalyst (**Figure S4.7A**).

Smaller Tafel slope of N-CoNi/PCS (85.1 mV dec^{-1}) further confirms the high ORR performance compared with that of N-Co/PCS (92.4 mV $decade^{-1}$), N-Ni/PCS (88.2 mV $decade^{-1}$) and CoNi/PCS (94.7 mV $decade^{-1}$) (**Figure 4.3B**). To further clarify the ORR kinetics of N-CoNi/PCS towards ORR, the composite electrocatalyst was further scanned by LSV at a rotation speed from 2500 to 400 rpm (**Figure 4.3C**). The electron transfer number per oxygen molecule (n) for ORR via these polarization LSV curves can be determined from the *Koutechy-Levich* (*K-L*) equation. **Figure 4.3D** displays the *K-L* plot where j^{-1} and $\omega^{-1/2}$ (j is the limit current density and ω is the electrode rotating speed) show a linear relationship at different potentials (0.45, 0.50, 0.55, and 0.60 V *vs.* RHE). The electron transfer number n was determined to be 3.96 which is higher relative to those reference electrocatalysts (n values are 3.75, 3.41 and 3.69 for N-Co/PCS, N-Ni/PCS and CoNi/PCS, respectively) (**Figure S4.8**), suggesting a four-electron transfer pathway in ORR process, which further confirms and explains the excellent kinetics of N-CoNi/PCS.

In order to explore the bifunctionality of N-CoNi/PCS composite electrocatalyst, the OER catalytic activity were also investigated in the 0.1 M KOH electrolyte. **Figure 4.3E** compares the LSV polarization curve of as-prepared N-CoNi/PCS with those of N-Co/PCS and N-Ni/PCS composite electrocatalysts in the voltage window ranging from 1.00 to 1.85 V (*vs.* RHE) at a scan rate of 10 mV s^{-1} and a rotation speed of 1600 rpm. Obviously, N-CoNi/PCS possesses an onset potential 1.60 V (*vs.* RHE), much lower than N-Co/PCS and N-Ni/PCS at 1.62 V and 1.63 V (*vs.* RHE), respectively. Although the response current shows a steep increase for all samples, only N-CoNi/PCS's increase is the most significant and it reaches 10 mA cm^{-1} at 1.77 V (*vs.* RHE), indicating the lowest overpotential of 540 mV and the best OER catalytic activity among the three. Moreover, N-CoNi/PCS also shows better performance than its counterpart CoNi/PCS without N-doping. This phenomenon further confirms that N-doping not only contributes to facilitating ORR process but also provides synergistic effect together with CoNi bimetallic alloy for better OER catalytic activity.[217] It further confirms that the OER performance of N-CoNi/PCS is superior to the commercial RuO_2 in **Figure S4.7B**. As displayed in **Figure 4.3F**, the lower Tafel slope value for N-CoNi/PCS (204.1 mV dec^{-1}) indicates its more preferential reaction kinetics compared to those of N-Co/PCS (243.9 mV dec^{-1}), N-Ni/PCS (219.1 mV dec^{-1}) and CoNi/PCS (232.6 mV dec^{-}

[1]). The significantly improved OER performance is also ascribed to the unique pomegranate-like composite architecture of the composite electrocatalysts. The high surface area originate from hierarchical pores ensures not only the large exposure of active sites (micropores) but also the fast access to them (mesopores).[218]

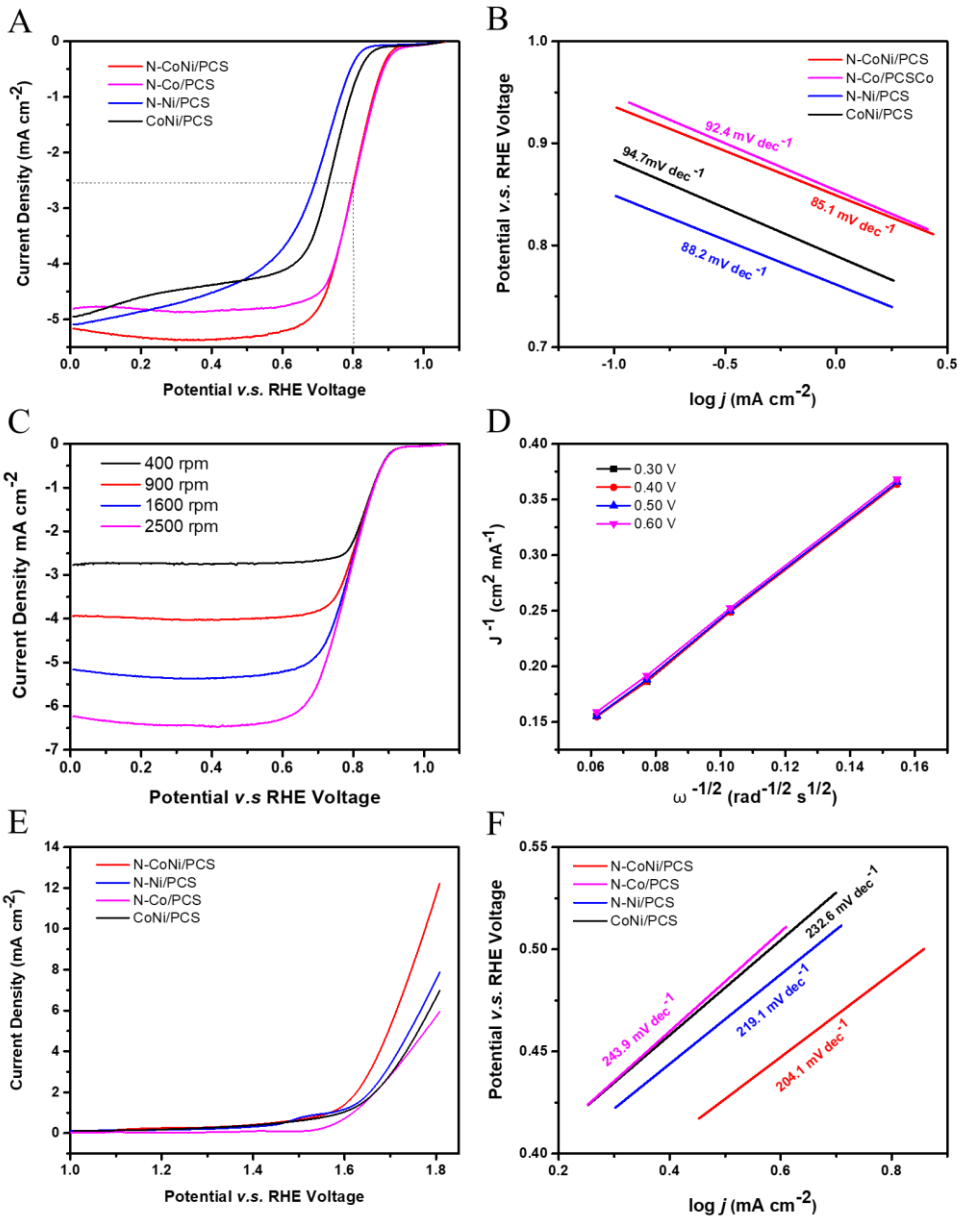

Figure 4.3 (A) Comparison of ORR polarization curves of N-CoNi/PCS, N-Co/PCS, N-Ni/PCS and CoNi/PCS electrocatalysts; (B) The corresponding Tafel plots in ORR process of four electrocatalysts; (C) ORR polarization curves of N-CoNi/PCS at different rotating speeds (400 to 2500 rpm); (D**)** *K-L* plot of N-CoNi/PCS; (E) OER polarization curves of N-CoNi/PCS, N-Co/PCS,

N-Ni/PCS and CoNi/PCS electrocatalysts at 1600 rpm rotating speed; (F) The corresponding Tafel plots in OER process of four electrocatalysts.

Moreover, the electrochemical double-layer capacitance (C_{dl}) and electrochemical active surface area (ECSA) for the four electrocatalysts have also been calculated from CV curves in the potential range of 0.92 V-1.1 V (*vs.* RHE). As shown in **Figure S4.9**, the C_{dl} of N-CoNi/PCS is estimated to be 32.52 mF cm^{-2}, higher than those of N-Co/PCS (19.50 mF cm^{-2}), N-Ni/PCS (30.02 mF cm^{-2}), and CoNi/PCS (10.16 mF cm^{-2}). This result indicates more exposed CoNi sites in N-CoNi/PCS is attributed to N-doped carbon structure and is also consistent with BET method. To investigate the electrocatalytic kinetics, electrochemical impedance spectroscopy (EIS) measurements for N-CoNi/PCS, N-Co/PCS, N-Ni/PCS and CoNi/PCS are examined at a potential of 1.65 V (*vs.* RHE). The profile of EIS at high frequency and low frequency refers to charge transfer and surface processes, respectively. As the **Figure 4.4A** shown, N-CoNi/PCS displays the smallest resistance among the four electrocatalyst, which further confirms its porous pomegranate architecture, synergistic effect of CoNi alloy nanoparticles and the decoration of nitrogen doping. **Figure 4.4B** displays chronoamperometric responses for ORR process of N-CoNi/PCS as well as N-Co/PCS, N-Ni/PCS, and CoNi/PCS at 0.51 V (*vs.* RHE) in O_2-saturated 0.1M KOH electrolyte. Obviously, N-CoNi/PCS exhibits the best durability with larger current density up to 60,000 seconds, whereas Pt/C catalyst electrode shows much higher current loss of 33.3%. Furthermore, stability test of OER process for N-CoNi/PCS and the commercial RuO_2 were also examined at 1.71 V (*vs.* RHE) in the same condition, and the results are displayed in **Figure 4.4C**. After 60000s, the current density of N-CoNi/PCS still keeps at 2.2 mA cm^{-2} which is superior to the current density of RuO_2 (1.2 mA cm^{-2}). The above results have revealed that N-CoNi/PCS exhibits superior stability, which can be explained by the following reasons. First, larger specific surface area of N-CoNi/PCS generates easy access to active sites which is confirmed by the ESCA results. Second, the bimetallic CoNi alloy creates special bonding effect which establish intrinsic polarity that leads to an electronic alternation and optimizes reaction pathways. The special bimetallic alloy uniformed decoration and intimate contact between CoNi alloy and carbon framework effectively protects the active sites preventing nanocrystals from agglomeration and corrosion, further providing good durability. Third, the highly graphitic carbon through the whole composite sphere forming highly

conductive networks not only facilitates fast electron transfer but also possesses both chemical and electrochemical stability which significantly contributes to the durability of the composite electrocatalyst. The combined effects of the exclusive morphology of such a pomegranate structure, strong coupling between graphitic sphere and N-doing/CoNi alloy-encapsulated structural contribute to the outstanding electrochemical performance.

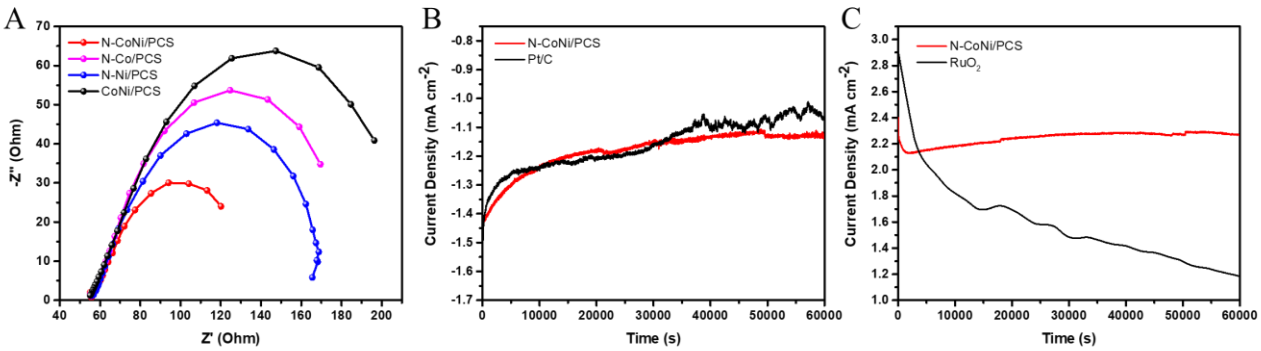

Figure 4.4 (A) Electrochemical impedance spectra (EIS) of N-CoNi/PCS tested in 0.1M KOH; (B) Chronoamperometric responses for ORR process at 0.51 V (vs. RHE); (C) Chronoamperometric responses for OER process at 1.71 V (vs. RHE).

4.1.4. Conclusion

In conclusion, we have designed and successfully developed a novel bifunctional electrocatalyst towards ORR and OER processes based on a pomegranate-like composite architecture. The highly active CoNi bimetallic alloy are synergistically integrated into nitrogen-doped highly graphitic carbon spheres. Such unique architecture enables the composite electrocatalyst with excellent electrocatalytic activity for both ORR and OER, where a half-wave potential of 0.80 V (*vs.* RHE) and a limit current density of -5.2 mA cm^{-2} can be achieved for ORR while a low overpotential of 540 mV for OER with excellent durability. This work paves an avenue to design advanced metal alloy nanocomposites electrocatalysts as a replacement of previous metals for reversible electrochemical energy storage devices and conversion technologies such as metal-air batteries and fuel cells.

4.2. Bimetallic Metal-Organic Framework Derived Doped Carbon Nanostructures as High-Performance Electrocatalyst Towards Oxygen Reactions

Besides CoNi alloy-based nanomaterials, transition metal sulfides are also widely explored as electrocatalysts for oxygen reactions as we discussed in section 2.2. Here, a high-performance electrocatalyst of cobalt and zinc sulfides nanocrystals embedded within nitrogen and sulfur co-doped porous carbon is successfully designed and derived from bimetallic metal-organic frameworks of cobalt and zinc containing zeolitic imidazolate frameworks. The unique nanostructure contains abundant electrocatalytic active sites of sulfides nanocrystals and nitrogen and sulfur dopants which can be fast accessed through highly porous structure originate from both zinc vaporization and sulfurization processes. Such bifunctional electrocatalyst delivers a superior half-wave potential of 0.86 V towards oxygen reduction reaction and overpotential of 350 mV towards oxygen evolution reaction, as well as excellent durability owing to the highly stable carbon framework with a great graphitized portion.

The outcome of this research is published in "Nano Research" (**Chen, L.**; Chen, Z.; Liu, X.; Wang, X., Bimetallic Metal-Organic Framework Derived Doped Carbon Nanostructures as High-Performance Electrocatalyst Towards Oxygen Reactions. *Nano Res.* **2020,** *14* (5), 1533-1540.)

4.2.1. Introduction

An exponential growth of energy consumption results in the fast depletion of fossil fuels and severe deterioration of environment, which in turn stimulates the discovery and development of renewable and sustainable energy technologies.[219] Over the past decades, electrochemical energy storage and conversion systems have been emerging as the most promising candidate in renewable energy sector, including fuel cells, rechargeable lithium-ion batteries (LIBs) and supercapacitors, etc.[220] Particularly, metal-air batteries are widely believed to be the next-generation power source due to their high theoretical energy density often a magnitude greater than that of LIBs, abundant feed (air), as well as reliable and safe operations.[221] However, their implementation towards electric vehicles and grid storage applications is still hindered by the inherently sluggish kinetics and consequent high overpotential and complex multiple reactions.[222] More specifically,

electrochemical oxygen redox reactions (i.e., oxygen reduction reaction (ORR) and oxygen evolution reactions (OER)) need significantly improved.[223-225] So far, noble-metal based materials, such as ruthenium oxide (RuO_2),[226] iridium oxide (IrO_2),[180] and platinum (Pt)[227] are found to be the most efficient OER and ORR electrocatalysts. Unfortunately, their limited reserves and uneven distribution resulted high price, easy aggregation and deactivation resulted poor stability place a major hurdle to the broad commercialization.[228-230] Hence, replacement of these noble-metal based electrocatalysts in metal-air batteries with low-cost and high-performance electrocatalyst is the key to the next-generation electrochemical energy technologies.

To date, many transition metal compounds including oxides (e.g., Co_3O_4), sulfides (e.g., MoS_2), phosphides (e.g., NiP), and carbon-based materials (e.g., N-doped graphene) have been extensively investigated for OER and ORR, respectively; while efficient combination of ORR and OER electrocatalysts facilitates the fabrication and integration of metal-air battery devices.[231-233] For example, Co_3O_4 nanocrystals embedded porous carbon spheres with a pomegranate-like architecture exhibit both ORR and OER electrocatalytic behavior, and such bifunctional electrocatalyst-based zinc-air battery prototype shows excellent device performance.[66] Generally, a high-performance oxygen electrocatalyst should possess several key features: i) abundant highly active sites for oxygen redox; ii) fast access to active sites for reactants and conductive networks for efficient electron transfer; iii) stable material structure and well-defined interfaces for durability.

Recently, metal organic frameworks (MOFs) have been reported promising for electrocatalysts as either precursors or sacrificial templates due to their highly porous feature, various morphologies, tunable compositions by engineering different metal ions and organic ligands.[129, 234] MOFs derived nanostructures are expected to possess all desired features that favor electrocatalytic oxygen reactions.[235-237] As a representative in MOFs family, zeolitic imidazolate frameworks (ZIFs) with its special structure where metal atoms and other elements are integrated into carbon skeleton have been already studied to fabricate nano-scale porous carbon materials for oxygen electrocatalysts.[238-241] For example, Zhang et al. synthesized NiFe-LDH/Co,N-CNF composites which displayed an OER overpotential of 0.312 V at 10 mA cm^{-2} and an ORR half-wave potential of 0.790 V;[242] while Co@NC-*x*/*y* was derived from pyrolysis of Co/Zn-ZIF and showed the superb ORR activity with onset potential of 1.15 V and half wave potential of 0.93 V.[243] Ma et al. reported a ZIF-67/PAN fiber that exhibited excellent bifunctional electrocatalytic activity.[244] Although performance improvement has been achieved, MOFs, especially ZIFs-derived electrocatalysts are

still hard to outperform those noble metals for ORR and OER.[245, 246] On the other hand, systematic study of catalytic mechanisms originated from element doping and change of local electronic structure of transition metals is insufficient.[247] Heteroatoms doping in carbon-based materials including S,[248] P,[249] and B[250] enables extra active sites, improved conductivity and tunable structure.[251, 252] For instance, Fe/N/S-CNTs derived from ZIF-8 exhibited superior ORR performance, which was ascribed to sulfate ions creating C-S-C bonds by reaction with carbon at a high temperature.[251] Cu_3P@NPPC with uniformed N and P doping synthesized from Cu-based MOFs showed excellent ORR performance due to synergistic effects between Cu_3P and doped carbon.[252] Nevertheless, further creation and understanding of such synergistic effect at molecular level are strongly in demand.

Herein, we demonstrate a unique nanostructure of N and S codoped porous carbon (N,S-Co/Zn-ZIF) derived from bimetallic ZIFs. As shown in **Scheme 4.2**, Co/Zn containing a ZIF-67 (Co/Zn-ZIF-67) precursor is prepared by a simple precipitation method where cobalt and zinc ions can coordinate with ligand links; while a facile one-step calcination and sulfurization directly converts Co/Zn-ZIF-67 precursor into N,S-Co/Zn-ZIF. Such electrocatalyst possesses a well-defined porous dodecahedron morphology and exhibits outstanding OER and ORR electrocatalytic performance. The bimetallic ZIFs provide more interactions between transition metals with doped N and S atoms and consequently create more synergistic catalytic effects. Moreover, existence of both Co and Zn protects rhombic dodecahedron morphology from decomposing after calcination. In addition, coordination effects between carbon matrix and Co/Zn compounds nanoclusters improve the contact between the nanostructure and the electrolyte, leading to an excellent OER performance with overpotential of 350 mV and ORR activity with half-wave potential of 0.86 V at 1,600 rpm. The design and realization of such nanostructured material derived from bimetallic ZIFs pave a new way of development and understanding of bifunctional electrocatalysts towards clean electrochemical energy technologies.

4.2.2. Experimental Section

4.2.2.1. Chemicals

Cobalt (II) nitrate hexahydrate ($Co(NO_3)_2 \cdot 6H_2O$, 99%), Zinc (II) nitrate hexahydrate ($Zn(NO_3)_2 \cdot 6H_2O$, >/=99%) and methanol (C_2H_6O, 95%) were purchased from Fisher Scientific; 2-

methylimidazole ($C_4H_6N_2$, 99.5%), sulfur (S, 99%), thiourea (CH_4N_2S, 99%), were purchased from Sigma-Aldrich.

4.2.2.2. Preparation of Co/Zn-ZIF precursor

In a typical preparation, two solutions of the following substances were prepared separately: $Co(NO_3)_2 \cdot 6H2O$ (0.45 g), $Zn(NO_3)_2 \cdot 6H_2O$ (0.55 g) were dissolved in methanol (50 mL); 2-methylimidazole (1.64 g) and thiourea (1.25 g) were dissolved in methanol (50 mL). The two solutions were then mixed and stirred at room temperature for 24 h. Finally, the resulting light purple powder Co/Zn-ZIF-67 was separated by centrifugation and washed by methanol for several times prior to drying in a vacuum oven at 80 °C.

4.2.2.3. Synthesis of N,S-Co/Zn-ZIF

Co/Zn-ZIF-67 precursor powder (400 mg) and sulfur powder (1.2 g) were separately in downstream and upstream in one boat and were annealed under Ar atmosphere at 400 °C for 60 min with a ramp rate of 2 °C per min and then at 800 °C for 60 min to obtain N,S-Co/Zn-ZIF. N,S-Co-ZIF and N,S-Zn-ZIF were synthesized using the same method but without adding zinc hexahydrate or cobalt hexahydrate. Also, Co/Zn-ZIF without adding thiourea was annealing under Ar atmosphere in the same condition without sulfur.

4.2.2.4. Structural Characterization

The morphology of the electrocatalysts were carried out by FEI Quanta 450 Environmental Scanning Electron Microscope (FE-ESEM) with EDAX Octane Super 60 mm2 SDD and TEAM EDS Analysis System. Transmission electron microscopy (TEM) was performed with a Thermo Scientific Talos F200X G2 S/TEM operated at 150 KV. The X-ray diffraction (XRD) measurements were carried out using a monochromatic Bruker D8 advance diffractometer with Cu Ka radiation. The study of the surface composition was recorded on a Thermo Scientific K-Alpha X-ray photoelectron spectroscopy (XPS). N2 sorption measurements of the various samples at 77 K were carried out using Quantachrome Autosorb-01 to determine the Brunauer-Emmert-Teller (BET) specific surface area, pore volume and pore size distribution. High-resolution transmission electron microscopy (HRTEM) has been used to define in detail the structures of the obtained materials.

4.2.2.5. Electrochemical Measurements

All the electrocatalytic tests were performed using electrochemical potentiostat workstation (Biologic VSP300) via a standard three-electrode system. The working electrode was glassy carbon (GC) electrode with surface area of 0.196 cm^2 loading electrocatalyst; a platinum wire was employed as the counter electrode; and a standard calomel electrode (SCE) was utilized as reference electrode. To prepare the working electrode, 2 mg of synthesized electrocatalyst and 2 mg of Vulcan Carbon (VC) were well dispersed in 400µL Nafion solution (0.5 wt%) under ultrasonication for 2 h to form a homogeneous slurry. 7 µL of slurry were casted on the glassy carbon electrode and dried at room temperature. Linear sweep voltammetry (LSV) was applied at a scan rate of 10 mV s^{-1}. Catalytic activity towards the ORR was recorded from 0.1 to -1.0 V (vs. SCE) at a scan rate of 10 mV s^{-1} with a rotating speed from 400 rpm to 2500 rpm in 0.1M KOH electrolyte; catalytic activity towards the OER was recorded from -0.1 to 0.8 V (vs. SCE) at a scan rate of 10 mV s^{-1} in 1M KOH electrolyte. N,S-Co-ZIF, N,S-Zn-ZIF and Co/Zn-ZIF were also measured in the same condition for comparison.

4.2.3. Results and Discussion

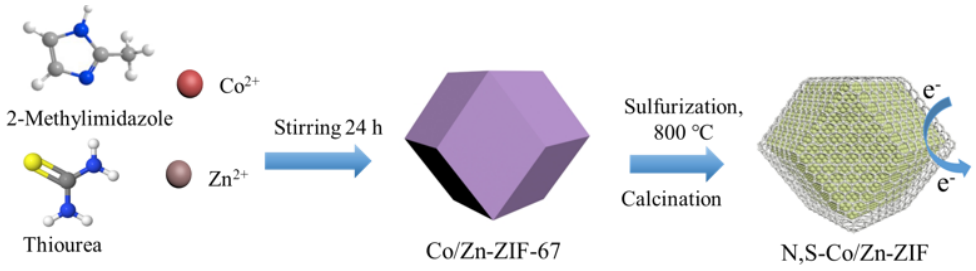

Scheme 4.2 Schematic of the synthetic process of N,S-Co/Zn-ZIF.

Highly porous N,S-Co/Zn-ZIF was successfully synthesized from bimetallic Co/Zn containing ZIF-67 (Co/Zn-ZIF-67) precursor which also possesses a rhombic dodecahedron morphology with smooth surface and a particle size of around 500 nm (**Figure S4.10**). After one-step calcination and sulfurization treatment, the nanostructured electrocatalyst of N,S-Co/Zn-ZIF was achieved (**Scheme 4.2**). The morphology and structure of N,S-Co/Zn-ZIF are characterized by scanning electron microscopy (SEM) and transmission electron microscopy (TEM). As shown in **Figure 4.5A** nanostructured N,S-Co/Zn-ZIF maintains the same rhombic dodecahedron morphology as

Co/Zn-ZIF-67 but exhibits a rough surface after the calcination and sulfurization (**Figure 4.5B**). The existence of bimetallic Co and Zn plays an important role in maintaining the morphology and developing porous structure of N,S-Co/Zn-ZIF. Although N,S-Co-ZIF still shows a rhombic dodecahedron morphology (**Figure S4.11A** and **S4.11B**), the existence of single metal results in the morphology decomposition. Also, the existence of only Zn leads to nanospheres with an average size of around 100 nm (**Figure S4.11C** and **S4.11D**). Moreover, due to its low boiling point, Zn containing compounds evaporate during calcination at high temperature, forming porous structure that can be reflected by the rough surface.[253] Thus, more active sites are created and exposed that facilitate electrocatalytic process. In addition, without sulfurization, nanofibers are inevitably formed, while the rhombic dodecahedron morphology is also hard to be defined (**Figure S4.11E** and **S4.11F**).

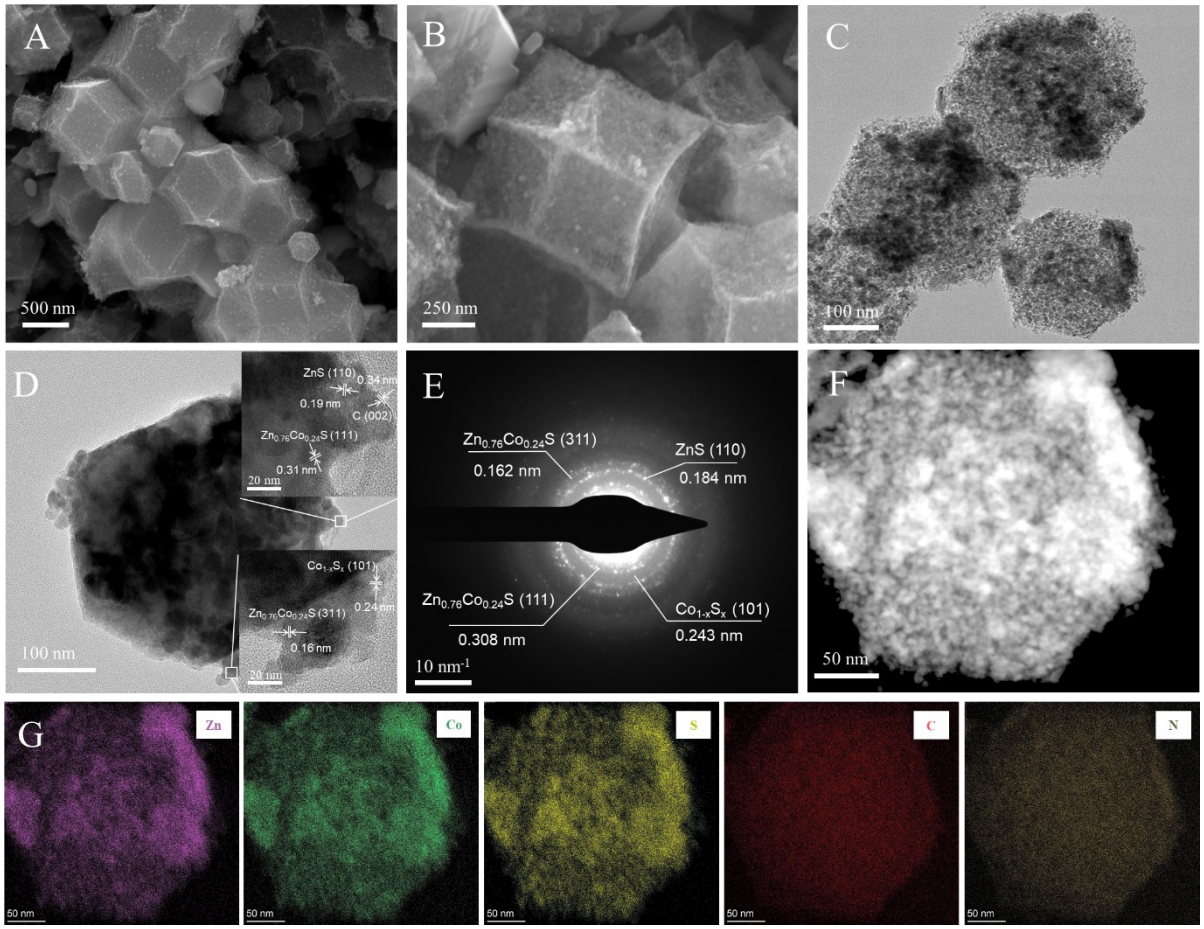

Figure 4.5 (A) Low and (B) high magnification SEM images of as-synthesized N,S-Co/Zn-ZIF; (C) TEM image of N,S-Co/Zn-ZIF nanoparticles; (D) TEM image of a single N,S-Co/Zn-ZIF nanoparticle (inset: HRTEM images of two selected areas); (E) The corresponding SAED patten recorded from a single nanoparticle; (F) HAADF-STEM image of a single N,S-Co/Zn-ZIF; and (G) the corresponding EDS element mapping spectra of element Zn, Co, S, C and N.

The highly porous nanostructure of N,S-Co/Zn-ZIF is clearly revealed by the TEM images in **Figure 4.5C**. The nanostructure is composed of nanoparticles implying the conversion of bimetallic Co and Zn precursors into their compounds embedded within the derived porous carbon. The high-resolution TEM (HRTEM) images in **Figure 4.5D** confirm the existence of metal sulfides with an average size of 25 nm, which is consistent with the selected area electron diffraction (SAED) observation in **Figure 4.5E**. Moreover, the carbon nanostructure is highly graphitized with an inter-lattice spacing of 0.34 nm, forming a highly conductive network for fast electron transfer. The

lattice fringes with an inter-planar spacing of 0.31 and 0.16 nm can be perfectly indexed to (111) and (311) crystal planes of the $Zn_{0.76}Co_{0.24}S$, while the lattice spacings of 0.19 and 0.24 nm are ascribed to the (110) and (101) planes of ZnS and $Co_{1-x}S_x$, respectively. The presence of bimetallic sulfide nanoparticles embedded within derived carbon nanostructure is further confirmed by high-angle annular dark-field (HAADF)-scanning transmission electron microscopy (STEM) image in **Figure 4.5F**. All of the elements Co, Zn, C, N, and S are uniformly distributed in the dodecahedra cluster in **Figure 4.5G**.

The crystal structures of transition metal compounds were analyzed by X-ray diffraction (XRD) technique. The Rietveld refinement of N,S-Co/Zn-ZIF can be perfectly fitted to the diffraction pattern with excellent agreement factors (*R*wp = 3.90%, *R*p = 7.91%) (**Figure 4.6A**). It demonstrates a dominant cubic system of $Zn_{0.76}Co_{0.24}S$ (JCPDS No. 47-1656) in N,S-Co/Zn-ZIF with a high phase content of 85.3 wt.%, while a small amount of ZnS (11.1 wt.%, JCPDS No. 36-1450) and $Co_{1-x}S_x$ (3.6 wt.%, JCPDS No. 42-0826) coexist. By comparison, as-synthesized N,S-Co-ZIF, N,S-Zn-ZIF and Co/Zn-ZIF show different phases (**Figure S4.12**), where the crystallographic parameters are illustrated in **Table S4.3**. Such XRD results are in good agreement with the HRTEM observations where ultrafine $Zn_{0.76}Co_{0.24}S$ nanocrystals are dominantly embedded in ZIF-derived porous carbon. The porous structure of N,S-Co/Zn-ZIF nanostructure was investigated by nitrogen adsorption/desorption isotherms. Type IV isotherms can be obtained with an identifiable hysteresis loop (**Figure 4.6B**), which indicates a dominant mesoporous structure with a high Brunauer-Emmett-Teller (BET) surface area of 197.8 m^2g^{-1}. The pore size distribution is calculated by the Barrett-Joyner-Halenda (BJH) method, which describes the majority of mesopores of 24.5 nm. It can be concluded that the synthesis transforms bimetallic Co/Zn-ZIF-67 into a hierarchically porous structure with abundant pore channels, which facilitates the ion and molecule transportation.[254]

The elemental composition and electronic structure of N,S-Co/Zn-ZIF nanostructure were investigated by X-ray photoelectron spectroscopy (XPS) analysis. The complete survey spectrum demonstrates the existence of Zn, Co, S, C, and N (**Figure S4.13**). The elemental ratios measured by XPS spectroscopy agree well with the results of energy dispersive X-ray (EDX) spectrum (**Table S4.4**). From the Zn 2p region exhibited in **Figure 4.6C**, the two main peaks observed at 1,044.84 and 1,021.74 eV belong to Zn $2p_{1/2}$ and Zn $2p_{3/2}$, respectively, which corresponds to the Zn^{2+}.[247] As for the Co 2p spectrum in **Figure 4.6D**, the main peaks at 780.48, 796.48 eV and 778.38,

793.38 eV demonstrate the co-existence of Co^{2+} and Co^{3+}, which is consistence with XRD and HRTEM analysis. In addition to the binding energy of C=O at 288.15 EV and C-C at 284.71 eV,[255, 256] C-N at 285.78 eV and C-S peak located at 286.25 eV in C 1s spectrum (**Figure 4.6E**) confirm the S and N doping in the C matrix. This indicates that N is distributed almost entirely on the carbon surface, which verifies the incorporation of N in the carbon matrix.[257] As depicts in **Tables S4.4** and **S4.5**, the amount of N element is higher in N,S-Co/Zn-ZIF (≈ 11.25 at.%) than Co/Zn-ZIF (≈ 9.55 at.%), owing to the thiourea in the precursor and thermal decomposition during pyrolysis. N 1s spectrum proves the existence of the pyridinic N (398.78 eV), pyrrolic N (400.01 eV), graphitic N (400.88 eV), and oxide N (402.68 eV), as shown in **Figure 4.6F**.[258, 259] It is reported that graphite and pyridine N are considered playing an essential role in prompting the catalytic ability for ORR and OER. In S 2p spectrum (**Figure 4.6G**), the two peaks located at 162.28 and 163.88 eV are ascribed to the S $2p_{1/2}$ and S $2p_{3/2}$ of Zn-S bond, while the other two peaks at 162.88 and 161.58 eV can be attributed to the S $2p_{1/2}$ and S $2p_{3/2}$ of the Co-S bond, which indicating the successful sulfurization on the Co/Zn-ZIF-67 precursor.[260, 261] The S element are both from thiourea and S powder from the vulcanization process. However, thiourea can be easily decomposed into gas during pyrolysis which favors the formation of porous structure, S powder can offer sufficient sulfur source. The excessive S element exists not only in the $Zn_{0.76}Co_{0.24}S$, ZnS and $Co_{1-x}S_x$ nanoparticles but also on the carbon surface, demonstrating the chemical contact between metal sulfur nanoparticles and the graphitized carbon layer which would greatly benefit to electrons transfer. Noted that excessive sulfur may also lead to a defect which is favorable to the enhancement of the electrocatalytic performance.[262]

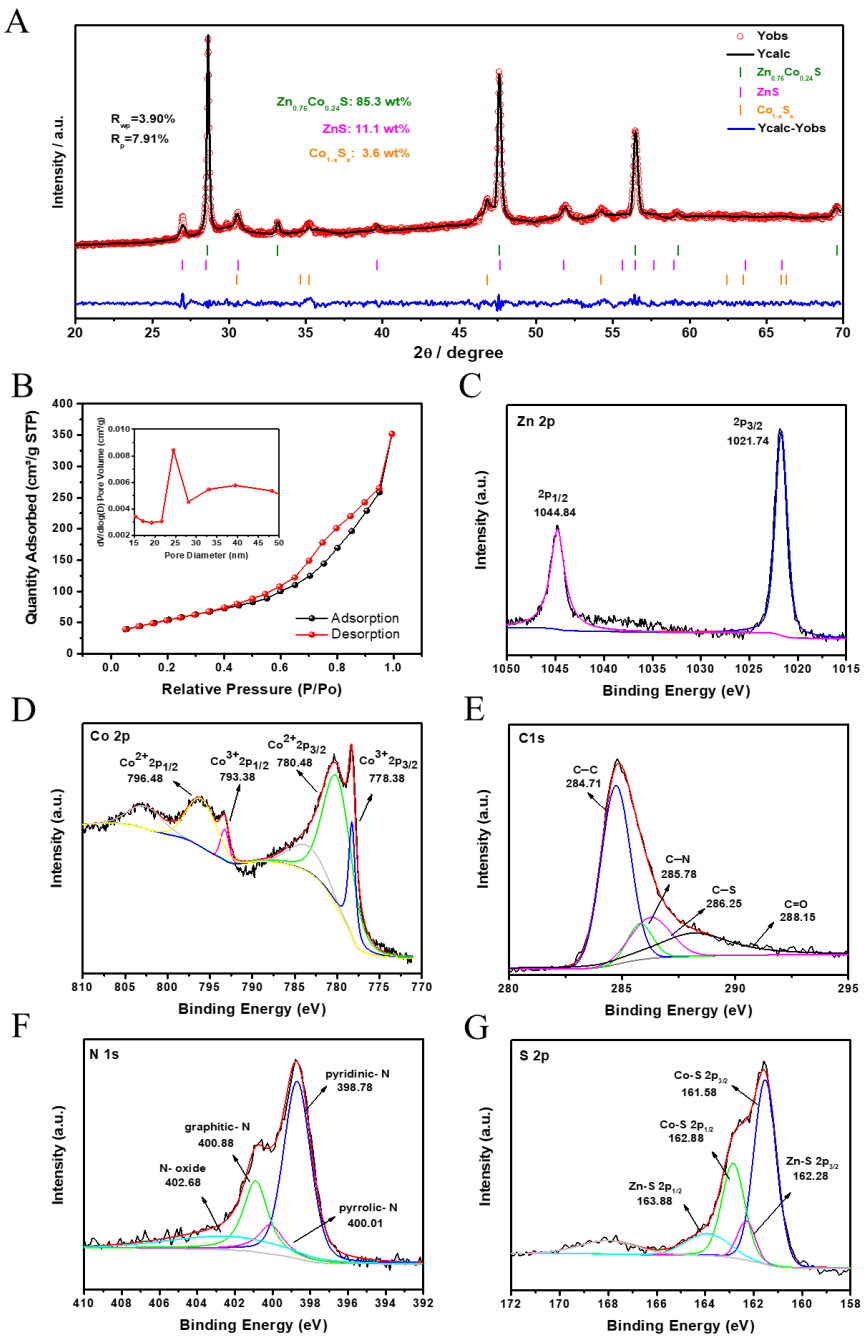

Figure 4.6 (A) XRD pattern and Rietveld refinement of N,S-Co/Zn-ZIF; (B) N_2 adsorption-desorption isotherms of N,S-Co/Zn-ZIF (inset: BJH pore size distribution profile); High-resolution XPS spectrum of (C) Zn 2p, (D) Co 2p, (E) C 1s, (F) N 1s; and (G) S 2p of the N,S-Co/Zn-ZIF, along with their corresponding fitting curves.

The bimetallic ZIF-67 derived N,S-codoped porous carbon material N,S-Co/Zn-ZIF was used as an electrocatalyst and investigated for electrochemical oxygen reactions. It was firstly characterized using linear sweep voltammetry (LSV) technique in KOH solution with a standard calomel electrode (SCE) as the reference. As shown by LSV profiles in **Figure 4.7A**, N,S-Co/Zn-ZIF exhibits a more positive onset potential of 0.96 V (vs. reversible hydrogen electrode, RHE), along with a significantly higher half-wave potential ($E_{1/2}$) of 0.86 V than those of any other materials for comparison, including N,S-Co-ZIF ($E_{1/2}$ = 0.76 V), N,S-Zn-ZIF ($E_{1/2}$ = 0.62 V), and Co/Zn-ZIF ($E_{1/2}$ = 0.73 V), for ORR process. Moreover, N,S-Co/Zn-ZIF exhibits comparable or even better ORR performance than commercial Pt/C electrocatalyst (**Fig. S4.14B**) in terms of half-wave potential. It is believed that the existence of bimetallic Co and Zn leads to the formation of more hierarchical pores during high-temperature calcination, bringing more active sites for sulfurization and prompt the formation of rough surfaces, as confirmed by N_2 sorption analysis and the XRD patterns of $Zn_{0.76}Co_{0.24}S$ and $Co_{1-x}S_x$. Moreover, S doping into the N-doped carbon alternates the surrounding electron density and hence increases the ORR activity of the electrocatalyst. In addition, electrocatalytic activity is greatly enhanced due to the high content of pyridine N and graphite N, where these defects are created to provide abundant active sites.[229] This result shows that the improved electrocatalytic ORR activity is dependent on a complex synergistic effect of higher and rougher surface area, graphitic N and pyridinic N. The notable ORR performance of N,S-Co/Zn-ZIF is further confirmed by the smaller Tafel slope of 103.9 mV dec^{-1} at low overpotentials compared to that of N,S-Co-ZIF (242.4 mV dec^{-1}), N,S-Zn-ZIF (391.1 mV dec^{-1}) and Co/Zn-ZIF (297.1 mV dec^{-1}) (**Figure 4.7B**).

In order to further study the kinetic behavior, N,S-Co/Zn-ZIF was tested using the LSV technique with the electrode at various rotating speeds (**Figure 4.7C**). It can be clearly seen that as the rotating speed increases, the onset potential of N,S-Co/Zn-ZIF remains unchanged, while the current density increases sharply due to the improvement of mass transport and shortened diffusion distance. The electron transfer number per oxygen molecule (n) for ORR is determined from the LSV curves according to the Koutechy-Levich (K-L) equation. The K-L curves (**Figure 4.7D**) display linear relationships between j_k^{-1} and $\omega^{-1/2}$ (where j_k is the kinetic current and ω is the electrode rotating rate), from which n was determined to be 3.94, suggesting a preferable four-electron pathway for ORR. By comparison, n values are calculated to be 3.78, 3.43 and 3.66 for

N,S-Co-ZIF, N,S-Zn-ZIF and Co/Zn-ZIF, respectively (**Figure S4.15**), suggesting a two-electron and four electron mixed transfer pathway in ORR process.

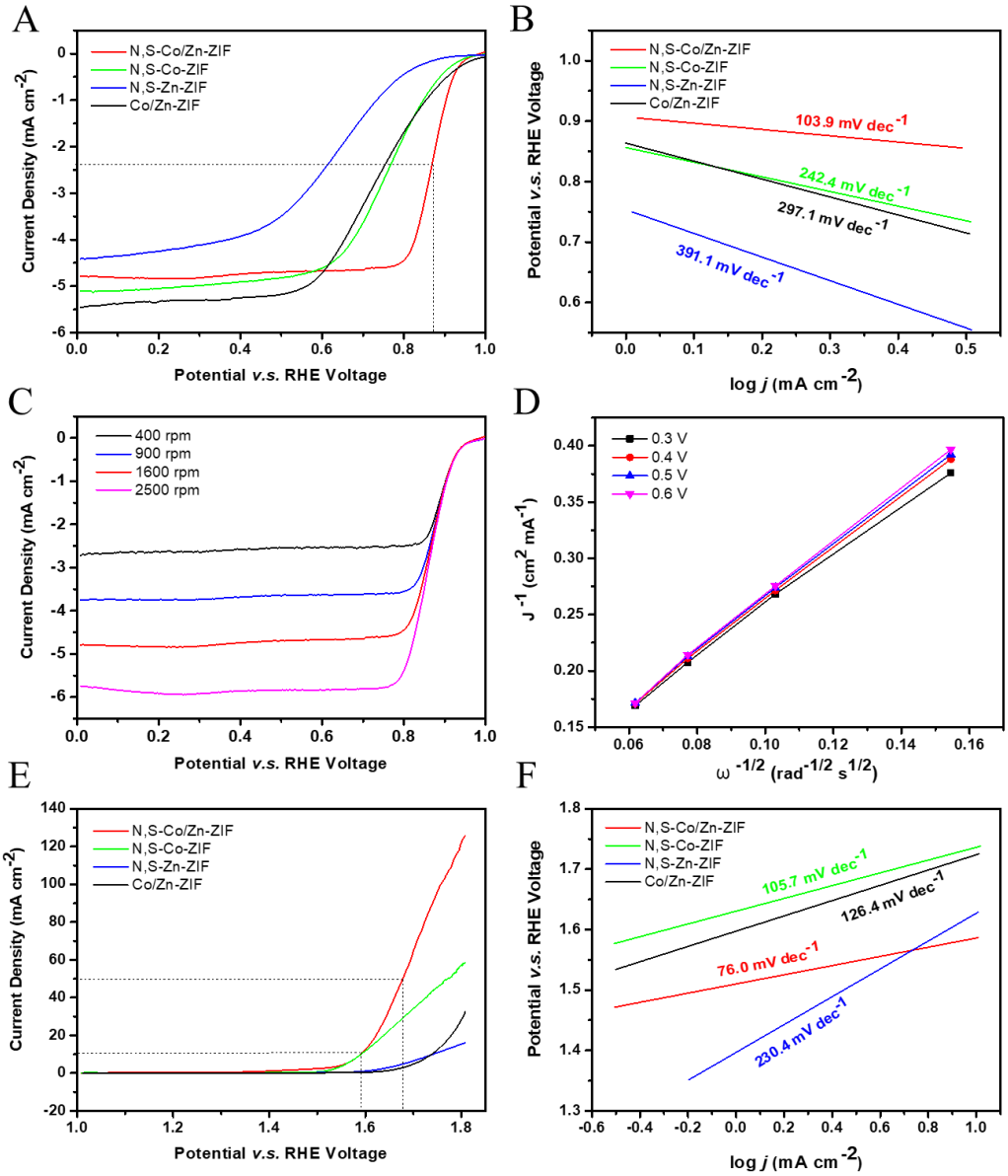

Figure 4.7 (A) Comparison of ORR polarization curves of N,S-Co/Zn-ZIF, N,S-Co-ZIF, N,S-Zn-ZIF and Co/Zn-ZIF electrocatalysts; (B) Corresponding Tafel plots of ORR with four electrocatalyst; (C) ORR polarization curves of N,S-Co/Zn-ZIF at different rotating speeds (400 to 2,500 rpm); (D) K-L plot of N,S-Co/Zn-ZIF; (E) OER polarization curves of N,S-Co/Zn-ZIF, N,S-Co-ZIF, N,S-Zn-ZIF and Co/Zn-ZIF electrocatalysts; (F) Corresponding Tafel plots of OER process with the four electrocatalysts.

In order to explore its bifunctional electrocatalytic behavior, the N,S-Co/Zn-ZIF and reference electrocatalysts are also investigated using the LSV technique in the OER process. LSV curves were obtained and compared at the rotating speed of 1,600 rpm at a scan rate of 10 mV s^{-1}. As displayed in **Figure 4.7E**, N,S-Co/ Zn-ZIF presents a significantly low onset potential (1.55 V) compared to N,S-Co-ZIF (1.56 V), N,S-Zn-ZIF (1.63 V) and Co/Zn-ZIF (1.65 V). Remarkably, N,S-Co/Zn-ZIF is found to possess the lowest overpotential (350 mV) and the best OER catalytic performance as it reaches 1.58 V at a current density of 10 mA cm^{-2} after ZIR-correction (**Figure S4.14A**). This finding confirms that the OER performance of N,S-Co/Zn-ZIF is superior to that of the commercial RuO_2 electrocatalyst (**Figure S4.14C**). The corresponding Tafel plots of OER process for the various catalysts are shown in **Figure 4.7F**. The lower Tafel slope value of N,S-Co/Zn-ZIF (76.0 mV dec-1) indicates that its reaction is more kinetically favorable than N,S-Co-ZIF (105.7 mV dec-1), N,S-Zn-ZIF (230.4 mV dec^{-1}) and Co/Zn-ZIF (126.4 mV dec^{-1}) (**Figure S4.15**). The enhancement in OER performance can be ascribed to the ternary metal sulfides nanocrystals embedded in a highly porous N and S co-doped carbon matrix. The hierarchical pores not only ensure a high surface area with exposed active sites but also open up transport channels facilitating fast access to them.

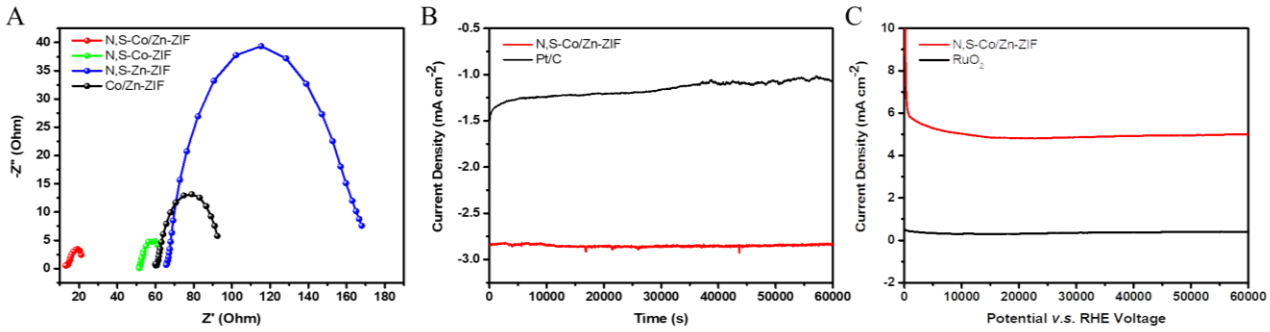

Figure 4.8 (A) Nyquist plots of N,S-Co/Zn-ZIF, N,S-Co-ZIF, N,S-Zn-ZIF and Co/Zn-ZIF electrocatalysts obtained in 0.1 M KOH; (B) Comparison of chronoamperometric responses for ORR process between N,S-Co/Zn-ZIF and Pt/C at 0.51 V in 0.1 M KOH (*vs.* RHE); (C) Comparison of chronoamperometric responses for OER process between N,S-Co/Zn-ZIF and RuO_2 at 1.71 V in 1M KOH (*vs.* RHE).

To further understand such superior electrocatalytic performance of N,S-Co/Zn-ZIF, the electrochemical double-layer capacitance (C_{dl}) and electrochemical active surface area (ECSA) were estimated via cyclic voltammetry (CV) curves in the potential range of 0.968-1.068 V (vs. RHE) (**Figure S4.16**). The C_{dl} of N,S-Co/ Zn-ZIF is determined to be 56.5734 mF cm^{-2}, higher than that of N,S-Co-ZIF (55.8482 mF cm^{-2}), N,S-Zn-ZIF (43.8338 mF cm^{-2}), and Co/Zn-ZIF (47.2634 mF cm^{-2}). This result is consistent with the N_2 sorption isotherms and reveals the presence of more exposed active sites in N,S-Co/Zn-ZIF which can be attributed to the N,S-doped carbon matrix. Furthermore, electrochemical impedance spectroscopy (EIS) measurements at a potential of 1.65 V (vs. RHE) is carried out for the discovery of the electrochemical kinetics and the internal resistance of different electrocatalytic materials. As can be seen in **Figure 4.8A**, N,S-Co/Zn-ZIF exhibits the smallest semi-circle, indicating the lowest resistance of electrolyte diffusion, the intrinsic resistance of the materials and the contact resistance between substrate and electrode materials.[260] This observation can be also explained by the open morphology, high specific surface area, abundant transport channels and active site of the N,S-Co/ Zn-ZIF nanostructure, which are in favor of the electrolyte diffusion during the electrochemical reaction processes. The N,S-Co/Zn-ZIF electrocatalyst was also tested at 0.51 V (vs. RHE) in O_2-saturated electrolyte for 60,000 s to measure the durability. Apparently, N,S-Co/Zn-ZIF displays a more stable performance with larger current density at -2.7 mA m^{-2}, whereas Pt/C catalyst electrode shows much higher current loss of 33.3% (**Figure 4.8B**). Notably, after 60,000 s, the ORR performance of the N,S-Co/Zn-ZIF shows only a 5 mV decrease in half-wave potential which the limiting current stays constant with a value of -5 mA cm^{-2} (**Figure S4.17A**). Long-term stability for OER process of N,S-Co/Zn-ZIF and the commercial RuO_2 is also tested at 1.71 V (vs. RHE) (**Figure 4.8C**). N,S-Co/Zn-ZIF retains current density at 4.8 mA cm^{-2} after 60,000 s which is much superior to the current density of RuO_2 (0.2 mA cm^{-2}). The **Figure S4.17B** further confirms that after 60,000 s, the overpotential of N,S-Co/Zn-ZIF almost remain the same and the potential only increased 13 mV at a limit current density of 50 mA cm^{-2}. Obviously, N,S-Co/Zn-ZIF has excellent durability for electrochemical oxygen redox processes. First, high OER activity is likely dominated by metal-based species. Since Zn species is inactive in both OER and ORR, it creates more defects, and thus it provides active and coordination sites during volatilization in high temperature. Second, the higher surface content of pyridinic N is favorable to afford the higher ORR mass and specific activities. Furthermore, the heteroatom sulfur

doping on the carbon skeleton leads to an increase in charge population and density, acting as the extra active sites for ORR.

4.2.4. Conclusion

In conclusion, a novel nitrogen and sulfur atom co-doped porous carbon nanostructure has been successfully achieved which is derived from bimetallic Co and Zn containing ZIF-67 structure. Such nanostructure possesses high surface area, highly porous feature, and excellent stable structure. When applied for electrochemical oxygen redox processes, it exhibits bifunctional catalytic behavior and outstanding electrocatalytic activity for both ORR and OER, where a high half-wave potential of 0.86 V (vs. RHE) and a limiting current density of -4.8 mA cm^{-2} are achieved for ORR and a low overpotential of 350 mV is obtained in OER. Such excellent electrocatalytic performance is mainly due to the unique morphology and nanostructure. The material design is expected to open new directions in the synthesis and exploration of novel low cost and efficient electrocatalysts and it would further promote their wider applications in energy storage and conversion systems.

4.3. Ni_9S_8/MoS_2 Nanosheets Decorated $NiMoO_4$ Nanorods Heterostructure for Enhanced Water Splitting

We already discussed two types of transition metal-based materials for oxygen reactions. Both of them exhibit the superior performance which lay the solid foundation to explore their properties. Encouraged by the above results, we further design Ni_9S_8/MoS_2 nanosheets decorated $NiMoO_4$ nanorods heterostructure as high-performance electrocatalysts for water splitting which is developed *via* a facile hydrothermal process followed by a direct sulfurization. The resulting hierarchical nanoarchitecture with outer Ni_9S_8/MoS_2 nanoflakes shell on the inner $NiMoO_4$ core supplies affordable active sites and plentiful charge transportation channels in continuous heterointerfaces. When it's applied for water splitting, the obtained nanomaterial only needs low overpotentials of 190 and 360 mV to enable a 10 mA cm^{-2} current density for HER and OER in alkaline solution, respectively.

4.3.1. Introduction

Faced with the increasing environmental challenges, the development of renewable and sustainable energy conversion and storage devices is highly in demand.[43] Among them, water electrolysis is regarded as an ideal candidate due to its output of green hydrogen with zero CO_2 emissions [41]. In general, water electrolysis can decoupled to hydrogen and oxygen evolution reaction (HER, OER), theoretically requiring 1.23 V to drive the reaction.[263, 264] However, due to the unfavorable kinetics and adverse thermodynamic process of the OER and HER, the demanded potential for splitting water far exceeds 1.23 V (*e.g.*, 1.61V [265]). As such, electrocatalysts should be utilized to facilitate the reaction and reduce the overpotential for the energy conversion. Although precious metal-based electrocatalysts, including platinum for HER and iridium/ruthenium for OER, show outstanding catalytic activity, their expensive price and scarcity hindered the wide application.[86, 266] Hence, it's compulsory to explore cost-effective, highly efficient, and long-life catalysts based on non-precious metals.[267]

Recently, transition metal-based electrocatalysts including transition-metal nitride, phosphides, and oxides have been widely used for water splitting.[254] Transition metal sulfides including both layered MS_2 (such as MoS_2, WS_2) and non-layered M_xS_y (such as Co_9S_8, ZnS) are at the cutting edge of material science owing to their structural diversity, electrical activity, and superior electrocatalytic performance.[39, 268-270] Particularly, molybdenum sulfide (MoS_2), possessing two-dimensional structure, stable physical and chemical properties, showed good activity towards HER in both acidic and alkaline media.[271, 272] However, the HER performance of layered MoS_2 materials still fails to surpass the Pt-based electrocatalysts due to poor conductivity and unexposed active sites.[42, 43] To overcome these shortcomings, hybriding MoS_2 with other active composites with high electrical conductivity to build hetero-structure is a promising strategy, which exhibit synergistically promoted kinetics and tune the electron configuration and possess diverse active sites.[273] For instance, nickel sulfide (Ni_xS_y) not only display good conductivity, but also are active for OER.[42, 274] Therefore, designing a heterostructure combined MoS_2 with nickel sulfides could significantly prompt the HER performance, even it provides a considerable solution to synthesize bifunctional electrocatalysts for water splitting.[275, 276] Many reports have illustrated that hybridizing two or more metal sulfides into a composite can significantly prompt the HER performance, even it provides a considerable solution to construct electrocatalysts for water

splitting. [42] The promoted performance for such binary nanostructure could be primarily ascribed to their abundant reactive redox sites, synergistic interfaces, and customized conductivity.[277, 278] For example, Liu et al. reported the yolk-shell MoS_2/NiS-based electrocatalyst for water splitting only requiring an voltage of 1.64 V in the base solution to reach the current density of 10 mA cm^{-2}.[279] Feng et al. constructed MoS_2/Ni_3S_2 heterostructures on nickel foam generating ample interfaces.[280] Zhai et al. reported $NiS_2/CoS_2/MoS_2$ nanosheets arrays vertically grown on Ni foam by two facile procedures.[281] Nonetheless, the scarcity of inherent conductivity hindered these bifunctional nanohybrids to be the best replacement for precious-metal based electrocatalysts.[282] Consequently, structural construction and optimization associated with conductivity and performance is significant to attain advanced binary hybrids.

The construction of two-dimensional (2D) heterostructures with other 2D or 1D building blocks with special electronic features forming the core-shell or yolk-shell structures have been demonstrated exhibiting superior electrocatalytic performances to the individual constitutional 2D nanomaterials. It's found that high tempertature solid-state reaction processes such as sulfuriztion and carbonizing are the simplest method to fabricate the such heterostructures bonded by weak van de Waals forces.[283] For example, TiO_2/g-C_3N_4 2D-2D heterostructure is fabriacated by in-situ grown method with strong interlayer charge transfer and coupling within the layers, endowing much enhanced catalytic activities.[27] Yamauchi et. al reported the self-assembly of uniform Ni-Co phosphate nanoplates into porous 1D chainlike particles synthesized by solvethermal process followed by facile calcination. Such special self-stacking strcuture with intimate contact between layers displayed lower overpotential of 310 mV for OER performance. According to previous reports, there are lots of advantages of heterostructures such as more exposed active sites donating from surface area and defects; tuned the electronic structure to optimize electrocatalytic reaction pathways; an interconnected open space with accessible channels and highly conductive networks for the fast transport of ions and electrons in the electrolyte, thus further leading to fast reaction kinetics. For example, Zheng et al. designed aligned NiS_2/MoS_2 on Ti foil via the hydrothermal method in which NiS_2 interlaced with MoS_2 fed ample active edge sites while MoO_3 cores fastened electron transport.[285] Wang et al. also reported MoS_2 nanosheets-stacked nanowires with decoration of NiS and MoO_3. Such architecture delivered a method to simultaneously enhance the density of active edge sites and provide more electron transfer pathway.[286] Inspired by this, we wonder if the 2D nanosheets congregated with a 1D nanorod can be achieved through facile

synthesis method to avoid the aggregation of 2D nanosheets instead of creating plentiful active sites and creating synergistic effect, further facilitating the electrocatalytic properties of the materials.

Herein, we developed a 3D hierarchical core-shell architecture in which $NiMoO_4$ nanorods as the core is wrapped with oriented Ni_9S_8 and MoS_2 nanosheets as the shell, giving rise to $Ni_9S_8/MoS_2@NiMoO_4$, through a simple sulfurization treatment of the Ni-Mo precursor. This unique structure synchronously provides ample active site and improve the conductivity for electron transportation. Due to synergistic effect of its special multiple interfacial heterostructure, fast ion/mass transportation in its porous structure and abundant electron transfer trails within the 2D nanosheets and 1D inner $NiMoO_4$ nanorods, the $Ni_9S_8/MoS_2@NiMoO_4$ displays low overpotentials of 190 and 360 mV to deliver a current density of 10 mA cm^{-2} for alkaline HER and OER, respectively. Furthermore, this study enlightens a simple strategy to synthesize economic and active electrocatalysts with heterostructures.

4.3.2. Experimental Section

4.3.2.1. Chemicals

Sodium molybdate dihydrate ($Na_2MoO_4 \cdot 2H_2O$), nickel (II) nitrate hexahydrate ($Ni(NO_3)_2 \cdot 6H_2O$), sulfur (S), potassium hydroxide (KOH) were purchased from Sigma-Aldrich.

4.3.2.2. Synthesis of Ni-Mo Precursor

Ni-Mo precursors were prepared by a facile hydrothermal method and followed with calcination process. In a typical case, $Na_2MoO_4 \cdot 2H_2O$ (0.2 g) and $Ni(NO_3)_2.6H_2O$(0.2 g) were dissolved in deionized water (60 mL) and under ultrasonication for 3 min. Then the green transparent solution was poured into a 100 mL Teflon autoclave and the hydrothermal reaction took place at 180 ℃ for 12 h. The final product was washed with copious water for several times and dried at 50 ℃ overnight, giving rise to Ni-Mo precursor.

4.3.2.3. Synthesis of $Ni_9S_8/MoS_2@NiMoO_4$

Powdery Ni-Mo precursor and sulfur with a mass ratio of 1:3 was put in one porcelain boat with the downstream and upstream side and annealed at 350℃ for 2 h under flowing Ar. The as-prepared

sample was identified as $Ni_9S_8/MoS_2@NiMoO_4$. For comparison, $NiMoO_4$ was also synthesized by calcining Ni-Mo precursor without sulfur under the same calcination condition.

4.3.2.4. Structural Characterization

The micro/nano-structure of samples were observed by Environmental Scanning Electron Microscope (ESEM, FEI Quanta 450) with EDAX Octane Super 60 mm^2 SDD and TEAM EDS Analysis System. Transmission electron microscopy (TEM, Thermo Scientific Talos F200X G2 S/TEM) was employed to obtain inner structures and crystalline information at an accelerating voltage of 150 KV. The X-ray diffraction (XRD) measurements were performed by a monochromatic Bruker D8 advance diffractometer with Cu Ka radiation. The composition and valence states were tested on a Thermo Scientific K-Alpha X-ray photoelectron spectroscopy (XPS). N_2 sorption measurements were performed using Micromeritics 3Flex Surface Characterization Analyzer with N_2 as the adsorbent.

4.3.2.5. Electrochemical Measurements

All electrocatalytic tests were conducted on the Biologic VMP300 electrochemical workstation in 1.0 M KOH with the three-electrode equipment including the glassy carbon (GC) electrode (area: 0.196 cm^2) as the working electrode, platinum wire as the counter electrode and the saturated calomel electrode (SCE) as the reference electrode. To prepare the electrode slurry, 3 mg of samples and 3 mg of Vulcan carbon were added into 400 μL Nafion solution (1 wt%) and the mixture was ultrasonicated for 2 h to form a homogeneous slurry. Then, 8.5 μL of slurry was drop coated onto the GC electrode to serve as the working electrode. Linear sweep voltammetry (LSV) was performed at a scan rate of 10 mV s^{-1}. Electrocatalytic activity towards OER was tested from -0.1 to 0.8 V (vs. SCE) while the HER performance was evaluated in the range from 0.1 to -0.6 V (vs. SCE). Meanwhile, the electrochemical active surface area (ECSA) was estimated by using C_{dl}. The ECSA can be calculated by the following equation: ECSA = C_{dl}/C_s, where C_s is the specific capacitance of the electrocatalyst under an identical electrolyte condition. Usually, C_s = 0.04 mF in 1.0 M KOH.

4.3.3. Results and Discussion

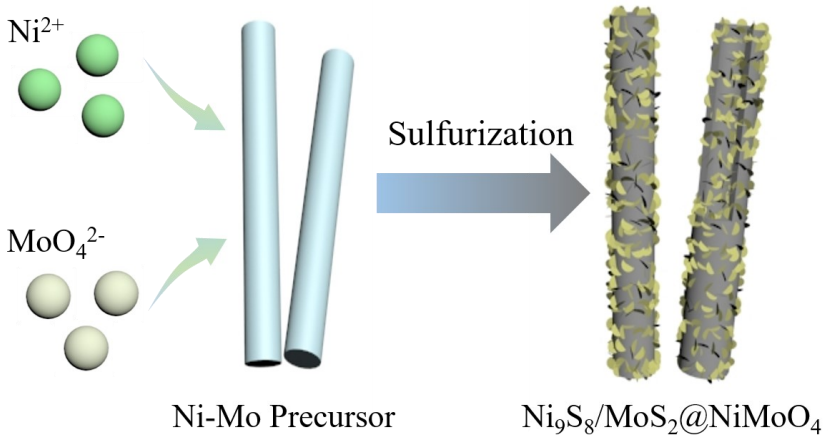

Scheme 4.3 Scheme of fabrication for core-shell structural $Ni_9S_8/MoS_2@NiMoO_4$ nanorods.

The core-shell $Ni_9S_8/MoS_2@NiMoO_4$ hetero-structured nanorods were fabricated by a simple thermal treatment of the Ni-Mo precursor in the presence of sulfur, as shown in **Scheme 4.3**. **Figure 4.9A** showed the representative scanning electron microscope (SEM) image of the Ni-Mo precursor, demonstrating a nanorod-like morphology with smooth surface and a diameter of 130 nm. The in-situ sulfurization method converted the surface of 1D Ni-Mo nanorod precursor to Ni_9S_8/MoS_2 with 2D ultrathin nanoflakes, forming the shell densely decorated an $NiMoO_4$ core (**Figure 4.9B**). While the $NiMoO_4$ nanorods in **Figure S4.18** still kept the same morphology with smooth surface without sulfurization and some of the nanorod were broken, which further confirmed that sulfurization could protect the structure from collapsing. **Figure 4.9C** showed that the diameters of the nanorods were around 180-200 nm with increased surface area which generated a hierarchical porous structure which further confirmed the formation of Ni_9S_8/MoS_2. This morphology and porous structure were beneficial for enhanced electrocatalytic performance due to rapid charge transfer pathways and ample exposed active sites.[287]

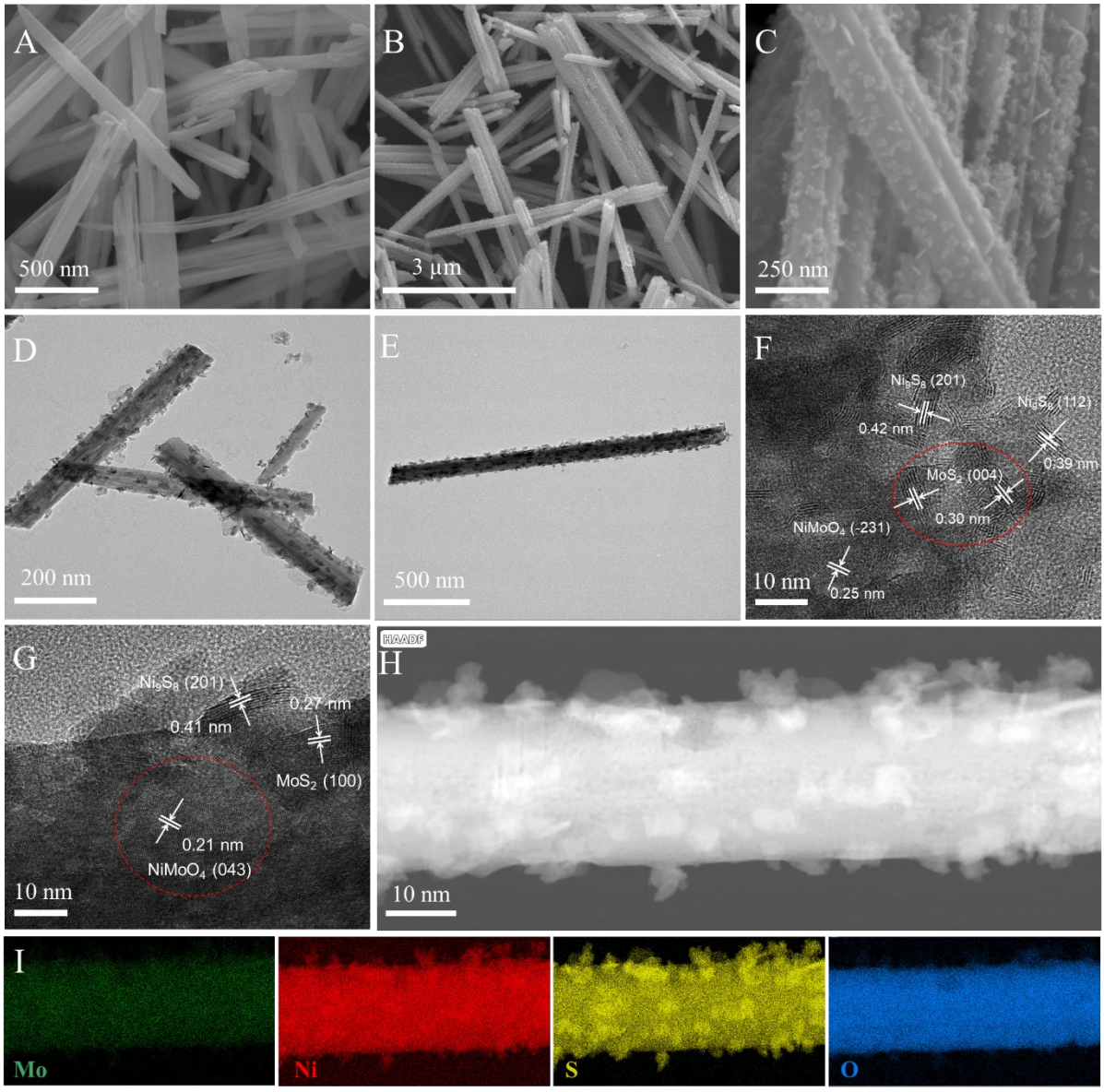

Figure 4.9 (A) SEM images of Ni-Mo precursor; (B-C) SEM images of Ni_9S_8/MoS_2@$NiMoO_4$ nanorods; (D) TEM image of Ni_9S_8/MoS_2@$NiMoO_4$ nanorods; (E) TEM image of a single Ni_9S_8/MoS_2@$NiMoO_4$ nanorod; (F-G) HRTEM images of selected area of Ni_9S_8/MoS_2@$NiMoO_4$ nanorod; (H) HAADF-STEM image of a single Ni_9S_8/MoS_2@$NiMoO_4$ nanorod; and (I) the corresponding EDS element mapping spectra of element Mo, Ni, S and O.

The detailed morphology of the Ni_9S_8/MoS_2@$NiMoO_4$ nanorods was further observed via transmission electron microscope (TEM). **Figure 4.9D** confirmed the formation of core-shell structure composed of 1D $NiMoO_4$ nanorods (core) and ultrathin 2D Ni_9S_8/MoS_2 nanosheets

(shell). Coherent heterointerfaces existed in the entire nanorod between the outside metal sulfides and the inner metal oxide core, which could form abundant charge transfer channels. The high-resolution TEM images of $Ni_9S_8/MoS_2@NiMoO_4$ are presented in **Figure 4.9E-G** in which **Figure 4.9F** displays crystalline spacings of 0.42 nm, 0.30 nm, and 0.25 nm, corresponding to the (201) plane of Ni_9S_8, (004) plane of MoS_2 and (-231) plane of $NiMoO_4$, respectively, confirming the composition of ternary components while **Figure 4.9G** demonstrated the existence of abundant interfaces between these components.[288] Furthermore, elemental mapping manifest the homogeneous distribution of Mo, Ni and S elements (**Figure 4.9H-I**) in the outer shell structure, revealing the binary compound of Ni_9S_8/MoS_2 in the shell. It should be mentioned that most of Mo and O element concentrates in the core center, which further confirmed $NiMoO_4$ nanorods as the core material in the hetero-structured composites.

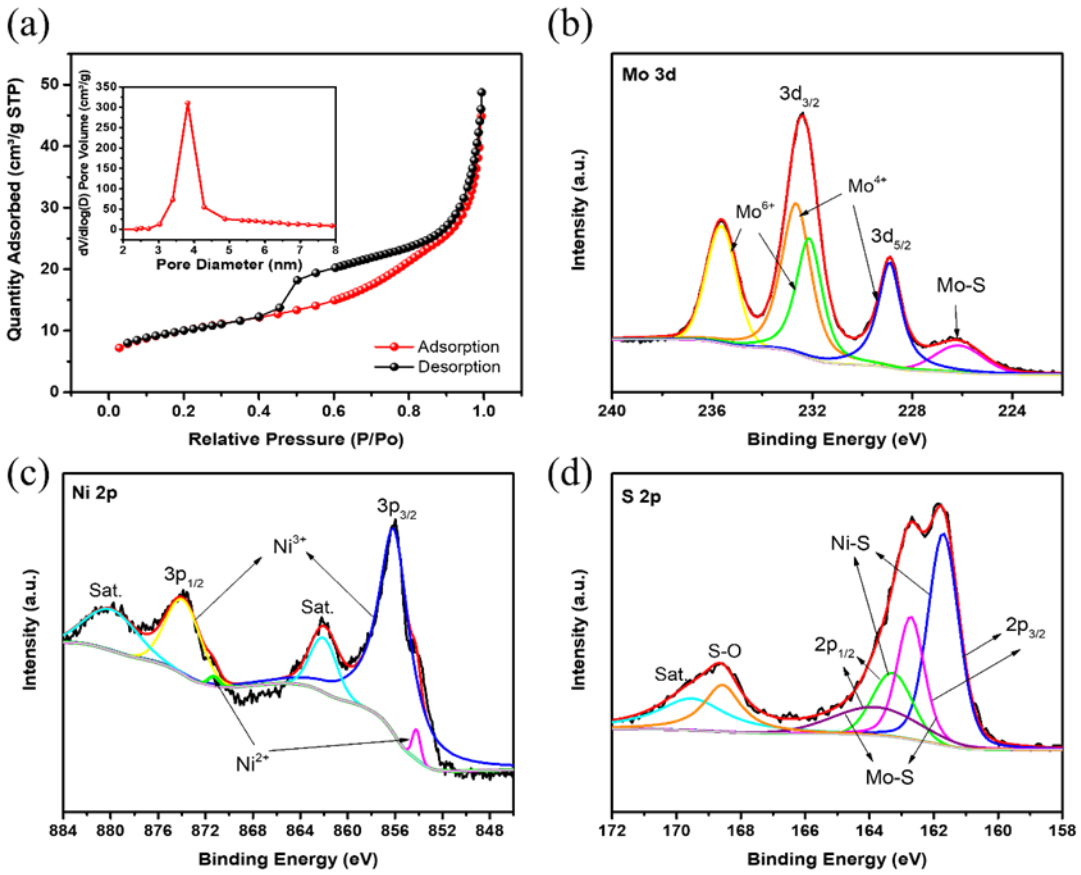

Figure 4.10 (A) N_2 sorption isotherm of $Ni_9S_8/MoS_2@NiMoO_4$ (inset: pore size distribution plot derived from BJH method); High-resolution XPS spectrum of (B) Mo 3d, (C) Ni 2p, and (D) S 2p of $Ni_9S_8/MoS_2@NiMoO_4$.

The phase and crystalline configuration of $Ni_9S_8/MoS_2@NiMoO_4$ nanorods were measured by the XRD investigation, presented in **Figure S4.19A**. Typical characteristic peaks located at 27.21°, 31.30°, 42.59°, 50.81° and 53.40° corresponded to the (202), (222), (332), (153) and (261) planes of Ni_9S_8 (JCPDS No. 22-1193) respectively, and peaks located at 33.48°, 35.81°, 44.10°, 49.72°, 55.98° and 58.30° corresponded to the (101), (102), (006), (105), (106) and (110) planes of MoS_2 (JCPDS No. 37-1492), respectively. Additional typical (-121), (220), (211), (040), (-204) and other diffraction peaks of α-$NiMoO_4$ (JCPDS No. 33-0948) were at 23.91°, 28.83°, 29.71°, 41.20° and 47.46°. **Figure S4.19B** showed the XRD patten of $NiMoO_4$ without sulfurization, confirming the synthesis of β-$NiMoO_4$ (JCPDS No. 45-1042). Combining with XRD and morphology patten Ni-Mo precursor in **Figure S4.19C** and **Figure 4.9A**, it can be observed that the ternary compositions

of Ni-Mo precursor with smooth surface area after hydrothermal process converted the 2D Ni_9S_8/MoS_2 nanosheets with 1D $NiMoO_4$ inner core after the sulfurization treatment while β-$NiMoO_4$ (JCPDS No. 12-0348) in Ni-Mo precursor formed another crystal $NiMoO_4$ via annealing process, which further confirmed the previous results. It should be mentioned that both α-$NiMoO_4$ and β-$NiMoO_4$ phases belonged to monoclinic crystal structure system and the most important difference between both phases was different coordination for the molybdenum ions in the crystal structure. It's reported that transformation between the α-$NiMoO_4$ and β-$NiMoO_4$ phases not only depended on temperature but also related with heteroatom doping, which effected structural and electronic order-disorder in the lattice and tuned the electronic configurations of composites, further effecting electrochemical performance discussed later. **Figure 4.10A** exhibited the N_2 sorption isotherm of Ni_9S_8/MoS_2@$NiMoO_4$ with a VI-type curve of a hysteresis loop, revealing the presence of mesopores. The calculated specific surface area was 34.4038 $m^2\ g^{-1}$, which was larger than that of the untreated $NiMoO_4$ (20.5 $m^2\ g^{-1}$). The pore size distribution plot (inset in **Figure 4.10A**) showed that Ni_9S_8/MoS_2@$NiMoO_4$ possesses pores mostly located around 4 nm, in agreement with isotherm curve.[289] The elemental states and material compositions of Ni_9S_8/MoS_2@$NiMoO_4$ and were $NiMoO_4$ conducted through X-ray spectroscopy. In the **Figure S4.20A**, distinct peaks placed at 856.10, 532.57, 285.01, 231.49 and 161.04 eV corresponding to Ni 2p, O 1s, C 1s, Mo 3d and S 2p, respectively. Compared with it, the much stronger Ni 2p (854.98 eV) and O 1s peaks (528.66 eV) and missing S 2p peak of $NiMoO_4$ further proved the successful synthesis of nickel molybdate without sulfurization (**Figure S4.20C**). In spectra of Mo 3d (**Figure 4.10B**), the peaks at bind energy of 235.66 and 232.14 eV were credited to Mo ion (VI) of nickel molybdate, and typical peaks placed at binding energy at 232.68 and 228.89 eV corresponding to Mo $3d_{3/2}$ and $3d_{5/2}$ of Mo ion (IV), respectively.[290] Obvious signal at 226.20 eV also agreed to the S 2s peak of metal-sulfur bond (Mo-S), respectively.[291] While for the Mo 3d spectrum of $NiMoO_4$, typical signals at 235.44 and 232.28 eV corresponded to Mo $3d_{3/2}$ and $3d_{5/2}$ of Mo ion (VI) of nickel molybdate (**Figure S4.20D**). **Figure 4.10C** showed two spin-orbit doublets with its satellites of Ni 2p. The $2p_{1/2}$ and $2p_{3/2}$ of nickel ion (II) could be found at binding energy signal at 871.33 and 854.22 eV and the signals at 874.10 and 856.18 eV were in accordance with the $2p_{1/2}$ and $2p_{3/2}$ of nickel ion (III), respectively.[274, 279] In **Figure S4.20E**, the four binding energy peaks at 855.84, 873.58, 862.11, and 879.91 eV are assigned to $2p_{3/2}$ and Ni $2_{p1/2}$ with satellite peaks, respectively, which confirmed the successfully synthesis of $NiMoO_4$. As presented

of S 2p spectrum in **Figure 4.10D**, the binding energy signals at 163.31 and 161.70 eV were allocated with the $2p_{1/2}$ and $2p_{3/2}$ of nickel-sulfur bonding, and the peaks at 163.92 and 162.73 eV were assigned to the molybdenum-sulfur bonding ($2p_{1/2}$ and $2p_{3/2}$), respectively.[292, 293] Also, typical peak of the sulfur-oxygen bond with oxidation state appeared at signal 168.55 eV.[294-296] **Figure S4.20B** revealed the two deconvoluted peaks of O 1s spectra. The signals located 530.55 and 531.76 eV corresponding to metal-oxygen (M-O) bond in nickel molybdate and oxygen vacancy of composites, respectively.[296, 297] The O 1s spectra of nickel molybdate only showed the metal-oxygen single at 530.67 eV (**Figure S4.20F**). The above results further confirmed the successful synthesis of two different composites through different calcination process.

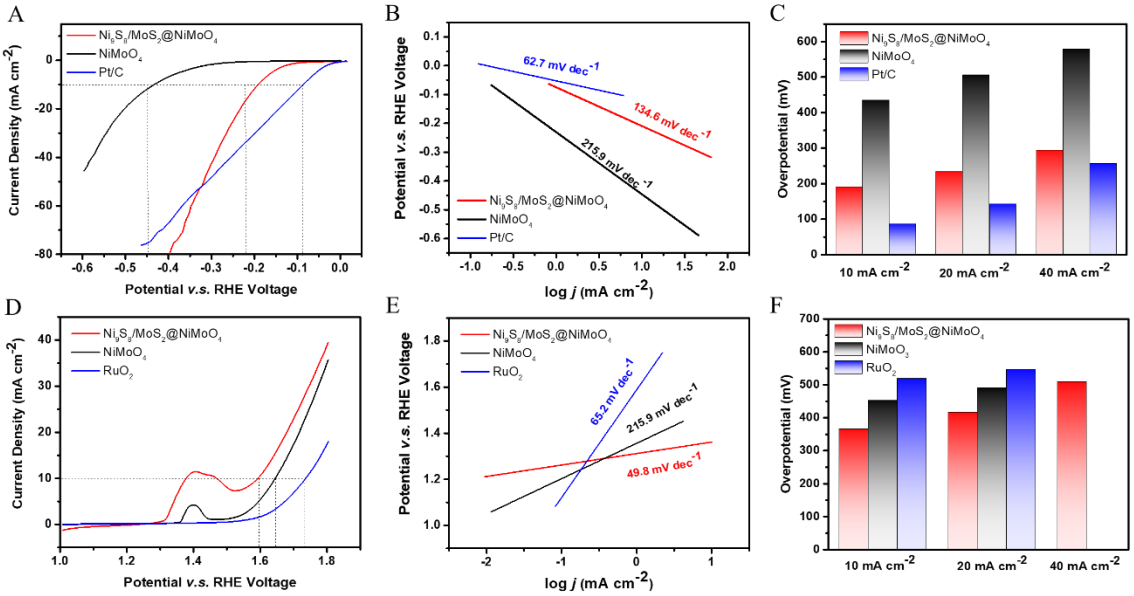

Figure 4.11 The electrocatalytic HER test in 1.0 M KOH: (A) Polarization curves conducted at a scan rate of 10 mV s-1 for Ni_9S_8/MoS_2@$NiMoO_4$, $NiMoO_4$ and Pt/C with iR-correction; (B) the corresponding Tafel plots of obtained sample for HER; (C) the histogram of the overpotential at different current density; The electrocatalytic OER test in 1.0 M KOH: (D) Polarization curves of Ni_9S_8/MoS_2@$NiMoO_4$, $NiMoO_4$ and RuO_2 with iR-correction; (E) the corresponding Tafel plots of obtained sample for OER; (F) the histogram of the overpotential at different current density.

The electrocatalytic activity of $Ni_9S_8/MoS_2@NiMoO_4$ towards HER was tested in 1.0 M KOH solution *via* the three-electrode configuration. For comparison, $NiMoO_4$ and commercial Pt/C was tested under the same condition. Polarization curves show that $Ni_9S_8/MoS_2@NiMoO_4$ exhibit high HER activity reaching the current density of 10 mV cm^{-2} at a small overpotential of 190 mV (*vs.* RHE, **Figure 4.11A** and **Figure S4.21A**, which was much lower than that of $NiMoO_4$ (434 mV). Although the overpotential of $Ni_9S_8/MoS_2@NiMoO_4$ nanorod was higher than Pt/C (86.3 mV) at 10 mV cm^{-2}, it exhibited lower overpotentials at high current densities surpassing 70 mV cm^{-2} compared with those of Pt/C. In order to further reveal the kinetics, Tafel plots of $Ni_9S_8/MoS_2@NiMoO_4$, $NiMoO_4$ and Pt/C electrocatalysts were calculated to 134.6, 215.9 and 62.7 mV per decade, respectively (**Figure 4.11B**). This improved HER activity of nanorods could credit to the synergistic effects from the interfaces between metal sulfide and metal oxide. Noting that the electronic interaction at the interfacial area could devitalize the adsorption of H-containing species, which could modify H chemisorption to facilitate the Volmer-Heyrovsky process.[286, 298] The performance of other electrocatalysts were listed in **Table 4.1**. A histogram with the overpotential of all electrocatalysts was shown in **Figure 4.11C**, providing clear evidence of the high HER efficiency of $Ni_9S_8/MoS_2@NiMoO_4$. Obviously, $NiMoO_4$ all displayed the highest overpotential at different current densities. Although $Ni_9S_8/MoS_2@NiMoO_4$ exhibited higher overpotential than Pt/C at current density of 10, 20 mA cm^{-2}, it showed the similar overpotential with Pt/C when the current density reached 40 mA cm^{-2}. Accordingly, for the interfacial area of Ni_9S_8 and MoS_2, the strong correlation of MoS_2 with H and Ni_9S_8 with OH may simultaneously prompted the dissociation of H-O bonds of the H_2O molecule. Thus, the interlayer of Ni_9S_8 and MoS_2 took a significant character in improving the electrocatalytic performance.[287] The OER performance of $Ni_9S_8/MoS_2@NiMoO_4$ nanorods was further tested in the same electrolyte. In order to display the synergistic effect of metal sulfide and $NiMoO_4$, bare $NiMoO_4$ and commercial RuO_2 were utilized for comparison. **Figure 4.11D** displayed the LSV curves of all materials. The LSV curve of the $Ni_9S_8/MoS_2@NiMoO_4$ and $NiMoO_4$ revealed two special properties, an obvious peak related with the Ni^{2+} oxidation presented at 1.41 V and the current density goes sharply after voltage at 1.52 V together the presence of bubbles on the surface of electrode, which demonstrating that proceeding of the OER.[275] Dramatically, the $Ni_9S_8/MoS_2@NiMoO_4$ nanorods exhibited a remarkable OER activity with *iR*-correction (**Figure S4.21B**). The required overpotential η_{10} of the $Ni_9S_8/MoS_2@NiMoO_4$ nanorods was 360 mV, which was much lower than those of $NiMoO_4$ (410

mV), and commercial RuO_2 (500 mV) after *iR*-correction. The calculated Tafel slope (**Figure 4.11E**) for Ni_9S_8/MoS_2@$NiMoO_4$ (49.8 mV dec^{-1}) was respectable lower than that of $NiMoO_4$ (215.9 mV dec^{-1}) and even better than that of RuO_2 (65.2 mV dec^{-1}), suggesting the favorable catalytic kinetics of Ni_9S_8/MoS_2@$NiMoO_4$ during the OER. For comparison, other electrocatalysts were listed in **Table 4.1**, which revealed that our nanorod catalyst was very competitive in alkaline medium. A histogram in **Figure 4.11F** further confirmed that the overpotential of Ni_9S_8/MoS_2@$NiMoO_4$ was much lower than others at different current density. Furthermore, the $NiMoO_4$ and RuO_2 even couldn't reach the higher current density. Furthermore, the $NiMoO_4$ and RuO_2 even couldn't reach the higher current density. This outstanding HER/OER activity were attributed to many different factors. First, 2D Ni_9S_8/MoS_2 nanosheets in situ transferred from the Ni-Mo precursor with ample defects could create more active sites for electrochemical process for improving the electrocatalytic properties. According to the previous results, interlayers of Ni_9S_8 and MoS_2 could create synergistic effect. For on hand, it's reported that the powerful correlation of MoS_2 with hydrogen and Ni_9S_8 with hydroxide might simultaneously prompt the dissociation of hydrogen-oxygen bonds of water molecule, indicating that MoS_2 was considered to be more effective for the HER while Ni_9S_8 was rather favorable for the OER. On the other hand, the existence of MoS_2 and introduce of sulfur could change the binding energy of Ni 2p which was consistence with XPS results and optimized electron density of Ni_9S_8, resulting in enhancing the binding with OH atoms, facilitating the kinetics of the OER/HER pathways, and the improved OER/HER activity. Furthermore, the multiple heterointerfaces, especially the long assistant interfaces between the outside metal sulfides and core $NiMoO_4$, providing electron transfer pathways, revealing the synergistic effect of $NiMoO_4$, Ni_9S_8, and MoS_2. As we explained before, introduce of sulfur during annealing process created structural and electronic order-disorder effects. Specificlly, transformation from β-$NiMoO_4$ phase in Ni-Mo precusor to α-$NiMoO_4$ phase caused the distortion between these complex clusters leading to polarization and/or difference in charge density in the local structure while it could also optimize the coordination of electrons to the central Ni atoms and efficiently promoted electron transfer improving the electrocatalytic acvitity. Therefore, combining the merits of bimetallic sulfide, the enhanced eletrochemical performances were accociated with a complex system of such core-shell hierarchical nanostructure with kinetically favorable abundant open mesopores would reduce diffusion distance for ion/electron transportation during electrochemical process.[299]

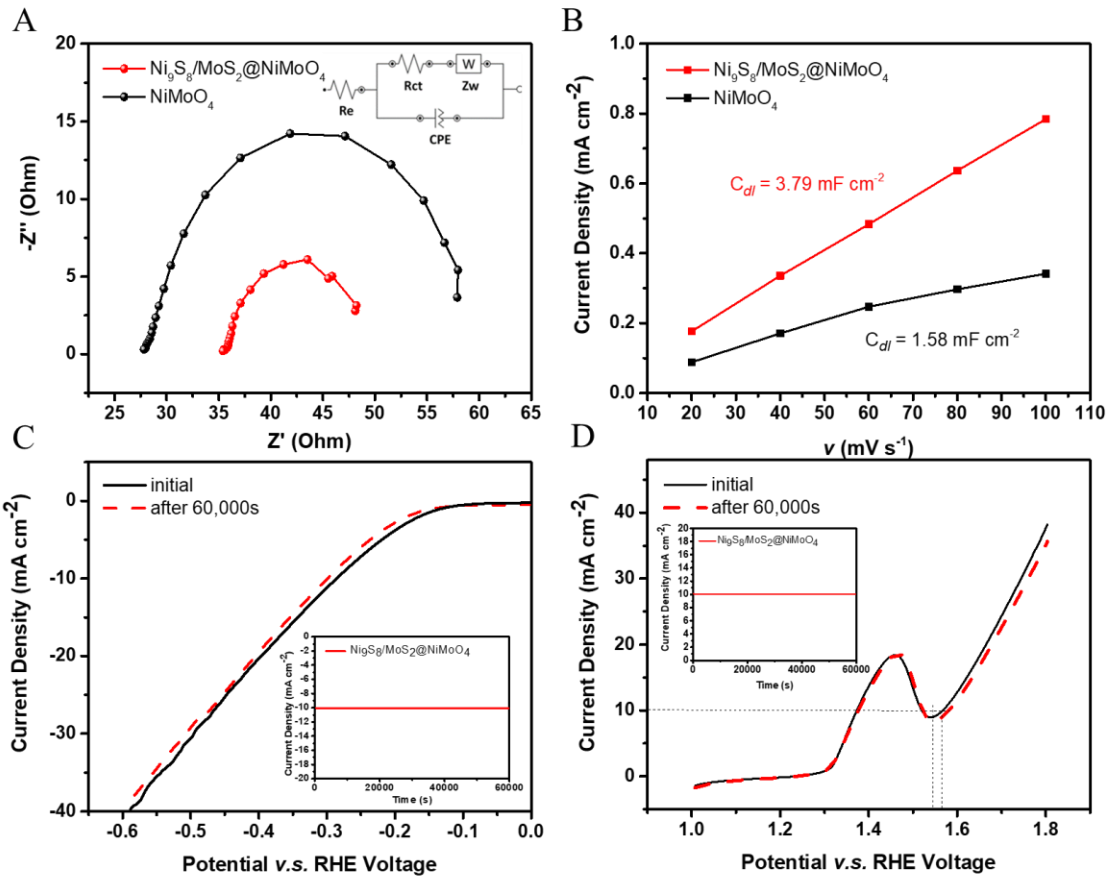

Figure 4.12 (A) EIS plots for Ni_9S_8/MoS_2@$NiMoO_4$ and $NiMoO_4$ before stability test (insert: the equivalent circuit model); (B) The fitting curve of the different current density (potential at 0.90 V vs. RHE) verse scan rate to analyze C_{dl}; (B) Polarization curves of Ni_9S_8/MoS_2@$NiMoO_4$ with initial and after durability of HER (inset: chronopotentiometric curve of Ni_9S_8/MoS_2@$NiMoO_4$ in 1.0 M KOH after 60,000s); (D) Polarization curves of Ni_9S_8/MoS_2@$NiMoO_4$ with initial and after durability of OER (inset: stability measurement by chronopotentiometric curve of Ni_9S_8/MoS_2@$NiMoO_4$ in 1.0 M KOH after 60,000s).

Table 4.1 Comparison of HER and OER Activities for Different Catalysts.

Catalyst	Electrolyte	Reaction	η10 (mV)	Tafel slope (mV dec $^{-1}$)	Ref
Ni_9S_8/MoS_2@$NiMoO_4$ nanorods	1.0 M KOH	HER	190	134.6	This work
		OER	360	49.8	
Co-NiS@MoS_2	1.0 M KOH	HER	139.9	106.7	300
		OER	170.6	136.5	
MoS_2/NiS yolk-shell microspheres	1.0 M KOH	HER	244	97	279
		OER	350	108	
NiS_2/MoS_2 yolk-shell NSs	1.0 M KOH	HER	135	82	301
		OER	293	102.3	
MoS_2-NiS_2/graphene nanohybrids	1.0 M KOH	HER	141	94	275
		OER	320	135	
MoS_2/NiS NCs	1.0 M KOH	HER	92	124	294
		OER	271 (15 mA cm^{-2})	60	
a-MoS_2-Ni_3S_2/NF	1.0 M KOH	HER	81	118.38	295
		OER	150 (100 mA cm^{-2})	91.1	
MoS_2/NiS_2 Nanosheets	1.0 M KOH	HER	62	93.7	288
		OER	278	128	
p-MoS_2/Ni_3S_2/NF	1.0 M KOH	HER	99	71	277
		OER	185	46	
Fe-CQDs/$NiMoO_4$/NF	1.0 M KOH	HER	117	88.7	302
		OER	336	71.8	
NiS/MoO_3/NF	1.0 M KOH	HER	150	122.3	303
		OER	221 (50 mA cm^{-2})	70.9	

To better understand study the kinetics and inherent resistance properties. the EIS measurements were conducted at overpotential of 134 mV in alkaline solution. The Nyquist plot was shown in **Figure 4.12A** and the inset of the equivalent circuit model. All the curves exhibited distinguishable semicircles, and the equivalent electronic circuit was utilized to fit the charge-transfer resistance (R_{ct}) of the composites. R_{ct} values of Ni_9S_8/MoS_2@$NiMoO_4$ showed a lower value of 13 Ω compared to $NiMoO_4$ (31 Ω) before stability testing, which is correlated with electron transfer kinetics of redox reactions near the surface of electrolyte and electrode. Based on previous reports, such low charge transfer resistance contributed from sufficient active sites and micropores of the binary Ni_9S_8/MoS_2 shell and interplayed with mass transport during the charge transport process. In addition, Ni_9S_8/MoS_2 shell formed flexible space preventing the decomposition of structure resulted from the different electronegativity of sulfur and oxygen atom, providing fast electron transfer channels. After stability testing, the R_{ct} values of Ni_9S_8/MoS_2@$NiMoO_4$ (22 Ω) was still lower than that of $NiMoO_4$ (50 Ω) in **Figure S4.21C**. It clearly demonstrated that coherent interfaces between the outside sulfides and inner core were favorable for the fast charge transportation between outside layer and inside core by the intermediate sulfur in the composite. In addition, hierarchical core-shell structure prompted the fast ion transport during the electrocatalytic process, resulting in the enhancement of the HER/OER performance. Furthermore, the electrochemically active surface area (ECSA) was a significant factor to measure electrocatalysts, which was conducted by measuring the CV in the potential range of 0.85-0.95 V at different scan rates.[304] The CV curves of Ni_9S_8/MoS_2@$NiMoO_4$ and $NiMoO_4$ were shown in **Figure S4.22A-B**. As shown in **Figure 4.12B**, the double-layer capacitance of Ni_9S_8/MoS_2@$NiMoO_4$ was 3.79 mF cm^{-2} , which was higher than that of $NiMoO_4$ (1.58 mF cm^{-2}). Accordingly, the calculated ECSA of Ni_9S_8/MoS_2@$NiMoO_4$ was 94.75 cm^{-2} which was much higher than that of $NiMoO_4$ (39.5 cm^{-2}), demonstrating more plentiful catalytic active sites. Furthermore, we obtained the ECSA-normalized LSV curves of HER and OER (**Figure S4.22C-D**), Ni_9S_8/MoS_2@$NiMoO_4$ exhibited the higher current density of -0.026 mA cm^{-2} compared to $NiMoO_4$ at potential of 200 mV which Ni_9S_8/MoS_2@$NiMoO_4$ presented lower current density at potential of 1.35 V. With respect to the above results, it can be concluded that the Ni_9S_8/MoS_2@$NiMoO_4$ nanorods had the largely exposed surface area, and Ni_9S_8/MoS_2 can produce abundant active sites from interlayer, leading that more electrons can be kept and

transferred faster from surface to inner core, resulting to the improved the electrocatalytic performance.

Stability is also meaningful to evaluate the performance of electrocatalysts. The long-term stability for HER performance of the $Ni_9S_8/MoS_2@NiMoO_4$ nanorods was assessed by performing at 0.866 V (*vs.* RHE) for 60,000s in the base solution. **Figure 4.12C** displayed the assessment of the polarization curves of the nanorods at initial and after 60,000 s, respectively. It's suggested that a negligible difference of the LSV curves and tiny loss of current density from the insert **Figure 4.12C** demonstrating the outstanding stability of $Ni_9S_8/MoS_2@NiMoO_4$. However, the compared $NiMoO_4$ exhibited low current density for durability testing and the overpotential increased largely after testing in **Figure S4.22E**. Similarly, the long-term stability for OER performance of the $Ni_9S_8/MoS_2@NiMoO_4$ nanorods was assessed by performing at 1.5 V (*vs.* RHE) for 60,000 s at the same condition. It could be observed that the current density exhibited no clear degradation after 60,000 s and the difference of the LSV curves before and after 60,000 s was not considerable, and the current density remained almost the same, which indicated its excellent electrochemical stability, as shown in **Figure 4.12D**. Also, the current density decayed intensively of compared $NiMoO_4$ after durability testing and overpotential increased to 470 mV at current density at 10 mA cm^{-2} (**Figure S4.22F**).

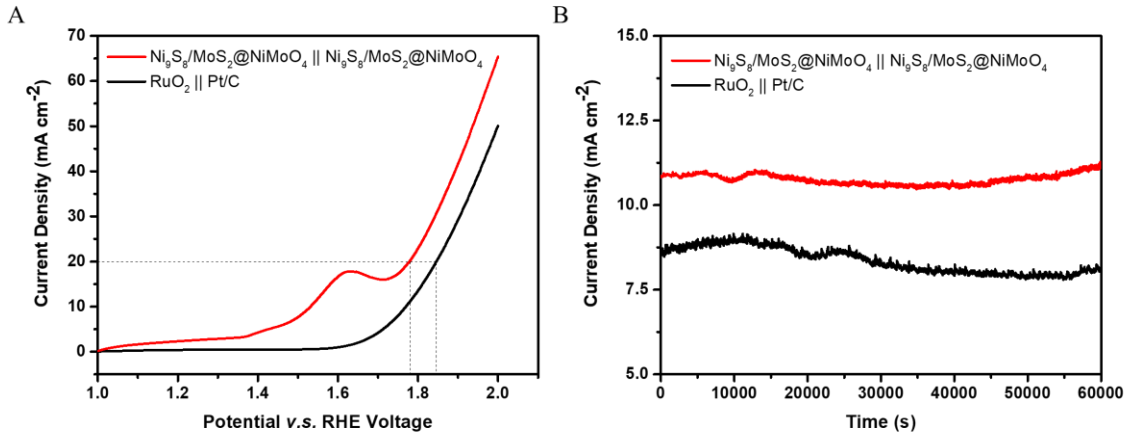

Figure 4.13 (A) LSV curves of the as-prepared samples in two-electrode system used as both the cathode and anode in 1.0 M KOH; (B) Chronopotentiometric curve at a voltage at 1.65 V for 60,000s.

Encouraged by the notable HER and OER activities, we further investigated the achievability of utilizing $Ni_9S_8/MoS_2@NiMoO_4$ as a bifunctional electrocatalyst for overall water splitting (**Figure 4.13A**). It was noted that a sharp signal located at around 1.58 V associated with the oxidation of Ni^{2+} corresponded to the previous OER testing. Impressively, the catalytic activity of $Ni_9S_8/MoS_2@NiMoO_4$ were competitive with most previously reported catalysts. (**Table 4.2**). At a current density of 20 mA cm^{-2} for $Ni_9S_8/MoS_2@NiMoO_4$ || $Ni_9S_8/MoS_2@NiMoO_4$ cell was delivered at a voltage of 1.78 V, surpassing those of electrocatalysts composed with RuO_2 || Pt/C (1.84 V). Over a 60,000 s a constant voltage at 1.60 V of the $Ni_9S_8/MoS_2@NiMoO_4$ nanorods showed a superior stability without obvious current degradation compared RuO_2 || Pt/C (**Figure 4.13B**). Based on the above measurements, the reasons of the excellent electrocatalytic performance of $Ni_9S_8/MoS_2@NiMoO_4$ can be concluded as follows: (i) the outer Ni_9S_8/MoS_2 nanosheets after sulfurization produced plentiful active sites in the surface of the material; (ii) the strong interaction between numerous Ni_9S_8/MoS_2 interfaces and inner core $NiMoO_4$ exhibited a synergistic effect with $NiMoO_4$, Ni_9S_8, and MoS_2 which modified the electronic interactions and prompted dissociation of water molecules; (iii) the hierarchical core-sell hereto-structure with kinetically favorable abundant pores endowed ion transfer pathways for fast ion diffusion during electrocatalysis and provide open area for the generation and release of the O_2/H_2.

Table 4.2 Comparison on the overall water splitting performance of the electrocatalysts.

Catalyst	Electrolyte	η10 (mV)	Overall water splitting cell voltage (V, at 10 mA·cm^{-2})	Ref
Ni_9S_8/MoS_2@$NiMoO_4$ nanorods	1.0 M KOH	550 (20 mA cm^{-2})	1.78 (20 mA cm^{-2})	This work
Co-NiS@MoS_2	1.0 M KOH	310 (50 mA cm^{-2})	1.54 V (50 mA cm^{-2})	[300]
MoS_2/NiS yolk-shell microspheres	1.0 M KOH	410	1.64	[279]
NiS_2/MoS_2 yolk-shell NSs	1.0 M KOH	350	1.58	[301]
MoS_2-NiS_2/graphene nanohybrids	1.0 M KOH	610	1.84	[275]
MoS_2/NiS NCs	1.0 M KOH	380	1.61	[294]
a-MoS_2-Ni_3S_2/NF	1.0 M KOH	310 (100 mA cm^{-2})	1.54 (100 mA cm^{-2})	[295]
MoS_2/NiS_2 Nanosheets	1.0 M KOH	360	1.59	[288]
p-MoS_2/Ni_3S_2/NF	1.0 M KOH	270	1.50	[277]
NiS/MoO_3/NF	1.0 M KOH	330	1.56	[303]
b-$NiMoO_4$/NF nanosheets	1.0 M KOH	320	1.55	[305]
MoS_2/NiS_2/CC	1.0 M KOH	400	1.63	[306]

4.3.4. Conclusion

In summary, a core-shell Ni_9S_8/MoS_2@$NiMoO_4$ heterostructured nanorods with hierarchical porous architecture was fabricated by a facile sulfurization method, which works as a bifunctional electrocatalyst for overall water splitting. The nanorods composite structure exhibited extremely low overpotential of 190 mV for HER and 360 mV for OER at 10 mA cm^{-2}, respectively. The electrocatalytic result displayed that the synergistic effect from the outer Ni_9S_8/MoS_2 2D nanoflakes and inner $NiMoO_4$ 1D nanorod with high surface area and electrical conductivity can greatly improve electrocatalytic activity. Furthermore, the hierarchical core-shell structure offers ion transport pathways for fast ion diffusion during electrocatalysis. This work demonstrates a facile and inexpensiveness method for the making of efficient and cost-effective transition metal-based catalysts for overall water splitting, which hold great promise for the development of green hydrogen energy.

Above all, we have successfully synthesized three types of nanomaterials including transition metal alloy-based, transition metal sulfides-based materials for oxygen reactions and water splitting with excellent electrochemical properties. By studying the morphology and structure, we have an understanding about relationship of structure control and electrochemical performance and know how to optimize the materials. The excellent performance encourage to exploring their properties in the energy storage area in order to further explore their electrochemical possibility in wide applications.

Chapter 5 Design Transition Metal-based Nanomaterials for Energy Storage

Based on the above results, we know that three types of transition metal-based nanomaterials show excellent performance in energy conversion area. The novel structure designs attribute to the excellent electrochemical performance. In addition, according to the literature, transition metal sulfides are reported to exhibit the superior properties as electrode materials in energy storage. Hence, in this chapter, we will further explore the above two types of transition metal sulfide nanomaterials as electrode materials for energy storage to confirm if they still exhibit the excellent electrochemical performance. The first one is N,S-codoped hollow carbon dodecahedron/sulfides composites as anode material for Li-ion intercalation, which we will present in section 5.1. Actually, it's the same nanomaterial as electrocatalyst for oxygen reactions and synthesized by the same method as N,S-Co/Zn-ZIF in section 4.2 of chapter 4. The section 5.2 is discussing core-shell $NiMoO_4$@Ni_9S_8/MoS_2 nanorods as an electrode material for supercapacitor which is also the same as Ni_9S_8/MoS_2@ $NiMoO_4$ in section 4.3 of chapter 4. Both of them still display the excellent performance for energy storage and realize our research objective, achieve our goal of "one type of material for multiapplication".

5.1. N,S-Codoped Hollow Carbon Dodecahedron/Sulfides Composites Enabling High-Performance Lithium-Ion Intercalation

The unique porous composite structure of N,S-codoped carbon dodecahedron/transition metal sulfides (N,S-Co/Zn@CN) is synthesized by the same method as the electrocatalyst in section 4.2 of chapter 4. This type of anode electrode constructed with cobalt and zinc sulfides nanocrystals embedded within a nitrogen and sulfur co-doped porous carbon is successfully designed bimetal-organic frameworks as the precursor. Benefiting from synergistic effects of bimetal sulfides, the unique rhombohedral dodecahedral nanostructure with rough surface area and N,S-codoped carbon matrix, such an anode material presents superior initial reversible capacity of 938.2 mA h g^{-1} with a high-capacity retention of 65.6% after 100 cycles at 150mA g^{-1}. The effective nanostructure design is expected to open a venue to construct high-performance materials.

for energy and environment applications.

The outcome of this research is published as a research paper in " Electrochemical Science Advances" (**Chen, L**.; Chen, Z.; Liu, X.; Ye, Z.; Wang, X., N,S-Codoped Hollow Carbon Dodecahedron/Sulfides Composites Enabling High - Performance Lithium - ion Intercalation. *Electrochemical Science Advances* ***2021***, e2100001.)

5.1.1. Introduction

To date, the requirements of sustainable energy storage devices are urgent for various applications, ranging from smart electric grids to electric vehicles.[307] As promising energy storage candidates, lithium-ion batteries (LIBs) have drawn mass attention due to their high energy density, long cycle life, outstanding rate capability, and good environmental compatibility.[308, 309] However, the theoretical capacity of the present commercial graphite anode is only 372 mA h g^{-1}, which cannot fulfill the demands for next-generation LIBs with the desired high energy density and stability.[310, 311] Therefore, numerous research endeavors have been contributed to exploring new high-performance anode materials for replacement of the conventional graphite anode.[312, 313] Among various anode materials, transition metal sulfides (TMSs) are regarded as potential candidates because of their good redox reaction, thermal stability, and high theoretical specific capacity.[132, 314] However, sluggish ion/electron transport kinetics and large volume expansion during the Li^+ insertion and extraction processes are the primary causes of the capacity fading of transition metal sulfide-based anode materials.[315, 316] Moreover, the low conductivity of the single metal sulfide leads to undesirable rate performance and poor cyclic stability.

Many strategies have been explored to address the above issues, such as adjusting the active material compositions, compounding with other materials, and engineering of unique hierarchical structures.[111, 317] Among them, designing bimetallic sulfides consisting of two elements, such as Co, Ni, Fe, Zn, Mn, and so on can greatly improve the electrical conductivity while retaining the good redox properties of the materials.[318-320] Due to synergistic effects of the two kinds of metals, bimetallic sulfides have a lower bandgap energy, resulting in higher specific capacity. It has been reported that zinc-cobalt sulfide displays lower optical band gap and superior conductivity compared to their binary sulfide counterparts. Moreover, it is expected that the electrochemical contributions from Zn or Co ions in ternary sulfides can offer more redox reactivity than those of the binary sulfides, leading to a better electrochemical performance. Therefore, compared with

cobalt sulfide or zinc sulfide, improved electrochemical performance with an enhanced capacity and stability can be achieved in their ternary transition metal sulfide for lithium batteries.[321] Another effective solution is designing carbon-based metal sulfide composites to alleviate the stress changes due to lithium insertion and extraction and accommodate the volume changes of the active materials.[322, 323] Furthermore, TMSs incorporated into the carbon matrix can suppress the dissolution of polysulfides into the electrolyte and further extend the cycling life.[324] For example, Cao et al. synthesized a honeycomb-like 3D N/S codoped porous carbon-coated cobalt sulfide nanostructure, favoring large contact area for electrolyte and ion transport.[325] One dimensional copper sulfide nanorods as a high-performance anode were found to exhibit excellent capacity retentions of 92% and 96% after 100 cycles at 100 mA g^{-1}.[326] Despite the great progress that has been obtained, there are still some obstacles for TMSs, like structure collapse. Therefore, more contributions should be devoted to design TMSs with a porous complex micro/nanostructure to buffer volume changes and increase the contact between the electrolyte and the electrode material.

Metal-organic frameworks (MOFs) are a new class of porous structure constructed with metallic ions coordinated with electron-donating organic ligands and featured with adjustable pore sizes, controllable architectures, and large surface areas. They have been regarded as appealing templates/precursors for construction of hollow/porous transition metal materials.[327-329] Hollow structured MOFs as precursors to derive metal-based porous carbon or related sulfides have attracted wide attention; some of the resulting materials are considered promising anode materials for LIBs.[330] For example, Chen et al. reported hollow hybrids composed of cobalt sulfides embedded within porous carbon polyhedra/carbon nanotubes using ZIF-67 as template.[25] MOF-derived hollow Co_9S_8 nanoparticles embedded in graphitic carbon nanocages with good mechanical flexibility and pronounced structure stability displayed a very high energy density (707 Wh kg^{-1}), superior rate capability in LIBs.[331] Wang et al. recently prepared ZnO/ZnS@N-C heterostructures decorated on carbon nanotubes with metal-organic framework assistance, which exhibited higher reversible capacity of 1020.6 mA h g^{-1} at 100 mA g^{-1} after 200 cycles and excellent high-cyclability with 386.6mAh g^{-1} at 1000 mA g^{-1} retained over 400 cycles.[332] Recently, the doping of heteroatoms such as N, P, and B into carbon has been demonstrated to enhance the conductivity of LIBs by providing a charge transport facilitated pathway, improving the mechanical flexibility and robustness of the active materials, which can prevent their pulverization and aggregation during lithiation and delithiation processes.[333] Moreover, the N atom doped

graphitic networks not only protect the morphology and restrain the volume expansion but also prompt the formation of strong interactions between the Li-ion and the networks, which are beneficial to Li-ion insertion.[35] For example, Chen et al. reported that the interconnected 3D N-doped carbon framework in bimetallic sulfide Co_8FeS_8/N-C dodecahedral nanocages enhanced electrical conductivity of composite and kept the integrity of structure which further prompted the performance in LIBs.[321] Despite the progress achieved to date, the construction of nanosized hollow MOFs is still relatively less reported. Therefore, in situ synthesis of TMSs/N-doped porous carbon composites by using MOFs as precursors/templates is a significant work.

Herein, we demonstrate a unique porous composite structure of N,S-codoped carbon dodecahedron/transition metal sulfides (N,S-Co/Zn@CN) via one-step calcination and sulfurization of bimetal-organic frameworks as the precursor (Co/Zn-ZIF-67). Due to the synergistic effects, metallic sulfide nanoclusters on the carbon matrix serving as active sites exhibit enhanced lithium storage. The porous carbon matrix with a large surface area enlarges electrode/electrolyte contact area, providing efficient conductive channels for the transport of Li^+, and shortening diffusion length in the nanoparticles for easier ions/electron transfer. In addition, existences of Co/Zn metal and N,S-codoping protect the rhombic dodecahedron morphology from decomposing after calcination so that the hollow structure can supply buffer volume for the conversion reaction and prevent the structural exfoliation from the current collector. N,S-Co/Zn@CN is explored as an anode material for the Li-ion battery, which delivers initial discharge and charge capacities are calculated as 1470.3 and 938.2 mA h g^{-1}, respectively, with a high-capacity retention of 65.59% after 100 cycles at 150 mA g^{-1}.

5.1.2. Experimental Section

5.1.2.1. Chemicals

Cobalt (II) nitrate hexahydrate ($Co(NO_3)_2{\cdot}6H_2O$, 99%), zinc (II) nitrate hexahydrate ($Zn(NO_3)_2{\cdot}6H_2O$, > / = 99%) and methanol (C_2H_6O, 95%) were purchased from Fisher Scientific; 2-methylimidazole ($C_4H_6N_2$, 99.5%), sulfur (S, 99%), thiourea (CH_4N_2S, 99%), LiPF6 electrolyte solution (1 M in mixed ethylene carbonate (EC)/diethyl carbonate (DEC), 1:1, w/w) were purchased from Sigma-Aldrich; water was purified with a Millipore Milli-Q system.

5.1.2.2. Preparation of Co/Zn-ZIF-67 Precursor

In a typical preparation, two solutions of the following substances were prepared separately: $Co(NO_3)_2 \cdot 6H_2O$ (0.45 g), $Zn(NO_3)_2 \cdot 6H_2O$ (0.55 g) were dissolved in methanol (50 mL); 2-methylimidazole (1.64 g) and thiourea (1.25 g) were dissolved in methanol (50 mL). The two solutions were then mixed and stirred at room temperature for 24 h. Finally, the resulting light purple powder Co/Zn-ZIF-67 was separated by centrifugation and washed by methanol several times prior to drying in a vacuum oven at 80℃.

5.1.2.3. Synthesis of N,S-Co/Zn@CN

Co/Zn-ZIF-67 precursor powder (400 mg) and sulfur powder (1.2 g) were separately in downstream and upstream in one boat and were annealed under Ar atmosphere at 400℃ for 60 min with a ramp rate of 2℃ per min and then at 800 ℃ for 60 min to obtain N,S-Co/Zn@CN. Co/Zn@CN without adding thiourea was annealing under Ar atmosphere in the same condition without sulfur.

5.1.2.4. Structural Characterization

The morphology of the electrocatalysts was carried out by FEI Quanta 450 Environmental Scanning Electron Microscope (FE-ESEM) with EDAX Octane Super 60 mm2 SDD and TEAM EDS Analysis System. Transmission electron microscopy (TEM) was performed with a Thermo Scientific Talos F200X G2 S/TEM operated at 150 KV. High resolution transmission electron microscopy (HRTEM) has been used to define in detail the structures of the obtained materials. The X-ray diffraction (XRD) measurements were carried out using a monochromatic Bruker D8 advance diffractometer with Cu-Ka radiation. The study of the surface composition was recorded on a Thermo Scientific K-Alpha X-ray photoelectron spectroscopy (XPS). N_2 sorption measurements were performed on a Micromeritics ASAP2020 physisorption analyzer at 77 K to determine the Brunauer-Emmert-Teller (BET) specific surface area, pore volume, and pore size distribution.

5.1.2.5. Electrochemical Measurements

To make the electrode, a mixture of N,S-Co/Zn@CN powders, Super-P conducting carbon, and polyvinylidene difluoride (PVDF) binder at a weight ratio of 60:30:10 was mixed in N-

methylpyrrolidinone (NMP) solvent to form a homogeneous slurry. Electrodes were prepared by coating the slurry on carbon-coated Cu foil at the N,S-Co/Zn@CN loading of ~1.5 mg cm^{-2}, followed by drying in an oven at 65 ℃ for 5 h and then in a vacuum oven at 50 ℃ for 5 h prior to use. CR2025-type coin cells were assembled with the N,S-Co/Zn@CN electrodes in an Ar-filled glove box. The electrolyte contained $LiPF_6$ at 1.0 M in a binary solvent of EC and DEC (1:1 in volume) was employed for 80 μL. A metal foil of lithium was used as the negative electrode and was physically separated from the electrode with one sheet of Celgard 2500 separators. Galvanostatic discharge/charge tests of the cells were performed on a battery testing system (Land, CT2001A, China). Current density and specific capacity were calculated based on the mass of N,S-Co/Zn@CN in the cathodes. CV measurements were recorded on a Metrohm Autolab PGSTAT128N electrochemical workstation at a scan rate of 0.02 mV s^{-1}. Electrochemical impedance spectroscopy (EIS) measurements were performed from 100 kHz to 0.01 Hz with a potentiostatic signal amplitude of 5 mV.

5.1.3. Results and Discussion

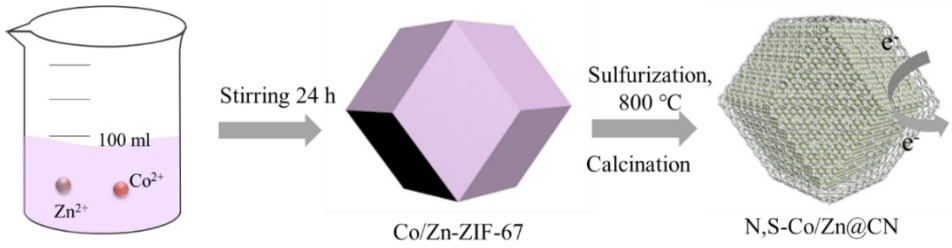

Scheme 5.1 Schematic of the synthetic process of N,S-Co/Zn@CN.

The synthetic procedure of N,S-Co/Zn@CN is illustrated by **Scheme 5.1**. Co/Zn-ZIF-67 is selected as templates to fabricate Co/Zn bimetal sulfide/carbon composites. The original Co/Zn-ZIF-67 precursor is synthesized by precipitation method that cobalt and zinc ions are coordinated with ligand links and embedded in carbon layer after calcination. The Co/Zn-ZIF-67 shows a dodecahedron morphology with a smooth surface and a particle size around 500 nm (appendix **Figure S5.1**). After sulfurization treatment, the precursor is finally converted to mesoporous bimetal sulfide nanoclusters with a N/S-codoped carbon layer (denoted as N,S-Co/Zn@CN).

Morphological and structural characterizations of N,S-Co/Zn@CN are investigated by scanning electron microscopy (SEM) and transmission electron microscopy (TEM). As shown in **Figure 5.1A**, N,S-Co/Zn@CN maintains the rhombic dodecahedron morphology of Co/Zn-ZIF-67 but with the rough surface after the calcination and sulfurization (**Figure 5.1B**). Due to its low boiling point, Zn-containing compounds evaporate during calcination at high temperature, forming a porous structure that can be reflected by the rough surface.[251] It confirms that the existence of bimetallic Co and Zn plays an important role in maintaining the morphology and developing the porous structure of N,S-Co/Zn@CN. Moreover, without N,S-doping, rhombic dodecahedron morphology is collapsed instead of forming nanofibers (**Figure S5.2**).

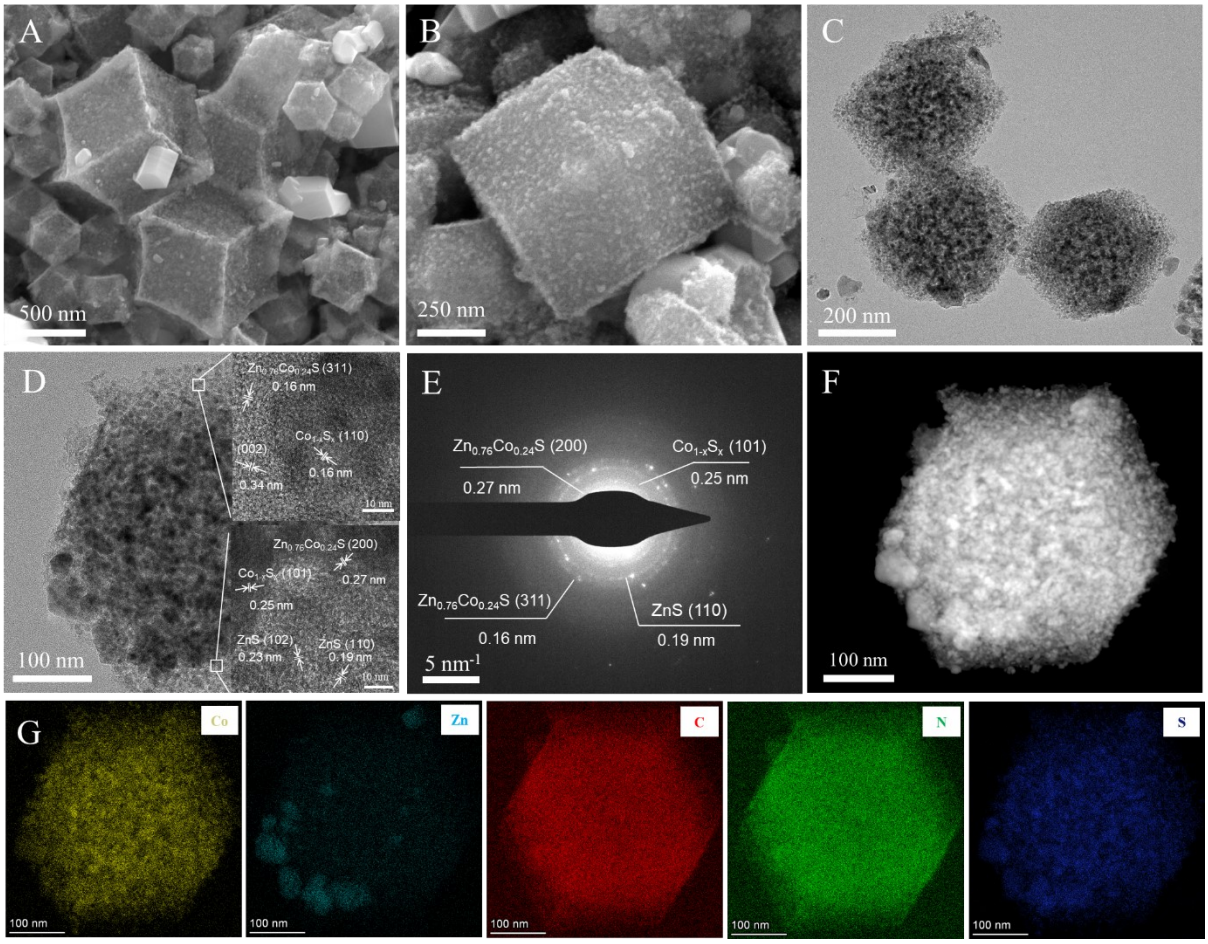

Figure 5.1 (A) Low and (B) high magnification SEM images of as-synthesized N,S-Co/Zn@CN. (C) TEM image of N,S-Co/Zn@CN nanoparticles. (D) TEM image of a single N,S-Co/Zn@CN nanoparticle (inset: HRTEM images of two selected areas). (E) The corresponding SAED pattern

recorded from a single nanoparticle. (F) HAADF-STEM image of a single N,S-Co/Zn@CN; and (G) the corresponding EDS element mapping spectra of element Co, Zn, C, N, and S.

Figure 5.1C shows a typical TEM image of the synthesized N,S-Co/Zn@CN, the nanostructures are composed of bimetallic nanoparticles embedded within the derived porous carbon matrix. According to the HRTEM images (**Figure 5.1D**), the existence of metal sulfides with an average size of 15 nm is consistent with the selected area electron diffraction (SAED) observation in **Figure 5.1E**. Moreover, the carbon is highly graphitized with an interlattice spacing of 0.34 nm, forming a highly conductive network for fast ion transfer. Well-defined lattice spacings within nanostructure are measured to be 0.16 nm and 0.27 nm, corresponding to the (311) and (200) crystalline plane of the $Zn_{0.76}Co_{0.24}S$ phase. While the lattice spacings of 0.19 and 0.25 nm are ascribed to the (110) and (101) planes of ZnS and $Co_{1-x}S_x$, respectively.[135, 256, 307] The presence of bimetallic sulfides nanoparticles embedded within derived carbon nanostructure is further confirmed by high-angle annular dark-field (HAADF)-scanning transmission electron microscopy (STEM) image in **Figure 5.1F**. Moreover, the energy dispersive spectrometer (EDS) mapping images in **Figure 5.1G** confirm that Co, Zn, C, N, and S are uniformly distributed on the dodecahedra cluster.

The crystal structures of the as-synthesized sample are characterized by XRD, as shown in **Figure 5.2A**. The characteristic peaks at 28.6°, 33.2°, 47.6°, 56.5°, and 59.3° observed are in good agreement with the Zn0.76Co0.24S, while the peaks at 26.9°, 39.7°, 56.5°, and 35.2°, 46.7°, 54.4° can be assigned to ZnS and $Co_{1-x}S_x$, respectively. By comparison, Co/Zn@CN without N,S-doping shows different phases after high-temperature calcination (**Figure S5.3**). The XRD result is in good agreement with the TEM image of N,S-Co/Zn@CN composite that is composed of different bimetal sulfides (**Figure 5.1D**). N_2 adsorption/desorption measurements are performed to characterize the surface area and porous structure of the N,S-Co/Zn@CN. As shown in **Figure 5.2B**, it exhibits typical type-IV isotherms with an identifiable hysteresis loop, indicating the porous structure with the high surface area of 120.13 $m^2 g^{-1}$. Pore size distribution is calculated by the Barrett-Joyner-Halenda (BJH) method, which describes that the structure consists of micro/meso/macropores, the featured mesopore size is around 12.2 nm. It confirms that the synthesis process transforms bimetallic Co/Zn-ZIF into a hierarchical pore structure with a high

surface area, which facilitates the transport Li ion and significantly improves the electrocatalytic performance delivered by the high surface area and low resistance.[254]

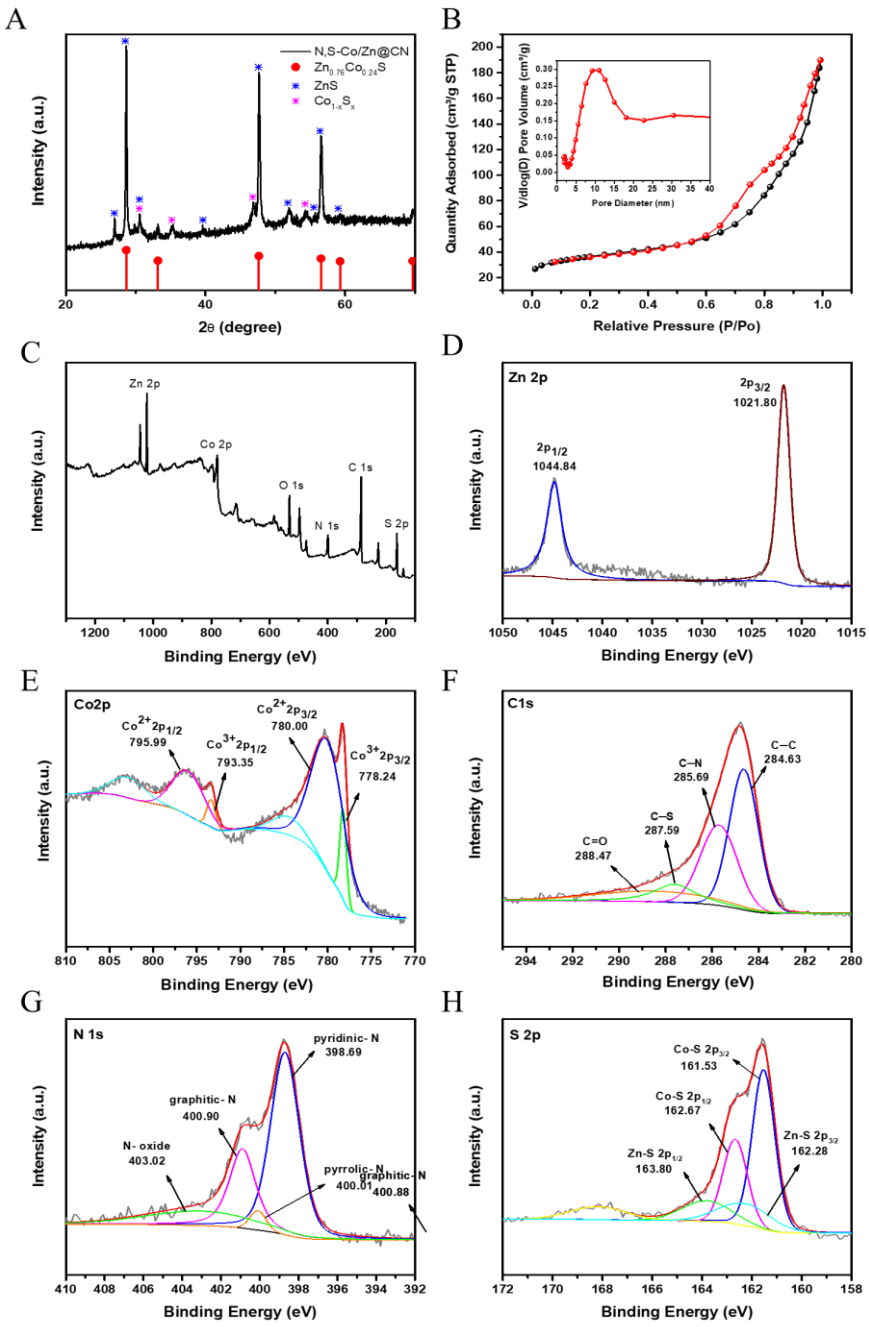

Figure 5.2 (A) XRD pattern of N,S-Co/Zn@CN; (B) N_2 adsorption-desorption isotherms of N,S-Co/Zn@CN (inserted BJH pore size distribution profile); (C) The survey-level scan XPS spectrum of N,S-Co/Zn@CN; High-resolution XPS spectrum of Zn 2p (D), Co 2p (E), C1s (F), N 1*s* (G), and S 2*p* (H) of the N,S-Co/Zn@CN, along with their corresponding fitting curves.

The surface chemical composition and chemical element valence of the N,S-Co/Zn@CN composites are further verified by XPS measurement. The full-survey-scan spectrum (**Figure 5.2C**) reveals the existence of Co, Zn, C, N, and S elements. The elemental ratios measured by XPS spectroscopy agree well with the results of EDS collected by SEM (**Table S5.1**). From the Zn 2*p* region exhibited in **Figure 5.2D**, the two main peaks observed at 1044.84 and 1021.81 eV belong to Zn $2p_{1/2}$ and Zn $2p_{3/2}$, respectively, which point to the Zn^{2+}.[334] The Co 2*p* core-level spectra in **Figure 5.2E** exhibit two predominant peaks at 780.00, 795.99 eV and 778.24, 793.35 eV demonstrating the existence of Co^{2+} and Co^{3+}.[131] The four peaks located at 284.63, 285.69, 287.59, and 288.47 eV in the XPS spectrum of C 1s (**Figure 5.2F**) are corresponding to the bonds energy of C-C, C-N, C-S and C=O, respectively, confirming the successful N and S doping in the C matrix.[255, 256] This implies that N is distributed almost entirely on the carbon surface, which verifies the incorporation of N in the carbon matrix.[124] Compared to the **Table S5.2**, the amount of N element is higher in N,S-Co/Zn@CN (≈ 11.30 at.%) than Co/Zn@CN (≈ 9.92 at.%), owing to the thiourea in the precursor and thermal decomposition during calcination.[46] N 1*s* spectrum proves the existence of the pyridinic N (398.69 eV), pyrrolic N (400.01 eV), graphitic N (400.90 eV), and oxide N (403.02 eV) as shown in **Figure 5.2G**.[258, 259] It is reported that the presences of pyridine N and pyrrolic N result in many defects on the surface of the carbon matrix, which is beneficial to the formation of ion transport channels for Li^+ diffusion.[132, 335] In S 2*p* high-resolution spectrum (**Figure 5.2H**), the two peaks located at 162.28 and 163.80 eV are ascribed to the S $2p_{3/2}$ and S $2p_{1/2}$ of Zn-S bond, while the other two peaks at 161.53 and 162.67 eV can be attributed to the S $2p_{3/2}$ and S $2p_{1/2}$ of the Co-S bond,[260, 261] which indicating the successful sulfurization on the Co/Zn-ZIF-67 precursor. The S element comes from both thiourea and S powder from the sulfurization process.[336] However, thiourea can be easily decomposed into gas during pyrolysis that favors the formation of the porous structure, S powder can offer a sufficient sulfur source.[337] The excessive S element not only combines with transition metal to form $Zn_{0.76}Co_{0.24}S$, ZnS, and $Co_{1-x}S_x$ nanoparticles but also on the carbon surface, demonstrating the chemical contact between metal sulfur nanoparticles and the graphitized carbon layer that improves the conductivity of the composites.[338]

To demonstrate the superiority of this unique structure, the electrochemical lithium storage behaviors of obtained N,S-Co/Zn@CN are evaluated. **Figure 5.3A** shows the consecutive cyclic voltammetry (CV) curves of the electrode at a scan rate of 0.02mV s^{-1} from 0.01 to 3.0 V (vs.

Li^+/Li).During the Li^+ insertion process, the cathodic peaks located at 1.90 and 1.37 V are typically assigned to the reduction process of $Co_{1-x}S_x$ to lithium polysulfides (Li_2S_n) and further to lithium sulfide (Li_2S).[339] The peaks located at 0.97 V involve the reduction process of ZnS and $Zn_{0.76}Co_{0.24}S$ to metallic Zn, Co in the associated Li_2S matrix while with the formation of the solid electrolyte interface (SEI) film on the anode surface.[111, 340] In Li^+ desertion process, the strong anodic peak located at 1.59 V corresponds to the electrochemical conversion from metallic Zn and Li_2S back to ZnS, whereas the peak located at 2.04 V represents the conversion of metallic Co, Zn, and Li_2S back to $Co_{1-x}S_x$ or $Zn_xCo_yS_z$ compounds.[341, 342] Based on the result reported previously, the reduction peak at 1.90 V and oxidation peak at 2.36V here are identified as the characteristic peaks corresponding to the mutual transformation between $Co_{1-x}S_x$ and Li polysulfides (Li_2S_n).[339] The weak peak at 2.36 V indicates the absence of this type of electrochemical conversion, which can be attributed to the fact that N-doped carbon acting as a matrix that prevents the aggregation of $Co_{1-x}S_x$ nanoparticles and the formation of polysulfides.[341] Meanwhile, the overlapped CV curves in the repeated cycles demonstrate the good reversible electrochemical reactions of the electrode.[256] For comparison, the CV curves of Co/Zn@CN are provided as **Figure S5.4A**. Although the location of the oxidation peak and reduction peak of Co/Zn@CN without sulfurization are slightly different from that of N,S-Co/Zn@CN composites, there is a continuous decrease in the peak density of Co/Zn@CN, indicating that the N,S-Co/Zn@CN electrode possesses the inferior electrochemistry stability compared to Co/Zn@CN composites. In general, the electrode with a conversion reaction mechanism will endure the large volume expansion and further result in the rapid capacity fading. The different lithium insertion and extraction voltages of two metal sulfide species can achieve a synergetic effect, where the inactive component can be regarded as a buffering material to buffer the large volume change associated with lithium insertion/extraction in the active component.

In consistence with the CV test, its galvanostatic discharge/charge profile at 30 mA g^{-1} (**Figure 5.3B**) displays three distinct discharge plateaus (1.91, 1.42, and 0.95 V) and charge plateaus (1.51, 2.01, and 2.41 V), confirming the electrochemical conversion as we descried. The initial discharge and charge specific capacities are 1470.3 and 938.2 mA h g^{-1}, with a corresponding coulombic efficiency (CE) of 63.81%. The large irreversible capacity loss of the N,S-Co/Zn@CN electrode observed during the first discharge process is ascribed to irreversible reactions such as the decomposition of electrolyte and formation of SEI film. However, the Coulombic efficiencies of

the second and third cycles reach 95.95% and 94.11%, respectively, indicating the good reversibility of the subsequent discharge/charge process. According to the literature and results, the reaction mechanism of N,S-Co/Zn@CN used as an anode for Li-ion battery can be summarized as follows[343, 344]:

First discharge:

$$Co_{1-x}S_x + 2x\ Li^+ \rightarrow (1-x)\ Co + x\ Li_2S\ (1.5\ to\ 1.2\ V) \quad (23)$$

$$Zn_{0.76}Co_{0.24}S + 2Li^+ + 2e^- \rightarrow 0.76Zn + 0.24Co + Li_2S\ (1.1\ to\ 0.7\ V) \quad (24)$$

$$ZnS + 2\ Li^+ + 2\ e^- \rightarrow Zn + Li_2S\ (1.1\ to\ 0.7\ V) \quad (25)$$

From first charge to subsequent cycles:

$$Zn + Li_2S - 2\ Li^+ - 2\ e^- \rightarrow ZnS\ (1.2\ to\ 1.6\ V) \quad (25)$$

$$(1-x)\ Co + x\ Li_2S - 2x\ Li^+ - 2x\ e^- \rightarrow Co_{1-x}S_x\ (1.6\text{-}2.1\ V) \quad (26)$$

$$x\ Zn + y\ Co + z\ Li_2S - 2z\ Li^+ - 2z\ e^- \rightarrow Zn_xCo_yS_z\ (1.6\text{-}2.1\ V) \quad (27)$$

Although no evidence can support the recovery of $Zn_{0.76}Co_{0.24}S$ structure currently, it is believed that the ZnS, $Co_{1-x}S_x$, and a type of $Zn_xCo_yS_z$ phase are responsible for the subsequent reversible discharge/charge cycles combined with the redox peak couples of 0.97/1.59 V and 1.37/2.04 V in the CV curves (**Figure 5.3A**). From the Nyquist plots shown in **Figure 5.3C** and **Figure S5.4B**, although the initial resistance of N,S-Co/Zn@CN and Co/Zn@CN are both large, the N,S-Co/Zn@CN electrode has a lower equivalent series resistance of only 2.1 Ω and a lower charge transfer resistance of 32.7 Ω than that 507 Ω of Co/Zn@CN after 100th cycles. Compared to Bode plots in Supporting Information **Figure S5.4C**, N,S-Co/Zn@CN has a smaller impedance than Co/Zn@CN in the low-frequency region that is confirmed with Nyquist plots. This proves that the incorporation of N,S-codoped carbon can preserve the high conductivity of the composite electrode and greatly enhance rapid electron transport during the electrochemical lithium insertion/extraction reaction, resulting in progressive improvement in the electrochemical properties.[345] **Figure 5.4D** shows typical charge-discharge profiles for N,S-Co/Zn@CN at various current densities. With increasing current density, the charge and discharge plateaus for N,S-Co/Zn@CN shift to lower voltages because of kinetic limitations at high current densities. The comparable electrochemical kinetics of N,S-Co/Zn@CN and Co/Zn@CN electrode are also reflected from their rate performances at varying discharge/charge current densities (30 to 200 mA g^{-1}). It is obvious that

the N,S-Co/Zn@CN exhibits better rate performance than Co/Zn@CN. Reversible capacities of 839.1, 815.7, 691.9, 617.3, 556.7, and 512.8 mA h $g^{-1}$are obtained at 30, 50, 80, 100, 150, and 200 mA g^{-1}, respectively (**Figure 5.3E**). Upon switching back to 20 mA g^{-1}, a favorable capacity of 624.1 mAh g^{-1} is recovered without any memory effect. In reference to the value at 50 mA g^{-1}, the capacity retention at 200 mA g^{-1} is 62.9% for N,S-Co/Zn@CN electrode confirming its excellent rate performance. Besides the enhanced electric contact offered by the N,S-codoped carbon, the superior rate performance of N,S-Co/Zn@CN electrode also benefits from the abundant large mesopores of short diffusion lengths of Li^+ in electrode. Meanwhile, the N,S-doped porous structure with a large specific surface area offers more active sites that facilitate the redox reaction kinetics and therefore contribute to fast Li^+ ion transport. In the long-term cycling test at 150 mA g^{-1} (**Figure 5.3F**), N,S-Co/Zn@CN electrode shows an outstanding capacity retention of 65.59% after 100 cycles, with CEs well maintained at around 100% throughout the cycling. The corresponding capacity decay rate is 0.34% per cycle in reference to the first charge capacity. By comparison, Co/Zn@CN shows rather lower capacity retention of 34.25% and higher capacity decay rate is 0.66% after 100 cycles, which is due to the low conductivity and the large volume change during lithiation-delithiation processes. The excellent cycling performance could be mostly ascribed to the synergistic effect of bimetallic sulfide with high catalytic activity and relatively low degree of aggregation, which can help each other to buffer the volume change and guarantee fast ion and electron transfer compared to one-type metal sulfide.

Above all, the excellent Li-intercalation performances of N,S-Co/Zn@CN, in terms of large initial capacity, superior cyclability, and excellent rate capability, can be attributed to the porous structure of ternary metal sulfides/N and S codoped carbon matrix. First, the porous structure derived from bimetal-organic frameworks precursor offers sufficient void space, which is beneficial for electrolyte penetration and can effectively mitigate the volume expansion during the charge/discharge process, resulting in stable electrode structure and cycling properties. On one hand, the presence of N and S codoped carbon matrix not only can function as the buffer layer to relieve the volume expansion of its trapped metal sulfide nanoparticles but also can enhance charge and ion transportation throughout the composite and electrode further improve the structural integrity. Meanwhile, ternary metal sulfide can achieve enhanced electrical conductivity compared to one-type metal sulfide. Finally, the interconnected carbon matrix connects individual $Zn_{0.76}Co_{0.24}S$ nanoclusters to obtain a highly electronic conductive network, while efficiently

alleviate large volume change during cycling and prevent direct contact of the electrolyte with the intermediate product during the lithiation/delithiation.

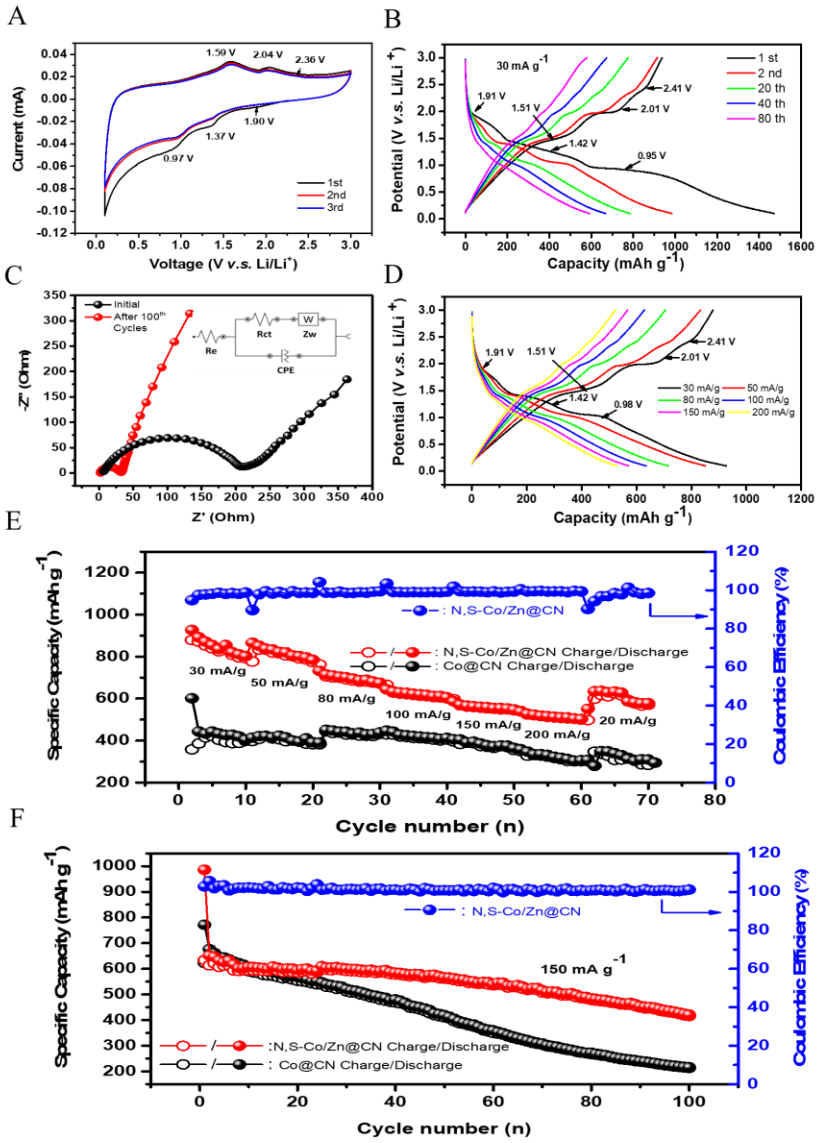

Figure 5.3 (A) Cyclic voltammograms of N,S-Co/Zn@CN electrode at a scanning rate of 0.02 mV s-1; (B) Galvanostatic charge/discharge curves of N,S-Co/Zn@CN electrode at a current density of 30 mA g-1 within 0.1 to 3.0 V versus Li+/Li; (C) Nyquist plots of N,S-Co/Zn@CN electrode tested at open circuit potential initial and after 100 cycles of galvanostatic discharge/charge at 150 mA g^{-1} with the inset showing the equivalent circuit; (D) Charge-discharge profiles of N,S-Co/Zn@CN at different current densities; Rate capability (E) and cycling properties at 150 mA g^{-1} (F) of N,S-Co/Zn@CN, Co/Zn@CN electrode.

5.1.4. Conclusion

A novel porous composite structure of N,S-codoped carbon dodecahedron/transition metal sulfides (N,S-Co/Zn@CN) is successfully developed using sulfurized Co/Zn-ZIF-67 precursor. When it's applied as a highly active anode material for LIBs, it delivers excellent electrochemical performance with a high initial reversible capacity of 938.2 mAh g^{-1} and an outstanding capacity retention of 63.6% after 100 cycles at a current density of 150 mA g^{-1}. The excellent electrochemical properties might be contributed to the synergistic effects of metallic sulfide nanoclusters and carbon matrix with hierarchical porous structure and rough surface area. It is believed that this strategy would open new directions in the synthesis and exploration of metal sulfides/carbon-based composites for the application in energy storage and conversion systems.

5.2. Hetero-Architectured Core-Shell $NiMoO_4@Ni_9S_8/MoS_2$ Nanorods Enabling High-Performance Supercapacitors

Except for the application in Li-ion batteries, transition metal sulfides also present the excellent behavior as electrodes for supercapacitors. In this section, we will introduce hetero-architectured core-shell $NiMoO_4@Ni_9S_8/MoS_2$ nanorods which is synthesized by the same method as electrocatalysts in section 4.3 in Chapter 4. The resulting hierarchical architecture with outer Ni_9S_8/MoS_2 nanoflakes shell on the inner $NiMoO_4$ core offers plenty of active sites and ample charge transfer pathways in continuous heterointerfaces. The obtained $NiMoO_4@Ni_9S_8/MoS_2$ as an electrode material presents an unsurpassed specific capacity of 373.4 F g^{-1} at 10 A g^{-1} and remarkable cycling performance in the base electrolyte. After investigating the performance, it's believed that these nanorods show both active performance both in energy conversion and storage, achieving our goal of multiapplication.

5.2.1. Introduction

Arising markets of high-energy density electronics and various electrical cars have prompted the production of efficient, cheap, and environmentally benign energy storage technologies and devices.[346] Among them, supercapacitors (SCs) have attracted wide-ranging research interests because of their outstanding energy density, rating performance and superior cycling

durability.[27, 347] The SCs have filled the storage gap within traditional batteries devices and capacitors, so that they have been considered as the promising and efficient storage devices. However, the energy density of supercapacitors still far below the Li-ion batteries which confines their large-print industrial employments.[291] Normally, supercapacitors are classified as two types depending on different working principles: electrical double layer capacitors (EDLCs) and faradaic pseudo-capacitors.[348] To boost the energy density and superior flexibility, asymmetric supercapacitors (ACS) consisted with the above two electrodes have aroused great interests, because they could utilize the merits of both batteries and supercapacitors, and thus remarkably enhance their energy and power densities.[349] It's known that carbon-based materials exhibit the excellent high conductivity and excellent density as battery-type electrodes. However, they still fail the expectation for long life durability. Compared to them, pseudo-capacitor materials possess rich Faradaic redox reactions active sites near the surface area of electrode, giving them excellent energy storage properties. Typical electrodes for pseudo-capacitors are RuO_2 and MnO_2, but their usages are hindered because of their environmental harmfulness and low conductivity.[60, 350] Recently, transition-metal based materials, including oxides,[60, 351] sulfides,[352, 353] and hydroxides[354, 355] have become advanced pseudo-capacitor electrode materials. Because of their abundant oxidation states and multiple morphology and structure, it's favorable to facilitate the fast and reversible Faradaic redox reactions, thus resulting in high theoretical capacities.[349] Particularly, $NiMoO_4$ belonging to the binary oxide family is a good candidate because of its morphology diversity and outstanding capacitive efficiency.[356] Normally, $NiMoO_4$ possesses two stable structures octahedral or tetrahedral configuration at low or high temperature, respectively.[357] Also, $NiMoO_4$ is an inexpensive, plentiful, environmentally benign commodity and has significant nickel atomic capacity and high conductivity (10^{-6} S cm^{-1}) from the molybdenum atom.[46, 358] For instance, Yun's group published that gravel-like $NiMoO_4$ grown on carbon cloth produced 970 F g^{-1} at 2.5 A g^{-1}.[359] Zhang, e.al synthesized hierarchical carbon sphere@$NiMoO_4$ which displayed good specific capacity of 268.8 F g^{-1} at 1.0 A g^{-1}.[360] Interestingly, Wang's group designed $NiMoO_4$ with two morphologies (nanospheres and nanorods), both of them showed the excellent specific capacitance, indicating $NiMoO_4$ could be a promising candidate for supercapacitor.[31] Frustratingly, because of the delayed kinetic reaction and intolerant morphology collapse during long charge/discharge procedure, $NiMoO_4$ impedes the low-rate capacity and poor cycling stabilities.[296] Even, it is still a big challenge to synthesize a $NiMoO_4$ nanomaterials with large specific area and

high electrical conductivity. Not many reports are related to $NiMoO_4$ electrode in application of supercapacitors. Consequently, structural modifications and constructions of $NiMoO_4$ related to capacity and stability are of considerable importance to obtain advanced binary hybrids.

By contrast with metal oxides, transition metal sulfides (TMS) have higher conductivity, chemical durability or redox kinetics and are regarded as other potential pseudo-capacitance candidates.[361] Unlike oxygen, sulfur possesses comparatively low electronegativity, favoring for developing different nanostructures between metal ions and other species.[349] In particular, nickel sulfides have abundant redox active sites, forceful reducibility and inexpensive advantage exhibiting the excellent property for supercapacitor. For instance, Zhang's group synthesized 3D flower-like nickel sulfide spheres with various morphologies exhibited initial discharge capacity of 550 mA h g^{-1}.[362] Osquian et al. reported three-dimensional starfish-like Ni_3S_4-NiS grown on graphene oxide with specific capacity of 1578 F g^{-1} at 0.5 A g^{-1}.[363] However, the cycle stability and rate performance of nickel sulfides still fail to reach the expectation. Wang's group announced the provision of high capacitance three-dimensional Ni_3S_4 nanosheet electrodes but retained only around 60% capability after 2000 cycles.[364] However, another type of molybdenum disulfides (MoS_2) displays superior cycling stability and pseudo-capacitance skills because of graphite-type layer structure and numerous valence states of Mo atoms, which can store charge between the different layers.[365, 366] In addition, atomic layers of MoS_2 forms a sandwich structure which molybdenum layer between two sulfur atomic layers bound together by Van der Waals forces favoring for ion intercalation and electron transfer.[367] Qi's group synthesized hierarchical MoS_2 nanospheres exhibited a specific capacitance of 142 F g^{-1}at 0.59 A g^{-1}.[155] Kim et al. reported MoS_2 spheres displayed capacitance retention of about 93.8% after 1000 cycles.[368] Unfortunately, chemically formulated MoS_2 nanosheets are likely to aggregate, reducing surface area and leading to poor conductive ability. Hence, designing and developing of hetero-structured materials are necessary to enhance the conductivity, shortening the electron/ ion transfer pathways and permit for high-rate capability.

One approach is to build hierarchical structures from multiple crystalline species that can effectively alternate electron configuration so that exhibit the superior electrochemical activity due to the synergistic effect of the heterostructure. A typical type of hierarchical structures is external structures which different porous structures such as nanowires, nanoparticles and nanosheets grown on the surface of the backbones such as nanorods or nanofibers with higher specific surface

current density and conductivity.[369] Hierarchical core-shell with strong interaction between the shell and core species greatly enhance the chemical and physical properties and offering the various interlayer.[370] Up to now, many contributions have been devoted to designing the external hierarchical structures, by combining of metal sulfides with metal oxides. For instance, Jae Cheo's group synthesized core-shell structural Co_3O_4@CdS showed 390 Fg^{-1} in symmetric supercapacitor device.[371] Tang et al. reported homogeneous core/shell $NiMoO_4$-based nanowire arrayed on nickel foam showed amazing achievements with 47.2 Wh kg^{-1} at high energy density.[372] Hierarchical core-shell $CoMoO_4$@$NiMoO_4$ grown on nickel foam was synthesized by Zhang's group, which showed a high capacity and excellent stability.[373] Qi et al. announced $MnCo_2S_4$@CoNi LDH core-shell heterostructure with high electrical conductivity and ample active sites offered better faradaic reactions as electrodes for supercapacitors.[374] Therefore, construction of core-shell architecture is proven to be an effective strategy to utilize the merits of multiple components to the maximum to realize high-performance supercapacitors.

Herein, we develop a core-shell hierarchical architecture that core $NiMoO_4$ nanorod is wrapped with Ni_9S_8/MoS_2 nanoflakes, defined as $NiMoO_4$@Ni_9S_8/MoS_2, which is converted from the Mo/Ni precursor after sulfurization. This configuration offers mechanical protection and serves as the bridge connecting the outer metal sulfides and inner core. Due to the synergistic effect of its special multi-interfacial structure, fast ion/mass transportation in and ample active sites within 2D nanoflakes and 1D inner $NiMoO_4$ nanorods, $NiMoO_4$@Ni_9S_8/MoS_2 nanorods demonstrated the excellent specific capacity of 373.4 F g^{-1} at 10 A g^{-1} and superior cycling property, implying that $NiMoO_4$@Ni_9S_8/MoS_2 can be a propitious electrode for high-efficiency energy storage system.

5.2.2. Experimental Section

5.2.2.1. Chemicals

Sodium molybdate dihydrate ($Na_2MoO_4 \cdot 2H_2O$), nickel (II) nitrate hexahydrate ($Ni(NO_3)_2 \cdot 6H_2O$), sulfur (S), potassium hydroxide (KOH) were purchased from Sigma-Aldrich.

5.2.2.2. Synthesis of Mo/Ni Precursor

The conventional hydrothermal approach was used to prepare Mo/Ni precursors, followed by sulfurization. Sodium molybdate dihydrate (0.2 g) and nickel nitrate hexahydrate (0.2 g) were dissolved in deionized water (70 mL). Then the green transparent solution was moved to a 100 mL

Telon autoclave and held at 180 °C for 12 hours. The green final material was cleaned with deionized water and kept at 50 ℃ overnight, giving rise to Mo/Ni precursor.

5.2.2.3. Synthesis of Nanorods $NiMoO_4@Ni_9S_8/MoS_2$

The Mo/Ni precursor and sulfur (mass ratio = 1:3) were put in one porcelain boat with the downstream and upstream side and calcinated at 350℃ for 2 h under flowing Ar. The obtained material was $NiMoO_4@Ni_9S_8/MoS_2$. For comparison, $NiMoO_4$ was also synthesized by calcining Mo/Ni precursor without sulfur in the same calcination process.

5.2.2.4. Structural Characterization

FEI Quanta 450 Environmental Scanning Electron Microscope was utilized to examine the anatomy of materials. Transmission electron microscopy (TEM, Thermo Scientific Talos F200X G2 S/TEM) was tested to examine the crystal details of the materials. X-ray diffraction (XRD) measurements were used by a monochromatic Bruker D8 advance diffractometer. The composition and valence states were performed on a Thermo Scientific X-ray photoelectron spectroscopy. N_2 sorption measurements were utilized using Micromeritics 3Flex Surface Characterization Analyzer with N_2 as the adsorbent.

5.2.2.5. Electrochemical Measurements

All electrocatalytic tests were conducted by Biologic VMP300 electrochemical workstation in 6.0 M KOH with three-electrode equipment including the glassy carbon (GC) electrode (area: 0.196 cm^2) as the working electrode, platinum wire as the counter electrode and the saturated calomel electrode (SCE) as the reference electrode. Working electrode was prepared by adding the active nanomaterial and super P in 600 μL of 10% polyvinylidene difluoride (PVDF) dissolved in N-methyl pyrrolidinone (NMP). Then slurry (120 μL) was spread on a clean nickel foam (1×1 cm^2) by drop casting and dried overnight. The dried electrode was then pressed using a hydraulic press at a pressure of 10 MPa. The mass loading of active material in single nickel foam was about 2 mg. The CV and GCD were determined within a possible window of -0.3-0.6 V, and the material's specific capacity was estimated using GCD curves. The specific capacitance, C_{sc} (F g^{-1}), were measured by the equation:

$$C_{sc} = \frac{I \times \Delta t}{m \times \Delta V}$$

where I (A) was the discharge current, Δt (s) represented the discharge time, ΔV (V) was the potential window, v (mV s^{-1}) represented the scan rate and m (g) was the mass of the active materials.

5.2.3. Results and Discussion

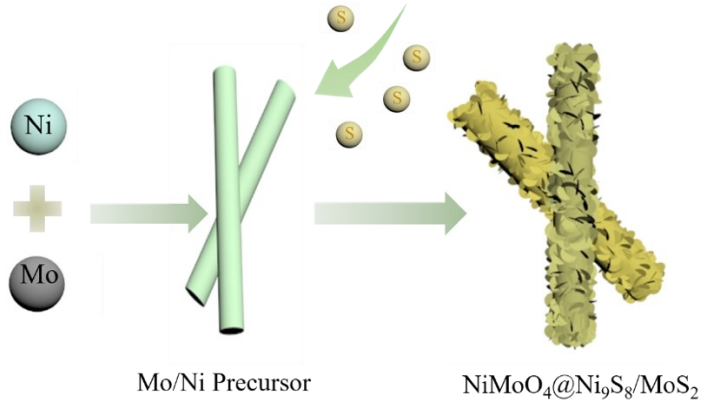

Scheme 5.2 Scheme of the formation process of core-shell $NiMoO_4@Ni_9S_8/MoS_2$ hetero-structured nanorods.

As illustrated in **Scheme 5.2**, the core-shell $NiMoO_4@Ni_9S_8/MoS_2$ heterostructure was converted from the Mo/Ni precursor by a simple sulfurization method, as demonstrated in detail in the experimental section. From the scanning electron microscope (SEM) image in **Figure 5.4A**, it could be observed that Mo/Ni precursor possessed nanorod-like morphology with smooth exterior and a diameter of 130 nm. After the sulfurization method, the shell of Mo/Ni precursor converted to metal sulfides (Ni_9S_8/MoS_2) with ultrathin nanoflakes shelling the inner core $NiMoO_4$ to form a core-shell structure (**Figure 5.4B**). By comparison, $NiMoO_4$ nanorods without sulfurization remained the morphology with the smooth surface even some of the nanorods were broken, confirming that sulfurization could protect the nanorods from collapsing (**Figure S5.5**). **Figure 5.4C** showed the clear structure and morphology of nanorods with a typical diameter of 180-200 nm with ultrathin nanoflakes and generated a hierarchical porous structure which further confirmed the formation of Ni_9S_8/MoS_2. Such architecture was favorable for charge transfer and ion transportation to improve the electrochemical performance.[293] The detailed morphology of nanorods was determined by transmission electron microscopy, which revealed that core-shell construction was consisted of 2D Ni_9S_8/MoS_2 nanoflakes as outer shell part and 1D nickel

molybdate nanorods inner core (**Figure 5.4D**). Coherent heterointerfaces could be observed in the entire nanorod between the outside metal sulfides and the inner metal oxide core, which could form the porous structure providing ample charge transfer channels.

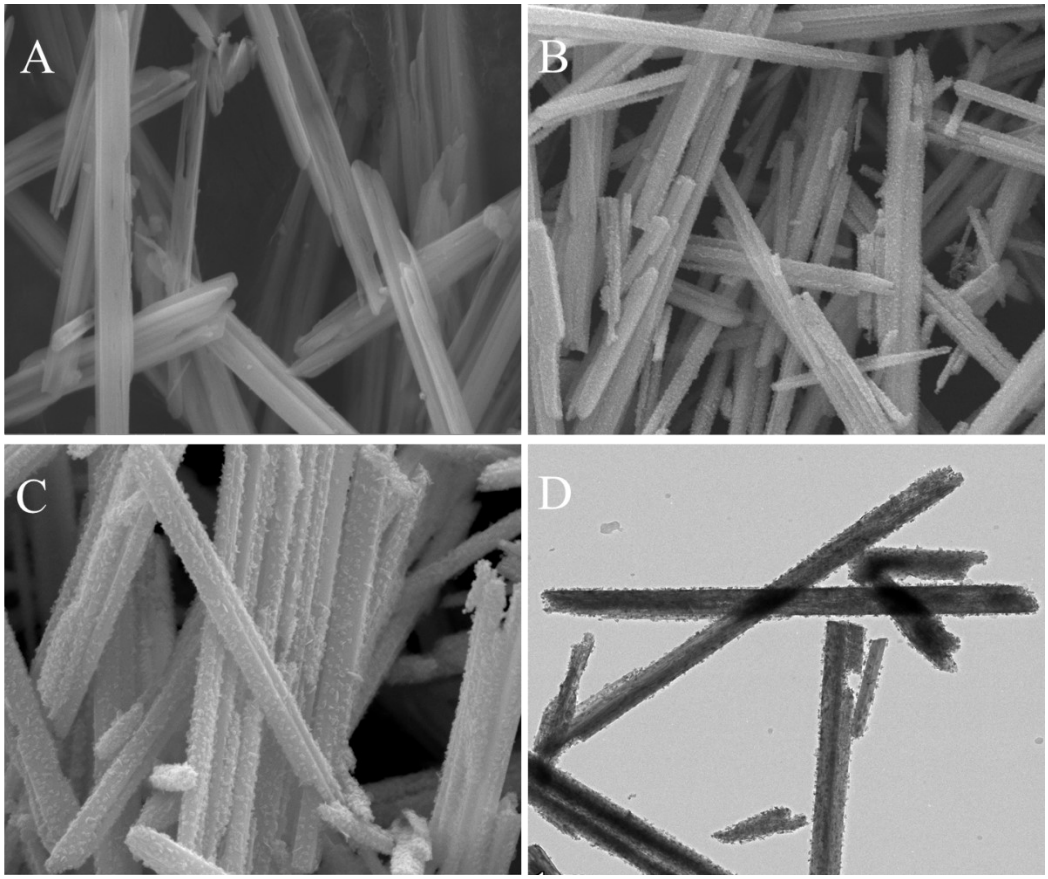

Figure 5.4 (A) SEM images of Mo/Ni precursor; (B-C) SEM images of $NiMoO_4$@Ni_9S_8/MoS_2 nanorods; (D) TEM image of $NiMoO_4$@Ni_9S_8/MoS_2 nanorods.

The high-resolution TEM images of $NiMoO_4$@Ni_9S_8/MoS_2 in **Figure 5.5A-C** which are selected from the upper (blue square) and lower part (orange square) from single nanorod. **Figure 5.5B** displayed the crystalline spacings of 0.22 nm, 0.36 nm, and 0.27 nm, corresponding to (-411) crystal lattice of $NiMoO_4$, (022) crystal lattice of Ni_9S_8 and (101) lattice distance of MoS_2, respectively, demonstrating ternary hybrids[290, 375] while **Figure 5.5C** showed demonstrated the existence of abundant interfaces between these components.[376] The uniformed distribution of Mo, Ni, S and O was shown in **Figure 5.5D-E**, confirming the binary compound of Ni_9S_8/MoS_2. It's

worth mentioning that most Mo and O elements mainly dispersed in the core center, indicating that the incorporation of $NiMoO_4$ inside the composite. XRD was investigated to depict the crystalline shapes of $NiMoO_4$@Ni_9S_8/MoS_2, as presented in **Figure 5.5F**. The characteristic peaks at 23.9°, 28.8°, 29.7°, 41.2° and 47.4° confirmed the formation of $NiMoO_4$ (JCPDS No. 33-0948).[358] The five sharp peaks located at 27.2°, 31.3°, 42.6°, 50.8° and 53.4° were attributed to (202), (222), (332), (153) and (261) planes of Ni_9S_8 (JCPDS No. 22-1193).[274] The typical peaks placed at 33.5°, 35.8°, 44.1°, 49.7°, 55.9° and 58.3°corresponded to the (101), (102), (006), (105), (106) and (110) planes of MoS_2 (JCPDS No. 37-1492), respectively, reinforcing formation of ternary composites.[279] However, in **Figure S5.6A**, Mo/Ni without sulfurization formed the nickel molybdate displayed as the XRD pattern of $NiMoO_4$. **Figure 5.5G** represented N_2 sorption isotherms of $NiMoO_4$@Ni_9S_8/MoS_2 with VI-type curve of a hysteresis loop. The $NiMoO_4$@Ni_9S_8/MoS_2 surface area was 27.9643 m^2 g^{-1}, above the NiMoO4 (20.5 m^2 g^{-1}). Pore distribution profile in **Figure 5.5G** and **Figure S5.6B** demonstrated that the main product possesses pores of 0.6 nm, 3 nm and 10 nm, confirming the existence of micropores from the Ni_9S_8/MoS_2 nanoflakes and mesopores from the inner core. This porous structure of the main product could result from the introduction of sulfur during the calcination process under the high temperature, further creating more active sites and fastening electron transportation during the electrochemical procedure. The above result confirmed that the formation of metal sulfides and nickel molybdate with abundant pores which created more active sites and offered more charge transfer channels.

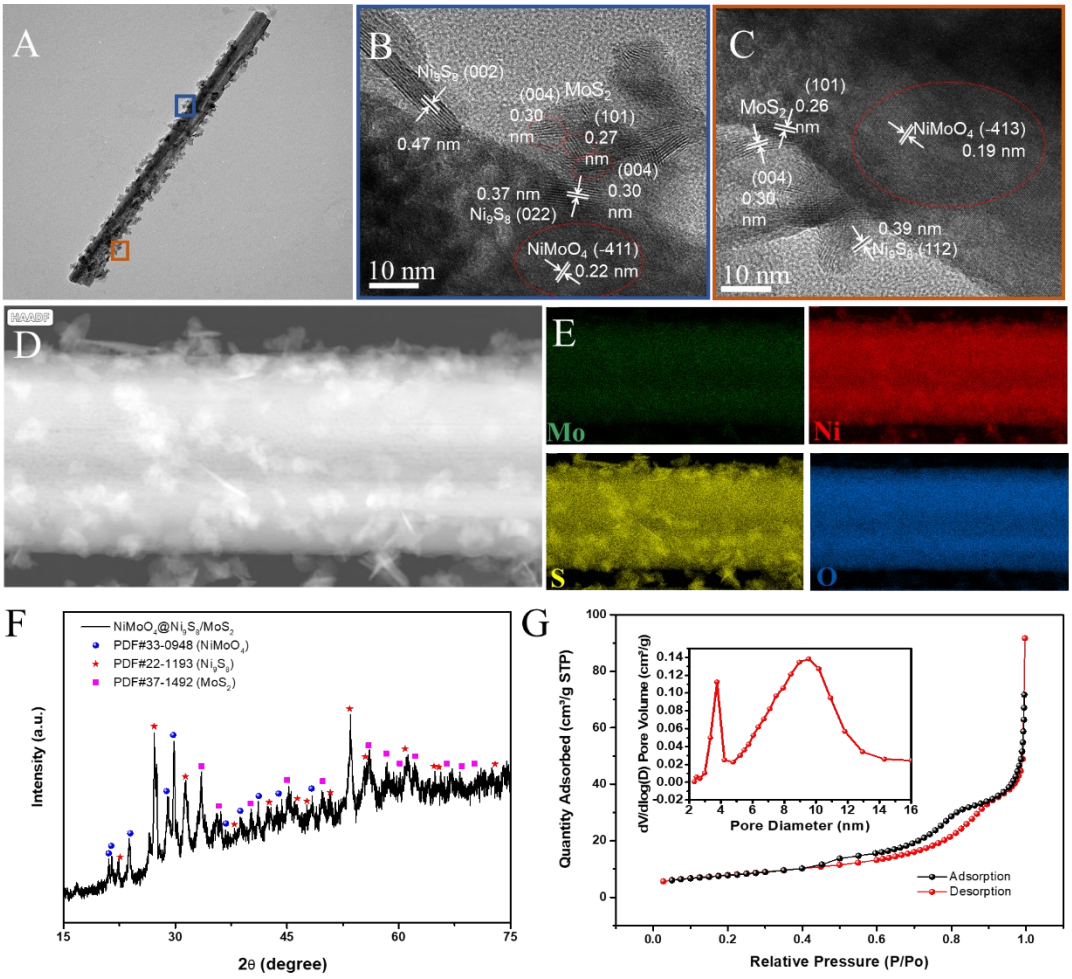

Figure 5.5 (A) TEM image of a single $NiMoO_4$@Ni_9S_8/MoS_2 nanorod; HRTEM images of (B) upper part (blue square) and (C) lower part (orange square) of $NiMoO_4$@Ni_9S_8/MoS_2 nanorod; (D) HAADF-STEM image of the selected part of $NiMoO_4$@Ni_9S_8/MoS_2 nanorod; and (E) the EDS element mapping spectra of element Mo, Ni, S and O; (F) XRD pattern and Rietveld refinement of $NiMoO_4$@Ni_9S_8/MoS_2; (G) N_2 sorption isotherms of $NiMoO_4$@Ni_9S_8/MoS_2 (inset: pore size distribution profile)

The element state analysis of the electrode was conducted through X-ray spectroscopy. In **Figure S5.7**, XPS survey spectra revealed co-occurrence of Ni, Mo, S, and O elements in the nanorods. The Mo 3d XPS spectrum at the core stage could be divided into five peaks. (**Figure 5.6A**). The two signals at 235.5 and 232.2 eV were accredited to Mo $3d_{3/2}$ and $3d_{5/2}$ of molybdate, and signals at 232.6 and 228.7 eV corresponded to Mo $3d_{3/2}$ and $3d_{5/2}$ of molybdenum disulfide,

respectively.[377, 378] The other signal at binding energy of 226.5 eV also agreed to S 2s orbital of metal sulfide bond (Mo-S), respectively.[42] **Figure 5.6B** showed the Ni 2p spectra of two spin-orbit doublets with its satellites. Distinct signals at binding energy of 855.9 and 873.7 eV were credited to $2p_{3/2}$ and $2p_{1/2}$ of nickel ion (II), and the other two peaks at 856.4 and 875.3 eV were associated with nickel ion (III) ($2p_{3/2}$ and $2p_{1/2}$), respectively.[379] As presented of S 2p spectrum in **Figure 5.6C**, the binding energy signals at 163.6, 161.5 eV were allocated with the $2p_{1/2}$ and $2p_{3/2}$ of nickel-sulfur bonding, two signals at163.5 and 161.6 eV were assigned to the molybdenum-sulfur bonding ($2p_{1/2}$ and $2p_{3/2}$), respectively.[272, 377] Also, a typical peak of the sulfur-oxygen bond with oxidation state appeared at signal 168.4 eV.[295] O1s spectrum was displayed as **Figure 5.6D**, the signals at 530.6 and 531.9 eV corresponded to metal-oxygen (M-O) bonds in nickel molybdate and oxygen vacancy of composites, respectively.[296]

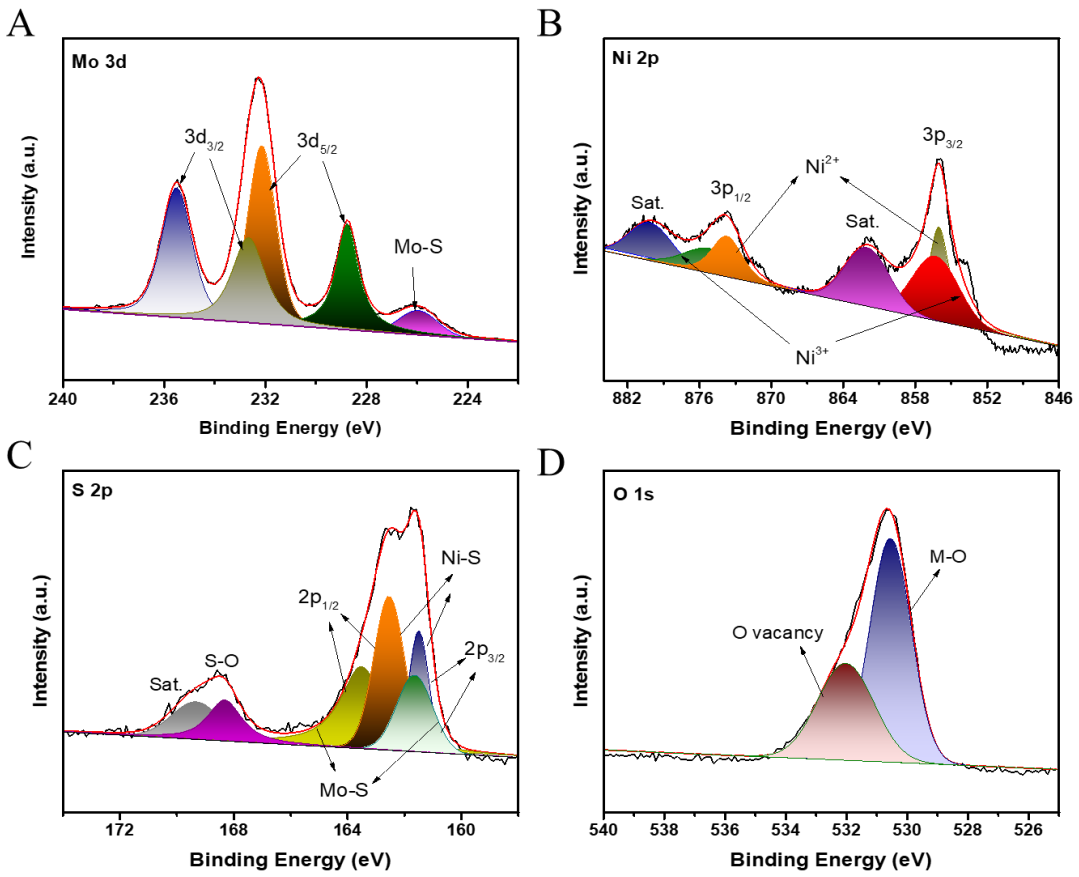

Figure 5.6 High-resolution XPS spectrum of (A) Mo 3d, (B) Ni 2p, (C) S 2p and (D) O 1s of $NiMoO_4$@Ni_9S_8/MoS_2.

The electrochemical outputs of all electrodes were delved by three-electrode configuration in alkaline solution. **Figure 5.7A** indicated CV curves of $NiMoO_4$@Ni_9S_8/MoS_2 from 5 to 200 mV s^{-1} in a voltage window of -0.3- 0.6 V (*vs.* SCE), respectively. Obviously, two redox summits were shown in a voltage window of 0.2 V- 0.4V and -0.1 - 0 V, implying the typical valence state change of Ni^{2+}/Ni^{3+} and faradaic redox between Mo^{4+} and Mo^{6+} during the electrochemical process.[377] Compared to the CV curves of $NiMoO_4$ (**Figure S5.8A**), the CV curves of the main product remained even at high 200 mV s^{-1}, showing outstanding durability of $NiMoO_4$@Ni_9S_8/MoS_2. In addition, the sharp peaks slightly changed to a wide voltage window as the enlarging scan rate indicated fast faradaic reactions. It further verified the synthesis of metal sulfides hybrids and their typical pseudocapacitive behavior.[365] In **Figure 5.7B**, CV plots of the main product and compared materials were illustrated to validate the merits of $NiMoO_4$@Ni_9S_8/MoS_2 nanorods for superior

electrodes. Compared with $NiMoO_4$ electrodes, the $NiMoO_4$@Ni_9S_8/MoS_2 nanorods had higher current densities and larger area, demonstrating a significant enhancement of capacitance due to multiple electron transport channels and synergistic effect within the metal sulfides and nickel molybdate.[380] Furthermore, the current density of the typical peak of $NiMoO_4$@Ni_9S_8/MoS_2 displayed a more linear and steep response than $NiMoO_4$, suggesting larger surface area from the BET result, higher electrical conductivities, more active sites, and faster ion exchange due to the porous core-shell shape. **Figure 5.7C** displayed the GCD plots of $NiMoO_4$@Ni_9S_8/MoS_2 nanorod with current densities ranging from 1 to 20 A g^{-1}. Compared with $NiMoO_4$ (**Figure S5.8B)**, $NiMoO_4$@Ni_9S_8/MoS_2 nanorod displayed a longer charge/discharge time of 446 s at 2 A g^{-1}. The corresponding charge-discharge profiles of $NiMoO_4$@Ni_9S_8/MoS_2 and $NiMoO_4$ were further provided in **Figure S5.8C** and **Figure S5.8D**. The obvious voltage plateau of $NiMoO_4$@Ni_9S_8/MoS_2 confirmed the "battery-type" pseudocapacitive behavior in comparison of $NiMoO_4$.[381] It's reported that the bimetal precursor after sulfurization produced hierarchical Ni_9S_8/MoS_2 nanoflakes with expanded interlayer spacing, which benefited ion diffusion with enhanced capacitance.[382] The nonlinear shape of GCD plots further depicted the reversible pseudocapacitive properties which were mainly derived from the chemical conversion in $NiMoO_4$, Ni_9S_8 and MoS_2, which can be represented by the following equations:[383, 384]

$$NiMoO_4 + OH^- \leftrightarrow NiMoO_4OH + e^- \quad (28)$$

$$Ni_9S_8 + OH^- \leftrightarrow Ni_9S_8OH + e^- \quad (29)$$

$$MoS_2 + K^+ + e^- \leftrightarrow MoS\text{-}SK \quad 30)$$

Because of the sluggish potential reduction resulted from interior resistance and the faradaic chemical reaction, the discharge time decreased significantly as the current density increased.[385] More apparent results were presented in **Figure 5.7D**. At 10 A g^{-1}, the total charge/discharge duration of $NiMoO_4$@Ni_9S_8/MoS_2 composite was much superior to $NiMoO_4$. Such excellent performance could be explained by more than one mechanism. First, the core-shell structure offered plentiful electron transportation pathways and functioned as a bridge connected the outer metal sulfides shell and inner $NiMoO_4$ core, provided mechanical assistance to prevent the structure from collapsing and agglomerating during the faradic reaction, resulting in increased electrical conductivity. Second, the Ni_9S_8/MoS_2 nanoflakes possessed high surface area and plentiful active

sites. Third, the synergistic effect between Ni_9S_8 and MoS_2 contributed to high capacitance in the energy storage procedure.

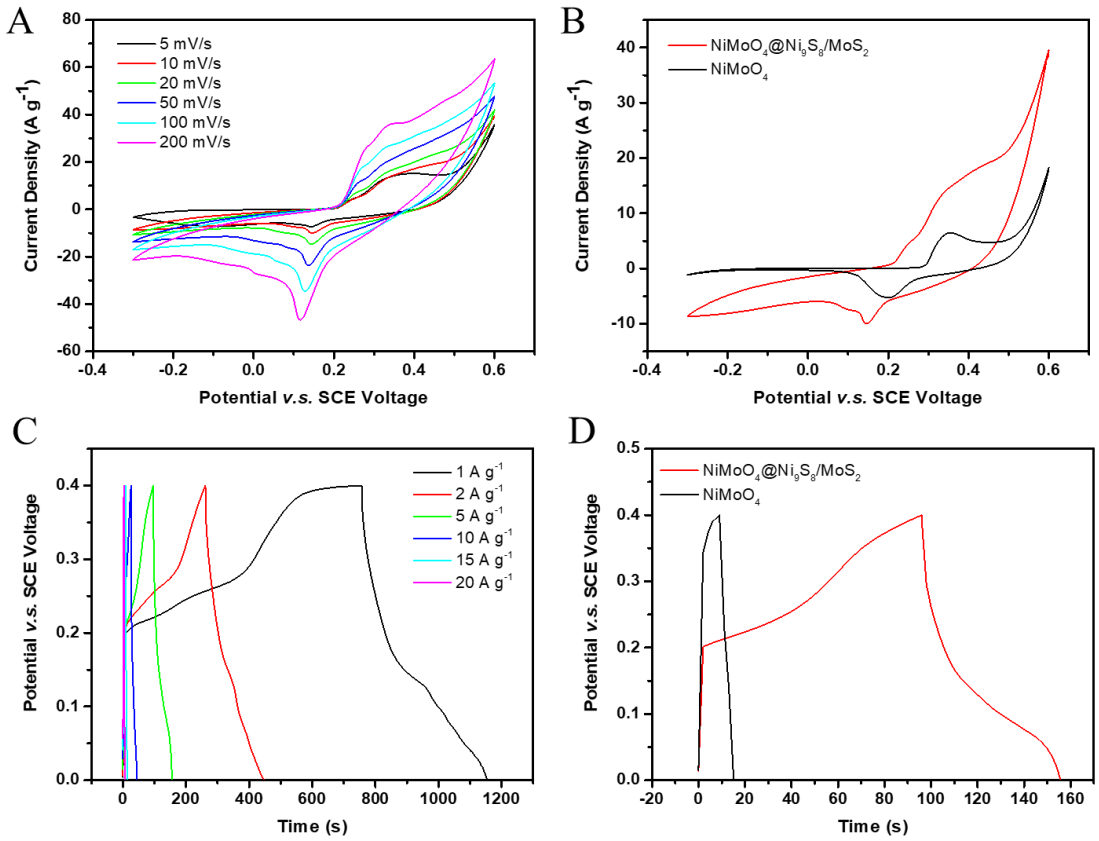

Figure 5.7 (A) CV curves of $NiMoO_4@Ni_9S_8/MoS_2$ at different scan rates; (B) CV curves of $NiMoO_4@Ni_9S_8/MoS_2$ and $NiMoO_4$ at a scan rate of 5 mV s^{-1}; (C) GCD plots of $NiMoO_4@Ni_9S_8/MoS_2$ nanorods at various current densities and (D) comparison of two electrodes at a current density of 10 A g^{-1}.

Figure 5.8A exhibited the plot of log with peak current and log with a scan speed at 5-200 mV·s^{-1} based on the CV plots of $NiMoO_4@Ni_9S_8/MoS_2$. Depending on the power-law:[386]

$$i = \alpha v^{\beta} \quad (31)$$

where α was coefficient, i represented the maximum current, υ represented the scan rate. And β was the slope of the log (i) and log(υ) plots. Accordingly, β=0.5 indicated a diffusion-

controlled process; β=1 implied that the reaction was surface-controlled or had a capacitor-like feature.[387] **Figure 5.8A** showed that the value of β was close to 0.55, indicating that the redox process kinetics were determined by ion diffusion, further verifying the faradaic reaction in the $NiMoO_4$@Ni_9S_8/MoS_2 electrode. The special capacitances with different current densities depending on the GCD plot were presented in **Figure 5.8B**. The specific capacitances of $NiMoO_4$@Ni_9S_8/MoS_2 electrode were 488.9, 467.6, 373.4, 240.1, 92.0, and 52.9 F g^{-1} at 1,2, 5, 10, 15, and 20 A g^{-1}, respectively. By comparing with values of $NiMoO_4$, it exhibited the superior rate performance. The cycling property of two electrodes was exhibited in **Figure 5.8C** at 10 A g^{-1}. After 10,000 cycles, the capacity retentiveness of the main product was 81.0% and coulombic efficiency remained almost at 100%, which is much better than $NiMoO_4$ (40.1%) and other electrodes in **Table 5.1**, indicating its excellent cycling stability. The main reason for capacitance attenuation might be the difficulty of ions/electrons reaching to the thick area of material under 10 A g^{-1}. However, the outstanding performance of $NiMoO_4$@Ni_9S_8/MoS_2 nanorods was ascribed to the core-shell structure which the outer metal sulfide shell protected the structure from collapsing and limiting fast electron transfer speed leading to the electrode decomposition, further confirming the merits of this architecture.[357] **Figure 5.8D** showed the typical EIS spectra of two electrodes before cycling. Obvious, the charge-transfer resistance of the main product (0.7 Ω) was much smaller than the compared sample (2.41 Ω), which is correlated with electron transfer kinetics of redox reactions near the surface of electrolyte and electrode. According to the previous studies, such low charge transfer resistance was ascribed to plentiful electrochemical active sites and large cavities of micropores of the binary Ni_9S_8/MoS_2 shell and interplayed with mass transport during the charge transport process.[388] It also should be mentioned that due to the lower electronegativity of sulfur than oxygen, bimetallic sulfides created a flexible space preventing the decomposition of structure caused by the elongation between atoms and made it easy for electrons to transport in the structure.[389] Consequently, after cycling, the resistance increasement of $NiMoO_4$@Ni_9S_8/MoS_2 from 0.7 Ω to 1.23 Ω (**Figure S5.8E**). By comparison, $NiMoO_4$ displayed the larger charge-transfer resistance due to the collapsing structure in **Figure S5.8F**. Depending on the above outcomes, the remarkable properties of $NiMoO_4$@Ni_9S_8/MoS_2 nanorods were credited to the subsequent explanations: (i) special core-shell architecture of nanorods protected the structure from collapsing and corrosion, serving as the bridge for outer metal sulfides and inner core leading to the high conductivity and supplied sufficient contact area between electrolyte and electrode; (ii) the ultrathin

nanoflake of Ni_9S_8/MoS_2 provided more active sites and increased surface area and multiple micro/mesopores which provided the massive ion transport channels; (iii) the synergistic effect of typical heterostructure also favored the transport of ion and electrons.

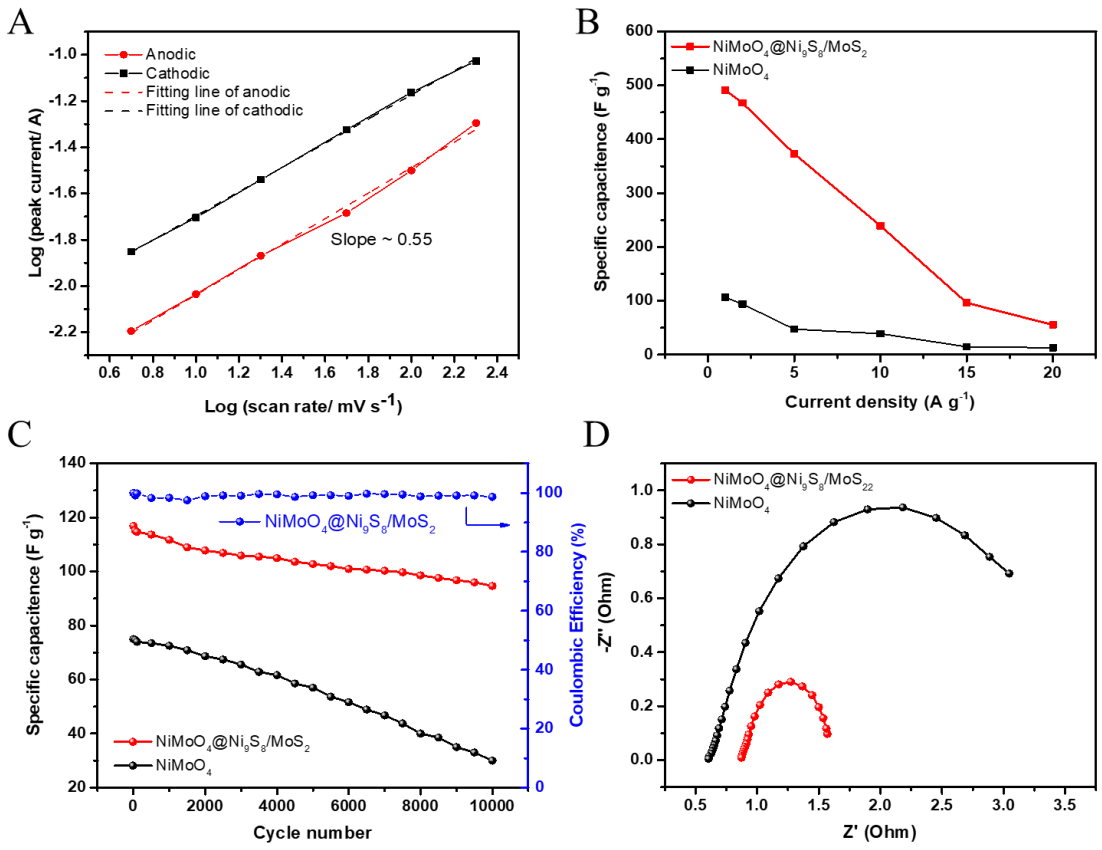

Figure 5.8 (A) Linear fitting plots of $NiMoO_4@Ni_9S_8/MoS_2$ for the log (peak current) and log (scan rate) for the cathodic and anodic peaks based on CV plots; (B) Specific capacitance of $NiMoO_4@Ni_9S_8/MoS_2$ and $NiMoO_4$ at different current densities; (C) Cycling property and coulombic efficiency of $NiMoO_4@Ni_9S_8/MoS_2$ and $NiMoO_4$ at a current density of 10 A g^{-1}; (D) Comparison of Nyquist plots of $NiMoO_4@Ni_9S_8/MoS_2$ and $NiMoO_4$.

Table 5.1 Comparison of the performances of this work and other reported work in alkaline electrolytes.

Electrode material	Electrolyte	Specific capacitance at the given current density	Cycle number and retention	Ref
$NiMoO_4$@Ni_9S_8/MoS_2 nanorods	6 M KOH	373.4 F g^{-1} at 10 A g^{-1}	81.0 %, 10,000 cycles at 10 A g^{-1}	This work
C@MoS_2/Ni_3S_4	2M KOH	604.4 F g^{-1} (10 A g^{-1})	80.1%, 10,000 cycles at 20 A g^{-1}	390
(Ni,Mo)S_2/G composite	2M KOH	2379 F g^{-1} at 1 A g^{-1}	60.7%, 10,000 cycles at 100 A g^{-1}	377
NiS_2@MoS_2	6 M KOH	848.2 C g^{-1} at 1 A g^{-1}	83.1%, 10,000 cycles at 10 A g^{-1}	391
Ni2Mo1	3 M KOH	169.44 mAh g^{-1} at 1 A g^{-1}	88.24%, 8000 cycles at 10 A g^{-1}	291
$NiMoO_4$@MoS_2	6 M KOH	2246.7 F g^{-1} at 1 A g^{-1}	88.4%, 5000 cycles at 5 A g^{-1}	392
NiS_2 rods	6 M KOH	1020.2 F g^{-1} at 1 A g^{-1}	84.1%, 4000 cycles at 2 A g^{-1}	383
NMS/CNT	3 M KOH	108 F g^{-1} at 0.5 A g^{-1}	100%, 10,000 cycles at 5 A g^{-1}	379
1-D $NiMoO_4$ nanostructures	1.0 M KOH	1335 F g^{-1} at 1 A g^{-1}	80.1%, 3000 cycles at 5 A g^{-1}	358
$NiMoO_4$ nanostructure	6 M KOH	1475 F g^{-1} at 1 A g^{-1}	87.9%, 5000 cycles at 20 A g^{-1}	384
$NiMoO_4$/Ni_3S_2 nanohybrid	3 M KOH	1195.7 C g^{-1} at 0.5 mA cm^{-2}	97.3%, 10,000 cycles, at 5 mA cm^{-2}	393

5.2.4. Conclusion

In conclusion, special core-shell $NiMoO_4$@Ni_9S_8/MoS_2 hetero-structured was converted from Mo/Ni precursor by a facile hydrothermal process and followed by sulfurization, which worked as an efficient electrode for supercapacitor. It unveiled unsurpassed specific capacity of 373.4 F g^{-1} at 10 A g^{-1}. Furthermore, the hybrid electrode remained excellent durability at 81.0 % after 10000 charge/discharge cycles. Such excellent electrochemical property was ascribed to special porous core-shell structure, increased surface area and ample active sites. This work demonstrated a facile method to design the hierarchical structure nanomaterials for supercapacitors.

Above all, we further explore the transition metal sulfides-based nanomaterials in energy storage area and investigate their morphology, structure, and electrochemical performance. It's found that all the nanomaterials show excellent performance and there is strong relationship between structure design and electrochemical performance. The superior performance prove their possibilities to be utilized in a wide-ranging application.

Chapter 6 Conclusion and Future Work

6.1. Conclusion and Contributions

In this study of designing transition metal-based nanomaterials for energy conversion and storage. We have summarized the current limitation and proposed three types of novel nanomaterials for multi-applications.

In chapter 3, we introduced bimetallic CoNi alloy nanoparticles embedded in pomegranate-like nitrogen-doped carbon spheres (N-CoNi/PCS) by the facile hydrothermal and calcination process. By conducting the different characterizations, we know that N-CoNi/PCS forming pomegranate-like configuration with high surface area is favorable for ion transport. Then we further investigate its electrochemical behavior, it displays a half-wave potential of 0.80 V (*vs.* RHE) for ORR with a limit current density of -5.2 mA cm^{-2} while a low overpotential of 540 mV for OER with excellent durability. By combining the study of structural characterization and electrochemical investigation, we have a rough understanding of the importance of structural design associated with the excellent electrochemical performance. Hence, beside metal alloys, in section 4.2, we also designed a unique nanostructure of N and S codoped porous carbon (N,S-Co/Zn-ZIF) derived from bimetallic ZIFs via precipitation and annealing procedure as electrocatalyst for oxygen reactions. Such electrocatalysts possess a well-defined porous dodecahedron morphology and exhibits outstanding OER and ORR electrocatalytic performance. Encouraged by the above results, we further investigated the transitional metal sulfides for water splitting. Hence, in section 4.3, Ni_9S_8/MoS_2 nanosheets decorated $NiMoO_4$ nanorods heterostructure was developed by hydrothermal and sulfurization as electrocatalyst for water splitting. By different types of characterization, the resulting hierarchical nanoarchitecture with outer Ni_9S_8/MoS_2 nanosheets shell on the inner $NiMoO_4$ core forms the rough surface acting as active sites. The porous structure provides plentiful charge transportation channels in continuous heterointerfaces. It's found out that such nanomaterials also present a high performance with low overpotentials of 190 and 360 mV for HER and OER in alkaline solution. Based on the above results, we have successfully designed the transition metal-based nanomaterials for energy conversion.

Encouraged by the excellent results, we further investigate the performance of above two types of materials applied in energy storage. First, we conducted the N,S-codoped carbon

dodecahedron/transition metal sulfides (N,S-Co/Zn@CN) which is the same material as the electrocatalyst in section 4.2. Surprisingly, such nanocomposites with rough surface area present high-performance Li-ion intercalation with superior initial reversible capacity of 938.2 mA h g^{-1} with a high-capacity retention of 65.6% after 100 cycles at 150mA g^{-1}. Based on these, it's known that this type of nanomaterial realized the goal of multi-functionalities. It can be used as both electrocatalysts and anode electrodes for Li-ion batteries based on the different mechanisms. It also verifies that transition metal sulfides have the ability as electrode for energy storage. Hence, we further investigate the hetero-architectured core-shell $NiMoO_4$@Ni_9S_8/MoS_2 nanorods as electrode for supercapacitor. It should be noted that these nanorods are also the same material as electrocatalysts in section 4.3. By conducting its electrochemical performance, it's found that the nanorods unveil unsurpassed specific capacity of 373.4 F g^{-1} at 10 A g^{-1}. Furthermore, the hybrid electrode remained excellent durability at 81.0 % after 10000 charge/discharge cycles. Such excellent electrochemical property was ascribed to a special porous core-shell structure, increased surface area and ample active sites through different characterizations.

Based on these, we have successfully achieved the research objectives and the contributions in this research could be listed by the following points:

1. We have designed three types of transition metal-based nanomaterials (bimetallic alloy nanoparticles embedded in carbon spheres; N,S-codoped carbon dodecahedron/sulfides composites; Ni_9S_8/MoS_2 nanosheets decorated $NiMoO_4$ nanorods heterostructure) for five different applications according to the design strategies proposed in methodology part.
2. By comprehensive study of their morphology and structure such as composition, pores/ surface area and valence state, we have confirmed the successful design and the strategies are effective. Since all the materials are prepared by hydrothermal process and calcination process, it proves that we have achieved the goal of economic synthesis.
3. Next, we studied the electrochemical performance of all the materials and all of them yield excellent performance according to different applications.
4. Then, we investigated the relationship between the morphology and structure and electrochemical performance. We found that there is a strong correlation between them and different compositions work differently in each application. For example, porous structures not only provide active sites for electrocatalyst but also are favorable for Li-

ion insertion/extraction. More dimensional structures not only enlarge the surface area but also serve as buffer layer relieving the volume change and collapsing. In addition, bimetallic doping/heteroatom doping can create the synergistic effect and further optimize the electronic configuration, contributing to excellent performance both in energy conversion and storage.

5. Thus, based on these, we found that our materials can be utilized in different area. We have accomplished the objective of "one material for multi-applications" and offer an opportunity for designing the high performance and economic materials for wide utilizations in the promising future.

6.2. Recommendations for the Further Studies

Based on the findings of this research, the following recommendations can be made to further design of transition metal-based nanomaterials for energy conversion and storage:

- We have conducted the fundamental study of electrochemical performances of transition metal-based materials. Based on the findings, practical applications such as assembling with metal-air batteries for electrocatalyst, and supercapacitors for electrode materials should be encouraged in the future to verify their capabilities for large-scale application.
- Although we have studied transition metal alloy, sulfides, unfortunately that we couldn't investigate the metal phosphides and other types of materials. The working and structural mechanism of metal phosphides are still unclear and electrochemical performance of them are still not satisfied. Hence, more studies should be devoted to improving their performance.
- The deeper study of structure design and morphology control in order to improve electrochemical performance should be forwarded. By studying their working mechanisms thorough more powerful characterization techniques combining the theoretical calculations such as DFT, a more in-depth understanding and design of superior materials could be achieved.
- For energy storage area, we only investigate the performance of electrode materials in Li-ion batteries and supercapacitors. In the future study, more applications such as Na-ion

battery, Li-S batteries and K-ion batteries are also recommended as there are still a lot of challenges in those types of batteries need to be solved.

- Although we have attained the goal of “multi-applications”, the electrochemical performance of materials for energy storage are still not superior and fail the requirement of high density and capacity. Hence, more studies should be contributed in the future to improve the performance and obtain the “super material” for multi-applications.

Bibliography

1. Zhong, Y.; Xia, X.; Shi, F.; Zhan, J.; Tu, J.; Fan, H. J., Transition Metal Carbides and Nitrides in Energy Storage and Conversion. *Adv. Sci.* **2016,** *3* (5), 1500286.

2. Poizot, P.; Dolhem, F., Clean Energy New Deal for a Sustainable World: From Non-CO_2 Generating Energy Sources to Greener Electrochemical Storage Devices. *Energy Environ. Sci.* **2011,** *4* (6), 2003.

3. Wang, C.; Yu, Y.; Niu, J.; Liu, Y.; Bridges, D.; Liu, X.; Pooran, J.; Zhang, Y.; Hu, A., Recent Progress of Metal-Air Batteries-a Mini Review. *Appl. Sci.* **2019,** *9* (14), 2787.

4. Gu, P.; Zheng, M.; Zhao, Q.; Xiao, X.; Xue, H.; Pang, H., Rechargeable Zinc-Air Batteries: A Promising Way to Green Energy. *J. Mater. Chem. A* **2017,** *5* (17), 7651-7666.

5. Zhang, J.; Zhou, Q.; Tang, Y.; Zhang, L.; Li, Y., Zinc-Air Batteries: Are They Ready for Prime Time? *Chem. Sci.* **2019,** *10* (39), 8924-8929.

6. Yang, D.; Zhang, L.; Yan, X.; Yao, X., Recent Progress in Oxygen Electrocatalysts for Zinc-Air Batteries. *Small Methods* **2017,** *1* (12), 1700209.

7. Cheng, F.; Chen, J., Metal-Air Batteries: From Oxygen Reduction Electrochemistry to Cathode Catalysts. *Chem Soc Rev* **2012,** *41* (6), 2172-92.

8. Wang, Z. L.; Xu, D.; Xu, J. J.; Zhang, X. B., Oxygen Electrocatalysts in Metal-Air Batteries: From Aqueous to Nonaqueous Electrolytes. *Chem Soc Rev* **2014,** *43* (22), 7746-86.

9. Gong, M.; Dai, H., A Mini Review of Nife-Based Materials as Highly Active Oxygen Evolution Reaction Electrocatalysts. *Nano Res.* **2014,** *8* (1), 23-39.

10. Shi, Y.; Zhang, B., Recent Advances in Transition Metal Phosphide Nanomaterials: Synthesis and Applications in Hydrogen Evolution Reaction. *Chem Soc Rev* **2016,** *45* (6), 1529-41.

11. Dou, S.; Wang, X.; Wang, S., Rational Design of Transition Metal-Based Materials for Highly Efficient Electrocatalysis. *Small Methods* **2019,** *3* (1), 1800211.

12. Yan, Y.; Xia, B. Y.; Zhao, B.; Wang, X., A Review on Noble-Metal-Free Bifunctional Heterogeneous Catalysts for Overall Electrochemical Water Splitting. *J. Mater. Chem. A* **2016,** *4* (45), 17587-17603.

13. Wang, Y.; Kong, B.; Zhao, D.; Wang, H.; Selomulya, C., Strategies for Developing Transition Metal Phosphides as Heterogeneous Electrocatalysts for Water Splitting. *Nano. Today.* **2017,** *15*, 26-55.

14. Zhu, X.; Dai, J.; Li, L.; Zhao, D.; Wu, Z.; Tang, Z.; Ma, L. J.; Chen, S., Hierarchical Carbon Microflowers Supported Defect-Rich Co_3S_4 Nanoparticles: An Efficient Electrocatalyst for Water Splitting. *Carbon* **2020,** *160*, 133-144.

15. Goodenough, J. B., Electrochemical Energy Storage in a Sustainable Modern Society. *Energy Environ. Sci.* **2014,** *7* (1), 14-18.

16. Bhatt, M. D.; Lee, J. Y., High Capacity Conversion Anodes in Li-Ion Batteries: A Review. *Int. J. Hydrog. Energy* **2019,** *44* (21), 10852-10905.

17. Broussely, M.; Archdale, G., Li-ion Batteries and Portable Power Source Prospects for the Next 5-10 Years. *J. Power Sources* **2004,** *136* (2), 386-394.

18. Nitta, N.; Wu, F.; Lee, J. T.; Yushin, G., Li-Ion Battery Materials: Present and Future. *Mater. Today* **2015,** *18* (5), 252-264.

19. Goodenough, J. B.; Kim, Y., Challenges for Rechargeable Li Batteries. *Chem. Mater.* **2009,** *22* (3), 587-603.

20. Demirocak, D.; Srinivasan, S.; Stefanakos, E., A Review on Nanocomposite Materials for Rechargeable Li-Ion Batteries. *Appl. Sci.* **2017,** *7* (7), 731.

21. Hausbrand, R.; Cherkashinin, G.; Ehrenberg, H.; Gröting, M.; Albe, K.; Hess, C.; Jaegermann, W., Fundamental Degradation Mechanisms of Layered Oxide Li-ion Battery Cathode Materials: Methodology, Insights and Novel Approaches. *Mater. Sci. Eng.* **2015,** *192*, 3-25.

22. de las Casas, C.; Li, W., A Review of Application of Carbon Nanotubes for Lithium Ion Battery Anode Material. *J. Power Sources* **2012,** *208*, 74-85.

23. Scrosati, B.; Garche, J., Lithium Batteries: Status, Prospects and Future. *J. Power Sources* **2010,** *195* (9), 2419-2430.

24. Wu, R.; Wang, D. P.; Rui, X.; Liu, B.; Zhou, K.; Law, A. W.; Yan, Q.; Wei, J.; Chen, Z., In-Situ Formation of Hollow Hybrids Composed of Cobalt Sulfides Embedded within Porous Carbon Polyhedra/Carbon Nanotubes for High-Performance Lithium-Ion Batteries. *Adv. Mater.* **2015,** *27* (19), 3038-44.

25. Wu, F.; Yushin, G., Conversion Cathodes for Rechargeable Lithium and Lithium-Ion Batteries. *Energy Environ. Sci.* **2017,** *10* (2), 435-459.

26. Ahn, W.; Lee, D. U.; Li, G.; Feng, K.; Wang, X.; Yu, A.; Lui, G.; Chen, Z., Highly Oriented Graphene Sponge Electrode for Ultra High Energy Density Lithium Ion Hybrid Capacitors. *ACS Appl Mater Interfaces* **2016,** *8* (38), 25297-305.

27. Afif, A.; Rahman, S. M. H.; Tasfiah Azad, A.; Zaini, J.; Islan, M. A.; Azad, A. K., Advanced Materials and Technologies for Hybrid Supercapacitors for Energy Storage - a Review. *J. Energy Storage* **2019,** *25*, 100852.

28. Zhang, L. L.; Zhou, R.; Zhao, X. S., Graphene-Based Materials as Supercapacitor Electrodes. *J. Mater. Chem.* **2010,** *20* (29), 5983.

29. Wang, T.; Chen, H. C.; Yu, F.; Zhao, X. S.; Wang, H., Boosting the Cycling Stability of Transition Metal Compounds-Based Supercapacitors. *Energy Storage Mater.* **2019,** *16*, 545-573.

30. Cai, D.; Wang, D.; Liu, B.; Wang, Y.; Liu, Y.; Wang, L.; Li, H.; Huang, H.; Li, Q.; Wang, T., Comparison of the Electrochemical Performance of $NiMoO_4$ Nanorods and Hierarchical Nanospheres for Supercapacitor Applications. *ACS Appl Mater Interfaces* **2013,** *5* (24), 12905-10.

31. Zhang, J.; Zhao, X. S., On the Configuration of Supercapacitors for Maximizing Electrochemical Performance. *ChemSusChem* **2012,** *5* (5), 818-41.

32. González, A.; Goikolea, E.; Barrena, J. A.; Mysyk, R., Review on Supercapacitors: Technologies and Materials. *Renewable Sustainable Energy Rev.* **2016,** *58*, 1189-1206.

33. Augustyn, V.; Simon, P.; Dunn, B., Pseudocapacitive Oxide Materials for High-Rate Electrochemical Energy Storage. *Energy Environ. Sci.* **2014,** *7* (5), 1597.

34. Wang, Y.; Song, Y.; Xia, Y., Electrochemical Capacitors: Mechanism, Materials, Systems, Characterization and Applications. *Chem Soc Rev* **2016,** *45* (21), 5925-5950.

35. Gao, Q.; Zhang, W.; Shi, Z.; Yang, L.; Tang, Y., Structural Design and Electronic Modulation of Transition-Metal-Carbide Electrocatalysts toward Efficient Hydrogen Evolution. *Adv. Mater.* **2019,** *31* (2), e1802880.

36. Anantharaj, S.; Ede, S. R.; Sakthikumar, K.; Karthick, K.; Mishra, S.; Kundu, S., Recent Trends and Perspectives in Electrochemical Water Splitting with an Emphasis on Sulfide, Selenide, and Phosphide Catalysts of Fe, Co, and Ni: A Review. *ACS Catal.* **2016,** *6* (12), 8069-8097.

37. Hu, C.; Dai, L., Doping of Carbon Materials for Metal-Free Electrocatalysis. *Adv. Mater.* **2019,** *31* (7), e1804672.

38. Chen, Z.; Duan, X.; Wei, W.; Wang, S.; Ni, B. J., Recent Advances in Transition Metal-Based Electrocatalysts for Alkaline Hydrogen Evolution. *J. Mater. Chem. A* **2019,** *7* (25), 14971-15005.

39. Zou, X.; Zhang, Y., Noble Metal-Free Hydrogen Evolution Catalysts for Water Splitting. *Chem Soc Rev* **2015,** *44* (15), 5148-80.

40. Jiao, Y.; Zheng, Y.; Jaroniec, M.; Qiao, S. Z., Design of Electrocatalysts for Oxygen- and Hydrogen-Involving Energy Conversion Reactions. *Chem Soc Rev* **2015,** *44* (8), 2060-86.

41. Guan, S.; Fu, X.; Lao, Z.; Jin, C.; Peng, Z., NiS-MoS_2 Hetero-Nanosheet Array Electrocatalysts for Efficient Overall Water Splitting. *Sustainable Energy Fuels* **2019,** *3* (8), 2056-2066.

42. Xu, X.; Zhong, W.; Zhang, L.; Liu, G.; Du, Y., Synergistic Effect of MoS_2 and Ni_9S_8 Nanosheets as an Efficient Electrocatalyst for Hydrogen Evolution Reaction. *J Colloid Interface Sci* **2019,** *556*, 24-32.

43. Zhang, Y.; Fan, X.; Jian, J.; Yu, D.; Zhang, Z.; Dai, L., A General Polymer-Assisted Strategy Enables Unexpected Efficient Metal-Free Oxygen-Evolution Catalysis on Pure Carbon Nanotubes. *Energy Environmental Science* **2017,** *10* (11), 2312-2317.

44. Fu, Y.; Yu, H. Y.; Jiang, C.; Zhang, T. H.; Zhan, R.; Li, X.; Li, J. F.; Tian, J. H.; Yang, R., Nico Alloy Nanoparticles Decorated on N-Doped Carbon Nanofibers as Highly Active and Durable Oxygen Electrocatalyst. *Adv. Funct. Mater.* **2018,** *28* (9), 1705094.

45. Cai, D.; Wang, D.; Liu, B.; Wang, L.; Liu, Y.; Li, H.; Wang, Y.; Li, Q.; Wang, T., Three-Dimensional Co_3O_4@$NiMoO_4$ Core/Shell Nanowire Arrays on Ni Foam for Electrochemical Energy Storage. *ACS Appl Mater Interfaces* **2014,** *6* (7), 5050-5.

46. Bing, Y.; Liu, H.; Zhang, L.; Ghosh, D.; Zhang, J., Nanostructured Pt-Alloy Electrocatalysts for Pem Fuel Cell Oxygen Reduction Reaction. *Chem Soc Rev* **2010,** *39* (6), 2184-202.

47. Xia, B. Y.; Ng, W. T.; Wu, H. B.; Wang, X.; Lou, X. W., Self-Supported Interconnected Pt Nanoassemblies as Highly Stable Electrocatalysts for Low-Temperature Fuel Cells. *Angew. Chem. Int. Ed. Engl.* **2012,** *51* (29), 7213-7216.

48. Maksimuk, S.; Yang, S.; Peng, Z.; Yang, H., Synthesis and Characterization of Ordered Intermetallic PtPb Nanorods. *J. Am. Chem. Soc.* **2007,** *129* (28), 8684-8685.

49. Liang, H. W.; Cao, X.; Zhou, F.; Cui, C. H.; Zhang, W. J.; Yu, S. H., A Free-Standing Pt-Nanowire Membrane as a Highly Stable Electrocatalyst for the Oxygen Reduction Reaction. *Adv. Mater.* **2011,** *23* (12), 1467-71.

50. Wang, D.; Luo, H.; Kou, R.; Gil, M. P.; Xiao, S.; Golub, V. O.; Yang, Z.; Brinker, C. J.; Lu, Y., A General Route to Macroscopic Hierarchical 3D Nanowire Networks. *Angew. Chem.* **2004,** *116* (45), 6295-6299.

51. Subbaraman, R.; Tripkovic, D.; Chang, K. C.; Strmcnik, D.; Paulikas, A. P.; Hirunsit, P.; Chan, M.; Greeley, J.; Stamenkovic, V.; Markovic, N. M., Trends in Activity for the Water Electrolyser Reactions on 3D M(Ni,Co,Fe,Mn) Hydr(Oxy)Oxide Catalysts. *Nat. Mater.* **2012,** *11* (6), 550-7.

52. Kim, J.; Lee, Y.; Sun, S., Structurally Ordered Fept Nanoparticles and Their Enhanced Catalysis for Oxygen Reduction Reaction. *J. Am. Chem. Soc*. **2010,** *132* (14), 4996-4997.

53. Venarusso, L. B.; Bettini, J.; Maia, G., Catalysts for Oxygen Reduction Reaction Based on Nanocrystals of a Pt or Pt-Pd Alloy Shell Supported on a Au Core. *J. Solid State Electrochem.* **2016,** *20* (6), 1753-1764.

54. Tahir, M.; Pan, L.; Idrees, F.; Zhang, X.; Wang, L.; Zou, J.-J.; Wang, Z. L., Electrocatalytic Oxygen Evolution Reaction for Energy Conversion and Storage: *Nano Energy* **2017,** *37*, 136-157.

55. Pi, Y.; Zhang, N.; Guo, S.; Guo, J.; Huang, X., Ultrathin Laminar Ir Superstructure as Highly Efficient Oxygen Evolution Electrocatalyst in Broad Ph Range. *Nano. Lett.* **2016,** *16* (7), 4424-4430.

56. Yao, Y.; Hu, S.; Chen, W.; Huang, Z.-Q.; Wei, W.; Yao, T.; Liu, R.; Zang, K.; Wang, X.; Wu, G.; Yuan, W.; Yuan, T.; Zhu, B.; Liu, W.; Li, Z.; He, D.; Xue, Z.; Wang, Y.; Zheng, X.; Dong, J.; Chang, C.-R.; Chen, Y.; Hong, X.; Luo, J.; Wei, S.; Li, W.-X.; Strasser, P.; Wu, Y.; Li, Y., Engineering the Electronic Structure of Single Atom Ru Sites Via Compressive Strain Boosts Acidic Water Oxidation Electrocatalysis. *Nat. Catal.* **2019,** *2*, 304-313.

57. Cherevko, S.; Geiger, S.; Kasian, O.; Kulyk, N.; Grote, J.-P.; Savan, A.; Shrestha, B. R.; Merzlikin, S.; Breitbach, B.; Ludwig, A.; Mayrhofer, K. J. J., Oxygen and Hydrogen Evolution Reactions on Ru, RuO_2 , Ir, and IrO_2 Thin Film Electrodes in Acidic and Alkaline Electrolytes: A Comparative Study on Activity and Stability. *Catal. Today* **2016,** *262*, 170-180.

58. Ibrahim, K. B.; Tsai, M. C.; Chala, S. A.; Berihun, M. K.; Kahsay, A. W.; Berhe, T. A.; Su, W. N.; Hwang, B. J., A Review of Transition Metal-Based Bifunctional Oxygen Electrocatalysts. *J. Chin. Chem. Soc.* **2019,** *66* (8), 829-865.

59. Allado, K.; Liu, M.; Jayapalan, A.; Arvapalli, D.; Nowlin, K.; Wei, J., Binary MnO_2/Co_3O_4 Metal Oxides Wrapped on Superaligned Electrospun Carbon Nanofibers as Binder Free Supercapacitor Electrodes. *Energy Fuels* **2021**.

60. Osgood, H.; Devaguptapu, S. V.; Xu, H.; Cho, J.; Wu, G., Transition Metal (Fe, Co, Ni, and Mn) Oxides for Oxygen Reduction and Evolution Bifunctional Catalysts in Alkaline Media. *Nano. Today.* **2016,** *11* (5), 601-625.

61. Yang, J.; Cooper, J. K.; Toma, F. M.; Walczak, K. A.; Favaro, M.; Beeman, J. W.; Hess, L. H.; Wang, C.; Zhu, C.; Gul, S.; Yano, J.; Kisielowski, C.; Schwartzberg, A.; Sharp, I. D., A Multifunctional Biphasic Water Splitting Catalyst Tailored for Integration with High-Performance Semiconductor Photoanodes. *Nat. Mater.* **2017,** *16* (3), 335-341.

62. Risch, M.; Ringleb, F.; Kohlhoff, M.; Bogdanoff, P.; Chernev, P.; Zaharieva, I.; Dau, H., Water Oxidation by Amorphous Cobalt-Based Oxides: In Situ Tracking of Redox Transitions and Mode of Catalysis. *Energy Environ. Sci.* **2015,** *8* (2), 661-674.

63. Yang, Y.; Fei, H.; Ruan, G.; Xiang, C.; Tour, J. M., Efficient Electrocatalytic Oxygen Evolution on Amorphous Nickel-Cobalt Binary Oxide Nanoporous Layers. *ACS. nano.* **2014,** *8* (9), 9518-9523.

64. Park, M. G.; Lee, D. U.; Seo, M. H.; Cano, Z. P.; Chen, Z., 3D Ordered Mesoporous Bifunctional Oxygen Catalyst for Electrically Rechargeable Zinc-Air Batteries. *Small* **2016,** *12* (20), 2707-14.

65. Li, G.; Wang, X.; Fu, J.; Li, J.; Park, M. G.; Zhang, Y.; Lui, G.; Chen, Z., Pomegranate-Inspired Design of Highly Active and Durable Bifunctional Electrocatalysts for Rechargeable Metal-Air Batteries. *Angew. Chem. Int. Ed. Engl.* **2016,** *55* (16), 4977-82.

66. Fominykh, K.; Feckl, J. M.; Sicklinger, J.; Döblinger, M.; Böcklein, S.; Ziegler, J.; Peter, L.; Rathousky, J.; Scheidt, E.-W.; Bein, T.; Fattakhova-Rohlfing, D., Ultrasmall Dispersible Crystalline Nickel Oxide Nanoparticles as High-Performance Catalysts for Electrochemical Water Splitting. *Adv. Funct. Mater.* **2014,** *24* (21), 3123-3129.

67. Jiao, Y.; Hong, W.; Li, P.; Wang, L.; Chen, G., Metal-Organic Framework Derived Ni/NiO Micro-Particles with Subtle Lattice Distortions for High-Performance Electrocatalyst and Supercapacitor. *Appl. Catal., B* **2019,** *244*, 732-739.

68. Gorlin, Y.; Jaramillo, T. F., A Bifunctional Nonprecious Metal Catalyst for Oxygen Reduction and Water Oxidation. *J. Am. Chem. Soc.* **2010,** *132* (39), 13612-13614.

69. Meng, Y.; Song, W.; Huang, H.; Ren, Z.; Chen, S.-Y.; Suib, S. L., Structure-Property Relationship of Bifunctional MnO_2 Nanostructures: Highly Efficient, Ultra-Stable Electrochemical Water Oxidation and Oxygen Reduction Reaction Catalysts Identified in Alkaline Media. *J. Am. Chem. Soc.* **2014,** *136* (32), 11452-11464.

70. Selvakumar, K.; Senthil Kumar, S. M.; Thangamuthu, R.; Kruthika, G.; Murugan, P., Development of Shape-Engineered A-MnO_2 Materials as Bi-Functional Catalysts for Oxygen Evolution Reaction and Oxygen Reduction Reaction in Alkaline Medium. *Int. J. Hydrog. Energy* **2014,** *39* (36), 21024-21036.

71. Fang, X.; Li, J.; Huang, K.; Liu, S.; Huang, C.; Zhuang, S.; Zhang, J., Synthesis and Electrochemical Properties of K-Doped $LiFePO_4$/C Composite as Cathode Material for Lithium-Ion Batteries. *J. Solid State Electrochem.* **2011,** *16* (2), 767-773.

72. Malavasi, L.; Fisher, C. A.; Islam, M. S., Oxide-Ion and Proton Conducting Electrolyte Materials for Clean Energy Applications: Structural and Mechanistic Features. *Chem Soc Rev* **2010,** *39* (11), 4370-87.

73. Yin, J.; Li, Y.; Lv, F.; Fan, Q.; Zhao, Y. Q.; Zhang, Q.; Wang, W.; Cheng, F.; Xi, P.; Guo, S., NiO/CoN Porous Nanowires as Efficient Bifunctional Catalysts for Zn-Air Batteries. *ACS. nano.* **2017,** *11* (2), 2275-2283.

74. Song, W.; Ren, Z.; Chen, S. Y.; Meng, Y.; Biswas, S.; Nandi, P.; Elsen, H. A.; Gao, P. X.; Suib, S. L., Ni- and Mn-Promoted Mesoporous Co_3O_4: A Stable Bifunctional Catalyst with Surface-Structure-Dependent Activity for Oxygen Reduction Reaction and Oxygen Evolution Reaction. *ACS Appl Mater Interfaces* **2016,** *8* (32), 20802-13.

75. Deng, D.; Tian, Y.; Li, H.; Xu, L.; Qian, J.; Pang, J.; Wang, B.; Zhang, Q.; Li, H., Nico Alloy Nanoparticles Encapsulated in Multi-Dimensional N-Doped Carbon Architecture as Efficient Bifunctional Catalyst for Rechargeable Zinc-Air Batteries. *J. Alloys Compd.* **2019,** *797*, 1041-1049.

76. Ma, X.; Chai, H.; Cao, Y.; Xu, J.; Wang, Y.; Dong, H.; Jia, D.; Zhou, W., An Effective Bifunctional Electrocatalysts: Controlled Growth of CoFe Alloy Nanoparticles Supported on N-Doped Carbon Nanotubes. *J Colloid Interface Sci* **2018,** *514*, 656-663.

77. Li, T.; Luo, G.; Liu, K.; Li, X.; Sun, D.; Xu, L.; Li, Y.; Tang, Y., Encapsulation of Ni_3Fe Nanoparticles in N-Doped Carbon Nanotube-Grafted Carbon Nanofibers as High-Efficiency Hydrogen Evolution Electrocatalysts. *Adv. Funct. Mater.* **2018,** *28* (51), 1805828.

78. Staszak-Jirkovský, J.; Malliakas, Christos D.; Lopes, Pietro P.; Danilovic, N.; Kota, Subrahmanyam S.; Chang, K. C.; Genorio, B.; Strmcnik, D.; Stamenkovic, Vojislav R.; Kanatzidis, M. G.; Markovic, N. M., Design of Active and Stable Co-Mo-Sx Chalcogels as Ph-Universal Catalysts for the Hydrogen Evolution Reaction. *Nat. materials* **2016,** *15* (2), 197-203.

79. Yang, Y.; Fei, H.; Ruan, G.; Xiang, C.; Tour, J. M., Edge-Oriented MoS_2 Nanoporous Films as Flexible Electrodes for Hydrogen Evolution Reactions and Supercapacitor Devices. *Adv. Mater.* **2014,** *26* (48), 8163-8168.

80. Kong, D.; Wang, H.; Cha, J. J.; Pasta, M.; Koski, K. J.; Yao, J.; Cui, Y., Synthesis of MoS_2 and $MoSe_2$ Films with Vertically Aligned Layers. *Nano. Lett.* **2013,** *13* (3), 1341-1347.

81. Yang, C.; Gao, M. Y.; Zhang, Q. B.; Zeng, J. R.; Li, X. T.; Abbott, A. P., In-Situ Activation of Self-Supported 3D Hierarchically Porous Ni_3S_2 Films Grown on Nanoporous Copper as Excellent Ph-Universal Electrocatalysts for Hydrogen Evolution Reaction. *Nano Energy* **2017,** *36*, 85-94.

82. Narasimman, R.; Waldiya, M.; K, J.; Vemuri, S. K.; Mukhopadhyay, I.; Ray, A., Self-Standing, Hybrid Three-Dimensional-Porous MoS_2/Ni_3S_2 Foam Electrocatalyst for Hydrogen Evolution Reaction in Alkaline Medium. *Int. J. Hydrog. Energy* **2021,** *46* (11), 7759-7771.

83. Long, X.; Li, G.; Wang, Z.; Zhu, H.; Zhang, T.; Xiao, S.; Guo, W.; Yang, S., Metallic Iron-Nickel Sulfide Ultrathin Nanosheets as a Highly Active Electrocatalyst for Hydrogen Evolution Reaction in Acidic Media. *J. Am. Chem. Soc.* **2015,** *137* (37), 11900-11903.

84. Jiang, J.; Lu, S.; Gao, H.; Zhang, X.; Yu, H. Q., Ternary $FeNiS_2$ Ultrathin Nanosheets as an Electrocatalyst for Both Oxygen Evolution and Reduction Reactions. *Nano Energy* **2016,** *27*, 526-534.

85. Joo, J.; Kim, T.; Lee, J.; Choi, S. I.; Lee, K., Morphology-Controlled Metal Sulfides and Phosphides for Electrochemical Water Splitting. *Adv. Mater.* **2019,** *31* (14), e1806682.

86. Weng, C. C.; Ren, J. T.; Yuan, Z. Y., Transition Metal Phosphide-Based Materials for Efficient Electrochemical Hydrogen Evolution. *ChemSusChem* **2020,** *13* (13), 3357-3375.

87. Zhang, R.; Zhang, C.; Chen, W., Fep Embedded in N, P Dual-Doped Porous Carbon Nanosheets: An Efficient and Durable Bifunctional Catalyst for Oxygen Reduction and Evolution Reactions. *J. Mater. Chem. A* **2016,** *4* (48), 18723-18729.

88. He, S.; He, S.; Gao, F.; Bo, X.; Wang, Q.; Chen, X.; Duan, J.; Zhao, C., Ni_2P@Carbon Core-Shell Nanorod Array Derived from ZIF-67-Ni: Effect of Phosphorization Temperature on Morphology, Structure and Hydrogen Evolution Reaction Performance. *Appl. Surf. Sci.* **2018,** *457*, 933-941.

89. Sun, J.; Li, S.; Zhang, Q.; Guan, J., Iron-Cobalt-Nickel Trimetal Phosphides as High-Performance Electrocatalysts for Overall Water Splitting. *Sustainable Energy Fuels* **2020,** *4* (9), 4531-4537.

90. Callejas, J. F.; Read, C. G.; Roske, C. W.; Lewis, N. S.; Schaak, R. E., Synthesis, Characterization, and Properties of Metal Phosphide Catalysts for the Hydrogen-Evolution Reaction. *Chem. Mater.* **2016,** *28* (17), 6017-6044.

91. Xie, Y.; Chen, M.; Cai, M.; Teng, J.; Huang, H.; Fan, Y.; Barboiu, M.; Wang, D.; Su, C. Y., Hollow Cobalt Phosphide with N-Doped Carbon Skeleton as Bifunctional Electrocatalyst for Overall Water Splitting. *Inorg. Chem.* **2019,** *58* (21), 14652-14659.

92. Fang, Z.; Peng, L.; Qian, Y.; Zhang, X.; Xie, Y.; Cha, J. J.; Yu, G., Dual Tuning of Ni-Co-a (a = P, Se, O) Nanosheets by Anion Substitution and Holey Engineering for Efficient Hydrogen Evolution. *J. Am. Chem. Soc.* **2018,** *140* (15), 5241-5247.

93. Mo, Q.; Zhang, W.; He, L.; Yu, X.; Gao, Q., Bimetallic Ni_2-XCo_XP/N-Doped Carbon Nanofibers: Solid-Solution-Alloy Engineering toward Efficient Hydrogen Evolution. *Appl. Catal., B* **2019,** *244*, 620-627.

94. Zhang, W.; Li, Y.; Zhou, L.; Zheng, Q.; Xie, F.; Lam, K. H.; Lin, D., Ultrathin Amorphous CoFeP Nanosheets Derived from CoFe LDHs by Partial Phosphating as Excellent Bifunctional Catalysts for Overall Water Splitting. *Electrochim. Acta* **2019,** *323*, 134595.

95. Jiang, X.; Li, Y.; He, M.; Zhou, L.; Zheng, Q.; Xie, F.; Jie, W.; Lin, D., Construction of NiFeP/CoP Nanosheets/Nanowires Hierarchical Array as Advanced Electrocatalysts for Water Oxidation. *Int. J. Hydrog. Energy* **2019,** *44* (36), 19986-19994.

96. Li, J.; Zheng, H.; Xu, C.; Su, Z.; Li, X.; Sun, J., Bimetallic Phosphides as High-Efficient Electrocatalysts for Hydrogen Generation. *Inorg. Chem.* **2021,** *60* (3), 1624-1630.

97. Fu, S.; Zhu, C.; Song, J.; Engelhard, M. H.; Li, X.; Du, D.; Lin, Y., Highly Ordered Mesoporous Bimetallic Phosphides as Efficient Oxygen Evolution Electrocatalysts. *ACS Energy. Lett* **2016,** *1* (4), 792-796.

98. Du, Y.; Qu, H.; Liu, Y.; Han, Y.; Wang, L.; Dong, B., Bimetallic CoFeP Hollow Microspheres as Highly Efficient Bifunctional Electrocatalysts for Overall Water Splitting in Alkaline Media. *Appl. Surf. Sci.* **2019,** *465*, 816-823.

99. Lin, Y.; Sun, K.; Chen, X.; Chen, C.; Pan, Y.; Li, X.; Zhang, J., High-Precision Regulation Synthesis of Fe-Doped Co_2P Nanorod Bundles as Efficient Electrocatalysts for Hydrogen Evolution in All-Ph Range and Seawater. *J. Energy Chem.* **2021,** *55*, 92-101.

100. Wen, L.; Sun, Y.; Zhang, C.; Yu, J.; Li, X.; Lyu, X.; Cai, W.; Li, Y., Cu-Doped CoP Nanorod Arrays: Efficient and Durable Hydrogen Evolution Reaction Electrocatalysts at All PH Values. *ACS Appl. Energy Mater.* **2018,** *1* (8), 3835-3842.

101. Yang, M.; Xie, J. Y.; Lin, Z. Y.; Dong, B.; Chen, Y.; Ma, X.; Wen, M. L.; Zhou, Y. N.; Wang, L.; Chai, Y.-M., N-Doped Fep Nanorods Derived from Fe-MoFs as Bifunctional Electrocatalysts for Overall Water Splitting. *Appl. Surf. Sci.* **2020,** *507*, 145096.

102. Zhang, W.; Sun, Y.; Liu, Q.; Guo, J.; Zhang, X., Vanadium and Nitrogen Co-Doped CoP Nanoleaf Array as PH-Universal Electrocatalyst for Efficient Hydrogen Evolution. *J. Alloys Compd.* **2019,** *791*, 1070-1078.

103. Yue, Y.; Liang, H., Hierarchical Micro-Architectures of Electrodes for Energy Storage. *J. Power Sources* **2015,** *284*, 435-445.

104. Liu, H.; Li, W.; Shen, D.; Zhao, D.; Wang, G., Graphitic Carbon Conformal Coating of Mesoporous TiO_2 Hollow Spheres for High-Performance Lithium Ion Battery Anodes. *J. Am. Chem. Soc.* **2015,** *137* (40), 13161-6.

105. Yi, T. F.; Jiang, L. J.; Shu, J.; Yue, C.-B.; Zhu, R. S.; Qiao, H.-B., Recent Development and Application of $Li_4Ti_5O_{12}$ as Anode Material of Lithium Ion Battery. *J. Phys. Chem. Solids.* **2010,** *71* (9), 1236-1242.

106. Balogun, M.-S.; Qiu, W.; Luo, Y.; Meng, H.; Mai, W.; Onasanya, A.; Olaniyi, T. K.; Tong, Y., A Review of the Development of Full Cell Lithium-Ion Batteries: The Impact of Nanostructured Anode Materials. *Nano Res.* **2016,** *9* (10), 2823-2851.

107. Zhang, X.; Cheng, X.; Zhang, Q., Nanostructured Energy Materials for Electrochemical Energy Conversion and Storage: A Review. *J. Energy Chem.* **2016,** *25* (6), 967-984.

108. Shen, Y.; Qian, J.; Yang, H.; Zhong, F.; Ai, X., Chemically Prelithiated Hard-Carbon Anode for High Power and High Capacity Li-Ion Batteries. *Small* **2020,** *16* (7), 1907602.

109. Yehezkel, S.; Auinat, M.; Sezin, N.; Starosvetsky, D.; Ein-Eli, Y., Bundled and Densified Carbon Nanotubes (CNT) Fabrics as Flexible Ultra-Light Weight Li-Ion Battery Anode Current Collectors. *J. Power Sources* **2016,** *312*, 109-115.

110. Li, H.; Su, Y.; Sun, W.; Wang, Y., Carbon Nanotubes Rooted in Porous Ternary Metal Sulfide@N/S-Doped Carbon Dodecahedron: Bimetal-Organic-Frameworks Derivation and Electrochemical Application for High-Capacity and Long-Life Lithium-Ion Batteries. *Adv. Funct. Mater.* **2016,** *26* (45), 8345-8353.

111. Goriparti, S.; Miele, E.; De Angelis, F.; Di Fabrizio, E.; Proietti Zaccaria, R.; Capiglia, C., Review on Recent Progress of Nanostructured Anode Materials for Li-Ion Batteries. *J. Power Sources* **2014,** *257*, 421-443.

112. Sun, Q.; Zhang, B.; Fu, Z.-W., Lithium Electrochemistry of SiO_2 Thin Film Electrode for Lithium-Ion Batteries. *Appl. Surf. Sci.* **2008,** *254* (13), 3774-3779.

113. Zhou, J.; Wang, Y.; Zhang, J.; Chen, T.; Song, H.; Yang, H. Y., Two Dimensional Layered $Co_{0.85}Se$ Nanosheets as a High-Capacity Anode for Lithium-Ion Batteries. *Nanoscale* **2016,** *8* (32), 14992-5000.

114. Mohana Reddy, A. L.; Gowda, S. R.; Shaijumon, M. M.; Ajayan, P. M., Hybrid Nanostructures for Energy Storage Applications. *Adv. Mater.* **2012,** *24* (37), 5045-64.

115. Zhang, W.-J., A Review of the Electrochemical Performance of Alloy Anodes for Lithium-Ion Batteries. *J. Power Sources* **2011,** *196* (1), 13-24.

116. Kasavajjula, U.; Wang, C.; Appleby, A. J., Nano- and Bulk-Silicon-Based Insertion Anodes for Lithium-Ion Secondary Cells. *J. Power Sources* **2007,** *163* (2), 1003-1039.

117. Gu, J.; Collins, S. M.; Carim, A. I.; Hao, X.; Bartlett, B. M.; Maldonado, S., Template-Free Preparation of Crystalline Ge Nanowire Film Electrodes Via an Electrochemical Liquid-Liquid-Solid Process in Water at Ambient Pressure and Temperature for Energy Storage. *Nano Lett* **2012,** *12* (9), 4617-23.

118. Chan, C. K.; Peng, H.; Liu, G.; McIlwrath, K.; Zhang, X. F.; Huggins, R. A.; Cui, Y., High-Performance Lithium Battery Anodes Using Silicon Nanowires. *Nat. Nanotechnol.* **2008,** *3* (1), 31-35.

119. Su, L.; Zhou, Z.; Ren, M., Core Double-Shell $Si@SiO_2@C$ Nanocomposites as Anode Materials for Li-Ion Batteries. *Chem. Commun.* **2010,** *46* (15), 2590-2.

120. Gurunathan, P.; Ette, P. M.; Ramesha, K., Synthesis of Hierarchically Porous SnO_2 Microspheres and Performance Evaluation as Li-Ion Battery Anode by Using Different Binders. *ACS Appl. Mater. Interfaces* **2014,** *6* (19), 16556-16564.

121. Wang, Z.; Chen, G.; Xia, D., Coating of Multi-Walled Carbon Nanotube with SnO_2 Films of Controlled Thickness and Its Application for Li-Ion Battery. *J. Power Sources* **2008,** *184* (2), 432-436.

122. Gong, Y.; Sun, L.; Si, H.; Zhang, Y.; Shi, Y.; Wu, L.; Gu, J.; Zhang, Y., Mno Nanorods Coated by Co-Decorated N-Doped Carbon as Anodes for High Performance Lithium Ion Batteries. *Appl. Surf. Sci.* **2020,** *504*, 144479.

123. Wu, Y.; Zhu, C.; Shu, L.; Duan, J.; Wei, D.; Xu, J.; Zhu, Z.; Li, L.; Peng, Z.; Chen, Z., Co_9S_8 Confined in Bifunctional N/S Co-Doped Carbon/Carbon with High Electrochemical Performance for Lithium-Ion Batteries. *Appl. Surf. Sci.* **2019,** *489*, 528-537.

124. Boyanov, S.; Annou, K.; Villevieille, C.; Pelosi, M.; Zitoun, D.; Monconduit, L., Nanostructured Transition Metal Phosphide as Negative Electrode for Lithium-Ion Batteries. *Ionics* **2007,** *14* (3), 183-190.

125. Yue, Y.; Han, P.; Dong, S.; Zhang, K.; Zhang, C.; Shang, C.; Cui, G., Nanostructured Transition Metal Nitride Composites as Energy Storage Material. *Chin. Sci. Bull.* **2012,** *57* (32), 4111-4118.

126. Ji, L.; Lin, Z.; Alcoutlabi, M.; Zhang, X., Recent Developments in Nanostructured Anode Materials for Rechargeable Lithium-Ion Batteries. *Energy Environ. Sci.* **2011,** *4* (8), 2682.

127. Amatucci, G. G.; Pereira, N., Fluoride Based Electrode Materials for Advanced Energy Storage Devices. *J. Fluorine Chem.* **2007,** *128* (4), 243-262.

128. Jayaramulu, K.; Dubal, D. P.; Schneemann, A.; Ranc, V.; Perez-Reyes, C.; Stráská, J.; Kment, Š.; Otyepka, M.; Fischer, R. A.; Zbořil, R., Shape-Assisted 2D MoF/Graphene Derived Hybrids as Exceptional Lithium-Ion Battery Electrodes. *Adv. Funct. Mater.* **2019,** *29* (38), 1902539.

129. Ionica, C. M.; Lippens, P. E.; Fourcade, J. O.; Jumas, J. C., Study of Li Insertion Mechanisms in Transition Metal Antimony Compounds as Negative Electrodes for Li-Ion Battery. *J. Power Sources* **2005,** *146* (1-2), 478-481.

130. Sennu, P.; Christy, M.; Aravindan, V.; Lee, Y. G.; Nahm, K. S.; Lee, Y.-S., Two-Dimensional Mesoporous Cobalt Sulfide Nanosheets as a Superior Anode for a Li-Ion Battery and a Bifunctional Electrocatalyst for the Li-O_2 System. *Chem. Mater.* **2015,** *27* (16), 5726-5735.

131. Luo, F.; Ma, D.; Li, Y.; Mi, H.; Zhang, P.; Luo, S., Hollow Co_3S_4/C Anchored on Nitrogen-Doped Carbon Nanofibers as a Free-Standing Anode for High-Performance Li-Ion Batteries. *Electrochim. Acta* **2019,** *299*, 173-181.

132. Zeng, P.; Li, J.; Ye, M.; Zhuo, K.; Fang, Z., In Situ Formation of Co_9S_8 /N-C Hollow Nanospheres by Pyrolysis and Sulfurization of ZIF-67 for High-Performance Lithium-Ion Batteries. *Chemistry* **2017,** *23* (40), 9517-9524.

133. Wang, B.; Chen, J. S.; Wu, H. B.; Wang, Z.; Lou, X. W., Quasiemulsion-Templated Formation of a-Fe_2O_3 Hollow Spheres with Enhanced Lithium Storage Properties. *J. Am. Chem. Soc.* **2011,** *133* (43), 17146-17148.

134. Li, J.; Fu, Y.; Shi, X.; Xu, Z.; Zhang, Z., Urchinlike ZnS Microspheres Decorated with Nitrogen-Doped Carbon: A Superior Anode Material for Lithium and Sodium Storage. *Chemistry* **2017,** *23* (1), 157-166.

135. Kwon, H. T.; Kim, J. H.; Jeon, K. J.; Park, C. M., Co_xP Compounds: Electrochemical Conversion/Partial Recombination Reaction and Partially Disproportionated Nanocomposite for Li-Ion Battery Anodes. *RSC Adv.* **2014,** *4* (81), 43227-43234.

136. Dangol, R.; Dai, Z.; Chaturvedi, A.; Zheng, Y.; Zhang, Y.; Dinh, K. N.; Li, B.; Zong, Y.; Yan, Q., Few-Layer $NiPS_3$ Nanosheets as Bifunctional Materials for Li-Ion Storage and Oxygen Evolution Reaction. *Nanoscale* **2018,** *10* (10), 4890-4896.

137. Huang, Y.; Peng, L.; Liu, Y.; Zhao, G.; Chen, J. Y.; Yu, G., Biobased Nano Porous Active Carbon Fibers for High-Performance Supercapacitors. *ACS Appl. Mater. Interfaces* **2016,** *8* (24), 15205-15215.

138. Song, X.; Ma, X.; Li, Y.; Ding, L.; Jiang, R., Tea Waste Derived Microporous Active Carbon with Enhanced Double-Layer Supercapacitor Behaviors. *Appl. Surf. Sci.* **2019,** *487*, 189-197.

139. Kanakaraj, S. N.; Hsieh, Y. Y.; Adusei, P. K.; Homan, B.; Fang, Y.; Zhang, G.; Mishra, S.; Gbordzoe, S.; Shanov, V., Nitrogen-Doped CNT on CNT Hybrid Fiber as a Current Collector for High-Performance Li-Ion Capacitors. *Carbon* **2019,** *149*, 407-418.

140. Wang, Q.; Liang, X.; Zhang, D.; Miao, M., A Multifunctional Supercapacitor Based on 2d Nanosheets on a Flexible Carbon Nanotube Film. *Dalton Trans* **2020,** *49* (27), 9312-9321.

141. Liu, S.; Xu, J.; Zhu, J.; Chang, Y.; Wang, H.; Liu, Z.; Xu, Y.; Zhang, C.; Liu, T., Leaf-Inspired Interwoven Carbon Nanosheet/Nanotube Homostructures for Supercapacitors with High Energy and Power Densities. *J. Mater. Chem. A* **2017,** *5* (37), 19997-20004.

142. Zhou, W.; Du, Y.; Zeng, J.; Liu, F.; Zhu, Y., A Modified "Gel-Blowing" Strategy toward the One-Step Mass Production of a 3D N-Doped Carbon Nanosheet@Carbon Nanotube Hybrid Network for Supercapacitors. *Nanoscale* **2019,** *11* (16), 7624-7633.

143. Yang, X.; He, X.; Li, Q.; Sun, J.; Lei, Z.; Liu, Z.-H., 3D Hierarchical $NiCo_2S_4$ Nanoparticles/Carbon Nanotube Sponge Cathode for Highly Compressible Asymmetric Supercapacitors. *Energy Fuels* **2021,** *35* (4), 3449-3458.

144. Cao, X.; Shi, Y.; Shi, W.; Lu, G.; Huang, X.; Yan, Q.; Zhang, Q.; Zhang, H., Preparation of Novel 3D Graphene Networks for Supercapacitor Applications. *Small* **2011,** *7* (22), 3163-3168.

145. Yan, J.; Wei, T.; Shao, B.; Ma, F.; Fan, Z.; Zhang, M.; Zheng, C.; Shang, Y.; Qian, W.; Wei, F., Electrochemical Properties of Graphene Nanosheet/Carbon Black Composites as Electrodes for Supercapacitors. *Carbon* **2010,** *48* (6), 1731-1737.

146. Islam, N.; Warzywoda, J.; Fan, Z., Edge-Oriented Graphene on Carbon Nanofiber for High-Frequency Supercapacitors. *Nano-Micro Lett.* **2017,** *10* (1), 9.

147. Lee, H.; Cho, M. S.; Kim, I. H.; Nam, J. D.; Lee, Y., RuO_x/Polypyrrole Nanocomposite Electrode for Electrochemical Capacitors. *Synth. Met.* **2010,** *160* (9), 1055-1059.

148. Wang, G.; Zhang, L.; Zhang, J., A Review of Electrode Materials for Electrochemical Supercapacitors. *Chem Soc Rev* **2012,** *41* (2), 797-828.

149. Yu, P.; Zhang, X.; Wang, D.; Wang, L.; Ma, Y., Shape-Controlled Synthesis of 3D Hierarchical MnO_2 Nanostructures for Electrochemical Supercapacitors. *Cryst. Growth Des.* **2009,** *9* (1), 528-533.

150. Xiong, S.; Yuan, C.; Zhang, X.; Xi, B.; Qian, Y., Controllable Synthesis of Mesoporous Co_3O_4 Nanostructures with Tunable Morphology for Application in Supercapacitors. *Chemistry* **2009,** *15* (21), 5320-5326.

151. Lang, J. W.; Kong, L. B.; Wu, W. J.; Luo, Y. C.; Kang, L., Facile Approach to Prepare Loose-Packed NiO Nano-Flakes Materials for Supercapacitors. *Chem. Commun.* **2008,** (35), 4213-5.

152. Guo, D.; Song, X.; Tan, L.; Ma, H.; Pang, H.; Wang, X.; Zhang, L., Metal-Organic Framework Template-Directed Fabrication of Well-Aligned Pentagon-Like Hollow Transition-Metal Sulfides as the Anode and Cathode for High-Performance Asymmetric Supercapacitors. *ACS Appl. Mater. Interfaces* **2018,** *10* (49), 42621-42629.

153. Mohammadi Zardkhoshoui, A.; Hosseiny Davarani, S. S.; Asgharinezhad, A. A., Designing Graphene-Wrapped $NiCo_2Se_4$ Microspheres with Petal-Like FeS_2 toward Flexible Asymmetric All-Solid-State Supercapacitors. *Dalton Trans.* **2019,** *48* (13), 4274-4282.

154. Wang, L.; Ma, Y.; Yang, M.; Qi, Y., Hierarchical Hollow MoS_2 Nanospheres with Enhanced Electrochemical Properties Used as an Electrode in Supercapacitor. *Electrochim. Acta* **2015,** *186*, 391-396.

155. Zhang, X.; Wu, A.; Wang, X.; Tian, C.; An, R.; Fu, H., Porous NiCoP Nanosheets as Efficient and Stable Positive Electrodes for Advanced Asymmetric Supercapacitors. *J. Mater. Chem. A* **2018,** *6* (37), 17905-17914.

156. Jin, Y.; Zhao, C.; Jiang, Q.; Ji, C., Hierarchically Mesoporous Micro/Nanostructured CoP Nanowire Electrodes for Enhanced Performance Supercapacitors. *Colloids Surf., A* **2018,** *553*, 58-65.

157. Zhang, N.; Xu, J.; Wei, B.; Li, J.; Amorim, I.; Thomas, R.; Thalluri, S. M.; Wang, Z.; Zhou, W.; Xie, S.; Liu, L., Mille-Crêpe-Like Metal Phosphide Nanocrystals/Carbon Nanotube Film Composites as High-Capacitance Negative Electrodes in Asymmetric Supercapacitors. *ACS Appl. Energy Mater.* **2020,** *3* (5), 4580-4588.

158. Chen, X.; Zhai, X.; Hou, J.; Cao, H.; Yue, X.; Li, M.; Chen, L.; Liu, Z.; Ge, G.; Guo, X., Tunable Nitrogen-Doped Delaminated 2D Mxene Obtained by Nh_3/Ar Plasma Treatment as Highly Efficient Hydrogen and Oxygen Evolution Reaction Electrocatalyst. *Chem. Eng. J.* **2021,** *420*, 129832.

159. Tan, Y.; Wang, H.; Liu, P.; Shen, Y.; Cheng, C.; Hirata, A.; Fujita, T.; Tang, Z.; Chen, M., Versatile Nanoporous Bimetallic Phosphides Towards Electrochemical Water Splitting. *Energy Environ. Sci.* **2016,** *9* (7), 2257-2261.

160. Jin, H.; Liu, X.; Chen, S.; Vasileff, A.; Li, L.; Jiao, Y.; Song, L.; Zheng, Y.; Qiao, S.-Z., Heteroatom-Doped Transition Metal Electrocatalysts for Hydrogen Evolution Reaction. *ACS Energy. Lett* **2019,** *4* (4), 805-810.

161. Ng, J. J.; Leong, K. H.; Sim, L. C.; Oh, W.-D.; Dai, C.; Saravanan, P., Chapter 10 - Environmental Remediation Using Nano-Photocatalyst under Visible Light Irradiation: The Case of Bismuth Phosphate. In *Nanomaterials for Air Remediation*, Abdeltif, A.; Assadi, A. A.; Nguyen-Tri, P.; Nguyen, T. A.; Rtimi, S., Eds. Elsevier: 2020; pp 193-207.

162. Rane, A. V.; Kanny, K.; Abitha, V. K.; Thomas, S., Chapter 5 - Methods for Synthesis of Nanoparticles and Fabrication of Nanocomposites. In *Synthesis of Inorganic Nanomaterials*, Mohan Bhagyaraj, S.; Oluwafemi, O. S.; Kalarikkal, N.; Thomas, S., Eds. Woodhead Publishing: 2018; pp 121-139.

163. Yan, Y., 7 - Tribology and Tribo-Corrosion Testing and Analysis of Metallic Biomaterials. In *Metals for Biomedical Devices*, Niinomi, M., Ed. Woodhead Publishing: 2010; pp 178-201.

164. Gladysz, G. M.; Chawla, K. K., Chapter 8 - Void Characterization. In *Voids in Materials*, Gladysz, G. M.; Chawla, K. K., Eds. Elsevier: Amsterdam, 2015; pp 157-172.

165. Chapter 3 - Methods for Assessing Surface Cleanliness. In *Developments in Surface Contamination and Cleaning, Volume 12*, Kohli, R.; Mittal, K. L., Eds. Elsevier: 2019; pp 23-105.

166. Ganesh Kumar, C.; Pombala, S.; Poornachandra, Y.; Vinod Agarwal, S., Chapter 4 - Synthesis, Characterization, and Applications of Nanobiomaterials for Antimicrobial Therapy. In *Nanobiomaterials in Antimicrobial Therapy*, Grumezescu, A. M., Ed. William Andrew Publishing: 2016; pp 103-152.

167. Thommes, M., Physical Adsorption Characterization of Nanoporous Materials. *Chem. Ing. Tech.* **2010,** *82* (7), 1059-1073.

168. Sanetuntikul, J.; Hang, T.; Shanmugam, S., Hollow Nitrogen-Doped Carbon Spheres as Efficient and Durable Electrocatalysts for Oxygen Reduction. *Chem. Commun.* **2014,** *50* (67), 9473-9476.

169. Elgrishi, N.; Rountree, K. J.; McCarthy, B. D.; Rountree, E. S.; Eisenhart, T. T.; Dempsey, J. L., A Practical Beginner's Guide to Cyclic Voltammetry. *J. Chem. Educ.* **2017,** *95* (2), 197-206.

170. Wang, H. F.; Tang, C.; Zhang, Q., A Review of Precious-Metal-Free Bifunctional Oxygen Electrocatalysts: Rational Design and Applications in Zn-Air Batteries. *Adv. Funct. Mater.* **2018,** *28* (46), 1803329.

171. Chen, Z.; Higgins, D.; Chen, Z., Nitrogen Doped Carbon Nanotubes and Their Impact on the Oxygen Reduction Reaction in Fuel Cells. *Carbon* **2010,** *48* (11), 3057-3065.

172. Cao, Z.; Hu, H.; Wu, M.; Tang, K.; Jiang, T., Planar All-Solid-State Rechargeable Zn-Air Batteries for Compact Wearable Energy Storage. *J. Mater. Chem. A* **2019,** *7* (29), 17581-17593.

173. Li, Y.; Lu, J., Metal-Air Batteries: Will They Be the Future Electrochemical Energy Storage Device of Choice? *ACS Energy. Lett* **2017,** *2* (6), 1370-1377.

174. Chen, Z.; Yu, A.; Higgins, D.; Li, H.; Wang, H.; Chen, Z., Highly Active and Durable Core-Corona Structured Bifunctional Catalyst for Rechargeable Metal-Air Battery Application. *Nano Lett* **2012,** *12* (4), 1946-52.

175. Zhou, T.; Xu, W.; Zhang, N.; Du, Z.; Zhong, C.; Yan, W.; Ju, H.; Chu, W.; Jiang, H.; Wu, C.; Xie, Y., Ultrathin Cobalt Oxide Layers as Electrocatalysts for High-Performance Flexible Zn-Air Batteries. *Adv. Mater.* **2019**, e1807468.

176. Hou, Y.-N.; Zhao, Z.; Zhang, H.; Zhao, C.; Liu, X.; Tang, Y.; Gao, Z.; Wang, X.; Qiu, J., Designed Synthesis of Cobalt Nanoparticles Embedded Carbon Nanocages as Bifunctional Electrocatalysts for Oxygen Evolution and Reduction. *Carbon* **2019,** *144*, 492-499.

177. Lim, B.; Lu, X.; Jiang, M.; Camargo, P. H. C.; Cho, E. C.; Lee, E. P.; Xia, Y., Facile Synthesis of Highly Faceted Multioctahedral Pt Nanocrystals through Controlled Overgrowth. *Nano. Lett.* **2008,** *8* (11), 4043-4047.

178. Lim, B.; Jiang, M.; Camargo, P. H. C.; Cho, E. C.; Tao, J.; Lu, X.; Zhu, Y.; Xia, Y., Pd-Pt Bimetallic Nanodendrites with High Activity for Oxygen Reduction. *Science* **2009,** *324* (5932), 1302.

179. Antolini, E., Iridium as Catalyst and Cocatalyst for Oxygen Evolution/Reduction in Acidic Polymer Electrolyte Membrane Electrolyzers and Fuel Cells. *ACS Catal.* **2014,** *4* (5), 1426-1440.

180. Suen, N. T.; Hung, S. F.; Quan, Q.; Zhang, N.; Xu, Y. J.; Chen, H. M., Electrocatalysis for the Oxygen Evolution Reaction: Recent Development and Future Perspectives. *Chem Soc Rev* **2017,** *46* (2), 337-365.

181. Yan, D.; Li, Y.; Huo, J.; Chen, R.; Dai, L.; Wang, S., Defect Chemistry of Nonprecious-Metal Electrocatalysts for Oxygen Reactions. *Adv. Mater.* **2017,** *29* (48).

182. Zhang, J.; Dai, L., Heteroatom-Doped Graphitic Carbon Catalysts for Efficient Electrocatalysis of Oxygen Reduction Reaction. *ACS Catal.* **2015,** *5* (12), 7244-7253.

183. Liang, J.; Jiao, Y.; Jaroniec, M.; Qiao, S. Z., Sulfur and Nitrogen Dual-Doped Mesoporous Graphene Electrocatalyst for Oxygen Reduction with Synergistically Enhanced Performance. *Angew. Chem. Int. Ed. Engl.* **2012,** *51* (46), 11496-500.

184. Jiang, H.; Zhu, Y.; Feng, Q.; Su, Y.; Yang, X.; Li, C., Nitrogen and Phosphorus Dual-Doped Hierarchical Porous Carbon Foams as Efficient Metal-Free Electrocatalysts for Oxygen Reduction Reactions. *Chemistry* **2014,** *20* (11), 3106-12.

185. Wu, J.; Yang, Z.; Li, X.; Sun, Q.; Jin, C.; Strasser, P.; Yang, R., Phosphorus-Doped Porous Carbons as Efficient Electrocatalysts for Oxygen Reduction. *J. Mater. Chem. A* **2013,** *1* (34), 9889.

186. Yang, L.; Jiang, S.; Zhao, Y.; Zhu, L.; Chen, S.; Wang, X.; Wu, Q.; Ma, J.; Ma, Y.; Hu, Z., Boron-Doped Carbon Nanotubes as Metal-Free Electrocatalysts for the Oxygen Reduction Reaction. *Angew. Chem. Int. Ed. Engl.* **2011,** *50* (31), 7132-5.

187. Tang, K.; Yuan, C.; Xiong, Y.; Hu, H.; Wu, M., Inverse-Opal-Structured Hybrids of N, S-Codoped-Carbon-Confined Co_9S_8 Nanoparticles as Bifunctional Oxygen Electrocatalyst for on-Chip All-Solid-State Rechargeable Zn-Air Batteries. *Appl. Catal., B* **2020,** *260*, 118209.

188. Deng, H.; Li, Q.; Liu, J.; Wang, F., Active Sites for Oxygen Reduction Reaction on Nitrogen-Doped Carbon Nanotubes Derived from Polyaniline. *Carbon* **2017,** *112*, 219-229.

189. Hou, Y.; Cui, S.; Wen, Z.; Guo, X.; Feng, X.; Chen, J., Strongly Coupled 3d Hybrids of N-Doped Porous Carbon Nanosheet/CoNi Alloy-Encapsulated Carbon Nanotubes for Enhanced Electrocatalysis. *Small* **2015,** *11* (44), 5940-8.

190. Chen, M.; Wang, L.; Yang, H.; Zhao, S.; Xu, H.; Wu, G., Nanocarbon/oxide Composite Catalysts for Bifunctional Oxygen Reduction and Evolution in Reversible Alkaline Fuel Cells: A Mini Review. *J. Power Sources* **2018,** *375*, 277-290.

191. Tian, Y.; Xu, L.; Qian, J.; Bao, J.; Yan, C.; Li, H.; Li, H.; Zhang, S., Fe_3C/Fe_2O_3 Heterostructure Embedded in N-Doped Graphene as a Bifunctional Catalyst for Quasi-Solid-State Zinc-Air Batteries. *Carbon* **2019,** *146*, 763-771.

192. Tian, Y.; Xu, L.; Bao, J.; Qian, J.; Su, H.; Li, H.; Gu, H.; Yan, C.; Li, H., Hollow Cobalt Oxide Nanoparticles Embedded in Nitrogen-Doped Carbon Nanosheets as an Efficient Bifunctional Catalyst for Zn–Air Battery. *J. Energy Chem.* **2019,** *33*, 59-66.

193. Han, C.; Bo, X.; Liu, J.; Li, M.; Zhou, M.; Guo, L., Fe, Co Bimetal Activated N-Doped Graphitic Carbon Layers as Noble Metal-Free Electrocatalysts for High-Performance Oxygen Reduction Reaction. *J. Alloys Compd.* **2017,** *710*, 57-65.

194. Wang, X.; Zheng, B.; Yang, D.; Sun, B.; Zhang, W.; Chen, Y., Self‐Assembled Cofe Nanoparticle‐Embedded Carbon Nanowires as Efficient Nonprecious Catalyst for Overall Water Splitting. *Energy Technol.* **2019,** *7* (6), 1801061.

195. Zhang, B.; Zhang, X.; Wei, Y.; Xia, L.; Pi, C.; Song, H.; Zheng, Y.; Gao, B.; Fu, J.; Chu, P. K., General Synthesis of Nico Alloy Nanochain Arrays with Thin Oxide Coating: A Highly Efficient Bifunctional Electrocatalyst for Overall Water Splitting. *J. Alloys Compd.* **2019,** *797*, 1216-1223.

196. Zhang, M.; Gao, J.; Hong, W.; Wang, X.; Tian, Q.; An, Z.; Wang, L.; Yao, H.; Liu, Y.; Zhao, X.; Qiu, H., Bimetallic Mn and Co Encased within Bamboo-Like N-Doped Carbon Nanotubes as Efficient Oxygen Reduction Reaction Electrocatalysts. *J Colloid Interface Sci* **2019,** *537*, 238-246.

197. Liu, X.; Park, M.; Kim, M. G.; Gupta, S.; Wu, G.; Cho, J., Integrating NiCo Alloys with Their Oxides as Efficient Bifunctional Cathode Catalysts for Rechargeable Zinc-Air Batteries. *Angew. Chem. Int. Ed. Engl.* **2015,** *54* (33), 9654-8.

198. Li, Z.; He, H.; Cao, H.; Sun, S.; Diao, W.; Gao, D.; Lu, P.; Zhang, S.; Guo, Z.; Li, M.; Liu, R.; Ren, D.; Liu, C.; Zhang, Y.; Yang, Z.; Jiang, J.; Zhang, G., Atomic Co/Ni Dual Sites and Co/Ni Alloy Nanoparticles in N-Doped Porous Janus-Like Carbon Frameworks for Bifunctional Oxygen Electrocatalysis. *Appl. Catal., B* **2019,** *240*, 112-121.

199. Yang, L.; Wang, D.; Lv, Y.; Cao, D., Nitrogen-Doped Graphitic Carbons with Encapsulated Coni Bimetallic Nanoparticles as Bifunctional Electrocatalysts for Rechargeable Zn-Air Batteries. *Carbon* **2019,** *144*, 8-14.

200. Lu, P.; Yang, Y.; Yao, J.; Wang, M.; Dipazir, S.; Yuan, M.; Zhang, J.; Wang, X.; Xie, Z.; Zhang, G., Facile Synthesis of Single-Nickel-Atomic Dispersed N-Doped Carbon Framework for Efficient Electrochemical Co_2 Reduction. *Appl. Catal., B* **2019,** *241*, 113-119.

201. Luo, W.; Wang, B.; Heron, C. G.; Allen, M. J.; Morre, J.; Maier, C. S.; Stickle, W. F.; Ji, X., Pyrolysis of Cellulose under Ammonia Leads to Nitrogen-Doped Nanoporous Carbon Generated through Methane Formation. *Nano Lett* **2014,** *14* (4), 2225-9.

202. Wang, X.; Liu, C.-G.; Neff, D.; Fulvio, P. F.; Mayes, R. T.; Zhamu, A.; Fang, Q.; Chen, G.; Meyer, H. M.; Jang, B. Z.; Dai, S., Nitrogen-Enriched Ordered Mesoporous Carbons through Direct Pyrolysis in Ammonia with Enhanced Capacitive Performance. *J. Mater. Chem. A* **2013,** *1* (27), 7920.

203. Geng, D.; Yang, S.; Zhang, Y.; Yang, J.; Liu, J.; Li, R.; Sham, T. K.; Sun, X.; Ye, S.; Knights, S., Nitrogen Doping Effects on the Structure of Graphene. *Appl. Surf. Sci.* **2011,** *257* (21), 9193-9198.

204. Jia, Y.; Gao, X.; Teng, C.; Li, X.; Liu, Y.; Zhi, M.; Hong, Z., Co_2Ni Alloy/N-Doped Cnts Composite as Efficient Hydrogen Evolution Reaction Catalyst in Alkaline Medium. *J. Alloys Compd.* **2019,** *791*, 779-785.

205. Ning, H.; Li, G.; Chen, Y.; Zhang, K.; Gong, Z.; Nie, R.; Hu, W.; Xia, Q., Porous N-Doped Carbon-Encapsulated CoNi Alloy Nanoparticles Derived from MoFs as Efficient Bifunctional Oxygen Electrocatalysts. *ACS Appl Mater Interfaces* **2019,** *11* (2), 1957-1968.

206. Wan, W.; Liu, X.; Li, H.; Peng, X.; Xi, D.; Luo, J., 3D Carbon Framework-Supported Coni Nanoparticles as Bifunctional Oxygen Electrocatalyst for Rechargeable Zn-Air Batteries. *Appl. Catal., B* **2019,** *240*, 193-200.

207. Sahu, S. C.; Satpati, B.; Besra, L.; Jena, B. K., A Bifunctional Nano-Electrocatalyst Based on a Flower-Like Gold/Palladium Bimetallic Alloy Nanostructure and Its Graphene Hybrid. *ChemCatChem* **2015,** *7* (24), 4042-4049.

208. Ran, J.; Guo, X.; Liu, P.; Peng, S.; Gao, X.; Gao, D., Bifunctional Catalysts of CoNi Nanoparticle-Embedded Nitrogen-Doped Carbon Nanotubes for Rechargeable Zn-Air Batteries. *Nanotechnology* **2019,** *30* (43), 435701.

209. Gavrilov, N.; Momčilović, M.; Dobrota, A. S.; Stanković, D. M.; Jokić, B.; Babić, B.; Skorodumova, N. V.; Mentus, S. V.; Pašti, I. A., A Study of Ordered Mesoporous Carbon Doped with Co and Ni as a Catalyst of Oxygen Reduction Reaction in Both Alkaline and Acidic Media. *Surf. Coat. Technol.* **2018,** *349*, 511-521.

210. Masa, J.; Zhao, A.; Xia, W.; Muhler, M.; Schuhmann, W., Metal-Free Catalysts for Oxygen Reduction in Alkaline Electrolytes: Influence of the Presence of Co, Fe, Mn and Ni Inclusions. *Electrochim. Acta* **2014,** *128*, 271-278.

211. Zhang, J.; Xia, Z.; Dai, L., Carbon-Based Electrocatalysts for Advanced Energy Conversion and Storage. *Sci. Adv.* **2015,** *1* (7), e1500564.

212. Zhao, S.; Rasimick, B.; Mustain, W.; Xu, H., Highly Durable and Active Co_3O_4 Nanocrystals Supported on Carbon Nanotubes as Bifunctional Electrocatalysts in Alkaline Media. *Appl. Catal., B* **2017,** *203*, 138-145.

213. Lai, L.; Potts, J. R.; Zhan, D.; Wang, L.; Poh, C. K.; Tang, C.; Gong, H.; Shen, Z.; Lin, J.; Ruoff, R. S., Exploration of the Active Center Structure of Nitrogen-Doped Graphene-Based Catalysts for Oxygen Reduction Reaction. *Energy Environ. Sci.* **2012,** *5* (7), 7936.

214. Wütscher, A.; Eckhard, T.; Hiltrop, D.; Lotz, K.; Schuhmann, W.; Andronescu, C.; Muhler, M., Nitrogen-Doped Metal-Free Carbon Materials Derived from Cellulose as Electrocatalysts for the Oxygen Reduction Reaction. *ChemElectroChem* **2019,** *6* (2), 514-521.

215. Ma, R.; Ma, Y.; Dong, Y.; Lee, J. M., Recent Advances in Heteroatom-Doped Graphene Materials as Efficient Electrocatalysts Towards the Oxygen Reduction Reaction. *Nano Advances* **2016**, 50-61.

216. Luo, M.; Zhao, Z.; Zhang, Y.; Sun, Y.; Xing, Y.; Lv, F.; Yang, Y.; Zhang, X.; Hwang, S.; Qin, Y.; Ma, J. Y.; Lin, F.; Su, D.; Lu, G.; Guo, S., Pdmo Bimetallene for Oxygen Reduction Catalysis. *Nature* **2019,** *574* (7776), 81-85.

217. Vineesh, T. V.; Mubarak, S.; Hahm, M. G.; Prabu, V.; Alwarappan, S.; Narayanan, T. N., Controllably Alloyed, Low Density, Free-Standing Ni-Co and Ni-Graphene Sponges for Electrocatalytic Water Splitting. *Sci Rep* **2016,** *6*, 31202.

218. Elizabeth, I.; Nair, A. K.; Singh, B. P.; Gopukumar, S., Multifunctional Ni-NiO-CNT Composite as High Performing Free Standing Anode for Li Ion Batteries and Advanced Electro Catalyst for Oxygen Evolution Reaction. *Electrochim. Acta* **2017,** *230*, 98-105.

219. Lee, S. H.; Jo, Y.-R.; Noh, Y.; Kim, B.-J.; Kim, W. B., Fabrication of Hierarchically Branched SnO_2 Nanowires by Two-Step Deposition Method and Their Applications to Electrocatalyst Support and Li Ion Electrode. *J. Power Sources* **2017,** *367*, 1-7.

220. Yu, W.; Shang, W.; Tan, P.; Chen, B.; Wu, Z.; Xu, H.; Shao, Z.; Liu, M.; Ni, M., Toward a New Generation of Low Cost, Efficient, and Durable Metal-Air Flow Batteries. *J. Mater. Chem. A* **2019,** *7* (47), 26744-26768.

221. Yao, R. Q.; Shi, H.; Wan, W. B.; Wen, Z.; Lang, X. Y.; Jiang, Q., Flexible Co-Mo-N/Au Electrodes with a Hierarchical Nanoporous Architecture as Highly Efficient Electrocatalysts for Oxygen Evolution Reaction. *Adv. Mater.* **2020,** *32* (10), e1907214.

222. Gebremariam, T. T.; Chen, F.; Jin, Y.; Wang, Q.; Wang, J.; Wang, J., Bimetallic NiCo/CNF Encapsulated in a N-Doped Carbon Shell as an Electrocatalyst for Zn-Air Batteries and Water Splitting. *Catal. Sci. Technol.* **2019,** *9* (10), 2532-2542.

223. Song, S.; Li, W.; Deng, Y.-P.; Ruan, Y.; Zhang, Y.; Qin, X.; Chen, Z., Tic Supported Amorphous Mnox as Highly Efficient Bifunctional Electrocatalyst for Corrosion Resistant Oxygen Electrode of Zn-Air Batteries. *Nano Energy* **2020,** *67*, 104208.

224. Shi, F.; Zhu, X.; Yang, W., Micro-Nanostructural Designs of Bifunctional Electrocatalysts for Metal-Air Batteries. *Chin. J. Catal.* **2020,** *41* (3), 390-403.

225. Kim, M.; Ju, H.; Kim, J., Dihydrogen Phosphate Ion Functionalized Nanocrystalline Thallium Ruthenium Oxide Pyrochlore as a Bifunctional Electrocatalyst for Aqueous Na-Air Batteries. *Appl. Catal., B* **2019,** *245*, 29-39.

226. Wang, X.; Sunarso, J.; Lu, Q.; Zhou, Z.; Dai, J.; Guan, D.; Zhou, W.; Shao, Z., High-Performance Platinum - Perovskite Composite Bifunctional Oxygen Electrocatalyst for Rechargeable Zn–Air Battery. *Adv. Energy Mater.* **2019,** *10* (5), 1903271.

227. Xiao, X.; Li, X.; Wang, Z.; Yan, G.; Guo, H.; Hu, Q.; Li, L.; Liu, Y.; Wang, J., Robust Template-Activator Cooperated Pyrolysis Enabling Hierarchically Porous Honeycombed Defective Carbon as Highly-Efficient Metal-Free Bifunctional Electrocatalyst for Zn-Air Batteries. *Appl. Catal., B* **2020,** *265*, 118603.

228. Guo, J.; Yu, Y.; Ma, J.; Zhang, T.; Xing, S., Facile Route to Achieve N, S-Codoped Carbon as Bifunctional Electrocatalyst for Oxygen Reduction and Evolution Reactions. *J. Alloys Compd.* **2020,** *821*, 153484.

229. Cui, C.; Gan, L.; Li, H. H.; Yu, S. H.; Heggen, M.; Strasser, P., Octahedral Ptni Nanoparticle Catalysts: Exceptional Oxygen Reduction Activity by Tuning the Alloy Particle Surface Composition. *Nano Lett* **2012,** *12* (11), 5885-9.

230. Parra-Puerto, A.; Ng, K. L.; Fahy, K.; Goode, A. E.; Ryan, M. P.; Kucernak, A., Supported Transition Metal Phosphides: Activity Survey for HER, ORR, OER, and Corrosion Resistance in Acid and Alkaline Electrolytes. *ACS Catal.* **2019,** *9* (12), 11515-11529.

231. Chen, D.; Zhu, J.; Mu, X.; Cheng, R.; Li, W.; Liu, S.; Pu, Z.; Lin, C.; Mu, S., Nitrogen-Doped Carbon Coupled $FeNi_3$ Intermetallic Compound as Advanced Bifunctional Electrocatalyst for OER, ORR and Zn-Air Batteries. *Appl. Catal., B* **2020,** *268*, 118729.

232. He, X.; Luan, S. Z.; Wang, L.; Wang, R. Y.; Du, P.; Xu, Y. Y.; Yang, H. J.; Wang, Y. G.; Huang, K.; Lei, M., Facile Loading Mesoporous Co_3O_4 on Nitrogen Doped Carbon Matrix as an Enhanced Oxygen Electrode Catalyst. *Mater. Lett.* **2019,** *244*, 78-82.

233. Xia, S. B.; Yu, S. W.; Yao, L. F.; Li, F. S.; Li, X.; Cheng, F. X.; Shen, X.; Sun, C. K.; Guo, H.; Liu, J. J., Robust Hexagonal Nut-Shaped Titanium(Iv) MOF with Porous Structure for Ultra-High Performance Lithium Storage. *Electrochim. Acta* **2019,** *296*, 746-754.

234. Yu, S. Z.; Luo, S. H.; Zhan, Y.; Huang, H. B.; Wang, Q.; Zhang, Y. H.; Liu, Y. G.; Hao, A. I., Metal-Organic Framework-Derived Cobalt Nanoparticle Space Confined in Nitrogen-Doped Carbon Polyhedra Networks as High-Performance Bifunctional Electrocatalyst for Rechargeable Li–O_2 Batteries. *J. Power Sources* **2020,** *453*, 227899.

235. Chen, D.; Yu, J.; Cui, Z.; Zhang, Q.; Chen, X.; Sui, J.; Dong, H.; Yu, L.; Dong, L., Hierarchical Architecture Derived from Two-Dimensional Zeolitic Imidazolate Frameworks as an Efficient Metal-Based Bifunctional Oxygen Electrocatalyst for Rechargeable Zn-Air Batteries. *Electrochim. Acta* **2020,** *331*, 135394.

236. Guan, Y.; Li, Y.; Luo, S.; Ren, X.; Deng, L.; Sun, L.; Mi, H.; Zhang, P.; Liu, J., Rational Design of Positive-Hexagon-Shaped Two-Dimensional ZIF-Derived Materials as Improved Bifunctional Oxygen Electrocatalysts for Use as Long-Lasting Rechargeable Zn-Air Batteries. *Appl. Catal., B* **2019,** *256*, 117871.

237. Li, Z.; Liu, H.; Huang, J.; Zhang, L., MoF-Derived A-MnSe/C Composites as Anode Materials for Li-Ion Batteries. *Ceram. Int.* **2019,** *45* (17), 23765-23771.

238. Duan, J.; Zou, Y.; Li, Z.; Long, B., Preparation of MOF-Derived Nicop Nanocages as Anodes for Lithium Ion Batteries. *Powder Technol.* **2019,** *354*, 834-841.

239. Wang, C. C.; Hung, K. Y.; Ko, T. E.; Hosseini, S.; Li, Y. Y., Carbon-Nanotube-Grafted and Nano-Co_3O_4-Doped Porous Carbon Derived from Metal-Organic Framework as an Excellent Bifunctional Catalyst for Zinc-Air Battery. *J. Power Sources* **2020,** *452*, 227841.

240. Chen, D.; Chen, X.; Cui, Z.; Li, G.; Han, B.; Zhang, Q.; Sui, J.; Dong, H.; Yu, J.; Yu, L.; Dong, L., Dual-Active-Site Hierarchical Architecture Containing NiFe-LDH and ZIF-Derived Carbon-Based Framework Composite as Efficient Bifunctional Oxygen Electrocatalysts for Durable Rechargeable Zn-Air Batteries. *Chem. Eng. J.* **2020,** *399*, 125718.

241. Wang, Q.; Shang, L.; Shi, R.; Zhang, X.; Zhao, Y.; Waterhouse, G. I. N.; Wu, L. Z.; Tung, C.-H.; Zhang, T., NiFe Layered Double Hydroxide Nanoparticles on Co,N-Codoped Carbon Nanoframes as Efficient Bifunctional Catalysts for Rechargeable Zinc-Air Batteries. *Adv. Energy Mater.* **2017,** *7* (21), 1700467.

242. Li, Y.; Jia, B.; Fan, Y.; Zhu, K.; Li, G.; Su, C. Y., Bimetallic Zeolitic Imidazolite Framework Derived Carbon Nanotubes Embedded with Co Nanoparticles for Efficient Bifunctional Oxygen Electrocatalyst. *Adv. Energy Mater.* **2018,** *8* (9), 1702048.

243. Guo, J.; Gao, M.; Nie, J.; Yin, F.; Ma, G., ZIF-67/Pan-800 Bifunctional Electrocatalyst Derived from Electrospun Fibers for Efficient Oxygen Reduction and Oxygen Evolution Reaction. *J Colloid Interface Sci* **2019,** *544*, 112-120.

244. Khalid, M.; Honorato, A. M. B.; Ticianelli, E. A.; Varela, H., Uniformly Self-Decorated Co_3O_4 Nanoparticles on N, S Co-Doped Carbon Layers Derived from a Camphor Sulfonic Acid and Metal-Organic Framework Hybrid as an Oxygen Evolution Electrocatalyst. *J. Mater. Chem. A* **2018,** *6* (25), 12106-12114.

245. Hang, C.; Zhang, J.; Zhu, J.; Li, W.; Kou, Z.; Huang, Y., In Situ Exfoliating and Generating Active Sites on Graphene Nanosheets Strongly Coupled with Carbon Fiber toward Self-Standing Bifunctional Cathode for Rechargeable Zn-Air Batteries. *Adv. Energy Mater.* **2018,** *8* (16), 1703539.

246. Wei, J.; Hu, Y.; Liang, Y.; Kong, B.; Zhang, J.; Song, J.; Bao, Q.; Simon, G. P.; Jiang, S. P.; Wang, H., Nitrogen-Doped Nanoporous Carbon/Graphene Nano-Sandwiches: Synthesis and Application for Efficient Oxygen Reduction. *Adv. Funct. Mater.* **2015,** *25* (36), 5768-5777.

247. Chen, Z.; Liu, M.; Wu, R., Strongly Coupling of Co_9S_8/Zn-Co-S Heterostructures Rooted in Carbon Nanocages Towards Efficient Oxygen Evolution Reaction. *J. Catal.* **2018,** *361*, 322-330.

248. Guan, C.; Xiao, W.; Wu, H.; Liu, X.; Zang, W.; Zhang, H.; Ding, J.; Feng, Y. P.; Pennycook, S. J.; Wang, J., Hollow Mo-Doped Cop Nanoarrays for Efficient Overall Water Splitting. *Nano Energy* **2018,** *48*, 73-80.

249. Zeng, K.; Su, J.; Cao, X.; Zheng, X.; Li, X.; Tian, J.-H.; Jin, C.; Yang, R., B, N Co-Doped Ordered Mesoporous Carbon with Enhanced Electrocatalytic Activity for the Oxygen Reduction Reaction. *J. Alloys Compd.* **2020,** *824*, 153908.

250. Jin, H.; Zhou, H.; Li, W.; Wang, Z.; Yang, J.; Xiong, Y.; He, D.; Chen, L.; Mu, S., In Situ Derived Fe/N/S-Codoped Carbon Nanotubes from ZIF-8 Crystals as Efficient Electrocatalysts for the Oxygen Reduction Reaction and Zinc-Air Batteries. *J. Mater. Chem. A* **2018,** *6* (41), 20093-20099.

251. Wang, R.; Dong, X. Y.; Du, J.; Zhao, J. Y.; Zang, S. Q., Mof-Derived Bifunctional Cu_3P Nanoparticles Coated by a N,P-Codoped Carbon Shell for Hydrogen Evolution and Oxygen Reduction. *Adv. Mater.* **2018,** *30* (6).

252. Chen, B.; He, X.; Yin, F.; Wang, H.; Liu, D.-J.; Shi, R.; Chen, J.; Yin, H., Mo-Co@N-Doped Carbon (M = Zn or Co): Vital Roles of Inactive Zn and Highly Efficient Activity toward Oxygen Reduction/Evolution Reactions for Rechargeable Zn-Air Battery. *Adv. Funct. Mater.* **2017,** *27* (37), 1700795.

253. He, W.; Wang, C.; Li, H.; Deng, X.; Xu, X.; Zhai, T., Ultrathin and Porous Ni_3S_2/$CoNi_2S_4$ 3D-Network Structure for Superhigh Energy Density Asymmetric Supercapacitors. *Adv. Energy Mater.* **2017,** *7* (21), 1700983.

254. Yang, Y.; Li, S.; Huang, W.; Shangguan, H.; Engelbrekt, C.; Duan, S.; Ci, L.; Si, P., Effective Synthetic Strategy for $Zn_{0.76}Co_{0.24}S$ Encapsulated in Stabilized N-Doped Carbon Nanoarchitecture Towards Ultra-Long-Life Hybrid Supercapacitors. *J. Mater. Chem. A* **2019,** *7* (24), 14670-14680.

255. Yin, X.; Sun, W.; Lv, L.-P.; Wang, Y., Boosting Lithium-Ion Storage Performance by Synergistically Coupling $Zn_{0.76}Co_{0.24}S$ with N-/S-Doped Carbon and Carbon Nanofiber. *Chem. Eng. J.* **2018,** *346*, 376-387.

256. Zhou, Y.; Leng, Y.; Zhou, W.; Huang, J.; Zhao, M.; Zhan, J.; Feng, C.; Tang, Z.; Chen, S.; Liu, H., Sulfur and Nitrogen Self-Doped Carbon Nanosheets Derived from Peanut Root Nodules as High-Efficiency Non-Metal Electrocatalyst for Hydrogen Evolution Reaction. *Nano Energy* **2015,** *16*, 357-366.

257. Wang, X.; Ma, Z.; Chai, L.; Xu, L.; Zhu, Z.; Hu, Y.; Qian, J.; Huang, S., MoF Derived N-Doped Carbon Coated CoP Particle/Carbon Nanotube Composite for Efficient Oxygen Evolution Reaction. *Carbon* **2019,** *141*, 643-651.

258. Zhang, S. L.; Guan, B. Y.; Lou, X. W. D., Co-Fe Alloy/N-Doped Carbon Hollow Spheres Derived from Dual Metal-Organic Frameworks for Enhanced Electrocatalytic Oxygen Reduction. *Small* **2019,** *15* (13), e1805324.

259. Yang, Y.; Huang, W.; Li, S.; Ci, L.; Si, P., Surfactant-Dependent Flower- and Grass-Like $Zn_{0.76}Co_{0.24}S/Co_3S_4$ for High-Performance All-Solid-State Asymmetric Supercapacitors. *J. Mater. Chem. A* **2018,** *6* (45), 22830-22839.

260. Zhao, Y.; Dong, H.; He, X.; Yu, J.; Chen, R.; Liu, Q.; Liu, J.; Zhang, H.; Li, R.; Wang, J., Design of 2D Mesoporous Zn/Co-Based Metal-Organic Frameworks as a Flexible Electrode for Energy Storage and Conversion. *J. Power Sources* **2019,** *438*, 227057.

261. Yang, L.; Zhang, L.; Xu, G.; Ma, X.; Wang, W.; Song, H.; Jia, D., Metal–Organic-Framework-Derived Hollow Cosx@Mos2 Microcubes as Superior Bifunctional Electrocatalysts for Hydrogen Evolution and Oxygen Evolution Reactions. *ACS Sustainable Chem. Eng.* **2018,** *6* (10), 12961-12968.

262. Yang, G.; Jiao, Y.; Yan, H.; Xie, Y.; Wu, A.; Dong, X.; Guo, D.; Tian, C.; Fu, H., Interfacial Engineering of MoO_2 -FeP Heterojunction for Highly Efficient Hydrogen Evolution Coupled with Biomass Electrooxidation. *Adv. Mater.* **2020,** *32* (17), e2000455.

263. Tong, J.; Li, Y.; Bo, L.; Li, W.; Li, T.; Zhang, Q.; Kong, D.; Wang, H.; Li, C., Cop/N-Doped Carbon Hollow Spheres Anchored on Electrospinning Core–Shell N-Doped Carbon Nanofibers as Efficient Electrocatalysts for Water Splitting. *ACS Sustainable Chem. Eng.* **2019,** *7* (20), 17432-17442.

264. Liu, Z.; Yu, X.; Xue, H.; Feng, L., A Nitrogen-Doped CoP Nanoarray over 3D Porous Co Foam as an Efficient Bifunctional Electrocatalyst for Overall Water Splitting. *J. Mater. Chem. A* **2019,** *7* (21), 13242-13248.

265. Yang, M. Q.; Wang, J.; Wu, H.; Ho, G. W., Noble Metal-Free Nanocatalysts with Vacancies for Electrochemical Water Splitting. *Small* **2018,** *14* (15), e1703323.

266. Xu, Z.; Jin, S.; Seo, M. H.; Wang, X., Hierarchical Ni-Mo_2C/N-Doped Carbon Mott-Schottky Array for Water Electrolysis. *Appl. Catal., B* **2021**, 120168.

267. Zhang, D.; Mou, H.; Chen, L.; Wang, D.; Song, C., Design and in-Situ Synthesis of Unique Catalyst Via Embedding Graphene Oxide Shell Membrane in NiS_2 for Efficient Hydrogen Evolution. *Appl. Surf. Sci.* **2020,** *510*, 145483.

268. Lonkar, S. P.; Pillai, V. V.; Alhassan, S. M., Three Dimensional (3D) Nanostructured Assembly of MoS_2-WS_2/Graphene as High Performance Electrocatalysts. *Int. J. Hydrog. Energy* **2020,** *45* (17), 10475-10485.

269. Guo, Y.; Park, T.; Yi, J. W.; Henzie, J.; Kim, J.; Wang, Z.; Jiang, B.; Bando, Y.; Sugahara, Y.; Tang, J.; Yamauchi, Y., Nanoarchitectonics for Transition-Metal-Sulfide-Based Electrocatalysts for Water Splitting. *Adv. Mater.* **2019,** *31* (17), e1807134.

270. Jiang, H.; Zhang, K.; Li, W.; Cui, Z.; He, S.-A.; Zhao, S.; Li, J.; He, G.; Shearing, P. R.; Brett, D. J. L., MoS_2/NiS Core-Shell Structures for Improved Electrocatalytic Process of Hydrogen Evolution. *J. Power Sources* **2020,** *472*, 228497.

271. Jiang, H.; Zhang, K.; Li, W.; Cui, Z.; He, S.-A.; Zhao, S.; Li, J.; He, G.; Shearing, P. R.; Brett, D. J. L., MoS_2/NiS Core-Shell Structures for Improved Electrocatalytic Process of Hydrogen Evolution. *J. Power Sources* **2020,** *472*, 228497.

272. Ma, Z.; Meng, H.; Wang, M.; Tang, B.; Li, J.; Wang, X., Porous Ni-Mo-S Nanowire Network Film Electrode as a High-Efficiency Bifunctional Electrocatalyst for Overall Water Splitting. *ChemElectroChem* **2018,** *5* (2), 335-342.

273. Jaramillo, T. F.; Jørgensen, K. P.; Bonde, J.; Nielsen, J. H.; Horch, S.; Chorkendorff, I., Identification of Active Edge Sites for Electrochemical H_2 Evolution from MoS_2 Nanocatalysts. *Science* **2007,** *317* (5834), 100.

274. Khalil, A.; Liu, Q.; Muhammad, Z.; Habib, M.; Khan, R.; He, Q.; Fang, Q.; Masood, H. T.; Rehman, Z. U.; Xiang, T.; Wu, C. Q.; Song, L., Synthesis of Ni_9S_8/MoS_2 Heterocatalyst for Enhanced Hydrogen Evolution Reaction. *Langmuir* **2017,** *33* (21), 5148-5153.

275. Lonkar, S. P.; Pillai, V. V.; Alhassan, S. M., Scalable Solid-State Synthesis of MoS_2-NiS_2/Graphene Nanohybrids as Bifunctional Electrocatalysts for Enhanced Overall Water Splitting. *Mater. Adv.* **2020,** *1* (4), 794-803.

276. Ge, Y.; Chu, H.; Chen, J.; Zhuang, P.; Feng, Q.; Smith, W. R.; Dong, P.; Ye, M.; Shen, J., Ultrathin MoS_2 Nanosheets Decorated Hollow CoP Heterostructures for Enhanced Hydrogen Evolution Reaction. *ACS Sustainable Chem. Eng.* **2019,** *7* (11), 10105-10111.

277. Li, F.; Zhang, D.; Xu, R. C.; Fu, W. F.; Lv, X. J., Superhydrophilic Heteroporous MoS_2/Ni_3S_2 for Highly Efficient Electrocatalytic Overall Water Splitting. *ACS Appl. Energy Mater.* **2018,** *1* (8), 3929-3936.

278. Escudero-Escribano, M.; Jensen, K. D.; Jensen, A. W., Recent Advances in Bimetallic Electrocatalysts for Oxygen Reduction: Design Principles, Structure-Function Relations and Active Phase Elucidation. *Curr. Opin. Electrochem.* **2018,** *8*, 135-146.

279. Qin, Q.; Chen, L.; Wei, T.; Liu, X., MoS_2/NiS Yolk-Shell Microsphere-Based Electrodes for Overall Water Splitting and Asymmetric Supercapacitor. *Small* **2019,** *15* (29), e1803639.

280. Zhang, J.; Wang, T.; Pohl, D.; Rellinghaus, B.; Dong, R.; Liu, S.; Zhuang, X.; Feng, X., Interface Engineering of MoS_2/Ni_3S_2 Heterostructures for Highly Enhanced Electrochemical Overall-Water-Splitting Activity. *Angew. Chem. Int. Ed. Engl.* **2016,** *55* (23), 6702-7.

281. Zhang, Y.; Shi, M.; Wang, C.; Zhu, Y.; Li, N.; Pu, X.; Yu, A.; Zhai, J., Vertically Aligned $NiS_2/CoS_2/MoS_2$ Nanosheet Array as an Efficient and Low-Cost Electrocatalyst for Hydrogen Evolution Reaction in Alkaline Media. *Science Bulletin.* **2020,** *65* (5), 359-366.

282. Chen, Z.; Cummins, D.; Reinecke, B. N.; Clark, E.; Sunkara, M. K.; Jaramillo, T. F., Core-Shell MoO_3-MoS_2 Nanowires for Hydrogen Evolution: A Functional Design for Electrocatalytic Materials. *Nano Lett* **2011,** *11* (10), 4168-75.

283. Wang, C.; Tian, B.; Wu, M.; Wang, J., Revelation of the Excellent Intrinsic Activity of $MoS_2|NiS|MoO_3$ Nanowires for Hydrogen Evolution Reaction in Alkaline Medium. *ACS Appl Mater Interfaces* **2017,** *9* (8), 7084-7090.

284. Xu, K.; Lin, X.; Wang, X.; Li, L.; Zhu, Z.; Tian, Y., Generating More Mn^{4+} Ions on Surface of Nonstoichiometric MnO_2 Nanorods Via Microwave Heating for Improved Oxygen Electroreduction. *Appl. Surf. Sci.* **2018,** *459*, 782-787.

285. An, T.; Wang, Y.; Tang, J.; Wei, W.; Cui, X.; Alenizi, A. M.; Zhang, L.; Zheng, G., Interlaced NiS_2-MoS_2 Nanoflake-Nanowires as Efficient Hydrogen Evolution Electrocatalysts in Basic Solutions. *J. Mater. Chem. A* **2016,** *4* (35), 13439-13443.

286. Li, Y.; Wang, C.; Cui, M.; Xiong, J.; Mi, L.; Chen, S., Heterostructured $MoO_2@MoS_2@Co_9S_8$ Nanorods as High Efficiency Bifunctional Electrocatalyst for Overall Water Splitting. *Appl. Surf. Sci.* **2021,** *543*, 148804.

287. Kuang, P.; Tong, T.; Fan, K.; Yu, J., In Situ Fabrication of Ni-Mo Bimetal Sulfide Hybrid as an Efficient Electrocatalyst for Hydrogen Evolution over a Wide Ph Range. *ACS Catal.* **2017,** *7* (9), 6179-6187.

288. Lin, J.; Wang, P.; Wang, H.; Li, C.; Si, X.; Qi, J.; Cao, J.; Zhong, Z.; Fei, W.; Feng, J., Defect-Rich Heterogeneous MoS_2/NiS_2 Nanosheets Electrocatalysts for Efficient Overall Water Splitting. *Advanced science* **2019,** *6* (14), 1900246.

289. Chen, D.; Li, L.; Xi, Y.; Li, J.; Lu, M.; Cao, J.; Han, W., Self-Assembly of Biomass Microfibers into 3D Layer-Stacking Hierarchical Porous Carbon for High Performance Supercapacitors. *Electrochim. Acta* **2018,** *286*, 264-270.

290. Li, H.; Qian, X.; Xu, C.; Huang, S.; Zhu, C.; Jiang, X.; Shao, L.; Hou, L., Hierarchical Porous Co_9S_8/Nitrogen-Doped Carbon@MoS_2 Polyhedrons as PH Universal Electrocatalysts for Highly Efficient Hydrogen Evolution Reaction. *ACS Appl Mater Interfaces* **2017,** *9* (34), 28394-28405.

291. Wang, N.; Pan, Q.; Yang, X.; Zhu, H.; Ding, G.; Jia, Z.; Wu, Y.; Zhao, L., High Performance Asymmetric Supercapacitor Based on Ni_xS_y/MoS_2 Nanoparticles. *ACS Appl. Nano Mater.* **2019,** *2* (8), 4910-4920.

292. Zhu, H.; Zhang, J.; Yanzhang, R.; Du, M.; Wang, Q.; Gao, G.; Wu, J.; Wu, G.; Zhang, M.; Liu, B.; Yao, J.; Zhang, X., When Cubic Cobalt Sulfide Meets Layered Molybdenum Disulfide: A Core-Shell System toward Synergetic Electrocatalytic Water Splitting. *Adv. Mater.* **2015,** *27* (32), 4752-9.

293. Li, S.; Chen, T.; Wen, J.; Gui, P.; Fang, G., In Situ Grown Ni_9S_8 Nanorod/O-MoS_2 Nanosheet Nanocomposite on Carbon Cloth as a Free Binder Supercapacitor Electrode and Hydrogen Evolution Catalyst. *Nanotechnology* **2017,** *28* (44), 445407.

294. Zhai, Z.; Li, C.; Zhang, L.; Wu, H.-C.; Zhang, L.; Tang, N.; Wang, W.; Gong, J., Dimensional Construction and Morphological Tuning of Heterogeneous MoS_2/NiS Electrocatalysts for Efficient Overall Water Splitting. *J. Mater. Chem. A* **2018,** *6* (21), 9833-9838.

295. Song, S.; Wang, Y.; Li, W.; Tian, P.; Zhou, S.; Gao, H.; Tian, X.; Zang, J., Amorphous MoS_2 Coated Ni_3S_2 Nanosheets as Bifunctional Electrocatalysts for High-Efficiency Overall Water Splitting. *Electrochim. Acta* **2020,** *332*, 135454.

296. Chen, D.; Lu, M.; Li, L.; Cai, D.; Li, J.; Cao, J.; Han, W., Hierarchical Core-Shell Structural $NiMoO_4$@NiS_2/MoS_2 Nanowires Fabricated Via an in Situ Sulfurization Method for High Performance Asymmetric Supercapacitors. *J. Mater. Chem. A* **2019,** *7* (38), 21759-21765.

297. Huang, L.; Xiang, J.; Zhang, W.; Chen, C.; Xu, H.; Huang, Y., 3D Interconnected Porous $NiMoO_4$ Nanoplate Arrays on Ni Foam as High-Performance Binder-Free Electrode for Supercapacitors. *J. Mater. Chem. A* **2015,** *3* (44), 22081-22087.

298. Deng, S.; Ai, C.; Luo, M.; Liu, B.; Zhang, Y.; Li, Y.; Lin, S.; Pan, G.; Xiong, Q.; Liu, Q.; Wang, X.; Xia, X.; Tu, J., Coupled Biphase (1t-2h)-$MoSe_2$ on Mold Spore Carbon for Advanced Hydrogen Evolution Reaction. *Small* **2019,** *15* (30), e1901796.

299. Yu, L.; Hu, H.; Wu, H. B.; Lou, X. W., Complex Hollow Nanostructures: Synthesis and Energy-Related Applications. *Adv. Mater.* **2017,** *29* (15).

300. Gao, H.; Zang, J.; Wang, Y.; Zhou, S.; Tian, P.; Song, S.; Tian, X.; Li, W., One-Step Preparation of Cobalt-Doped NiS@MoS_2 Core-Shell Nanorods as Bifunctional Electrocatalyst for Overall Water Splitting. *Electrochim. Acta* **2021,** *377*, 138051.

301. Zhang, Q.; Liu, B.; Ji, Y.; Chen, L.; Zhang, L.; Li, L.; Wang, C., Construction of Hierarchical Yolk-Shell Nanospheres Organized by Ultrafine Janus Subunits for Efficient Overall Water Splitting. *Nanoscale* **2020,** *12* (4), 2578-2586.

302. Wang, Z.; Wang, H.; Ji, S.; Wang, X.; Zhou, P.; Huo, S.; Linkov, V.; Wang, R., A High Faraday Efficiency $NiMoO_4$ Nanosheet Array Catalyst by Adjusting the Hydrophilicity for Overall Water Splitting. *Chemistry* **2020,** *26* (52), 12067-12074.

303. Jin, L.; Xu, H.; Wang, C.; Wang, Y.; Shang, H.; Du, Y., Multi-Dimensional Collaboration Promotes the Catalytic Performance of 1D MoO_3 Nanorods Decorated with 2D Nis Nanosheets for Efficient Water Splitting. *Nanoscale* **2020,** *12* (42), 21850-21856.

304. Muthurasu, A.; Ojha, G. P.; Lee, M.; Kim, H. Y., Zeolitic Imidazolate Framework Derived Co_3S_4 Hybridized MoS_2-Ni_3S_2 Heterointerface for Electrochemical Overall Water Splitting Reactions. *Electrochim. Acta* **2020,** *334*, 135537.

305. Zhang, X.; Su, H.; Du, X., A Nickel Molybdenum Oxide Nanoarray as an Efficient and Stable Electrocatalyst for Overall Water Splitting. *New J. Chem.* **2020,** *44* (20), 8176-8182.

306. Xu, J.; Rong, J.; Zheng, Y.; Zhu, Y.; Mao, K.; Jing, Z.; Zhang, T.; Yang, D.; Qiu, F., Construction of Sheet-on-Sheet Hierarchical MoS_2/NiS_2 Heterostructures as Efficient Bifunctional Electrocatalysts for Overall Water Splitting. *Electrochim. Acta* **2021,** *385*, 138438.

307. Lian, X.; Xu, N.; Ma, Y.; Hu, F.; Wei, H.; Chen, H. Y.; Wu, Y.; Li, L.; Li, D.; Peng, S., In-Situ Formation of $Co_{1-X}S$ Hollow Polyhedrons Anchored on Multichannel Carbon Nanofibers as Self-Supporting Anode for Lithium/Sodium-Ion Batteries. *Chem. Eng. J.* **2020**, 127755.

308. Wu, Q.; Xu, R.; Zhao, R.; Zhang, X.; Li, W.; Diao, G.; Chen, M., Tube-in-Tube Composite Nanofibers with High Electrochemistry Performance in Energy Storage Applications. *Energy Storage Mater.* **2019,** *19*, 69-79.

309. Liu, X.; Zhao, Y.; Dong, Y.; Kuang, Q.; Fan, Q.; Jing, Z.; Hou, S., A Promising Sol-Gel Method to Synthesize $NaVO_3$ as Anode Material for Lithium Ion Batteries. *J. Solid State Electrochem.* **2016,** *20* (6), 1803-1812.

310. Liu, G.; Liu, X.; Li, X.; Jin, X.; Xiao, H.; Wu, N.; Guo, D.; Tang, S., Coordination Engineering Construction of Si@ZnS@N,S‐Doped Reduced Graphene Oxide Nanocomposite as Anode Material with Enhanced Lithium Storage Performance. *Energy Technol.* **2019,** *7* (6), 1900186.

311. Yu, X. Y.; David Lou, X. W., Mixed Metal Sulfides for Electrochemical Energy Storage and Conversion. *Adv. Energy Mater.* **2018,** *8* (3), 1701592.

312. Jiao, Z.; Zhao, P.; He, Y.; Ling, L.; Sun, W.; Cheng, L., Mesoporous Yolk-Shell CoS_2/Nitrogen-Doped Carbon Dodecahedron Nanocomposites as Efficient Anode Materials for Lithium-Ion Batteries. *J. Alloys Compd.* **2019,** *809*, 151854.

313. Liao, W.; Tian, J.; Shan, Z.; Lin, H.; Na, R., Double-Shelled Co_3O_4@TiO_2@C Yolk-Shell Spheres as Anode Material for Enhanced Cycling Stability of Lithium Ion Batteries. *J. Alloys Compd.* **2018,** *739*, 746-754.

314. Yu, X.-Y.; Yu, L.; Lou, X. W. D., Metal Sulfide Hollow Nanostructures for Electrochemical Energy Storage. *Adv. Energy Mater.* **2016,** *6* (3), 1501333.

315. Yu, L.; Yang, J. F.; Lou, X. W., Formation of CoS_2 Nanobubble Hollow Prisms for Highly Reversible Lithium Storage. *Angew. Chem. Int. Ed. Engl.* **2016,** *55* (43), 13422-13426.

316. Chen, X.; Wang, P.; Zhang, Z.; Yin, L., Bi_2S_3-CoS@C Core- Shell Structure Derived from ZIF-67 as Anodes for High Performance Lithium-Ion Batteries. *J. Alloys Compd.* **2020,** *844*, 156008.

317. Meng, X.; Deng, D., Trash to Treasure: Waste Eggshells Used as Reactor and Template for Synthesis of Co_9S_8 Nanorod Arrays on Carbon Fibers for Energy Storage. *Chem. Mater.* **2016,** *28* (11), 3897-3904.

318. Chen, J.; Li, S.; Kumar, V.; Lee, P. S., Carbon Coated Bimetallic Sulfide Hollow Nanocubes as Advanced Sodium Ion Battery Anode. *Adv. Energy Mater.* **2017,** *7* (19), 1700180.

319. Gao, X.; Wang, J.; Zhang, D.; Adair, K.; Feng, K.; Sun, N.; Zheng, H.; Shao, H.; Zhong, J.; Ma, Y.; Sun, X.; Sun, X., Carbon Coated Bimetallic Sulfide Nanodots/Carbon Nanorod Heterostructure Enabling Long-Life Lithium-Ion Batteries. *J. Mater. Chem. A* **2017,** *5* (48), 25625-25631.

320. Li, S.; Ge, P.; Jiang, F.; Shuai, H.; Xu, W.; Jiang, Y.; Zhang, Y.; Hu, J.; Hou, H.; Ji, X., The Advance of Nickel-Cobalt-Sulfide as Ultra-Fast/High Sodium Storage Materials: The Influences of Morphology Structure, Phase Evolution and Interface Property. *Energy Storage Mater.* **2019,** *16*, 267-280.

321. Zhou, K.; Tang, D.; Li, W.; Han, Y.; Wu, H.; Diao, G.; Chen, M., Synergetic Lithium Storage of Bimetallic Sulfide Co_8FeS_8/N-C Dodecahedral Nanocages with Enhanced Lithium-Ion Battery Performance. *Chem. Eng. Sci.* **2019,** *208*, 115142.

322. Guo, S.; Feng, Y.; Qiu, J.; Li, X.; Yao, J., Leaf-Shaped Bimetallic Sulfides@N-Doped Porous Carbon as Advanced Lithium-Ion Battery Anode. *J. Alloys Compd.* **2019,** *792*, 8-15.

323. Li, Z.; Tang, B., Mn_3O_4/Nitrogen-Doped Porous Carbon Fiber Hybrids Involving Multiple Covalent Interactions and Open Voids as Flexible Anodes for Lithium-Ion Batteries. *Green Chem.* **2017,** *19* (24), 5862-5873.

324. Xu, L.; Hu, Y.; Zhang, H.; Jiang, H.; Li, C., Confined Synthesis of FeS_2 Nanoparticles Encapsulated in Carbon Nanotube Hybrids for Ultrastable Lithium-Ion Batteries. *ACS Sustainable Chem. Eng.* **2016,** *4* (8), 4251-4255.

325. Yin, B.; Cao, X.; Pan, A.; Luo, Z.; Dinesh, S.; Lin, J.; Tang, Y.; Liang, S.; Cao, G., Encapsulation of CoS Nanocrystals into N/S Co-Doped Honeycomb-Like 3D Porous Carbon for High-Performance Lithium Storage. *Adv. Sci.* **2018,** *5* (9), 1800829.

326. Li, X.; He, X.; Shi, C.; Liu, B.; Zhang, Y.; Wu, S.; Zhu, Z.; Zhao, J., Synthesis of One-Dimensional Copper Sulfide Nanorods as High-Performance Anode in Lithium Ion Batteries. *ChemSusChem* **2014,** *7* (12), 3328-3333.

327. Liu, T.; Wang, W.; Yi, M.; Chen, Q.; Xu, C.; Cai, D.; Zhan, H., Metal-Organic Framework Derived Porous Ternary $ZnCo_2O_4$ Nanoplate Arrays Grown on Carbon Cloth as Binder-Free Electrodes for Lithium-Ion Batteries. *Chem. Eng. J.* **2018,** *354*, 454-462.

328. Park, S.-K.; Kim, J. K.; Kim, J. H.; Kang, Y. C., Metal–Organic Framework-Templated Hollow Co_3O_4 Nanosphere Aggregate/N-Doped Graphitic Carbon Composite Powders Showing Excellent Lithium-Ion Storage Performances. *Mater. Charact.* **2017,** *132*, 320-329.

329. Zhang, J.; Hu, H.; Li, Z.; Lou, X. W., Double-Shelled Nanocages with Cobalt Hydroxide Inner Shell and Layered Double Hydroxides Outer Shell as High-Efficiency Polysulfide Mediator for Lithium-Sulfur Batteries. *Angew. Chem. Int. Ed. Engl.* **2016,** *55* (12), 3982-6.

330. Chen, Y. M.; Yu, L.; Lou, X. W., Hierarchical Tubular Structures Composed of Co_3O_4 Hollow Nanoparticles and Carbon Nanotubes for Lithium Storage. *Angew. Chem. Int. Ed. Engl.* **2016,** *55* (20), 5990-5993.

331. Liu, J.; Wu, C.; Xiao, D.; Kopold, P.; Gu, L.; van Aken, P. A.; Maier, J.; Yu, Y., Mof-Derived Hollow Co_9S_8 Nanoparticles Embedded in Graphitic Carbon Nanocages with Superior Li-Ion Storage. *Small* **2016,** *12* (17), 2354-64.

332. Guo, C.; Wang, Q.; He, J.; Wu, C.; Xie, K.; Liu, Y.; Zhang, W.; Cheng, H.; Hu, H.; Wang, C., Rational Design of Unique ZnO/ZnS@N-C Heterostructures for High-Performance Lithium-Ion Batteries. *J. Phys. Chem. Lett* **2020,** *11* (3), 905-912.

333. Shuang, W.; Kong, L.; Zhong, M.; Wang, D.; Liu, J.; Bu, X. H., Rational Design of Co Embedded N,S-Codoped Carbon Nanoplates as Anode Materials for High Performance Lithium-Ion Batteries. *Dalton Trans* **2018,** *47* (35), 12385-12392.

334. Zhang, W.; Huang, Z.; Zhou, H.; Li, S.; Wang, C.; Li, H.; Yan, Z.; Wang, F.; Kuang, Y., Facile Synthesis of ZnS Nanoparticles Decorated on Defective CNTs with Excellent Performances for Lithium-Ion Batteries Anode Material. *J. Alloys Compd.* **2020,** *816*, 152633.

335. Chen, Z.; Wu, R.; Liu, M.; Wang, H.; Xu, H.; Guo, Y.; Song, Y.; Fang, F.; Yu, X.; Sun, D., General Synthesis of Dual Carbon-Confined Metal Sulfides Quantum Dots toward High-Performance Anodes for Sodium-Ion Batteries. *Adv. Funct. Mater.* **2017,** *27* (38), 1702046.

336. Ye, J.; Zhao, H.; Song, W.; Wang, N.; Kang, M.; Li, Z., Enhanced Electronic Conductivity and Sodium-Ion Adsorption in N/S Co-Doped Ordered Mesoporous Carbon for High-Performance Sodium-Ion Battery Anode. *J. Power Sources* **2019,** *412*, 606-614.

337. Cao, Q. C.; Ding, X. B.; Li, F.; Qin, Y. H.; Wang, C., Zinc, Sulfur and Nitrogen Co-Doped Carbon from Sodium Chloride/Zinc Chloride-Assisted Pyrolysis of Thiourea/Sucrose for Highly Efficient Oxygen Reduction Reaction in Both Acidic and Alkaline Media. *J Colloid Interface Sci* **2020,** *576*, 139-146.

338. Xia, J.; Jiang, K.; Xie, J.; Guo, S.; Liu, L.; Zhang, Y.; Nie, S.; Yuan, Y.; Yan, H.; Wang, X., Tin Disulfide Embedded in N-, S-Doped Carbon Nanofibers as Anode Material for Sodium-Ion Batteries. *Chem. Eng. J.* **2019,** *359*, 1244-1251.

339. Yang, Z.; Wang, J.; Wu, H. T.; Kong, F. J.; Yin, W. Y.; Cheng, H. J.; Tang, X. Y.; Qian, B.; Tao, S.; Yi, J.; Ma, Y.-S.; Yuan, R.-X., Mofs Derived CoS Nanoparticles Embedded in N-Doped Carbon Nanosheets with Improved Electrochemical Performance for Lithium Ion Batteries. *Appl. Surf. Sci.* **2019,** *479*, 693-699.

340. Mao, M.; Jiang, L.; Wu, L.; Zhang, M.; Wang, T., The Structure Control of ZnS/Graphene Composites and Their Excellent Properties for Lithium-Ion Batteries. *J. Mater. Chem. A* **2015,** *3* (25), 13384-13389.

341. Zhu, X.; Li, J.; Ali, R. N.; Huang, M.; Liu, P.; Xiang, B., Toward a High-Performance Li-Ion Battery: Constructing a $Co_{1-X}S$/Zns@C Composite Derived from Metal-Organic Framework @3D Disordered Polystyrene Sphere Template. *Mater. Des.* **2018,** *160*, 636-641.

342. Park, G. D.; Choi, S. H.; Lee, J. K.; Kang, Y. C., One-Pot Method for Synthesizing Spherical-Like Metal Sulfide-Reduced Graphene Oxide Composite Powders with Superior Electrochemical Properties for Lithium-Ion Batteries. *Chemistry* **2014,** *20* (38), 12183-9.

343. Li, H.; Liang, M.; Sun, W.; Wang, Y., Bimetal-Organic Framework: One-Step Homogenous Formation and Its Derived Mesoporous Ternary Metal Oxide Nanorod for High-Capacity, High-Rate, and Long-Cycle-Life Lithium Storage. *Adv. Funct. Mater.* **2016,** *26* (7), 1098-1103.

344. Yang, J.; Zhang, Y.; Sun, C.; Guo, G.; Sun, W.; Huang, W.; Yan, Q.; Dong, X., Controlled Synthesis of Zinc Cobalt Sulfide Nanostructures in Oil Phase and Their Potential Applications in Electrochemical Energy Storage. *J. Mater. Chem. A* **2015,** *3* (21), 11462-11470.

345. Yuan, D.; Huang, G.; Yin, D.; Wang, X.; Wang, C.; Wang, L., Metal-Organic Framework Template Synthesis of $NiCo_2S_4$@C Encapsulated in Hollow Nitrogen-Doped Carbon Cubes with Enhanced Electrochemical Performance for Lithium Storage. *ACS Appl. Mater. Interfaces* **2017,** *9* (21), 18178-18186.

346. Liu, X.; Ye, Z., Nitroaromatics as High - Energy Organic Cathode Materials for Rechargeable Alkali - Ion (Li^+, Na^+, and K^+) Batteries. *Adv. Energy Mater.* **2020,** *11* (4), 2003281.

347. Jayaramulu, K.; Dubal, D. P.; Nagar, B.; Ranc, V.; Tomanec, O.; Petr, M.; Datta, K. K. R.; Zboril, R.; Gomez-Romero, P.; Fischer, R. A., Ultrathin Hierarchical Porous Carbon Nanosheets for High-Performance Supercapacitors and Redox Electrolyte Energy Storage. *Adv. Mater.* **2018,** *30* (15), e1705789.

348. Yang, R.; Guo, X.; Song, K.; Bai, X.; Jia, L.; Chen, X.; Wang, X.; Wang, J., Influence of Ph on the Crystal Structure of $NiMoO_4$ Nanomaterials and Their Supercapacitor Performances. *Ceram. Int.* **2021,** *47* (8), 11349-11357.

349. Guan, S.; Fu, X.; Lao, Z.; Jin, C.; Peng, Z., NiS-MoS_2 Hetero-Nanosheet Arrays on Carbon Cloth for High-Performance Flexible Hybrid Energy Storage Devices. *ACS Sustainable Chem. Eng.* **2019,** *7* (13), 11672-11681.

350. Asbani, B.; Robert, K.; Roussel, P.; Brousse, T.; Lethien, C., Asymmetric Micro-Supercapacitors Based on Electrodeposited RuO_2 and Sputtered Vn Films. *Energy Storage Mater.* **2021,** *37*, 207-214.

351. Xiong, S.; Jiang, S.; Wang, J.; Lin, H.; Lin, M.; Weng, S.; Liu, S.; Jiao, Y.; Xu, Y.; Chen, J., A High-Performance Hybrid Supercapacitor with Nio Derived NiO@Ni-MOF Composite Electrodes. *Electrochim. Acta* **2020,** *340*, 135956.

352. Yue, L.; Wang, X.; Sun, T.; Liu, H.; Li, Q.; Wu, N.; Guo, H.; Yang, W., Ni-MOF Coating MoS_2 Structures by Hydrothermal Intercalation as High-Performance Electrodes for Asymmetric Supercapacitors. *Chem. Eng. J.* **2019,** *375*, 121959.

353. Zhang, J.; Li, Y.; Han, M.; Xia, Q.; Chen, Q.; Chen, M., Constructing Ultra-Thin Ni-MOF@NiS_2 Nanosheets Arrays Derived from Metal Organic Frameworks for Advanced All-Solid-State Asymmetric Supercapacitor. *Mater. Res. Bull.* **2021,** *137*, 111186.

354. Zhang, D.; Guo, X.; Tong, X.; Chen, Y.; Duan, M.; Shi, J.; Jiang, C.; Hu, L.; Kong, Q.; Zhang, J., High-Performance Battery-Type Supercapacitor Based on Porous Biocarbon and Biocarbon Supported Ni-Co Layered Double Hydroxide. *J. Alloys Compd.* **2020,** *837*, 155529.

355. Elsonbaty, A.; Elshaer, A. M.; Harb, M.; Soliman, M.; Ebrahim, S.; Eltahan, A., Novel Zif67/Mn/Mwcnts Decorated with Layer Double Hydroxide Supercapacitor Electrodes. *Electrochim. Acta* **2021,** *368*, 137577.

356. Neeraj, N. S.; Mordina, B.; Srivastava, A. K.; Mukhopadhyay, K.; Prasad, N. E., Impact of Process Conditions on the Electrochemical Performances of $NiMoO_4$ Nanorods and Activated Carbon Based Asymmetric Supercapacitor. *Appl. Surf. Sci.* **2019,** *473*, 807-819.

357. Seevakan, K.; Manikandan, A.; Devendran, P.; Shameem, A.; Alagesan, T., Microwave Combustion Synthesis, Magneto-Optical and Electrochemical Properties of $NiMoO_4$ Nanoparticles for Supercapacitor Application. *Ceram. Int.* **2018,** *44* (12), 13879-13887.

358. Hong, J.; Lee, Y. W.; Hou, B.; Ko, W.; Lee, J.; Pak, S.; Hong, J.; Morris, S. M.; Cha, S.; Sohn, J. I.; Kim, J. M., Solubility-Dependent $NiMoO_4$ Nanoarchitectures: Direct Correlation between Rationally Designed Structure and Electrochemical Pseudokinetics. *ACS Appl Mater Interfaces* **2016,** *8* (51), 35227-35234.

359. Hussain, S.; Javed, M. S.; Asim, S.; Shaheen, A.; Khan, A. J.; Abbas, Y.; Ullah, N.; Iqbal, A.; Wang, M.; Qiao, G.; Yun, S., Novel Gravel-Like $NiMoO_4$ Nanoparticles on Carbon Cloth for Outstanding Supercapacitor Applications. *Ceram. Int.* **2020,** *46* (5), 6406-6412.

360. Wei, C.; Huang, Y.; Yan, J.; Chen, X.; Zhang, X., Synthesis of Hierarchical Carbon Sphere@ $NiMoO_4$ Composite Materials for Supercapacitor Electrodes. *Ceram. Int.* **2016,** *42* (14), 15694-15700.

361. Jiang, B.; Ban, X.; Wang, Q.; Cheng, K.; Zhu, K.; Ye, K.; Wang, G.; Cao, D.; Yan, J., Anionic P-Substitution toward Ternary Ni-S-P Nanoparticles Immobilized Graphene with Ultrahigh Rate and Long Cycle Life for Hybrid Supercapacitors. *J. Mater. Chem. A* **2019,** *7* (42), 24374-24388.

362. Mi, L.; Ding, Q.; Chen, W.; Zhao, L.; Hou, H.; Liu, C.; Shen, C.; Zheng, Z., 3D Porous Nano/Micro Nickel Sulfides with Hierarchical Structure: Controlled Synthesis, Structure Characterization and Electrochemical Properties. *Dalton Trans* **2013,** *42* (16), 5724-30.

363. Azizi Darsara, S.; Seifi, M.; Askari, M. B.; Osquian, M., Hierarchical 3D Starfish-Like Ni_3S_4-NiS on Reduced Graphene Oxide for High-Performance Supercapacitors. *Ceram. Int.* **2021**.

364. Wang, L.; Liu, J.; Zhang, L. L.; Dai, B.; Xu, M.; Ji, M.; Zhao, X. S.; Cao, C.; Zhang, J.; Zhu, H., Rigid Three-Dimensional Ni_3S_4 Nanosheet Frames: Controlled Synthesis and Their Enhanced Electrochemical Performance. *RSC Adv.* **2015,** *5* (11), 8422-8426.

365. Yan, J.; Wang, S.; Chen, Y.; Yuan, M.; Huang, Y.; Lian, J.; Qiu, J.; Bao, J.; Xie, M.; Xu, H.; Li, H.; Zhao, Y., Smart in Situ Construction of NiS/MoS_2 Composite Nanosheets with Ultrahigh Specific Capacity for High-Performance Asymmetric Supercapacitor. *J. Alloys Compd.* **2019,** *811*, 151915.

366. Wu, W.; Wang, L.; Li, Y.; Zhang, F.; Lin, L.; Niu, S.; Chenet, D.; Zhang, X.; Hao, Y.; Heinz, T. F.; Hone, J.; Wang, Z. L., Piezoelectricity of Single-Atomic-Layer MoS_2 for Energy Conversion and Piezotronics. *Nature* **2014,** *514* (7523), 470-4.

367. Huang, L.; Hou, H.; Liu, B.; Zeinu, K.; Zhu, X.; Yuan, X.; He, X.; Wu, L.; Hu, J.; Yang, J., Ultrahigh-Performance Pseudocapacitor Based on Phase-Controlled Synthesis of MoS_2 Nanosheets Decorated Ni_3S_2 Hybrid Structure through Annealing Treatment. *Appl. Surf. Sci.* **2017,** *425*, 879-888.

368. Krishnamoorthy, K.; Veerasubramani, G. K.; Radhakrishnan, S.; Kim, S. J., Supercapacitive Properties of Hydrothermally Synthesized Sphere Like MoS_2 Nanostructures. *Mater. Res. Bull.* **2014,** *50*, 499-502.

369. Liu, Q.; Hong, X.; You, X.; Zhang, X.; Zhao, X.; Chen, X.; Ye, M.; Liu, X., Designing Heterostructured Metal Sulfide Core-Shell Nanoneedle Films as Battery-Type Electrodes for Hybrid Supercapacitors. *Energy Storage Mater.* **2020,** *24*, 541-549.

370. Zhang, X.; Liang, H.; Li, H.; Xia, Y.; Zhu, X.; Peng, L.; Zhang, W.; Liu, L.; Zhao, T.; Wang, C.; Zhao, Z.; Hung, C. T.; Zagho, M. M.; Elzatahry, A. A.; Li, W.; Zhao, D., Sequential Chemistry toward Core-Shell Structured Metal Sulfides as Stable and Highly Efficient Visible-Light Photocatalysts. *Angew. Chem. Int. Ed. Engl.* **2020,** *59* (8), 3287-3293.

371. Patil, D. S.; Pawar, S. A.; Shin, J. C., Core-Shell Structure of Co_3O_4@CdS for High Performance Electrochemical Supercapacitor. *Chem. Eng. J.* **2018,** *335*, 693-702.

372. Dong, J. Y.; Xu, J. C.; Hui, K. N.; Yang, Y.; Su, S. C.; Li, L.; Zhang, X. T.; Ng, K. W.; Wang, S. P.; Tang, Z. K., Homogeneous Core/Shell $NiMoO_4$ and Activated Carbon for High Performance Asymmetric Supercapacitor. *Nanomaterials* **2019,** *9* (7).

373. Zhang, Z.; Zhang, H.; Zhang, X.; Yu, D.; Ji, Y.; Sun, Q.; Wang, Y.; Liu, X., Facile Synthesis of Hierarchical $CoMoO_4$@ $NiMoO_4$ Core-Shell Nanosheet Arrays on Nickel Foam as an

Advanced Electrode for Asymmetric Supercapacitors. *J. Mater. Chem. A* **2016,** *4* (47), 18578-18584.

374. Liang, H.; Lin, T.; Wang, S.; Jia, H.; Li, C.; Cao, J.; Feng, J.; Fei, W.; Qi, J., A Free-Standing Manganese Cobalt Sulfide@Cobalt Nickel Layered Double Hydroxide Core-Shell Heterostructure for an Asymmetric Supercapacitor. *Dalton Trans* **2020,** *49* (1), 196-202.

375. Luo, X.; Zhou, Q.; Du, S.; Li, J.; Zhong, J.; Deng, X.; Liu, Y., Porous Co_9S_8/Nitrogen, Sulfur-Doped Carbon@Mo_2C Dual Catalyst for Efficient Water Splitting. *ACS Appl Mater Interfaces* **2018,** *10* (26), 22291-22302.

376. Chen, S.; Zhang, M.; Jiang, G.; Zhang, Z.; Zhou, X., $NiMoO_4$ Nanorods@Hydrous $NiMoO_4$ Nanosheets Core-Shell Structured Arrays for Pseudocapacitor Application. *J. Alloys Compd.* **2020,** *814*, 152253.

377. Yang, X.; Mao, J.; Niu, H.; Wang, Q.; Zhu, K.; Ye, K.; Wang, G.; Cao, D.; Yan, J., NiS_2/MoS_2 Mixed Phases with Abundant Active Edge Sites Induced by Sulfidation and Graphene Introduction Towards High-Rate Supercapacitors. *Chem. Eng. J.* **2021,** *406*, 126713.

378. Yu, B.; Jiang, G.; Xu, W.; Cao, C.; Liu, Y.; Lei, N.; Evariste, U.; Ma, P., Construction of $NiMoO_4$/ $CoMoO_4$ Nanorod Arrays Wrapped by Ni-Co-S Nanosheets on Carbon Cloth as High Performance Electrode for Supercapacitor. *J. Alloys Compd.* **2019,** *799*, 415-424.

379. Yang, X.; Zhao, L.; Lian, J., Arrays of Hierarchical Nickel Sulfides/MoS_2 Nanosheets Supported on Carbon Nanotubes Backbone as Advanced Anode Materials for Asymmetric Supercapacitor. *J. Power Sources* **2017,** *343*, 373-382.

380. Li, Y.; Cao, L.; Qiao, L.; Zhou, M.; Yang, Y.; Xiao, P.; Zhang, Y., Ni-Co Sulfide Nanowires on Nickel Foam with Ultrahigh Capacitance for Asymmetric Supercapacitors. *J. Mater. Chem. A* **2014,** *2* (18), 6540-6548.

381. Yu, L.; Chen, G. Z., Supercapatteries as High-Performance Electrochemical Energy Storage Devices. *Electro.Energy.Rev* **2020,** *3* (2), 271-285.

382. Sarkar, D.; Das, D.; Das, S.; Kumar, A.; Patil, S.; Nanda, K. K.; Sarma, D. D.; Shukla, A., Expanding Interlayer Spacing in MoS_2 for Realizing an Advanced Supercapacitor. *ACS Energy. Lett* **2019,** *4* (7), 1602-1609.

383. Ruan, Y.; Jiang, J.; Wan, H.; Ji, X.; Miao, L.; Peng, L.; Zhang, B.; Lv, L.; Liu, J., Rapid Self-Assembly of Porous Square Rod-Like Nickel Persulfide Via a Facile Solution Method for High-Performance Supercapacitors. *J. Power Sources* **2016,** *301*, 122-130.

384. Kumbhar, V. S.; Nguyen, V. Q.; Lee, Y. R.; Lokhande, C. D.; Kim, D.-H.; Shim, J.-J., Electrochemically Growth-Controlled Honeycomb-Like $NiMoO_4$ Nanoporous Network on Nickel Foam and Its Applications in All-Solid-State Asymmetric Supercapacitors. *New J. Chem.* **2018,** *42* (18), 14805-14816.

385. Pang, H.; Wei, C.; Li, X.; Li, G.; Ma, Y.; Li, S.; Chen, J.; Zhang, J., Microwave-Assisted Synthesis of NiS_2 Nanostructures for Supercapacitors and Cocatalytic Enhancing Photocatalytic H2 Production. *Sci Rep* **2014,** *4*, 3577.

386. Karade, S. S.; Lalwani, S.; Eum, J.-H.; Kim, H., Coin Cell Fabricated Symmetric Supercapacitor Device of Two-Steps Synthesized V_2O_5 Nanorods. *J. Electroanal. Chem.* **2020,** *864*, 114080.

387. Chodankar, N. R.; Bagal, I. V.; Ryu, S. W.; Kim, D.-H., Hybrid Material Passivation Approach to Stabilize the Silicon Nanowires in Aqueous Electrolyte for High-Energy Efficient Supercapacitor. *Chem. Eng. J.* **2019,** *362*, 609-618.

388. Seeber, R.; Zanardi, C.; Inzelt, G., The Inherent Coupling of Charge Transfer and Mass Transport Processes: The Curious Electrochemical Reversibility. *ChemTexts* **2016,** *2* (2).

389. Lokhande, P. E.; Chavan, U. S.; Pandey, A., Materials and Fabrication Methods for Electrochemical Supercapacitors: Overview. *Electro.Energy.Rev* **2019,** *3* (1), 155-186.

390. Qin, S.; Yao, T.; Guo, X.; Chen, Q.; Liu, D.; Liu, Q.; Li, Y.; Li, J.; He, D., MoS_2/Ni_3S_4 Composite Nanosheets on Interconnected Carbon Shells as an Excellent Supercapacitor Electrode Architecture for Long Term Cycling at High Current Densities. *Appl. Surf. Sci.* **2018,** *440*, 741-747.

391. Hou, S.; Lian, Y.; Xu, Z.; Wang, D.; Ban, C.; Zhao, J.; Zhang, H., Construction of Ball-Flower Like $NiS_2@MoS_2$ Composite for High Performance Supercapacitors. *Electrochim. Acta* **2020,** *330*, 135208.

392. Wan, L.; Liu, J.; Li, X.; Zhang, Y.; Chen, J.; Du, C.; Xie, M., Fabrication of Core-Shell $NiMoO_4@MoS_2$ Nanorods for High-Performance Asymmetric Hybrid Supercapacitors. *Int. J. Hydrog. Energy* **2020,** *45* (7), 4521-4533.

393. Zhang, L.; Zheng, D.; Pei, S.; Ye, L.; Geng, S.; Lian, J., Rational Fabrication of Nanosheet-Dewy $NiMoO_4/Ni_3S_2$ Nanohybrid for Efficient Hybrid Supercapacitor. *J. Alloys Compd.* **2019,** *783*, 399-408.

Appendix

The extra figures and tables are listed below that are mentioned in the thesis.

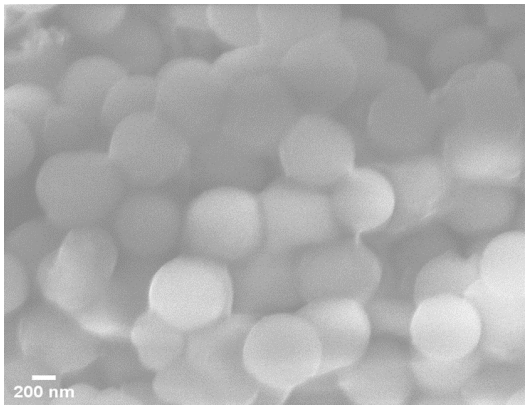

Figure S4. 1 High-magnification SEM image of as-synthesized CoNi precursor.

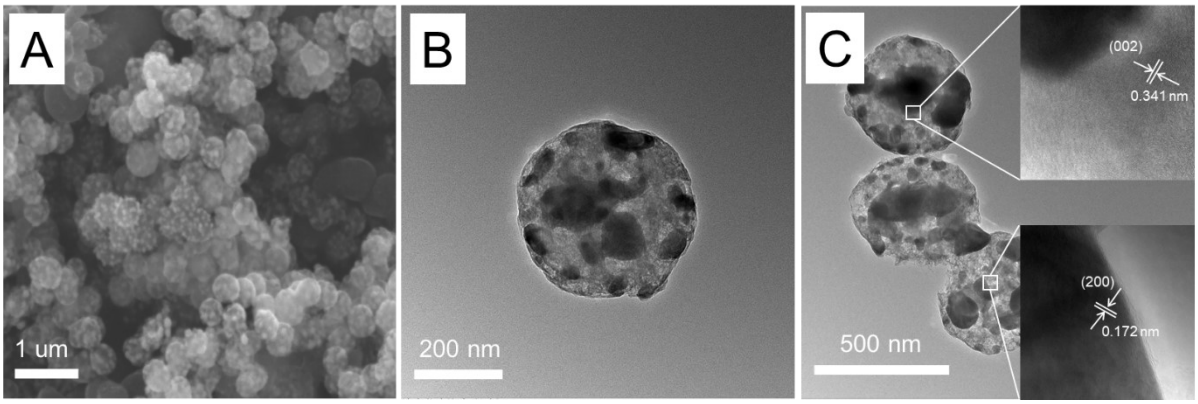

Figure S4. 2 (A) High-magnification SEM image of as-synthesized N-Ni/PCS; (B) TEM image of N-Ni/PCS; (C) HRTEM image of the selected area of N-Ni/PCS composites spheres.

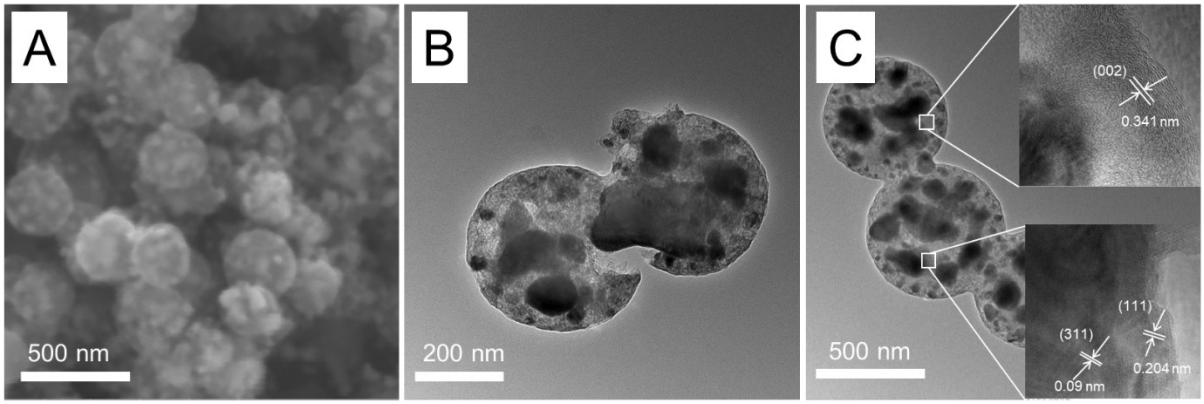

Figure S4. 3 (A) High-magnification SEM image of as-synthesized N-Co/PCS; (B) TEM image of N-Co/PCS; (C) HRTEM image of selected area of N-Co/PCS composites spheres.

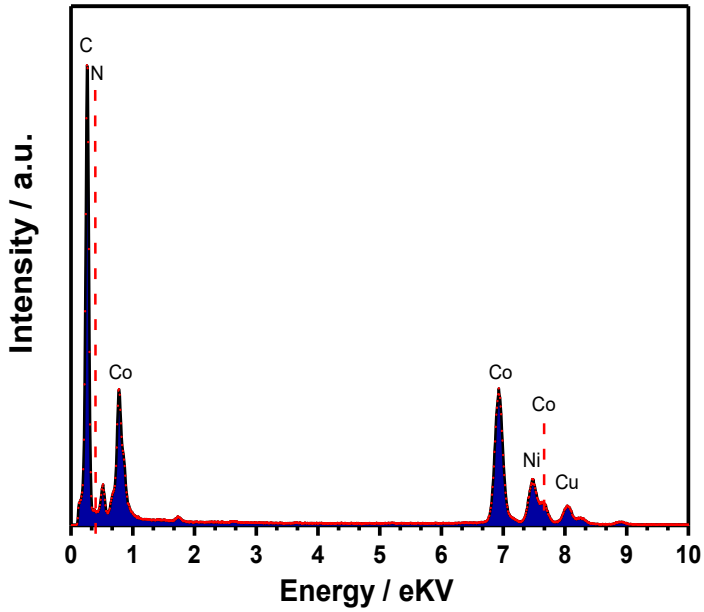

Figure S4. 4 EDX spectrum of N-CoNi/PCS.

Table S4. 1 The lattice parameters are between pure Co (ICSD No. 622442), pure Ni (ICSD No. 260172) and Co1Ni1 (ICSD NO. 187983).

Metal	Lattice Spacing (nm)		
	(111)	(200)	(311)
Co	0.204	0.177	0.107
Ni	0.203	0.176	0.106
Co1Ni1	0.204	0.177	0.107

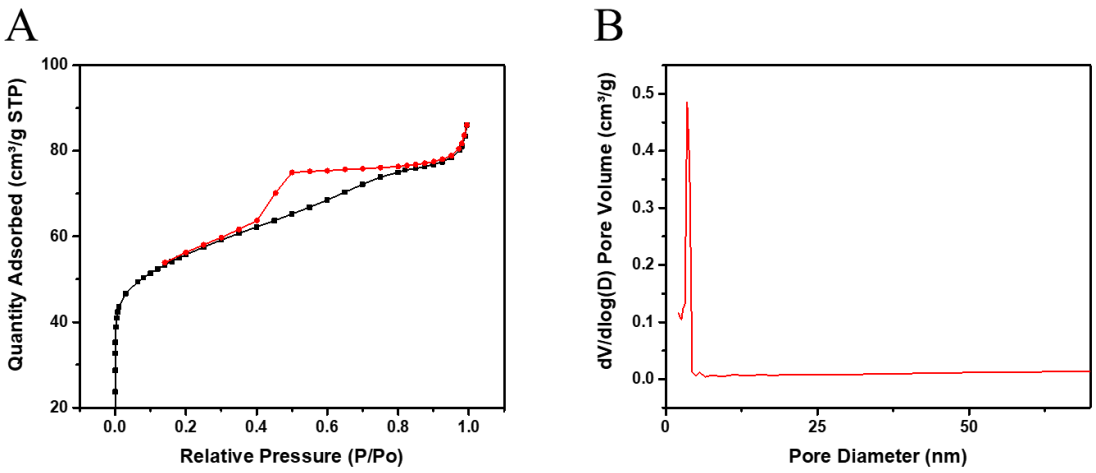

Figure S4. 5 (A) N_2 adsorption-desorption isotherms of CoNi/PCS; (B) Barrett-Joyner-Halenda pore size distribution profile of CoNi/PCS.

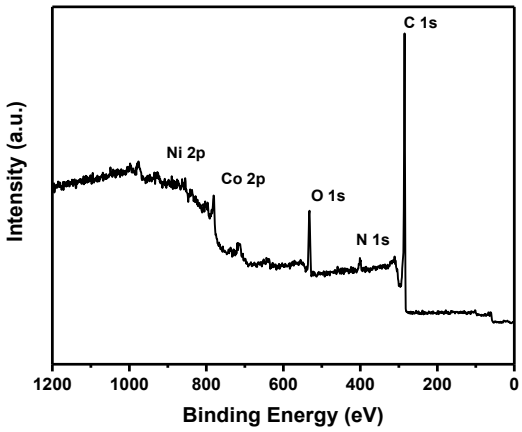

Figure S4. 6 The survey-level scan XPS spectrum of N-CoNi/PCS.

Table S4. 2 Elements distribution from XPS spectrum of N-CoNi/PCS.

Elements	Atoms %
Co	2.62
Ni	1.45
N	4.77
C	91.16

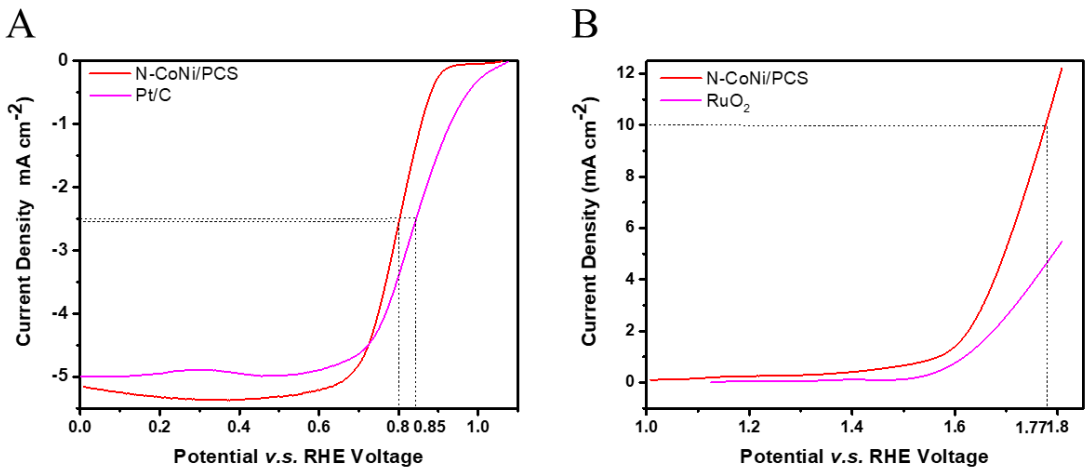

Figure S4. 7 (A) ORR curves of N-CoNi/PCS electrocatalysts and Pt/C at 1600 rpm rotating speed, respectively; (B) OER polarization curves of N-CoNi/PCS electrocatalysts and RuO2 at 1600 rpm rotating speed, respectively.

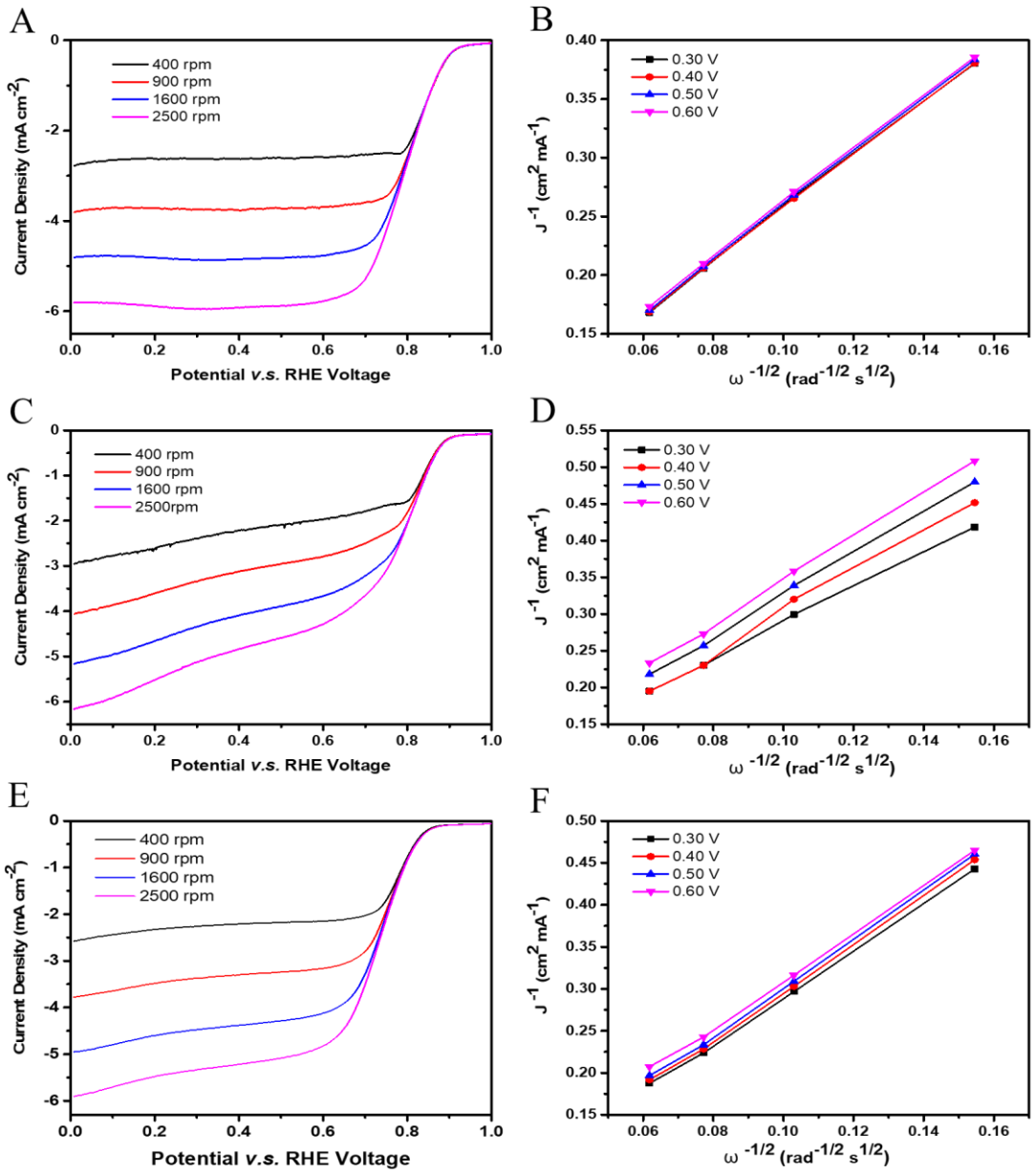

Figure S4. 8 ORR polarization curves of (A) N-Co/PCS, (C) N-Ni/PCS and (E) CoNi/PCS at different rotating speeds (400 to 2500 rpm); (B), (D) and (F) K-L plot derived from (A), (C) and (E), respectively.

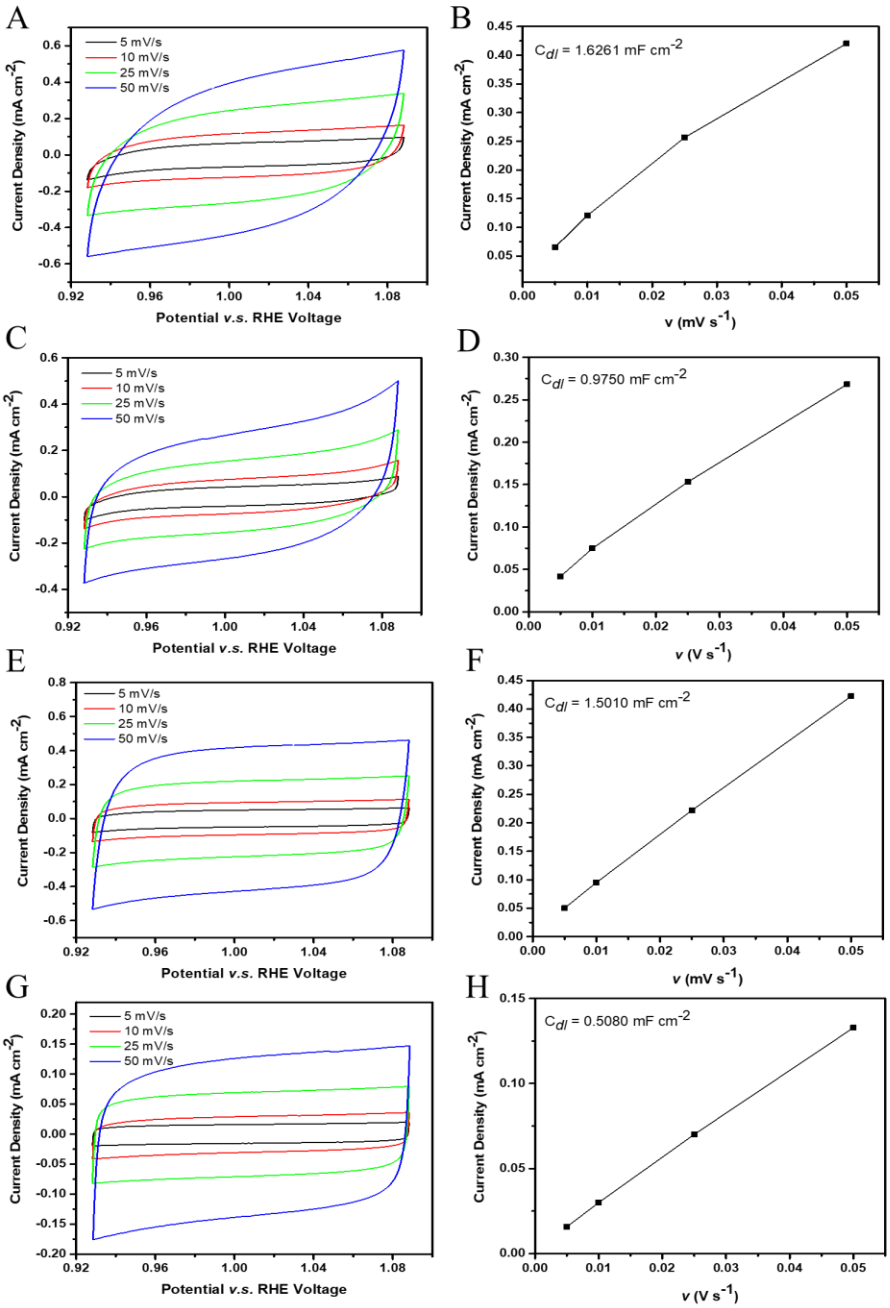

Figure S4. 9 CV curves of (A) N-Co/Ni/PCS, (C) N-Co/PCS, (E) N-Ni/PCS and (G) CoNi/PCS at scan rates of 5, 10, 25, and 50 mV s-1 in 0.1 M KOH aqueous electrolyte; (B), (D), (F) and (H) current density (taken at the potential of 1.00 V) as a function of scan rate derived from (A), (C), (E) and (G), respectively.

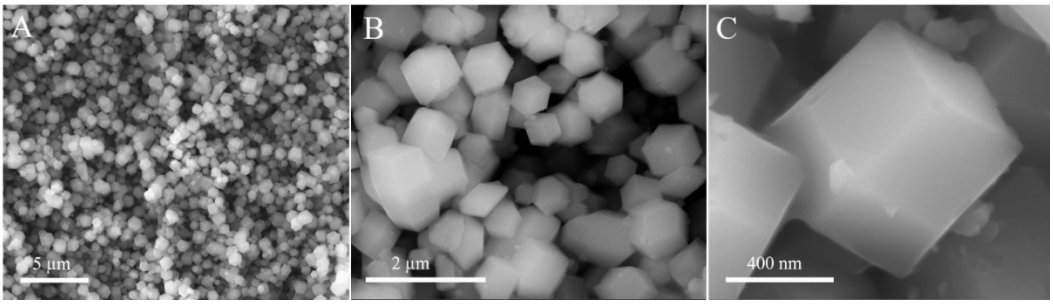

Figure S4. 10 (A)-(C) Low- and high-magnification SEM image of as-synthesized Co/Zn-ZIF-67 precursor. The rhombic dodecahedron morphology of Co/Zn-ZIF-67 precursor confirms the successful synthesis of MOF structure.

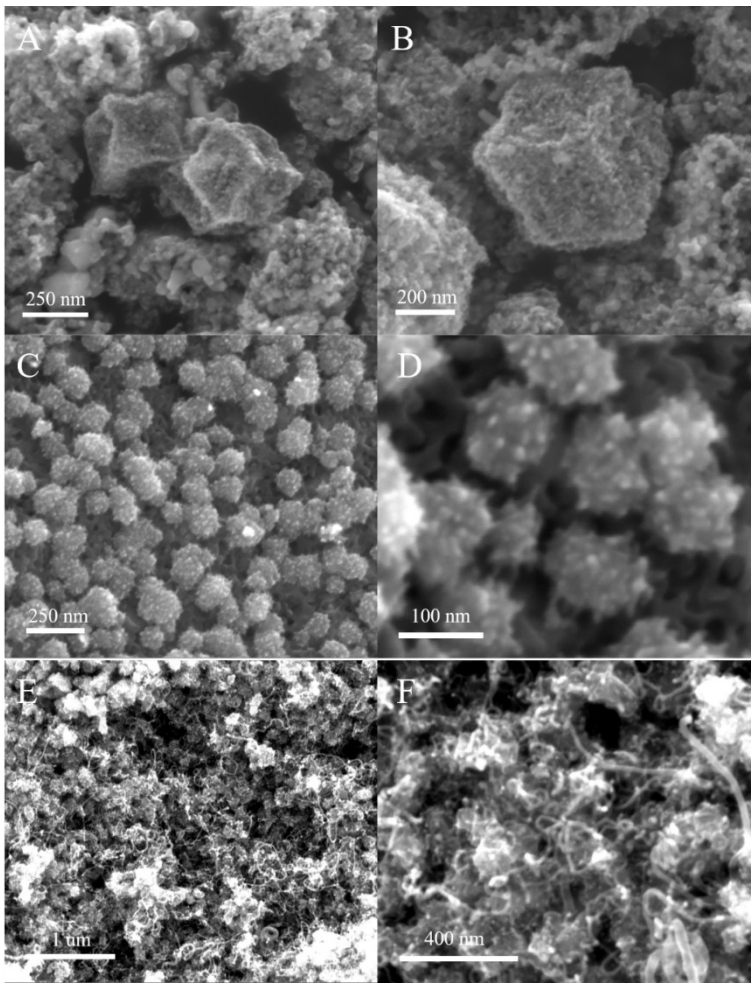

Figure S4. 11 Low- and high-magnification SEM image of as-synthesized (A) and (B) N,S-Co/ZIF, (C) and (D) N,S-Zn/ZIF, and (E) and (F) Co/Zn-ZIF.

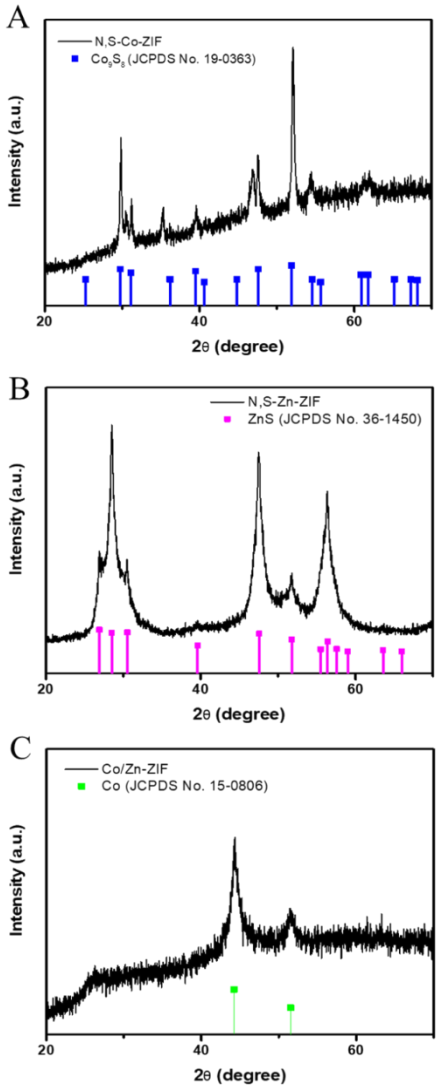

Figure S4. 12 Powder XRD patterns of N,S-Co-ZIF (A), N,S-Zn-ZIF (B), and Co/Zn-ZIF (C).

Table S4. 3 Crystal structural parameters of $Zn_{0.76}Co_{0.24}S$, $Co_{1-x}S_x$ and ZnS.

Compounds	Crystal system	*a*(Å)	*b* (Å)	*c* (Å)	*α*	*β*	*γ*	V (Å^3)
$Zn_{0.76}Co_{0.24}S$	F-43m	5.3995(1)	5.3995(1)	5.3995(1)	90º	90º	90º	157.42(1)
$Co_{1-x}S_x$	P63/mmc	3.3800(4)	3.3800(4)	5.1773(1)	90º	90º	120º	51.05(3)
ZnS	P63mc	3.8144(9)	3.8144(9)	6.2583(6)	90º	90º	120º	78.87(3)

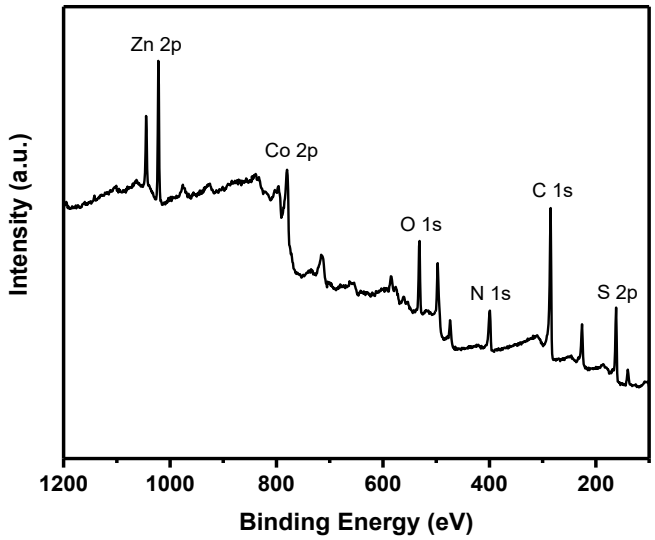

Figure S4. 13 The survey-level scan XPS spectrum of N,S-Co/Zn-ZIF.

Table S4. 4 Elements distribution from XPS spectrum of N,S-Co/Zn-ZIF.

Elements	Atoms %
Co	5.09
Zn	4.35
N	11.25
C	56.97
S	11.78
O	10.57

Table S4. 5 Elements distribution from XPS spectrum of Co/Zn-ZIF.

Elements	Atoms %
Co	1.49
Zn	1.44
N	9.55
C	84.55
O	3.02

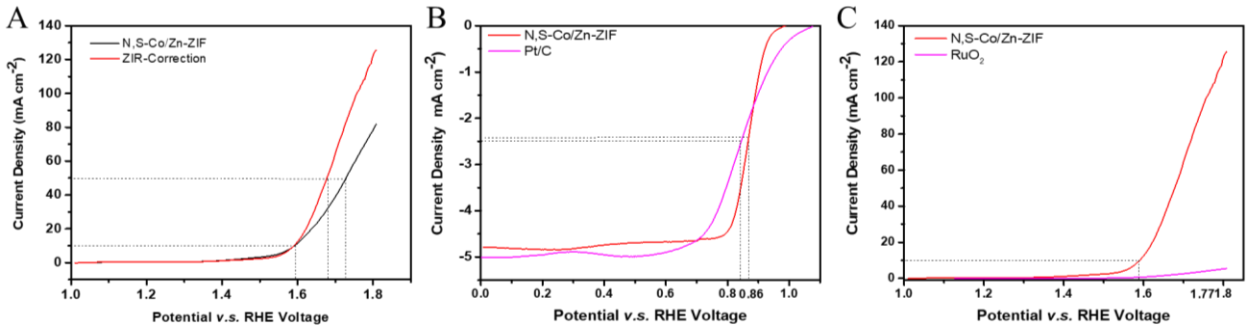

Figure S4. 14 (A) OER polarization curves of N,S-Co/Zn-ZIF electrocatalysts with ZIR-Correction; (B) ORR curves of N,S-Co/Zn-ZIF electrocatalysts and Pt/C in 0.1M KOH at 1600 rpm rotating speed, respectively; (C) OER polarization curves of N,S-Co/Zn-ZIF electrocatalysts and RuO_2 in 1M KOH at 1600 rpm rotating speed, respectively.

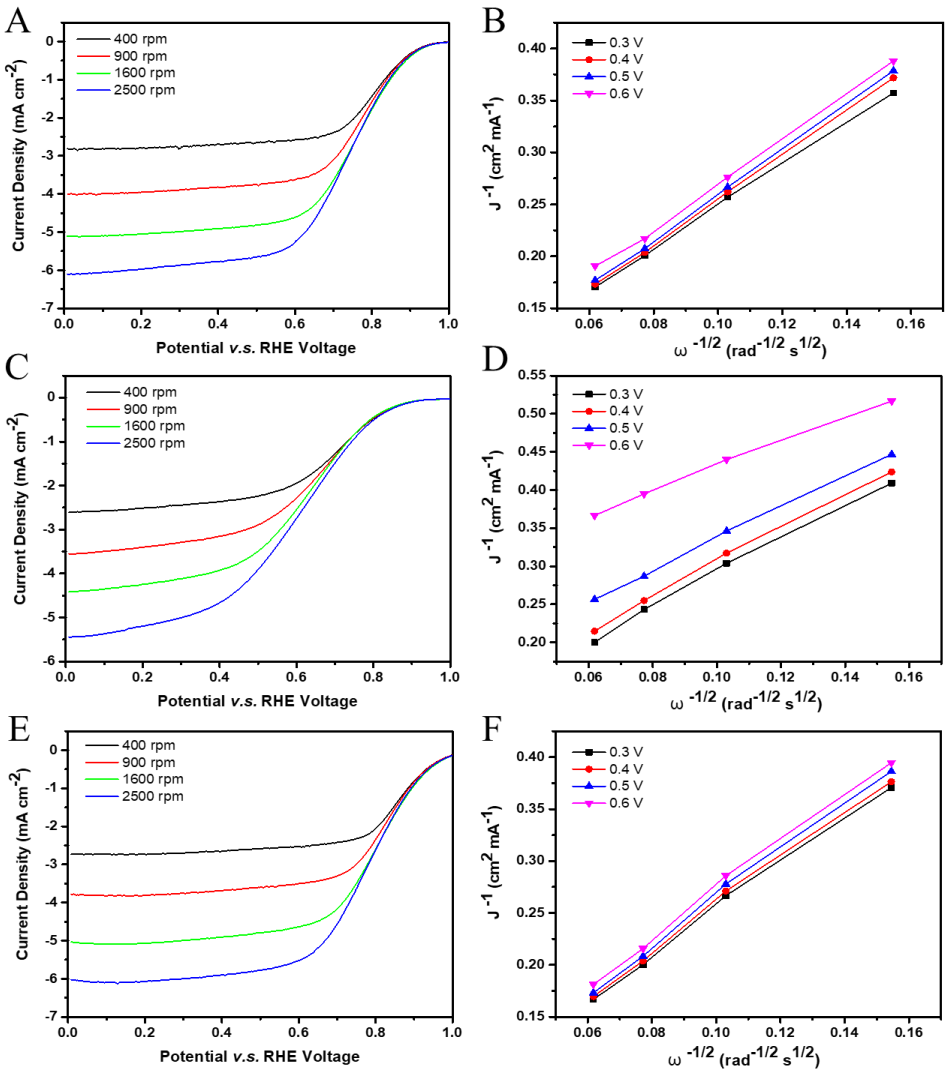

Figure S4. 15 (A), (C) and (E) ORR polarization curves of N,S-Co-ZIF, N,S-Zn-ZIF and Co/Zn-ZIF in 0.1M KOH at different rotating speeds (400 to 2500 rpm); (B), (D) and (F) K-L plot derived from (A), (C) and (E).

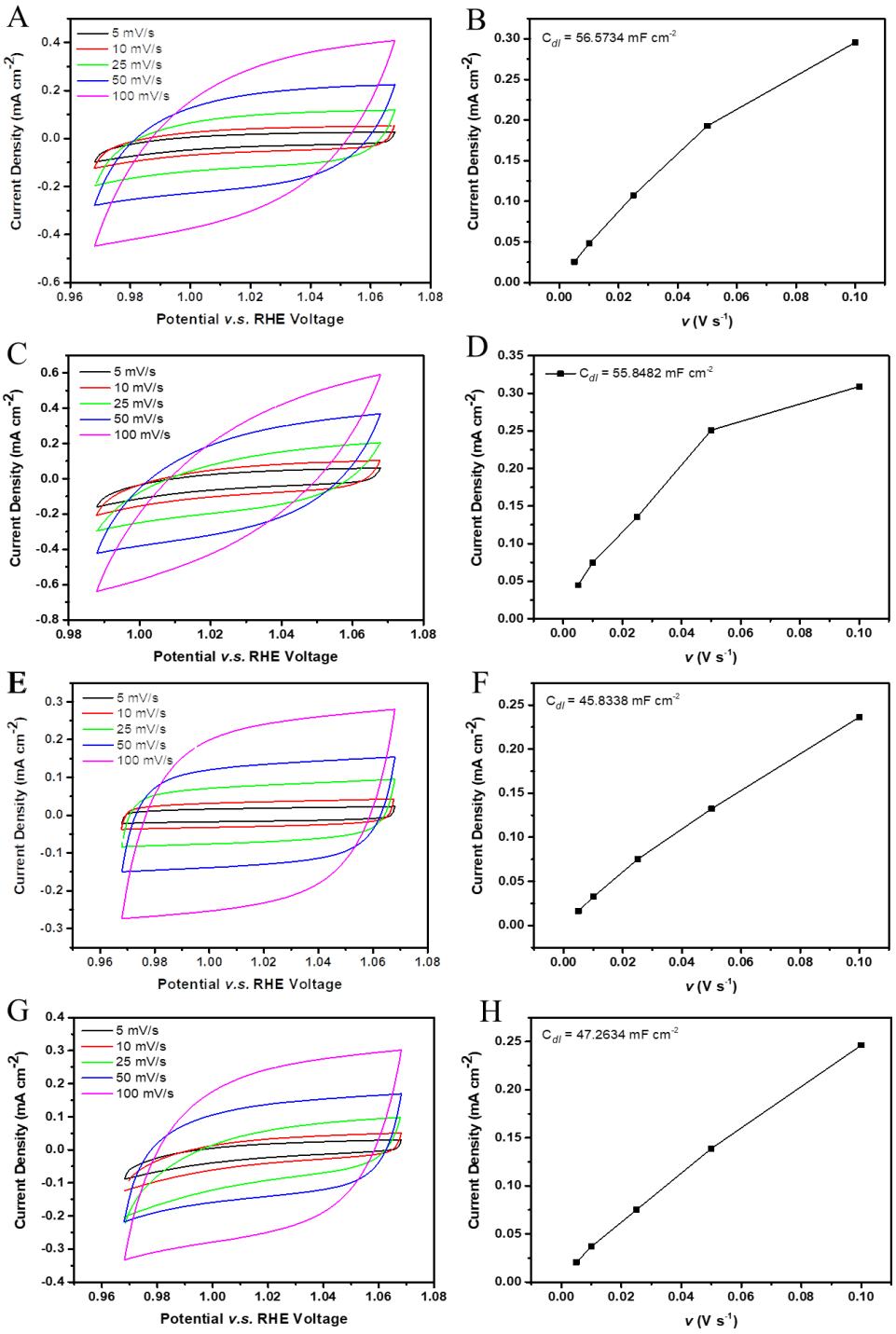

Figure S4. 16 CV curves of (A), (C), (E) and (G) N,S-Co-ZIF, N,S-Zn-ZIF and Co/Zn-ZIF at scan rates of 5, 10, 25, and 50 mV s-1 in 0.1M KOH aqueous electrolyte; (B), (D), (F)and (H) current density (taken at the potential of 1.00 V) as a function of scan rate derived from (A), (C), (E) and (G).

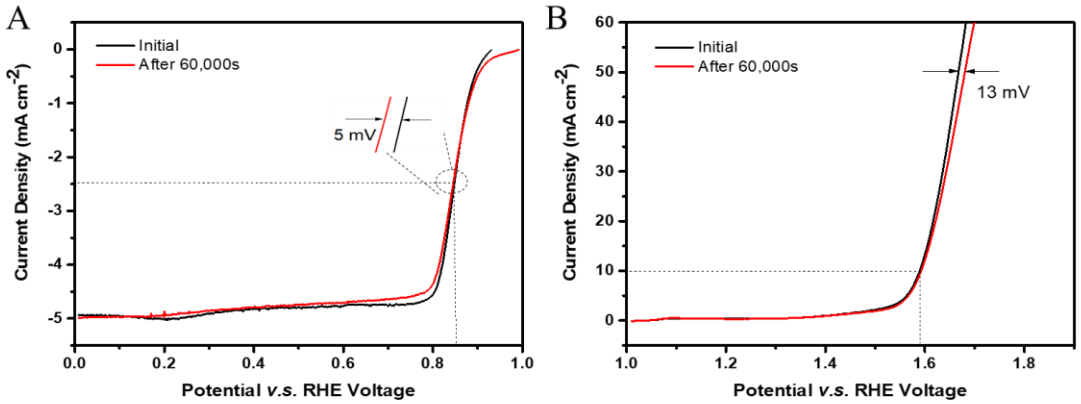

Figure S4. 17 (A) Comparison ORR polarization curves of N,S-Co/Zn-ZIF before and after 60,000s; (B) OER polarization curves of N,S-Co/Zn-ZIF before and after 60,000s.

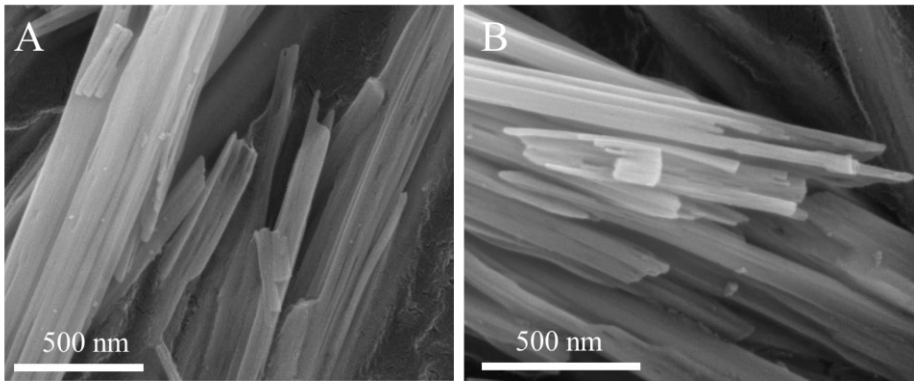

Figure S4. 18 SEM images of $NiMoO_4$ nanorods.

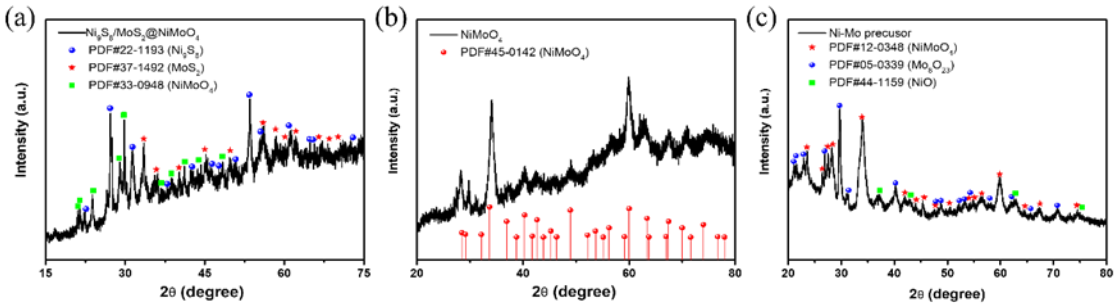

Figure S4. 19 XRD pattern of (A) Ni_9S_8/MoS_2@$NiMoO_4$, (B) $NiMoO_4$ and (C) Ni-Mo precursor

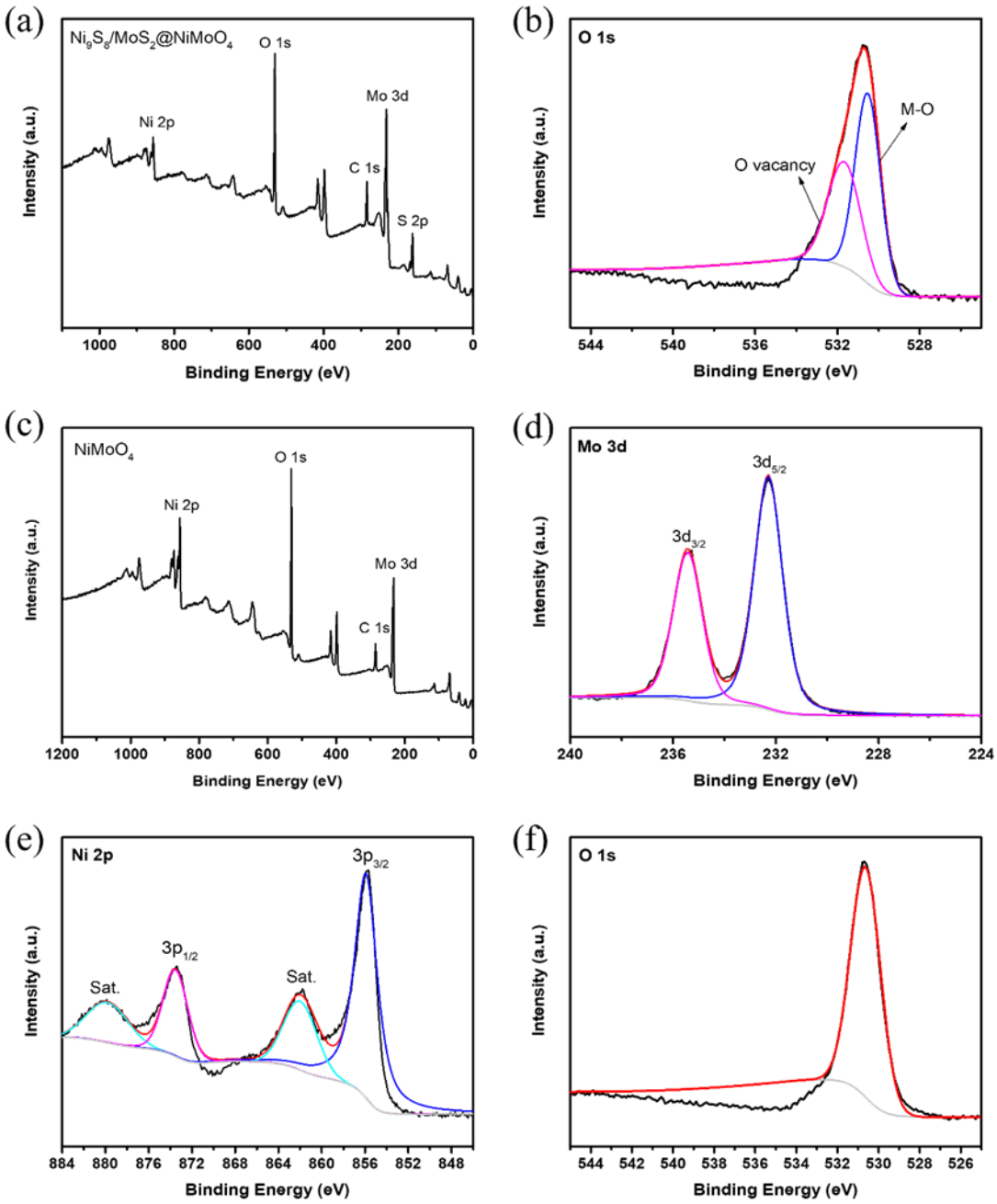

Figure S4. 20 XPS survey spectrum (A), and high resolution XPS spectrum of (B) O 1s in Ni_9S_8/MoS_2@$NiMoO_4$; (C) XPS survey spectrum, and high-resolution XPS spectrum of (D) Mo 3d, (E) Ni 2p, and (F) O 2p of $NiMoO_4$.

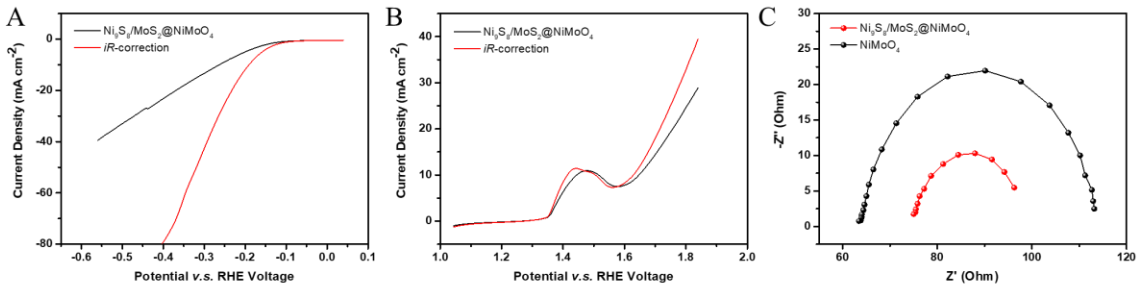

Figure S4. 21 (A) HER polarization curves of $Ni_9S_8/MoS_2@NiMoO_4$ electrocatalysts with *iR*-correction; (B) OER polarization curves of $Ni_9S_8/MoS_2@NiMoO_4$ electrocatalysts with *iR*-correction; (C) EIS curves for $Ni_9S_8/MoS_2@NiMoO_4$ and $NiMoO_4$ after stability test.

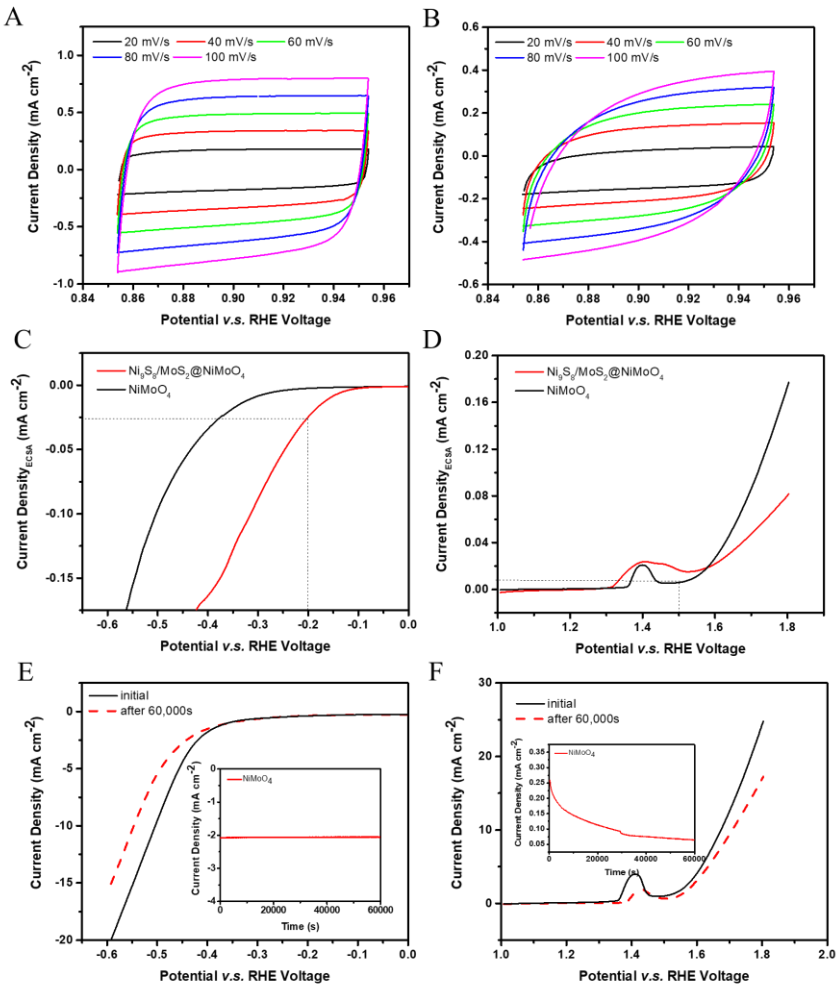

Figure S4. 22 CV curves of (A) and (B) Ni_9S_8/MoS_2@$NiMoO_4$ and $NiMoO_4$ at scan rates of 20, 40, 60, 80 and 100 mV s^{-1} in 1.0 M KOH aqueous electrolyte; ECSA-normalized LSV curves of (C) HER and (D) OER for different electrocatalysts; (E) Initial and after stability test polarization curves of $NiMoO_4$ of HER (inset: stability measurement by chronoamperometry in 1.0 M KOH for the duration of 60,000s); (F) Initial and after stability test polarization curves of $NiMoO_4$ of OER (inset: stability measurement by chronoamperometry 1.0 M KOH for the duration of 60,000s).

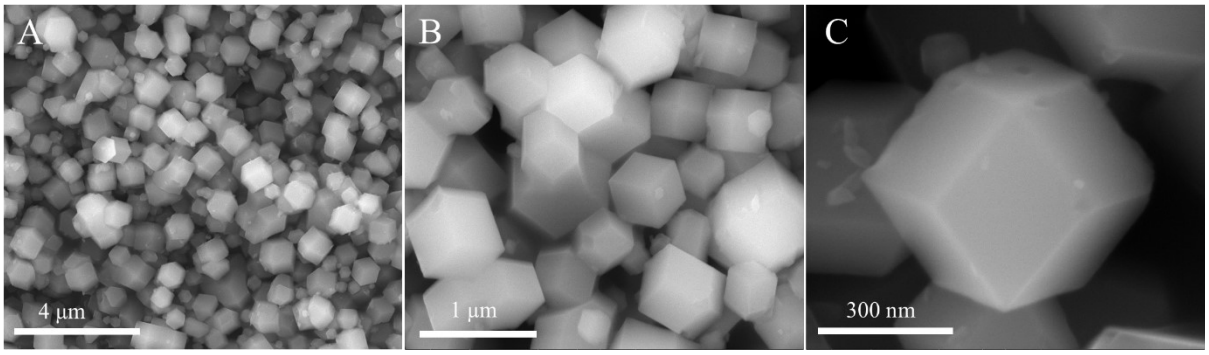

Figure S5. 1 (A)-(C) Low- and high-magnification SEM image of as-synthesized Co/Zn-ZIF-67 precursor.

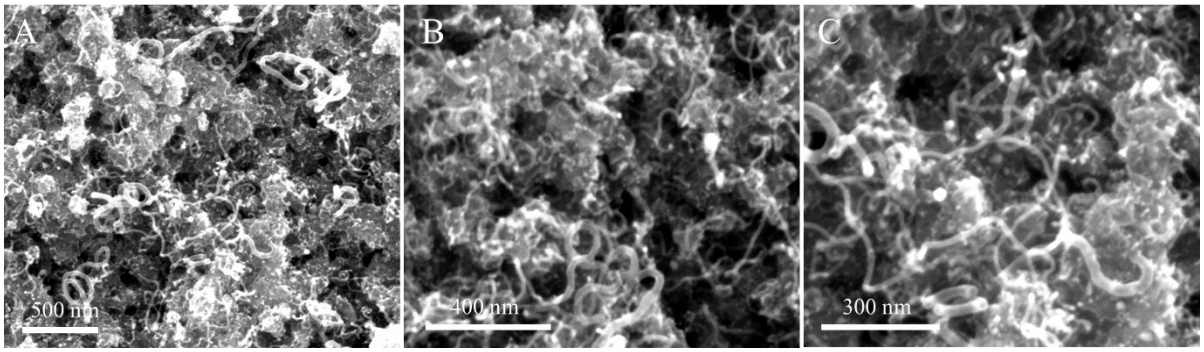

Figure S5. 2 Low- and high-magnification SEM image of as-synthesized Co/Zn@CN.

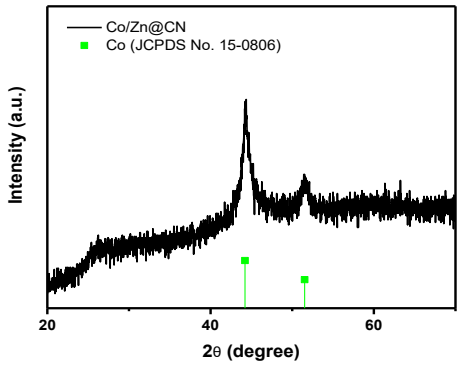

Figure S5. 3 Powder XRD patterns Co/Zn@CN.

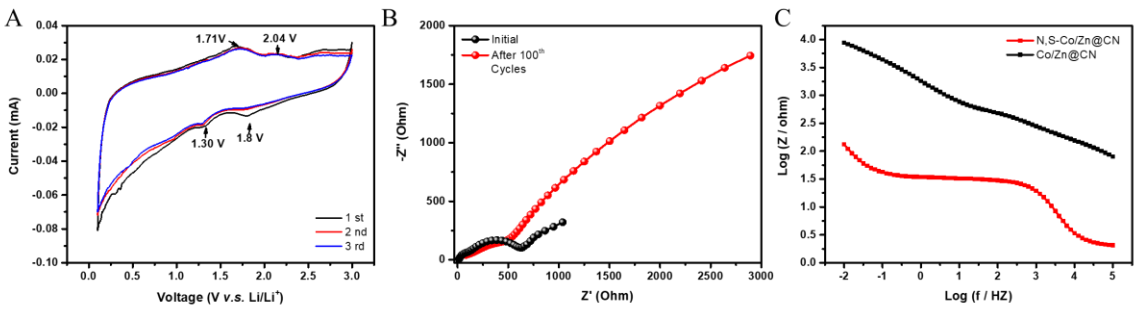

Figure S5. 4 (A) Cyclic voltammograms of Co/Zn@CN electrode at a scanning rate of 0.02 mV s^{-1}; (B) Nyquist plots of Co/Zn@CN electrode tested at open circuit potential initial and after 100 cycles of galvanostatic discharge/charge at 150 mA g^{-1}; (C) Bode plot of N,S-Co/Zn@CN and Co/Zn@CN.

Table S5. 1 Elements distribution from XPS spectrum of N,S-Co/Zn@CN.

Elements	Atoms %
Co	4.62
Zn	4.64
N	11.30
C	55.27
S	13.74
O	10.43

Table S5. 2 Elements distribution from XPS spectrum of Co/Zn@CN.

Elements	Atoms %
Co	1.21
Zn	1.45
N	9.92
C	84.55
O	2.86

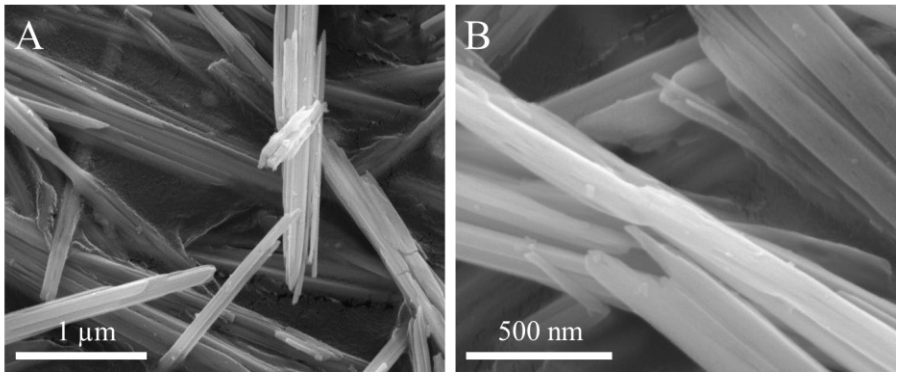

Figure S5. 5 SEM images of $NiMoO_4$ nanorods.

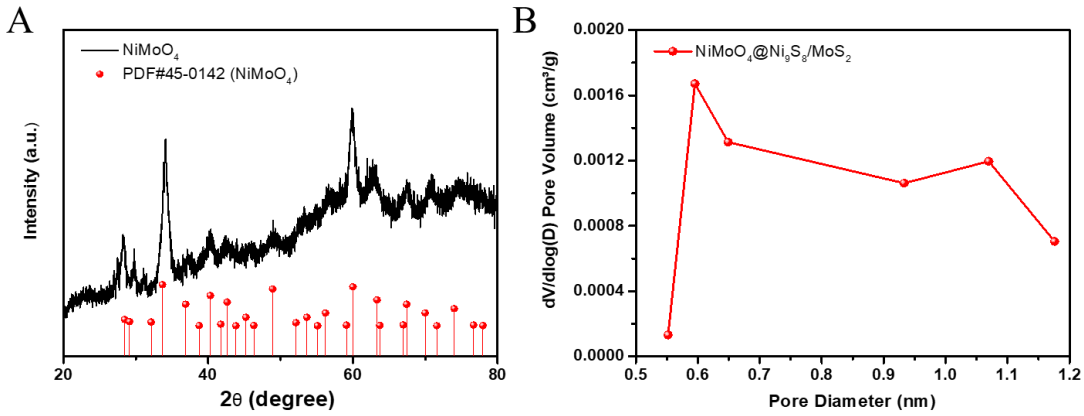

Figure S5. 6 (A) XRD pattern and Rietveld refinement of $NiMoO_4$; (B) Micropore size distribution profile of $NiMoO_4@Ni_9S_8/MoS_2$.

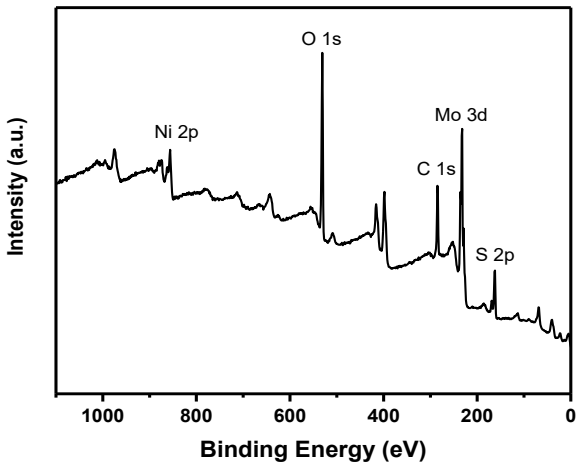

Figure S5. 7 XPS survey spectrum, and high resolution XPS spectrum of $NiMoO_4@Ni_9S_8/MoS_2$.

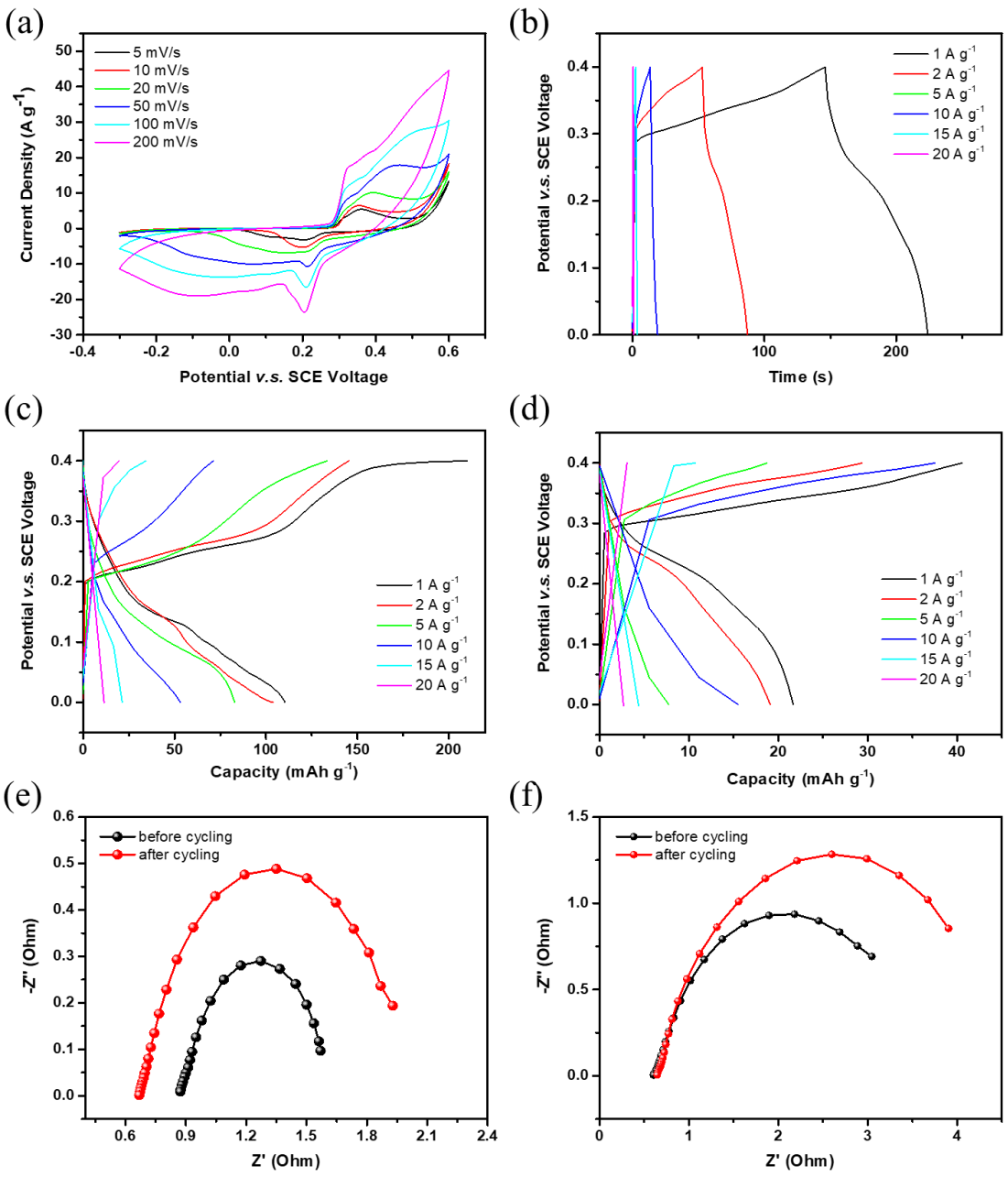

Figure S5. 8 (A) CV curves of $NiMoO_4$ at different scan rates; (B) GCD curves of $NiMoO_4$ at various current densities; Charge-discharge profiles of (C) $NiMoO_4$@Ni_9S_8/MoS_2 and (d) $NiMoO_4$ at different current densities; Nyquist plots of (E) $NiMoO_4$@Ni_9S_8/MoS_2 and (F) $NiMoO_4$ before and after cycling.